SLAC–272
UC-34D
(T/E)

Radiative Decays of the $\psi(3097)$ to Two Meson Final States *

Kevin F. Einsweiler

Stanford Linear Accelerator Center
Stanford University
Stanford, California 94305

May 1984

Prepared for the Department of Energy
under contract number DE-AC03-76SF00515

Printed in the United States of America. Available from the National Technical Information Service, U.S. Department of Commerce, 5285 Port Royal Road, Springfield, Virginia 22161. Price: Printed Copy A13, Microfiche A01.

---

* Ph. D. Dissertation.

Abstract

The MARK III detector operating at the SPEAR storage ring has recently acquired a sample of 2.7×10^6 produced $\psi(3097)$'s. These events are used to investigate the radiative decays of the ψ to two meson final states. Such decays are of topical interest because of the unusual QCD laboratory they provide—of particular interest is the possibility of observing 'glueball' states.

The process $\psi \to \gamma\pi^+\pi^-$ is studied. The $f(1270)$ tensor meson is observed and the helicity structure of its production is measured. The data indicate that helicity 2 is suppressed, in disagreement with lowest order QCD calculations. Evidence is presented for the first observation of the $\theta(1700)$ in the $\pi^+\pi^-$ final state. The strong, but not complete, suppression of this state in the $\pi\pi$ channel, combined with the absence of a $J^P = 2^+$ signal in a recent MARK III analysis of $\psi \to \gamma\rho\rho$, suggest a very mysterious nature for the $\theta(1700)$. Additional structure in the 2 GeV $\pi^+\pi^-$ mass region is also discussed.

The process $\psi \to \gamma K^+K^-$ is also studied. The $f'(1515)$ tensor meson is observed with a branching ratio in agreement with the $SU(3)$ symmetry prediction for the standard two gluon radiative decay diagram with no mixing corrections. The helicity structure of the $f'(1515)$ is measured for the first time, and is found to be similar to that of the $f(1270)$. The observation of helicity 2 suppression in both $f(1270)$ and $f'(1515)$ is difficult to explain by gluonic admixtures in their wave-functions.

The $\theta(1700)$ is observed with high statistics. Its spin and parity are measured, with the result that $J^P = 2^+$ is preferred over $J^P = 0^+$ at the 99.9% C.L. The helicity amplitude ratios for this state indicate approximately equal amplitudes for helicity 0, 1 and 2. This is in marked contrast to the results for the $f(1270)$ and $f'(1515)$ meson states.

In addition, evidence is presented for a remarkable narrow state, designated the $\xi(2220)$. Its parameters are measured to be:

$$m = 2.218 \pm 0.003 \pm 0.010 \text{ GeV} \quad , \quad \Gamma \leq 0.040 \text{ GeV at 95\% C.L.},$$

$$\text{BR}(\psi \to \gamma\xi(2220))\text{BR}(\xi(2220) \to \text{K}^+\text{K}^-) = (5.7 \pm 1.9 \pm 1.4) \times 10^{-5}.$$

The statistical significance of the signal is $\sim 5\sigma$, but the number of events observed is too small to allow a determination of the spin of the state. A signal is also seen in the K_SK_S channel with $\sim 2\sigma$ statistical significance, and limits are placed on the observation of the $\xi(2220)$ in other final states. Several plausible interpretations for this state exist, but none are compelling.

Acknowledgements

A project of the magnitude and complexity of the MARK III is the result of many individual contributions—too numerous to mention here...

I thank all of the MARK III collaboration for their contributions throughout the design, construction, and operation of the experiment—it has been a tremendously rewarding endeavor. The democratic, often unstructured, environment of the collaboration was occasionally frustrating but allowed the younger members of the group many opportunities, for which I am grateful. Special thanks go to my adviser, Bob Mozley, and to the group of friends and colleagues who, more than any others, made the experiment work and provided an atmosphere of collaboration and integrity: Rose Mary Baltrusaitis, John Brown, Ralph Fabrizio, Jeff Richman, Jimmy Roehrig, J.J. Russell, Tony Spadafora, Walter Toki, Norbert Wermes, and Bill Wisniewski. My debt to them is far too large to be acknowledged here. I also thank Marty Breidenbach and Dave Nelson for their endless supply of advice on detectors and electronics—without their aid, the MARK III would not have been the same experiment. The results in this thesis owe much to the SPEAR staff, in particular the enthusiastic machine operators Gary Johnston, Roz Pennacchi, and Jim Turner.

On a more personal level, I owe a great deal to the many friends who offered support and diversion over the long years of my graduate career. My heartfelt thanks go to Grant Bratrud, John Fox, Melissa Franklin, Eric Linstadt, Jan Lundgren, Jean Murray, Nan Phinney and Cathy Van Ingen. Their presence carried me through the bleak as well as the joyful days of the last six years. Finally, I thank my family for their advice and unwavering support throughout my time as a graduate student.

Table of Contents

List of Tables

List of Figures

Chapter 1. Introduction

1.1 Charm and the OZI Rule

A fourth quark, possessing a large mass, was a theoretical speculation long before it became an experimental fact. The idea was proposed by Bjorken and Glashow,[1] who invented the name 'charm', in 1964, as an extension of the highly successful 'eightfold way' of Gell-Mann and Ne'eman. The charmed quark found its first real application in the classic 1970 paper of Glashow, Iliopoulos and Maiani.[2] They showed that a fourth quark provided a natural mechanism for suppressing strangeness changing neutral currents. This was very desirable; the presence of neutral currents was essential for a gauge theory of weak interactions, but processes involving strangeness changing neutral currents were known to be very small. An example of such a process is:

$$K_L \to \mu^+\mu^- \quad \text{where} \quad BR(K_L \to \mu^+\mu^-) \sim 10^{-8}.$$

In a four quark model, this branching ratio is proportional to $G_F^2(m_c^2 - m_u^2)$. A calculation of this process by Gaillard and Lee[3] suggested a mass scale of $1 - 2$ GeV for the charm quark. A similar calculation for the K_L - K_S mass difference suggested the same mass scale.

Thus, the stage was set for the remarkable discovery of the J/ψ (hereafter referred to as the $\psi(3097)$) at both SPEAR and Brookhaven.[4] This was followed a mere ten days later by the discovery of a second state, the $\psi'(3685)$, at SPEAR. These states were remarkable for their very narrow width, and were confirmed to have $J^{PC} = 1^{--}$ and $I = 0$. They were associated with the 1^3S_1 and the 2^3S_1 bound states of the charm system. Subsequent studies, conducted largely at

e^+e^- colliding beam machines, have explored the rich structure of the $c\bar{c}$ system. Figure 1.1 shows a diagram of the levels as they are currently measured.

The previously known $^3S_1$ states are the $\rho(770)$, the $\omega(780)$, and the $\phi(1020)$. These states consist of u, d, and s quarks. The ρ and the ω are isospin eigenstates rather than pure $u\bar{u}$ or $d\bar{d}$ states. However, the $SU(3)$ nonet containing these states is almost ideally mixed and hence the $\phi(1020)$ is almost a pure $s\bar{s}$ state. The $\phi(1020)$ lies just above the threshold for decays to open strangeness, but it is a narrow resonance because there is very limited phase space available for its decay to strange particles. In the charm system, the dynamics is such that the $\psi(3095)$ and the $\psi'(3685)$ both lie below the threshold for open charm production. Thus, these states embody a previously unknown situation—they are narrow because their strong decays are all OZI suppressed.

The OZI mechanism was first proposed by Okubo[5] in 1963 to explain the suppression of $\phi(1020)$ decays to non-strange final states. In its original form, the OZI rule was a statement about the $SU(3)$ structure of the Hamiltonian for decays like $\phi \rightarrow 3\pi$. This form is indicated diagrammatically in Zweig's original pictorial notation in Fig. 1.2(a). In this figure, mesons or 'deuces' are represented by pairs of quarks or 'aces'. In the decay $\phi \rightarrow K^+K^-$, it is possible for the 'aces' to annihilate, leaving the vacuum projected onto itself. In the decay $\phi \rightarrow \rho^+\pi^-$, this annihilation is not possible and the matrix element vanishes. In this form, the OZI rule allows $\phi \rightarrow 3\pi$ only to the extent that the ω mixes with the ϕ, and introduces non-strange quarks into the ϕ. The OZI rule acquired a more refined definition through quark line diagrams. In this form, it is a statement that diagrams with 'detached' quark lines are suppressed, as shown in Fig. 1.2(b). Finally, within the framework of QCD, OZI suppression is described in terms of gluon counting and the relative smallness of α_s, the strong coupling constant. In this language, the decays of the $\psi(3097)$ are

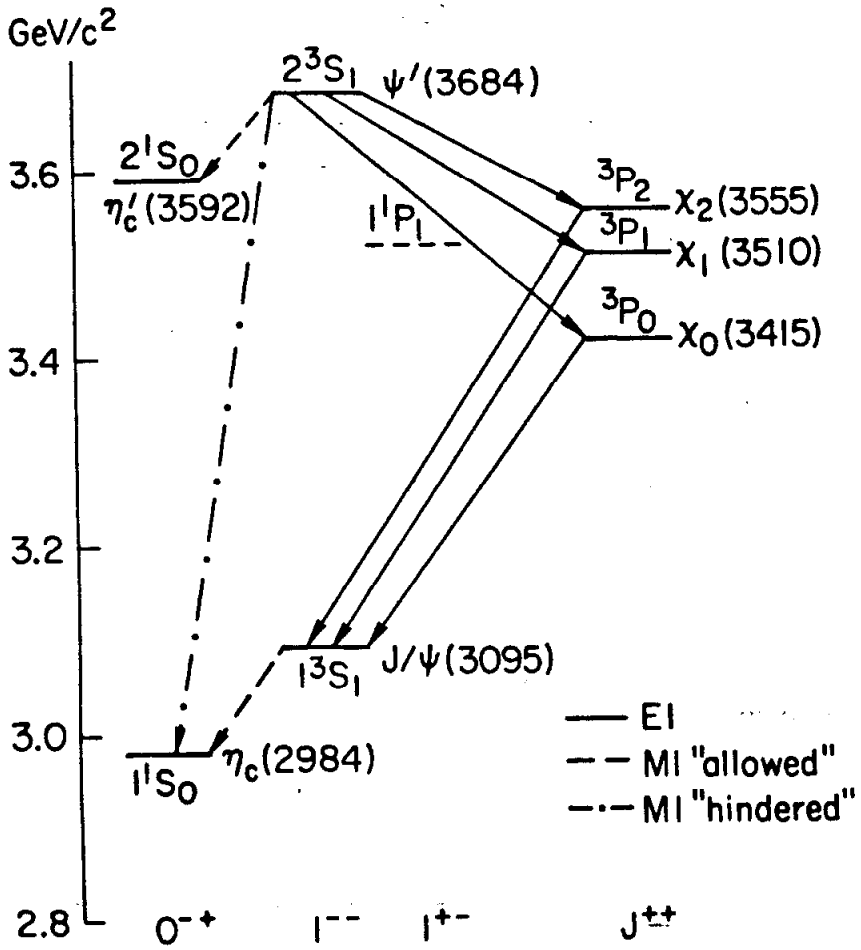

Figure 1.1. The Charmonium system. The status of the levels below charm threshold are shown. The $^1P_1$ state has not yet been observed.

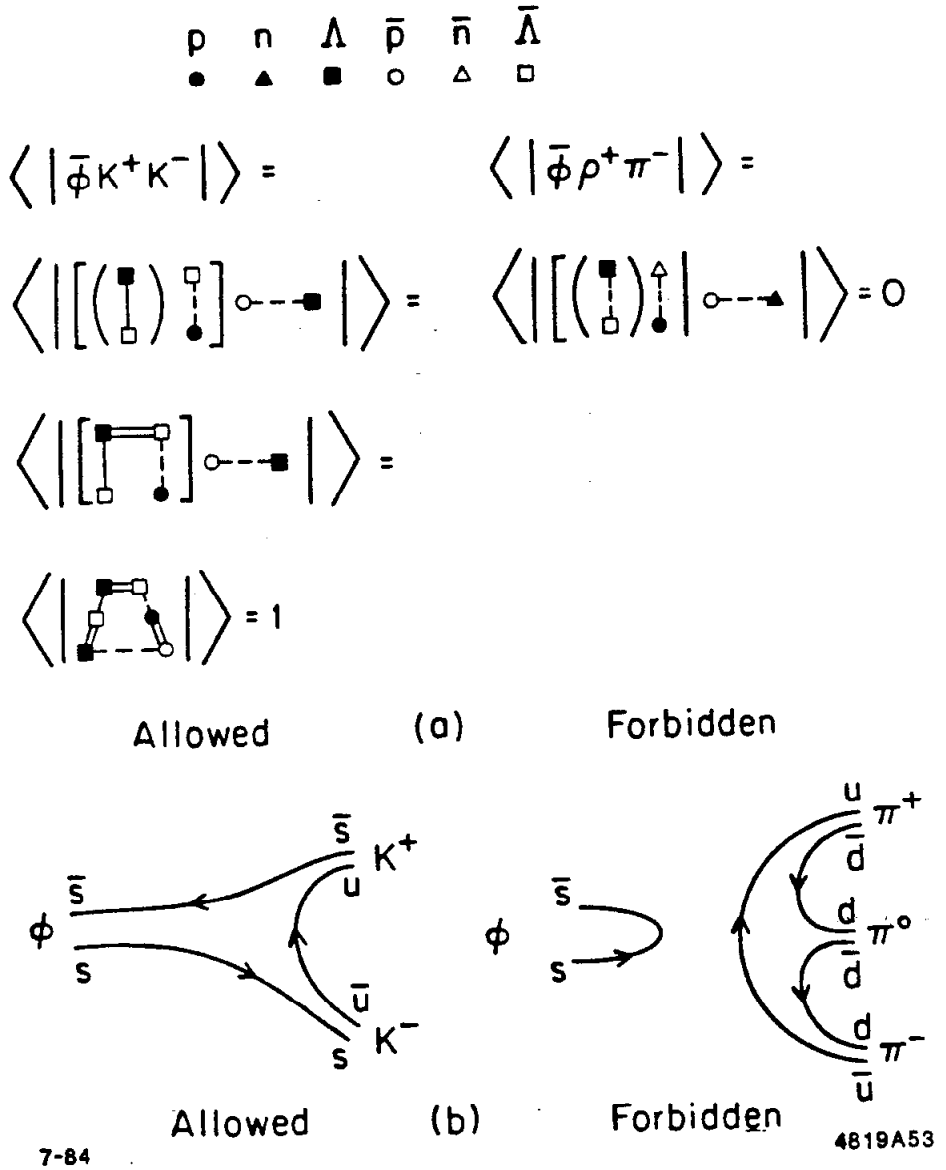

Figure 1.2. The OZI rule for $\phi(1020)$ decays. (a) shows the original formulation of Zweig. The symbols represent 'aces', now known as quarks, and the connecting lines represent binding energies. Both $SU(3)$ and electromagnetic symmetry breaking have occurred, and so all the 'aces' are distinct. (b) shows a more contemporary formulation in terms of quark line diagrams.

expected to proceed predominantly through the OZI suppressed strong diagrams shown in Fig. 1.3(c) and 1.3(d), and the electromagnetic decay diagrams shown in Fig. 1.3(a) and Fig. 1.3(b). Due to the strength of the OZI suppression, the electromagnetic decay rate of the $\psi(3097)$ to hadrons is only a factor of 5 smaller than its strong decay rate to hadrons—a remarkable situation for a meson with a mass of 3 GeV.

Assuming that the strong decay mechanisms for the $\psi(3097)$ are those shown in Fig. 1.3(c) and Fig. 1.3(d), it becomes possible to calculate the decay rates in the context of perturbative QCD. This was first done for $Q\bar{Q} \rightarrow 3g$, just prior to the discovery of the ψ, by Appelquist and Politzer.[6] Chanowitz added the calculation of $\psi \rightarrow \gamma 2g$.[7] The results are:

$$\Gamma(\psi \rightarrow 3g) = \frac{40}{81\pi}(\pi^2 - 9)\alpha_s^3 \frac{|\Psi(0)|^2}{M_\psi^2},$$

$$\Gamma(\psi \rightarrow \gamma 2g) = \frac{32}{9\pi}(\pi^2 - 9)\alpha_s^2 \alpha e_q^2 \frac{|\Psi(0)|^2}{M_\psi^2},$$

where e_q is the charge of the charm quark and $\Psi(0)$ is the radial wave-function at the origin. These calculations, when added together with those for the electromagnetic decays in Fig. 1.3(a) and Fig. 1.3(b), should give the total width of the $\psi(3097)$. Using the measured total width for the $\psi(3097)$, this allows a determination of the strong coupling constant:[8]

$$\alpha_s(M_\psi) = 0.19.$$

This value is somewhat smaller than would be expected from other sources. Improved calculations, including the next order in α_s, have been done by Mackenzie and Lepage.[9] Their results also indicate a small value for α_s.

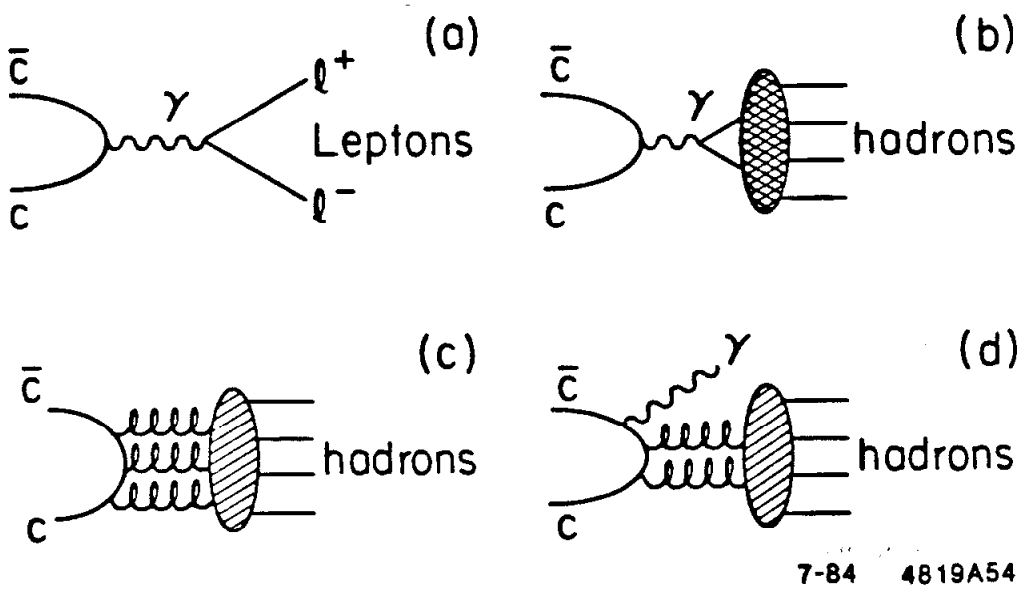

Figure 1.3. The $\psi(3097)$ decay mechanisms. (a) shows the electromagnetic decay to a lepton final state. (b) shows the electromagnetic decay to a hadron final state. (c) shows the QCD strong decay diagram. (d) shows the QCD strong radiative decay diagram.

1.2 RADIATIVE DECAYS OF THE $\psi(3097)$

The calculations just described predict a value for the relative rate for the radiative decays of the $\psi(3097)$:

$$\frac{\Gamma(\psi \to \gamma 2g)}{\Gamma(\psi \to 3g)} = \frac{36}{5} e_q^2 \frac{\alpha}{\alpha_s} \left[1 + \frac{2.2\alpha_s}{\pi} + \cdots\right].$$

This value includes higher order corrections from Brodsky *et al.*[10] Substituting the previous α_s value gives a value of 0.14 for the ratio. Correcting for the electromagnetic decays of the $\psi(3097)$ gives:

$$\mathrm{BR}(\psi \to \gamma 2\mathrm{g}) \sim 0.09.$$

Thus, a substantial fraction of all ψ decays are expected to proceed through the radiative decay diagram. The hadronic final states which are produced from the two gluon system will have $C = +$ and $I = 0$.

The inclusive photon spectrum for this decay can be calculated in analogy with the Ore-Powell calculation[11] for positronium decay to 3γ. The result[12] is a spectrum which increases almost linearly with $x_\gamma = 2E_\gamma/m_\psi = 1 - m_X^2/m_\psi^2$, where m_X is the mass of the two gluon system. The spectrum is shown in Fig. 1.4(a). This spectrum does not include the effects of resonances in the mass region displayed. It has been argued that the effects of resonances should agree, on the average, with the smooth field theoretic calculation. This goes under the label of 'duality', since the resonance and QCD-parton languages are viewed as complementary descriptions of the same phenomena. The inclusive photon spectrum has been measured,[13] and the data indicates a softer dependence as $x_\gamma \to 1$ than does the lowest order QCD calculation. This serves as an indication that lowest order QCD calculations in the ψ region should not be taken too literally. Nevertheless, such calculations may offer insight and lead to a qualitative understanding of the features of ψ radiative

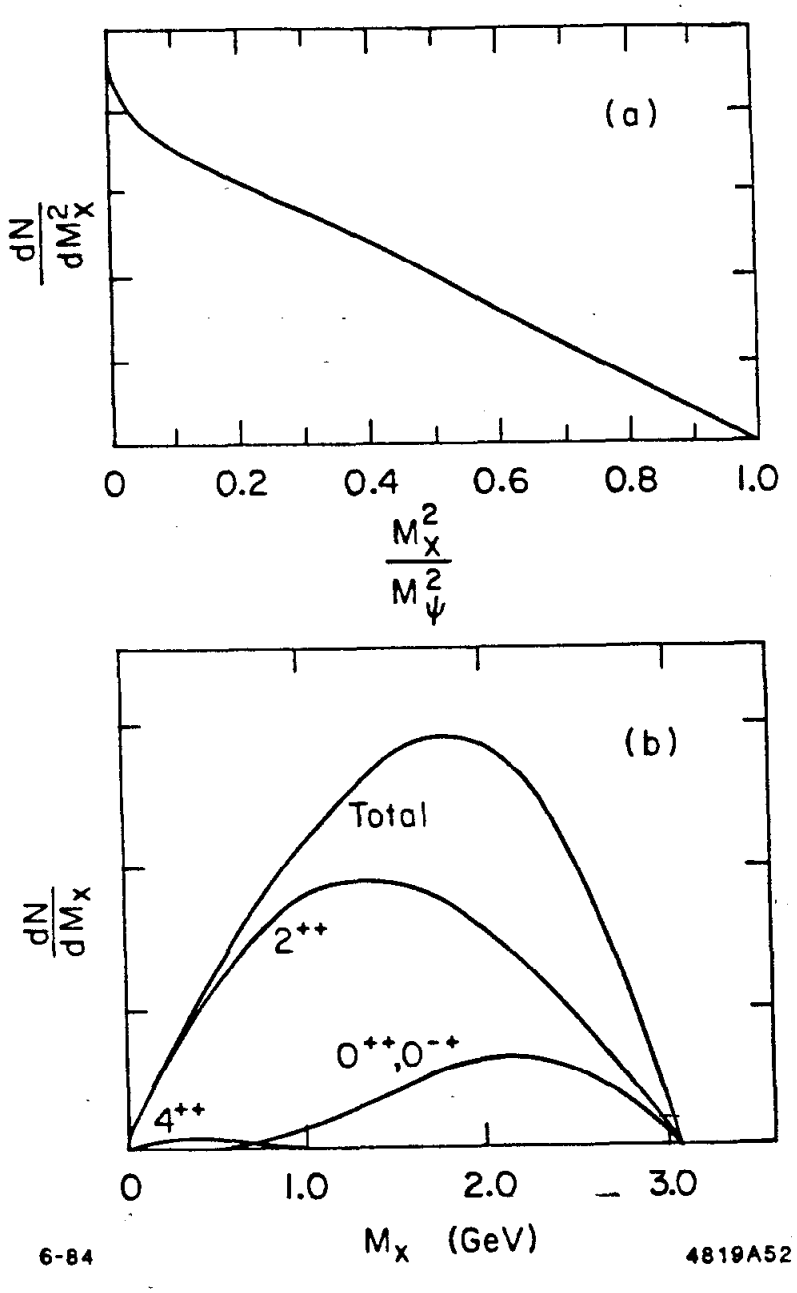

Figure 1.4. The photon spectrum for $\psi(3097)$ radiative decays. (a) shows the distribution in recoil mass expected for the decay $\psi \rightarrow \gamma X$. (b) shows the relative contributions to the spectrum from different spin-parities.

decays. A further step in this direction is a calculation performed by Billoire *et al.*[14] They carried out a spin-parity analysis of the produced two gluon system and found the results shown in Fig. 1.4(b). (Beware of the Jacobian $\sim m_X$ when comparing dN/dm_X^2 in Fig. 1.4(a) and dN/dm_x in Fig. 1.4(b)). The interesting features are the strong presence of $J^{PC} = 0^{++}, 0^{-+}$, and 2^{++} final states. The suppression of $J^{PC} = 1^{--}$ and 1^{-+} occurs because of the assumption of massless gluons—the coupling of $J^P = 1^-$ states to two massless vectors is forbidden by Yang's theorem. More complete calculations, including the effects of virtual gluons, indicate that the vector states may not be totally suppressed.

The discussion up to this point has concerned the perturbative regime, where the world is viewed as consisting of QCD partons—quarks and gluons. However, eventually these partons interact strongly and find themselves, with unit probability, as the mesons and baryons observed in the final state. This process is non-perturbative and very poorly understood, but one would like to describe some of the expected features.

The majority (if not all) of the observed meson spectrum appears to be well explained as bound states of $q\bar{q}$. This spectrum is described remarkably well by the quark model, which contains no gluon degrees of freedom. However, one of the more interesting consequences* of QCD is the prediction that glueballs, flavorless states of bound gluons containing no valence quarks, should exist. The possibility that

---

* The question of understanding to what extent observable glueballs are predicted by QCD is a subtle one. Perhaps the most rigorous evidence is that in $SU(3)$ lattice QCD without fermions, gluons are confined and there appears to be a 'mass gap', *i.e.*, a separation between the vacuum and the first gluonic bound state.[15] One then needs to argue that the presence of fermions in the theory may quantitatively change the spectrum, but will not affect the qualitative features.

such bound states could exist was first discussed by Fritzsch and Gell-Mann[16] in 1972, when QCD was just being created. It was not until 1977 that Brodsky *et al.*[12] made the suggestion that radiative ψ decays, because of their gluon content, were an excellent place to look for such unusual states. Since then, similar suggestions have been made by numerous other physicists. In addition, as Close[17] has pointed out, the kinds of resonances which may appear in radiative ψ decays are not limited to $q\bar{q}$ states and glueballs. Figure 1.5 shows four different resonant configurations where the 'hard' perturbative physics is represented by explicit parton lines and the 'soft' non-perturbative physics is represented by a blob. Besides finding the usual $q\bar{q}$ meson states, one would expect to see: glueballs—also known as gluonium or gluonic mesons, $q\bar{q}g$ states—also known as hermaphrodites, meiktons or hybrid mesons, and four quark states. It appears that the gluon rich channel $\psi \rightarrow \gamma X$ provides fertile ground for exploring unusual bound states.

One can then discuss what the expected characteristics of these unusual bound states might be. This is a controversial subject. It will be summarized here, and will be presented at greater length in a later chapter. The theoretical picture of glueballs has been widely studied, and will be briefly reviewed here. The discussion for hybrid mesons and four quark states is at least as controversial and will be deferred until later. The mass spectrum for glueballs cannot be calculated rigorously, but there are several models for estimating it. The most popular among these models are: lattice Monte Carlo models, bag models and potential models. These models all point to the conclusion that the lowest lying glueball states*

* Lattice models also suggest the presence of a 1^{-+} exotic 'oddball' among the low-lying states. It does not appear in the ground state spectrum of the bag or potential models because, in their language, three gluons are required to construct it.

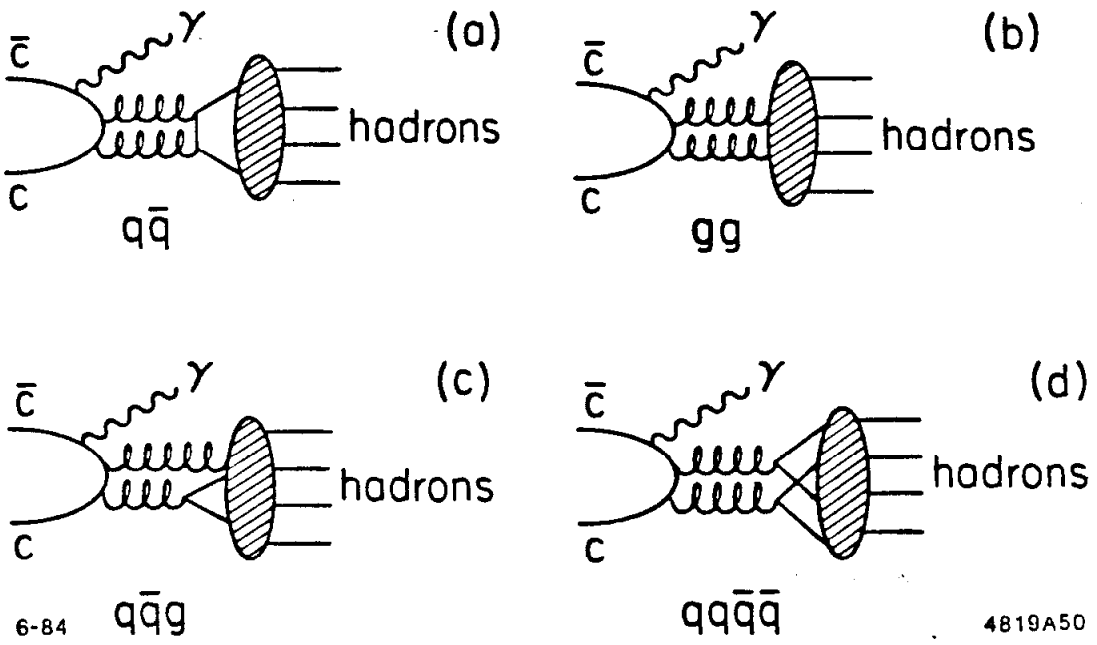

Figure 1.5. Different resonant configurations in radiative ψ decay. (a) shows a case where a $q\bar{q}$ state is produced. (b) shows a case where a gg state is produced. (c) shows a case where a $q\bar{q}g$ state is produced. (d) shows a case where a $qq\bar{q}\bar{q}$ state is produced.

have $J^{PC} = 0^{++}, 0^{-+}, 2^{++}$ and lie in the $1 - 2$ GeV region. These are just the spin-parities which, according to Fig. 1.4(b), are expected to have the largest cross-section in ψ radiative decays. However, this mass region is already dense with poorly understood radial and orbital excitations of the usual $q\bar{q}$ mesons. This means that to isolate a glueball, one first needs to distinguish the state from possible $q\bar{q}$ excitations, and then one needs to contend with the problem of mixing with nearby states with the same J^P.

It can be concluded that the mass of a glueball is not particularly distinctive, and there is a need to look for additional clues. Glueballs are flavorless and they should decay in the manner expected for an $SU(3)$ singlet. This is useful because Nature seems to prefer ideally mixed $q\bar{q}$ nonets, and $SU(3)$ singlets are unusual. For example, the $I = 0$ members of an ideally mixed nonet, *e.g.*, the $f(1270)$ and the $f'(1515)$, are neither $SU(3)$ singlet nor $SU(3)$ octet and they decay into either all non-strange or all strange final states. Unfortunately, the simple $SU(3)$ singlet expectation for a glueball can be considerably modified by additional dynamics, and probably cannot be relied upon. It has also been predicted that glueballs should be narrow, with widths of tens of MeV. This is because their decays are partially OZI suppressed. This argument may fail in the presence of mixing with $q\bar{q}$ states, and has been criticized even for pure glueball states.

It seems that all the observable characteristics for glueball states appear to be somewhat less than reliably determined. Perhaps the most that can be expected is that, on a case by case basis, there will be enough signs pointing in the direction of a glueball interpretation to lead to a definite conclusion. This ambiguous situation has been described by Gottfried[18] in the following manner:

> By simply staring at the Hamiltonian of QCD we cannot tell whether or not low-lying hadrons will be dominantly states

> with gluons as constituents, just as the structure of solids is hardly evident from a visual inspection of the Hamiltonian of interacting electrons, nuclei, and photons. In both cases little headway could be made without experimental exploration, though on occasion the theoretical priesthood delivers itself of an oracle that proves to be a good omen. In our endeavor there is a further problem: While a toddler in diapers knows whether an object is solid, it may turn out that only those who have gone through a long apprenticeship under messianic tutelage will have the wisdom to know a gluonic state from a conventional hadron.

With this 'squishy' theoretical situation[19] in mind, we turn to the current experimental situation.

1.3 Experimental Results on Radiative ψ Decays

The experimental study of the radiative decays of the $\psi(3097)$ has proven to be very fruitful, although somewhat inconclusive. In the previous section, it was claimed that $J^{PC} = 0^{++}, 0^{-+}, 2^{++}$ would dominate the $\psi \to \gamma X$ final state. The best studied final states are those containing two or three pseudoscalars. The two pseudoscalar final state (*e.g.*, $\pi\pi$, $K\bar{K}$, $\eta\eta$) is accessible to $J^{PC} = 0^{++}, 2^{++}$. The three pseudoscalar state (*e.g.*, $K\bar{K}\pi$, $\eta\pi\pi$) is accessible to $J^{PC} = 0^{-+}$.

Thus far, there is no evidence for 0^{++} states in radiative $\psi(3097)$ decays. The only well established $I = 0$ state is the $S^*(975)$, and it appears to be notably absent from radiative decays. This is somewhat surprising, but could have something to do with the possible four quark identity of the $S^*(975)$.

In the 0^{-+} channel, the isoscalar η and η' appear with large branching ratios. The η' is the second largest radiative branching ratio of the $\psi(3097)$. A

surprising new state, the $\iota(1440)$, is also observed. This state has been seen in the $K\bar{K}\pi$ decay mode by both the MARK II experiment[20] and the Crystal Ball experiment.[21] The signal seen by Crystal Ball is shown in Fig. 1.6(a). It currently has the distinction of being the largest radiative decay mode of the $\psi(3097)$ to a non-charmed final state, in spite of the fact that it has only been observed in one decay mode. It has been suggested that, due to this large branching ratio and the lack of strong evidence for the $\iota(1440)$ in other experiments, it may be a glueball. However, the situation is far from definitive.

In the 2^{++} channel, the $f(1270)$ appears very prominently in the $\pi\pi$ channel. The signals seen by the Crystal Ball experiment[22] and MARK II experiment[23] are shown in Fig. 1.6(b). The $f'(1515)$ has been seen by the MARK II experiment[24] in the K^+K^- final state, as shown in Fig. 1.7(b). Once again, there is a surprising new state observed: the $\theta(1700)$. This state was first seen in the $\eta\eta$ decay mode by the Crystal Ball experiment,[25] as shown in Fig. 1.7(a). It has also been seen by the MARK II experiment,[24,26] as shown in Fig. 1.7(b). Both experiments have searched for a $\theta(1700)$ signal in the $\pi\pi$ mode but it is apparent from Fig. 1.6(b) that there is no prominent signal. The $\theta(1700)$ has also been suggested as a glueball candidate, but the situation is murky.

The physics analyses which will be presented here include detailed studies of several two pseudoscalar meson channels. The $\pi^+\pi^-$, K^+K^- and K_SK_S channels will be investigated with the goal of improving the present understanding of the $f(1270)$ and $f'(1515)$ tensor mesons, as well as the mysterious $\theta(1700)$ state.

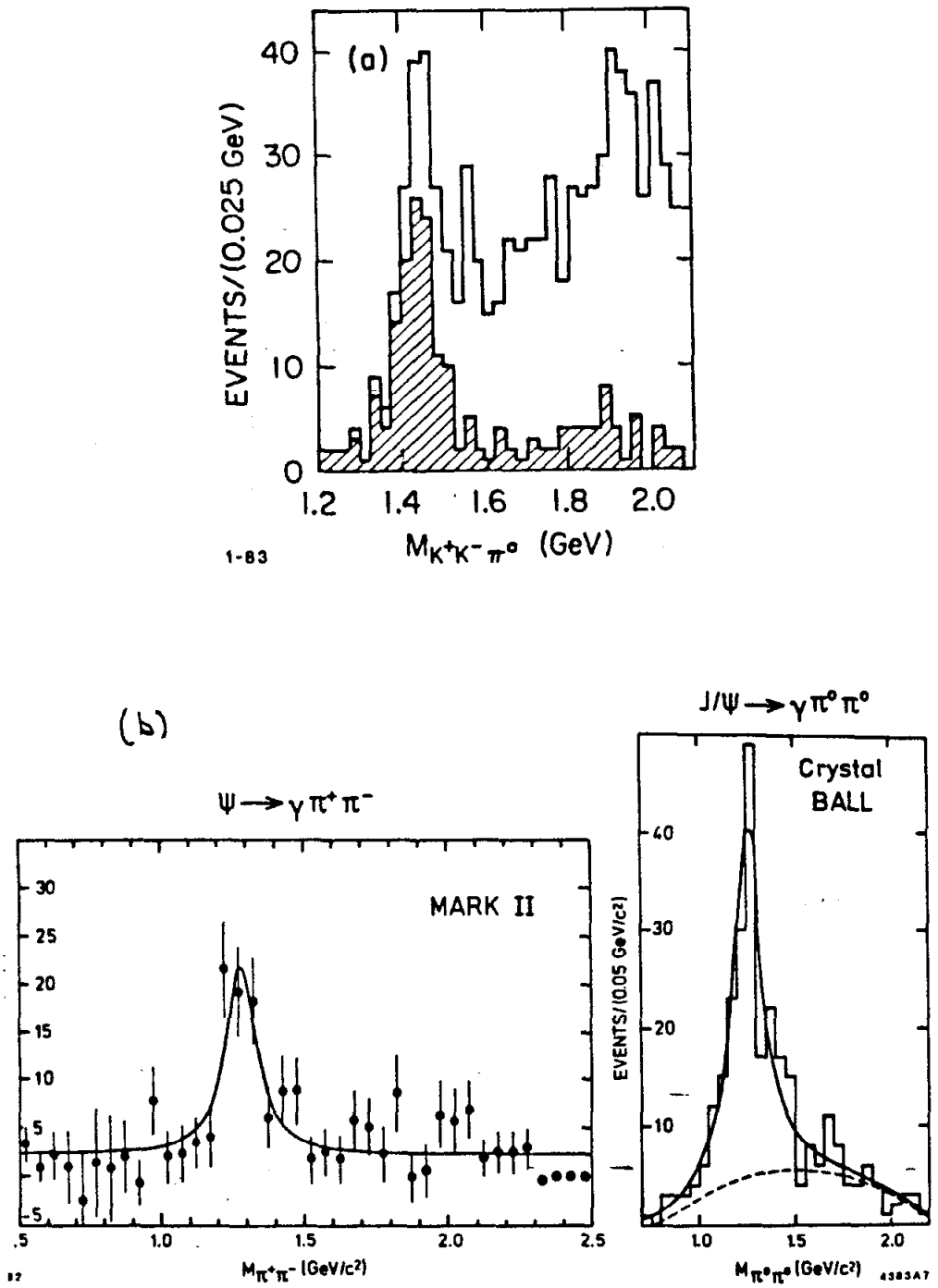

Figure 1.6. The $K\bar{K}\pi$ and $\pi\pi$ final states. (a) is the Crystal Ball $\iota(1440)$ signal in $K^+K^-\pi^0$. (b) shows both the Crystal Ball and the MARK II signals in the $\pi\pi$ final state.

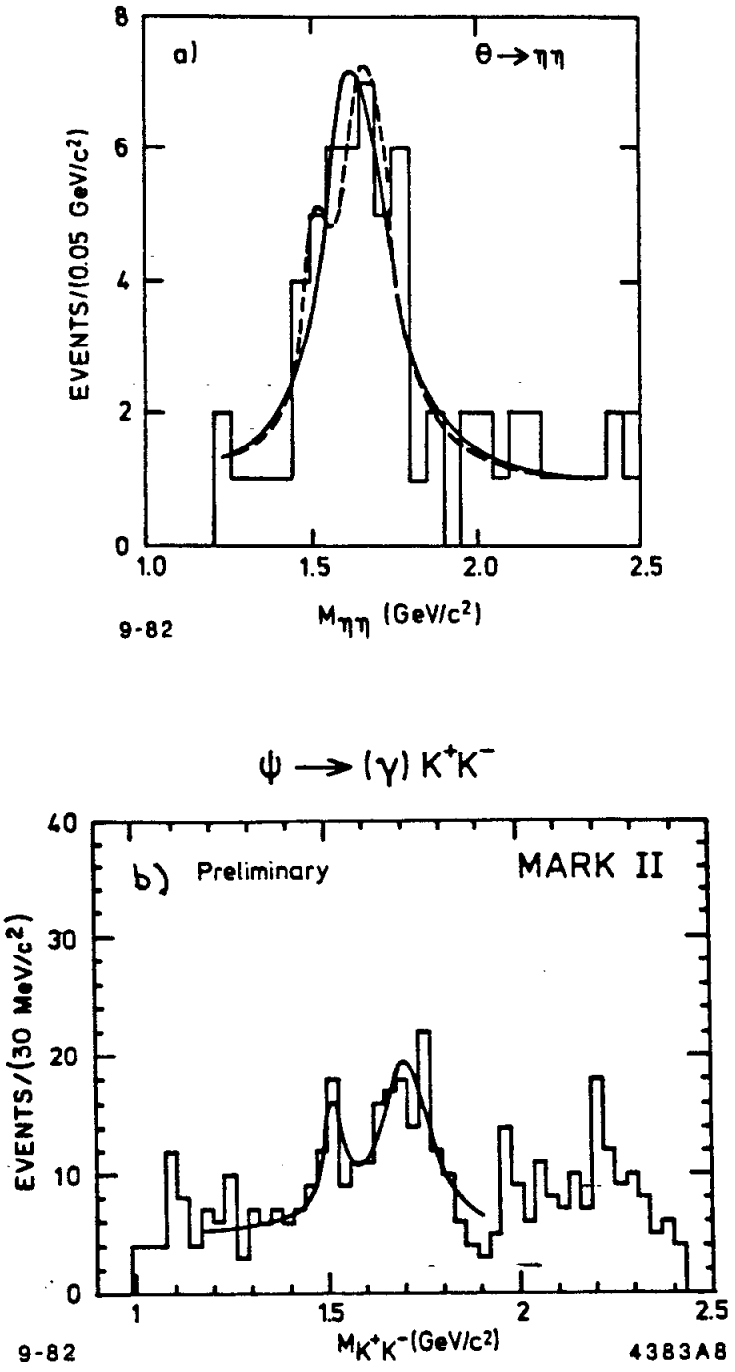

Figure 1.7. The $\theta(1700)$ signals seen by Crystal Ball and MARK II. (a) shows the Crystal Ball result in the $\eta\eta$ final state. (b) shows the MARK II result, including the $f'(1515)$, in the K^+K^- final state.

Chapter 2. The Apparatus

This chapter gives a brief introduction to the apparatus used to perform the experiment. A lightning review of SPEAR is presented, followed by a detailed description of the MARK III detector. The individual components of the detector will be discussed in conjunction with the associated analysis software. Finally, a brief chronology is offered.

2.1 THE SPEAR STORAGE RING

The SPEAR storage ring is an electron-positron annihilation ring in which counter-rotating bunches cross in each of two interaction regions. It is a relatively small ring, with a bend radius of ~ 32 meters. This gives it a characteristic crossing period of 781 nsecs. The bunches typically contain $\sim 10^{11}$ electrons or positrons and produce a peak luminosity of $\mathcal{L} = (4-5)\times 10^{29}\ \mathrm{cm}^{-2}\mathrm{sec}^{-1}$ at the $\psi(3097)$. The energy spread of the beams is determined by quantum fluctuations and is $\sigma_E \sim 0.7$ MeV at the $\psi(3097)$. This is unfortunate because the natural width of the $\psi(3097)$ is 0.063 ± 0.009 MeV, and so the apparent cross-section is reduced by roughly a factor of ten from the true cross-section. The peak hadronic cross-section measured at SPEAR is about 2200 nb, corresponding to a $\psi(3097)$ production rate of ~ 1 Hz. This should be compared with the total hadronic cross-section just below the $\psi(3097)$, which is a factor of 100 smaller.

The size of the beams at the interaction point, for the $\psi(3097)$ running conditions, is:

$$\sigma_x \sim 0.4\ \mathrm{mm} \quad , \quad \sigma_y \sim 0.03\ \mathrm{mm} \quad , \quad \sigma_z \sim 26\ \mathrm{mm}.$$

The horizontal beam size is determined by synchrotron radiation losses and the vertical beam size is determined by the coupling between the horizontal and vertical

oscillations in the ring.

2.2 THE MARK III DETECTOR

The MARK III detector is a general purpose magnetic detector whose design has been optimized for the SPEAR energy region. The goal is the complete reconstruction of exclusive final states. The mean charged multiplicity, as well as the mean neutral multiplicity, is about 4. The momentum spectrum for both charged and neutral tracks is very soft, with the average being well below 500 MeV. The salient features required of a detector in this energy region are:

1. Efficient reconstruction for complete final states requires a large solid angle for both charged and neutral tracks. The MARK III has a charged track solid angle coverage of 85% of 4π and a neutral track coverage of 94% of 4π.

2. Photon measurements must be made with high efficiency, as well as good angular resolution, for low energy photons. The MARK III shower counter is placed inside the solenoidal coil to minimize the material in front of the shower counter, and it is finely segmented to provide good angular resolution.

3. Charged track momentum measurements should be optimized for low momentum. This means that the material prior to the drift chamber should be kept to a minimum in order to reduce multiple scattering. The MARK III has a beryllium beam pipe and a low mass trigger chamber in order to achieve this goal.

4. Good particle identification is required for the charged tracks. There are several aspects of the MARK III which reflect this goal:

   (a) The time of flight system was optimized for the best time resolution, providing good $\pi/K/p$ separation.

(b) The shower counter is highly segmented to aid in electron/hadron separation.

(c) dE/dx measurements are made in the drift chamber to provide an independent means of π/K separation.

(d) There are two layers of steel and muon counters outside the solenoidal coil for muon/hadron separation.

The detector design which resulted from these considerations is shown in the axial view in Fig. 2.1, and in the transverse view in Fig. 2.2. The coordinate system to be used for future reference is: the x axis is in the horizontal plane and points towards the center of the ring, the y axis is vertical, and the z axis is along the direction of the positron beam in the ring. This Cartesian system has corresponding cylindrical and spherical coordinate systems which are more convenient for detector and analysis discussions.

The individual components of the detector have been described in detail elsewhere,[27] and the current discussion will offer a summary of each detector element. An attempt is made to discuss the detector elements on several levels in order to emphasize the linkage between the detector hardware, the reconstruction software, and the Monte Carlo modeling.

2.3 THE DRIFT CHAMBER

The MARK III drift chamber[28] consists of two sections: the trigger chamber and the main drift chamber. The main drift chamber is further divided into seven separate layers of cells sharing a common gas volume. The chamber is immersed in a uniform 4 kG magnetic field supplied by a conventional solenoidal coil.

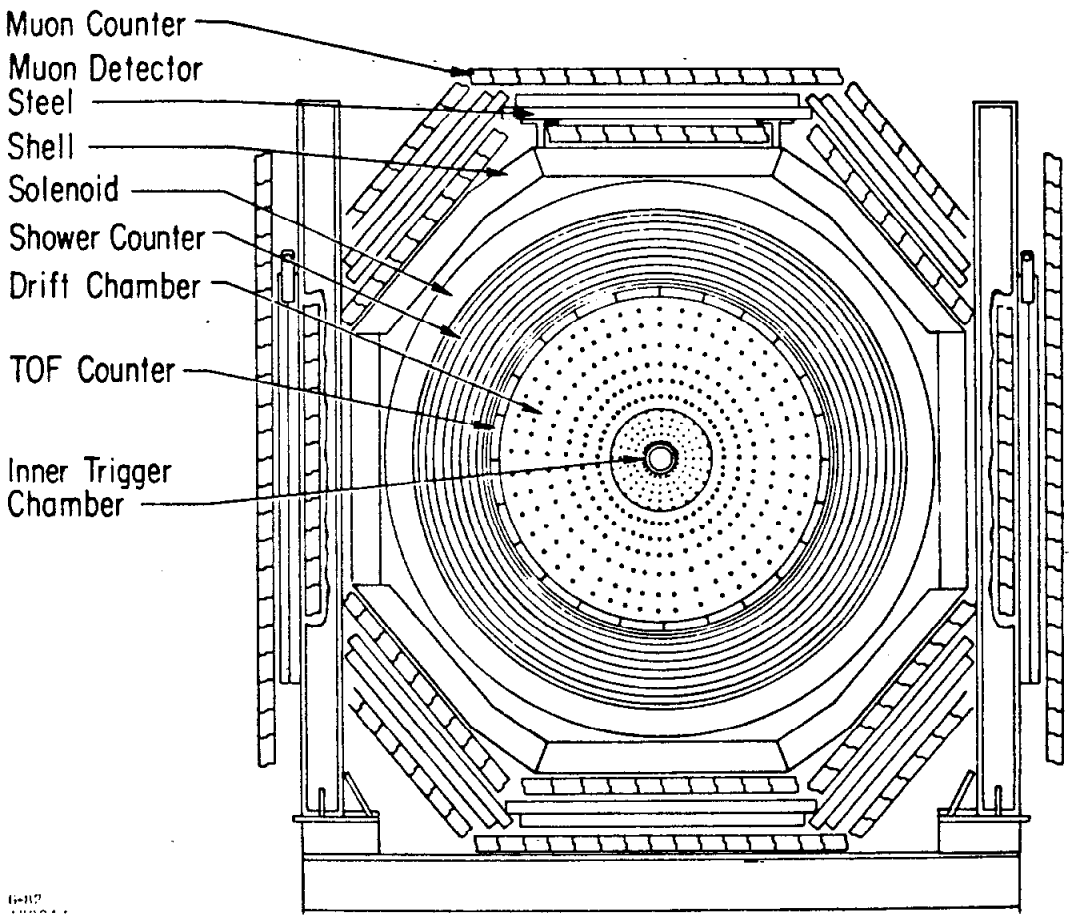

Figure 2.1. The axial view of the MARK III detector.

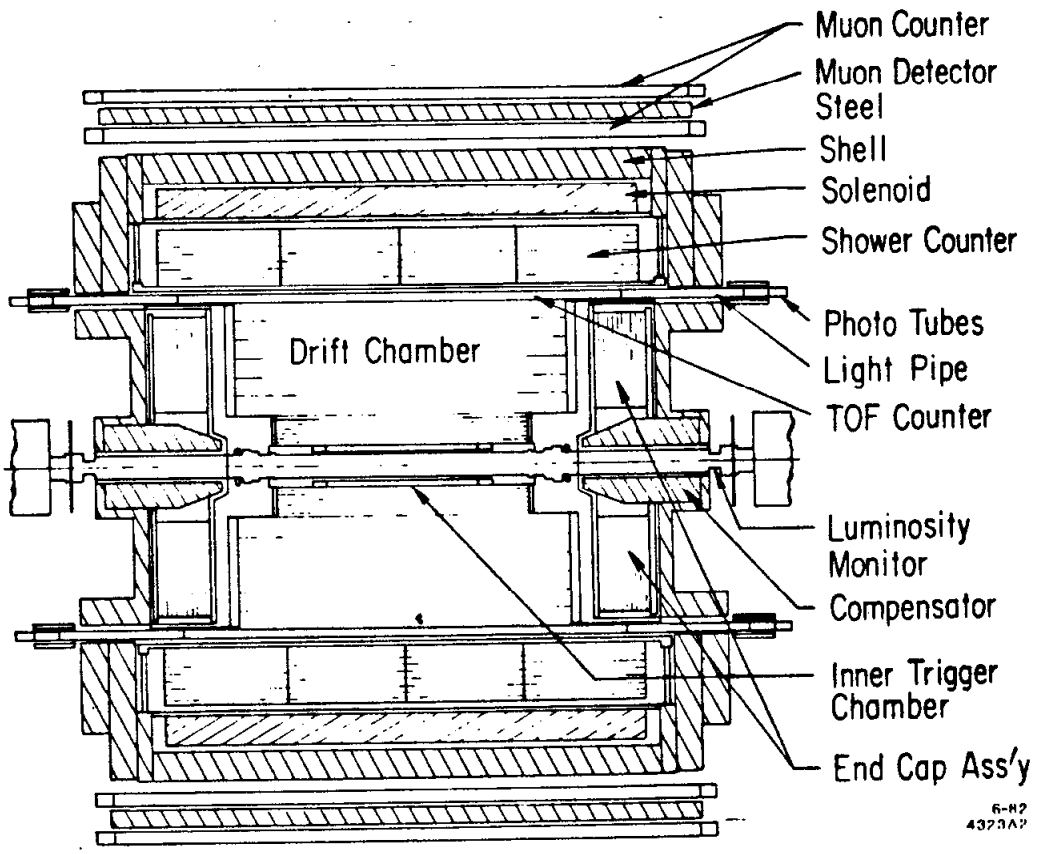

Figure 2.2. The transverse view of the MARK III detector.

The trigger chamber, also known as layer 1, is shown in an axial view in Fig. 2.3(a). The chamber consists of 4 sub-layers, each containing 32 cells arranged in a cylinder 1.10 meters in length. The sense wires are stainless steel and allow a z measurement using the current division technique. The cells in alternate layers are staggered by one half cell, making the sum of the drift times from two adjacent layers approximately constant, as shown in Fig. 2.3(b). This time sum is used in the trigger to provide better timing information than would be possible using the individual times.

A section of the endplate for the main drift chamber is shown in Fig. 2.3(c), indicating the presence of seven layers of cells. Five of these layers are axial and two, layers 4 and 6, are stereo, with angles of $+7.7°$ and $-9.0°$ respectively. The number of cells in a given layer is 16 times the number of that layer (*e.g.*, 48 cells in layer 3). There are two types of cells: one type, found in layer 2, contains 15 field wires adjacent to 13 sense wires and 2 guard wires. The other type, found in the outer layers, contains 5 field wires adjacent to 3 sense wires and 2 guard wires. In order to aid in resolving the left-right ambiguity within a given cell, the sense wires are staggered about the cell centerline. This stagger is ± 150 μm in layer 2 and ± 400 μm in the other layers. In addition to the timing measurements which are made on all the sense wires, two other groups of measurements are made. In layer 2, the pulse height on each sense wire is measured in order to find the dE/dx for the track. In layers 3, 5 and 7, the induced pulse on the guard wires is measured in order to find a z position using the current division technique.

The drift chamber signals are first discriminated for time measurements or amplified for pulse height measurements, and then fed to the next level of electronics. This electronics consists of a multi-hit time-amplitude converter (MTAC) or a sample-hold module (MSHAM). These modules store the time/amplitude

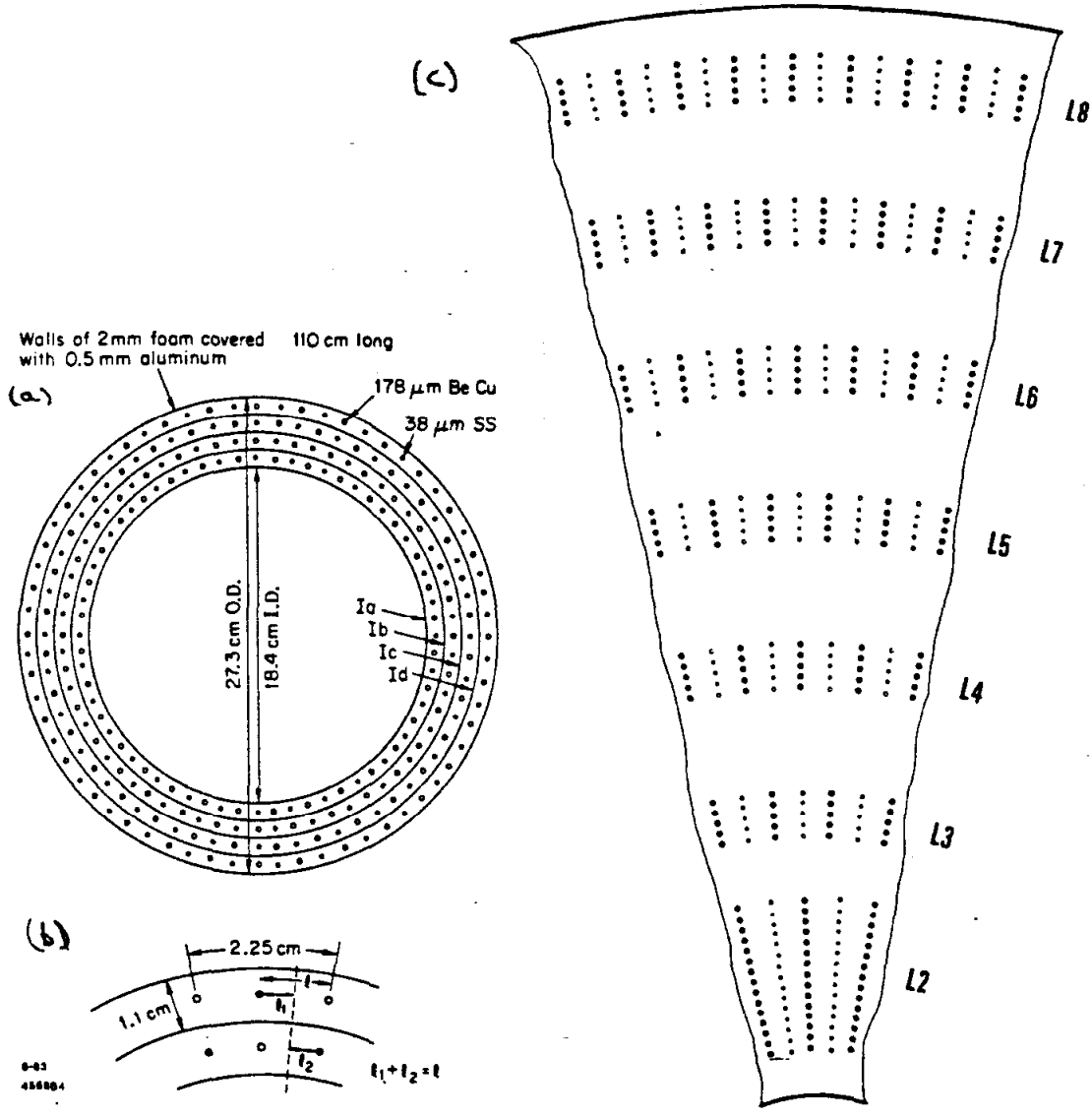

Figure 2.3. The MARK III drift chamber. (a) shows the trigger chamber in an axial view. (b) shows a detail of the half-cell offset in the trigger chamber. (c) shows a section of the endplate of the main drift chamber.

information on internal capacitors which are buffered and read out by a smart processor, the Brilliant ADC (BADC). This processor performs simple quadratic corrections to the data and suppresses the un-hit channels.

The measured quantities in the (r, ϕ) plane are drift times. In order to produce the corresponding spatial locations, several corrections need to be applied. The times are individually corrected for cable variations, etc., using a t_0 subtraction. A time to distance conversion function, describing the drift properties of the cell in several regions, is then used to find the correct spatial location within the cell. Finally, the wire locations are used to produce a true location. The reconstruction program next performs pattern recognition on the wire information to assemble track candidates. This is done by constructing a direction for each cell in the (r, ϕ) plane using the information from the three sense wires in the outer cells. Only the axial layers are used, and their cell vectors are connected together to form tracks. Finally, a search is made to associate information from the stereo cells and the current division with the track candidate in the (r, ϕ) plane. Once the three dimensional track candidates exist, they are fit by a precision helix fitting program which includes numerous corrections for: exact wire locations, electrostatic deflection of the sense wires, gravitational sagging, multiple scattering, etc. The result of this lengthy procedure is a set of tracks whose resolution is given by:

$$\sigma_p/p = 0.015\sqrt{1+p^2}, \quad p \text{ in GeV},$$

$$\sigma_\theta = 2 \text{ mrad} \quad , \quad \sigma_\phi = 10 \text{ mrad}.$$

This resolution is available over a solid angle of 85% of 4π. The spatial resolution for individual wires is found to be:

$$\sigma_x \sim 300\ \mu m \quad \text{in layers 1-2,}$$

$$\sigma_x \sim 225\ \mu m \quad \text{in layers 3-8,}$$

and the current division information has $\sigma_z/z \sim 1\%$.

The modeling of the drift chamber seeks to take Monte Carlo 4-vectors and produce the corresponding raw data in such a way that all the measurement errors and correlations are correctly embodied. This can be done fairly accurately and simply because, at the level of the raw data (*i.e.*, the time measurements), the drift chamber behavior is well modeled by a series of independent measurements with Gaussian errors. The influence of other factors, such as correlated hits or extra hits, is relatively small. The procedure is to perform the inverse of the reconstruction process: trace the path of the track in space, convert the spatial points to time measurements with the inverse of the time to distance relationship used in the reconstruction program, and then smear the time measurements with the proper errors. This procedure includes dE/dx losses in the detector material as well as multiple scattering, and the result is a Monte Carlo drift chamber model which is a good approximation to the real data.

The agreement with the data has been checked by using clean samples of events, such as $\psi \rightarrow \rho\pi$ and $\psi \rightarrow \mu^+\mu^-$. Since subsequent analyses will perform kinematic fits, it is important that the Monte Carlo describes not only the efficiency and resolution of the drift chamber, but also that it reproduce the correct correlated error matrix for each reconstructed track. This has been studied in detail, and the agreement between Monte Carlo data and real data, within the fiducial volume of .85 of 4π, is good.

2.4 The Time of Flight System

The time of flight system for the MARK III detector[29] consists of 48 scintillation counters, each 5.1 cm thick and 317.5 cm long. The counters cover

a total of 80% of 4π and are made of Nuclear Enterprises Pilot F scintillator. The thickness of the counters was chosen to give the best possible resolution. A thickness of $\sim$ 5 cm provides a good match between the available phase space in the phototube/light-guide system and the scintillator—increases beyond this value should give little additional improvement. The design of the light guides placed at each end of the counters was optimized to minimize the time dispersion for the early photons which are most important for the time measurement. At the end of the light guide, a 2 inch diameter Amperex XP2020 phototube is attached and shielded from the residual magnetic field by layers of mu metal and soft steel. The signal from the phototube is sent to a discriminator/time-amplitude converter/sample-hold module for measurement. This module makes timing measurements at two different discriminator thresholds and also measures the total charge of the pulse. These modules are in turn read out by a smart processor (BADC) which performs quadratic corrections and suppresses un-hit channels.

The combination of two time measurements and a pulse height measurement for each end of the counters allows greater freedom in extracting the best TOF measurement, and results in improved resolution. The TOF measurement is made relative to a beam pick-off signal derived from an electrode on the SPEAR beampipe. The calibration of the electronics is done using a series of calibrated delay cables, and the stability of the entire system is monitored using a nitrogen laser coupled to the scintillators by fiber optic cables.

The reconstruction program for the TOF system is straight forward, and consists largely of myriad corrections which must be systematically applied to the raw measurements in order to produce the optimal time resolution.[30] These corrections are derived using Bhabha events, since they are plentiful and monochromatic. The corrections consist of a pedestal subtraction, pulse height

corrections which are polynomial in the measured charge, and z corrections which are again polynomial. The application of this procedure results in the distribution for the measured time minus the expected time shown in Fig. 2.4(a). This plot indicates the resolution, averaged over all counters, which is obtained for a well-identified pion sample from the $\psi(3097)$. The resolution is measured to be 190 psecs for hadrons, and corresponds to the particle separation capability displayed in Fig. 2.4(b). Figure 2.4(b) is a scatter plot of the particle velocity measured by TOF versus the particle momentum measured by the drift chamber. One finds that π/K separation at the 2σ level is possible at momenta up to 1.0 GeV.

The modeling of the TOF system would appear to be a simple task, but it is in fact quite complex. The quantity which needs to be modeled correctly is the distribution of measured times. A typical analysis requires that a given track be consistent or inconsistent with a given particle hypothesis. In order to ascertain the efficiency for such a cut, the tails of the time distribution need to be correctly simulated. In addition, the inefficiencies caused by overlapping tracks must be accounted for.

The simulation generates a charge and a time at each phototube for a drift chamber track which hits a TOF counter. The charge distribution at the phototube is generated using average attenuation lengths and a Gaussian distribution. The time measurement is more difficult to generate. It is well known that this time distribution has non-Gaussian tails, as is apparent in Fig. 2.4(a). There are many sources for this effect, including: anomalous pulse shapes due to energy deposition/light collection fluctuations, fluctuations in the time measurement, etc. None of these effects are well understood or easily modeled. An additional difficulty arises from the location of the TOF counters in the MARK III detector. Since they are just inside the shower counter, the pulse height which is measured in the

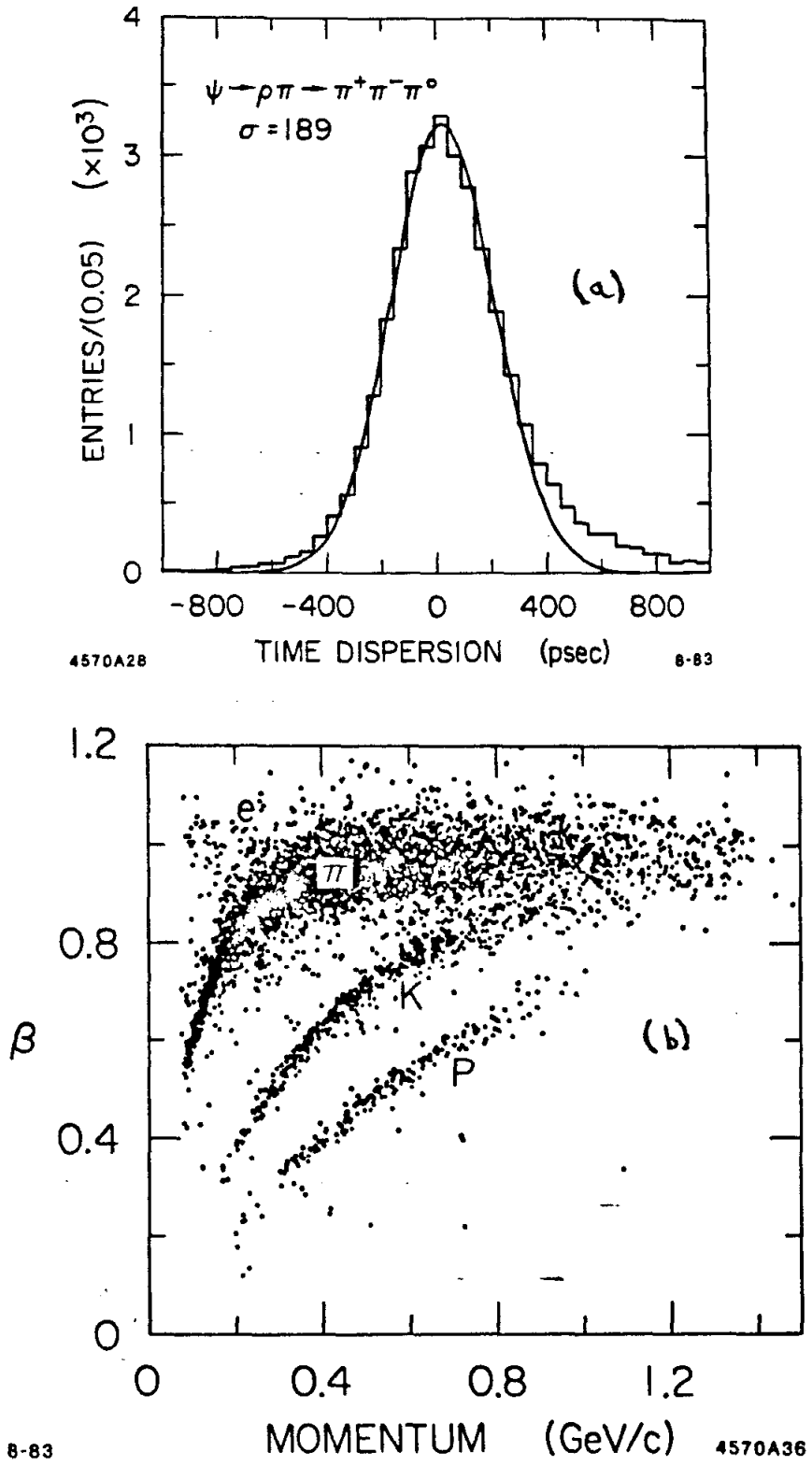

Figure 2.4. The performance of the MARK III TOF system. (a) shows the resolution obtained on a pure pion sample. (b) shows the separation of different particle types versus momentum.

scintillator will often be much larger than that expected for a minimum ionizing track, due to backscatter from the shower counter. Such an effect is very hard to model, especially for interacting hadrons. The effect is apparent in the data as a variation in the time resolution for different incident particle types: electrons, muons or hadrons. The solution used by MARK III is to take an empirical distribution for the events in the tails, parameterize it and coax the Monte Carlo to reproduce it. The model which has been used includes a Gaussian core with additional uniform tails. Events are generated with empirically derived weights for each component of the model. This gives a Monte Carlo time distribution which has a non-Gaussian component in addition to the usual Gaussian component, and models the real data fairly accurately. The accuracy of the model has been tested by studying event samples, such as $\psi \rightarrow \rho\pi$ and $\psi \rightarrow \mu^+\mu^-$, which can be isolated without using TOF information. With such samples, the time distributions can be directly compared with the Monte Carlo. A further check has been made using the $\psi \rightarrow K^+K^-\pi^0$ channel and comparing the particle identification available from a kinematic fit with that available from the TOF system.

2.5 THE SHOWER COUNTER

The shower counter for the MARK III detector[31] consists of three physically separate pieces: two endcap shower counters, encompassing 17% of 4π between them, and a barrel shower counter covering 76% of 4π. There were several stringent criteria which shaped the design of this device. The shower counter was to cover as much solid angle as possible with a uniform detection structure. It was to be efficient for photons with energies below 100 MeV, and still have good angular resolution. It was also desirable to have very fine segmentation to aid in separating low energy electrons from pions. The energy resolution was of less importance because for exclusive analyses, poor energy resolution can be largely

compensated for by good angular resolution. Initially, both a lead/scintillator design and a lead/proportional tube design were considered. The lead/proportional tube design proved to be more practical and economical as well as possessing much better segmentation, although with some sacrifice in energy resolution. The design which resulted was novel in several ways, and is shown schematically in Fig. 2.5.

The barrel shower counter is a truly cylindrical device with no dead regions in azimuth. It is built upon an aluminum spool, using 0.5 radiation length lead sheets sandwiched between thin layers of aluminum for strength. There are 320 cells per layer, with 24 layers, corresponding to 12 radiation lengths or about 1/3 of an interaction length, in total. The cells are formed by aluminum I beams which are placed between the lead/aluminum sandwiches. These I beams are supported at intermediate points by aluminum ribs, as shown in Fig. 2.5(a). The lead/aluminum sheets are attached to the spool, one layer at a time, by stainless steel straps.

The sense wires are made of stainless steel in order to allow use of current division to establish the z position. The wires are read out by integrated amplifier/sample-hold electronics (ISHAM) mounted directly on the detector. In order to limit the total number of electronics channels, the 24 physical samples are reduced to 12 segments. The first 6 segments correspond to individual layers, whereas the last 6 segments consist of groups of three layers ganged together. Once again, the sample-hold electronics is read out by a smart processor (BADC). The data is corrected for non-linearities in the electronics and un-hit channels are suppressed.

The endcap shower counter construction is similar to that of the barrel, although much simpler due to the planar geometry. The detailed layout is shown in Fig. 2.5(b). The detector again consists of alternating layers of lead and proportional tubes. In the endcap case, the cells are made of extruded aluminum tubes which are

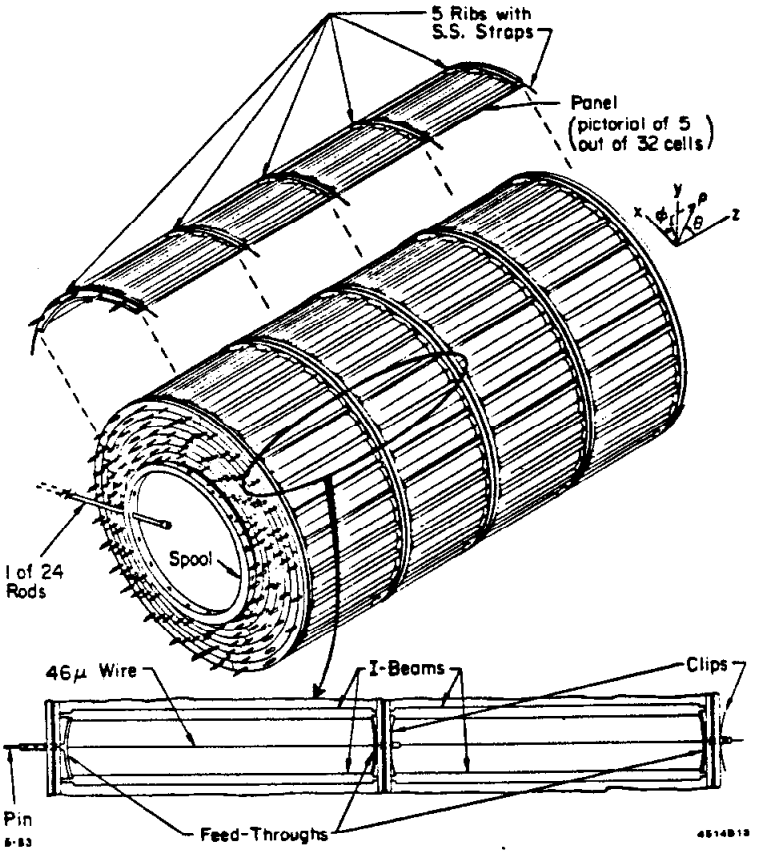

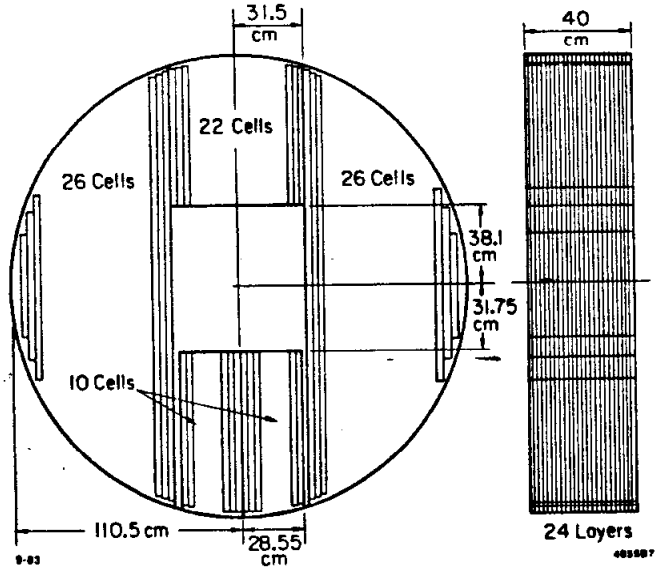

Figure 2.5. The MARK III shower counter. (a) shows the barrel shower counter. (b) shows one of the endcap shower counters.

glued to the lead sheets. Stainless steel wires are strung in the tubes and supported by feed-throughs in the ends of the tubes.

When an electromagnetically interacting particle is incident on the shower counter, it produces a shower. This shower typically deposits a total pulse height in the gas sampling layers which is equivalent to 1 minimum ionizing particle per 10 MeV of incident energy. This pulse height is distributed over a number of cells; typically about 35 cells are hit for a 1 GeV shower. The design of the shower counter produces two quantities per cell: a current division position measurement and a total energy measurement. When this information is combined with the location of the cell, the result is a three dimensional point with an associated energy. This 'space-point' measurement capability, when combined with the highly segmented readout, provides a very powerful pattern recognition ability, since there are no ambiguities to resolve.

The definition of a photon in the shower counter is much more ambiguous than that of a charged track in the drift chamber. This is due to the irregular and fragmented patterns of energy deposited in the shower counter. It is especially true for photons below about 0.5 GeV in energy, where the shower fluctuations prevent the formation of the dense core of deposited energy, surrounded by a halo of smaller deposited energy, which characterizes high energy showers. For this reason, the shower counter reconstruction program is initially concerned with making qualitative pattern recognition decisions. The pattern recognition starts by associating the input 'space-points' into 'clusters' using simple adjacency criteria. In order to obtain the maximum efficiency for low energy photons, the pattern recognition procedure uses a very minimal definition for these initial clusters—they need only contain two space points, both of which need to have current division measurements. This process will be described in more detail for the barrel; the

endcaps are treated in an identical manner. The clustering is first performed by using only the cell information, corresponding to the ϕ coordinate in the barrel. This coordinate has 'digital' errors, since either a cell is hit or not hit, making the clustering simple and unambiguous. The primitive ϕ clusters are then explored in the current division coordinate, corresponding to z in the barrel. This coordinate has 'analog' errors as well as suffering from ambiguities when two tracks hit the same cell at different z positions. A not un-common situation is when two photons with different z positions hit the same ϕ region in the barrel. In this case, there will usually appear to be three visible 'clusters' of energy: two at the correct z positions for those cells hit by tracks from only one of the showers, and an intermediate cluster from cells hit by tracks from both incident photons. In this case, the intermediate points are not allowed to form an independent cluster, but are distributed among the two real clusters. Complications such as this make the pattern recognition task in the z direction more difficult.

Once the simple clustering has been performed in (z, ϕ), a more complex algorithm is used to explore the three dimensional structure of the photon candidate. At this state, the pattern recognition problem has several contradictory goals. For photons, it will want to separate overlapping showers, but it will not want to isolate fragments of the same photon. For hadrons, the pattern of energy deposit is already very fragmentary and further splitting is not desirable. The three dimensional algorithm is defined to make use of the shower development process, which proceeds radially outward, to make additional decisions about the photon candidates. After all of these pattern recognition decisions have been made, the remaining clusters are fitted to extract the best position and energy measurement for each cluster. The positions of the fitted clusters are then compared with the charged track information from the drift chamber, and associations are made with these tracks when the

clusters are close enough to the charged track entry point. The remaining clusters are then promoted to the status of 'photons', and it is these objects, with their associated measurements, which will be used for further analysis.

The resolutions and efficiencies for the shower counter system have been studied using Bhabhas and photons. Figure 2.6(a) shows a plot of the measured photon energy for $\psi \rightarrow \rho\pi \rightarrow \gamma\gamma\pi^+\pi^-$ events versus the energy predicted for one of the photons using a kinematic fit. This indicates that the shower counter has a linear energy response. The measured resolutions are:

$$\sigma_E = 0.18\sqrt{E(\mathrm{GeV})},$$

$$\sigma_\phi = 7 \text{ mrad} \quad , \quad \sigma_\theta = 20 \text{ mrad}.$$

The efficiency of the shower counter versus energy has been determined in a similar manner. The plot shown in Fig. 2.6(b) was extracted from $\psi \rightarrow \rho^0\pi^0$ events by studying the energy distribution for the monochromatic π^0. This curve indicates the single most important feature of the MARK III shower counter: it has a high efficiency for detecting photons with an energy above 50 MeV. When this high efficiency is combined with the powerful pattern recognition capabilities and good angular resolutions, the result is the ability to reconstruct exclusive final states with up to 5 photons. This is a significant improvement over previous detectors working in this energy region.

Unfortunately, this complex, high performance shower counter has a price. It is extremely difficult to model it correctly. The major problem arises because of the gas sampling technique. The density of the gas sampling medium is $\sim .1\%$ of the density of the lead. This means that the energy measurement is being made by sampling a tiny fraction of the total electromagnetic energy. The situation is made more difficult by the fact that the proportional tubes are a very imperfect

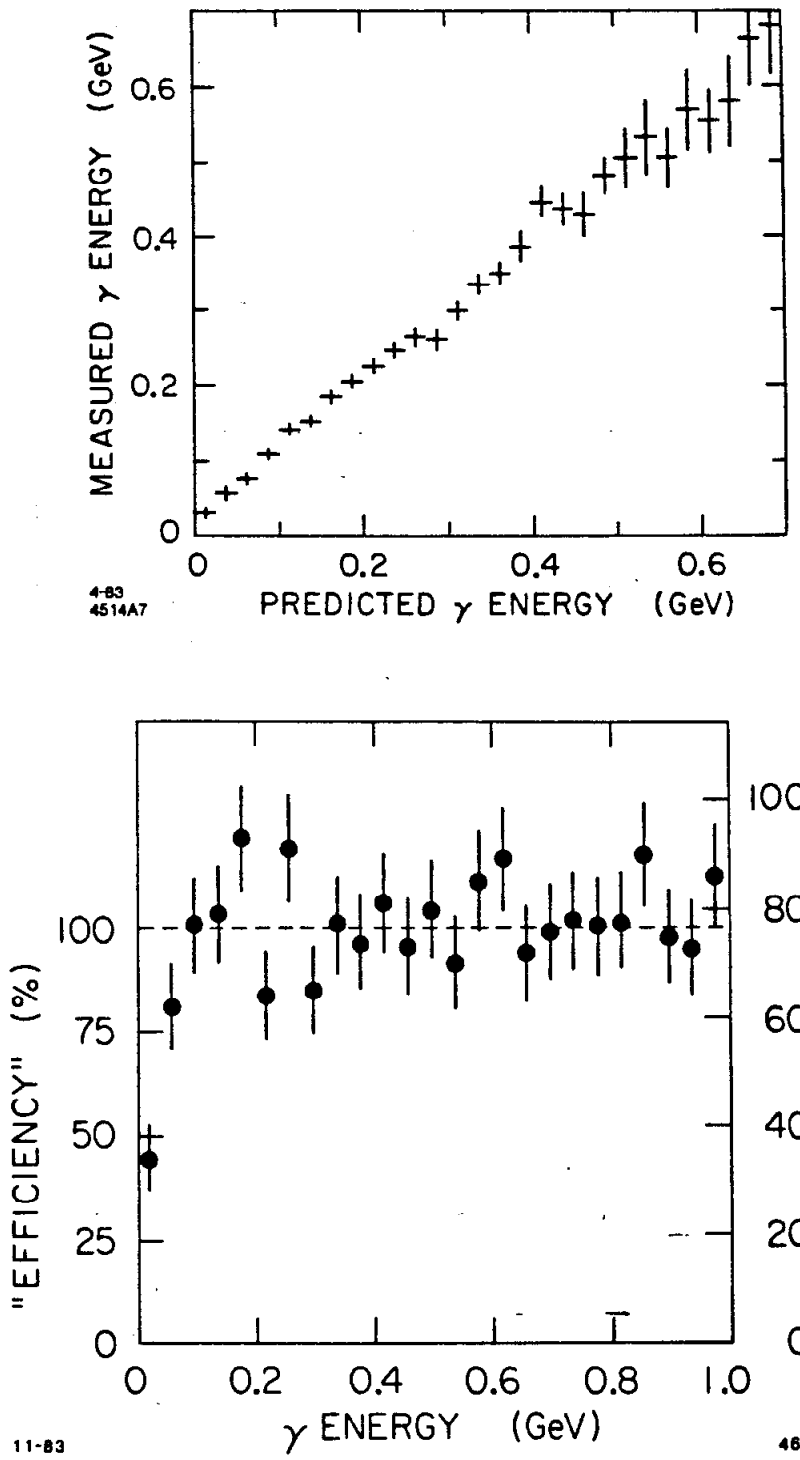

Figure 2.6. The performance of the MARK III shower counter. (a) shows a plot of the measured versus the expected energy for a highly constrained hadronic final state. (b) shows the detection efficiency as a function of energy.

sampling device—the energy deposited by a charged track passing through the gas is subject to Landau fluctuations. These fluctuations arise because of the nature of the energy loss process in a thin sample. The distribution of deposited energy has two components. The first is a broad 'Gaussian' body with a width of: FWHM/mean $\sim 50-100\%$ arising from statistical fluctuations in the number of soft collisions. In these soft collisions, the gas atom as a whole absorbs a virtual photon which in turn ionizes the atom. Even in a thin gas sample, there are many such collisions and the resulting distribution is well-behaved. The second component is a long tail arising from Rutherford scattering off of quasi-free atomic electrons. These hard collisions occur infrequently and result in a large energy loss per collision, hence contributing a tail of Landau fluctuations to the energy deposition. The energy deposited by low energy photons is an additional complication. A single photon with an energy of 10 KeV can deposit all of its energy in the gas, giving a pulse height equivalent to 5 minimum ionizing particles. This means that this 10 KeV photon can produce an energy deposit which is as large as that of a 50 MeV photon. Such confusion about very low energy photons makes the detector more sensitive to complications from fragments of hadronic showers. All of these factors combine to give a very complex shower counter behavior, not readily simulated.

The current model for the shower counter is limited in scope. There is no attempt to create the effects of hadronic interactions—only the electromagnetic showers are simulated. There are two shower generation procedures, one is simple and somewhat empirical while the other incorporates the full EGS3 shower simulation package. These two procedures provide a relatively accurate description of the shower counter performance in terms of energy and position resolutions. They provide a less accurate picture of the low energy photon efficiency, although this is a topic of continued study. The difficulties arise below 100 MeV, where the photon

efficiency is difficult to measure accurately, and do not affect any of the analyses described here.

The problem with 'hadronic split-offs'—detached fragments of hadronic showers—has been encountered previously by detectors such as the Crystal Ball, and is enhanced by the large resonant πN and KN cross-sections that occur at low momentum. The confusion about the total energy of very low energy photons, when combined with the sensitivity of the shower counter to any photons below 100 MeV, leads to the presence of extra 'fake' photons which are not associated with electronics noise, but correspond to real, although ambiguous, physics in the detector. These 'fake' photons are the most difficult problem associated with this shower counter. There presence is not only a problem for detector modeling, but also a serious problem for physics analysis. In the absence of any reasonable algorithm for dealing with these 'fake' photons, the approach used is to consider all photons in the event analysis. It is then possible to use the kinematics of the event to try to decide which are the 'real' and which are the 'fake' photons. This process has been studied for the large decay mode $\psi \rightarrow \rho\pi$. The technique is very successful, and some statistics on the magnitude of the extra photon problem are: approximately 35% of the $\rho\pi$ events contain an extra gamma with a measured energy of 20 MeV or more. If one excludes gammas inside of cones around charged tracks, defined so that the angle between the charged track entry in the shower counter and the gamma position $\cos\theta_{ch-\gamma} > .95$, then about 10% of the $\rho\pi$ events contain an extra gamma.

2.6 The Muon System

Outside of the octagonal steel flux return, there are two layers of proportional tubes which serve as muon counters. These counters cover 65% of 4π and are sensitive to muons above a momentum of ~ 0.7 GeV.

2.7 THE TRIGGER AND DATA ACQUISITION

The MARK III trigger decision is based on information provided by the TOF counters and the drift chamber. The trigger has been described in a previous publication,[32] and is reviewed here. Due to the short SPEAR crossing period of 781 nsecs, the triggering system is implemented as a hierarchy of levels, each involving a more complex trigger decision. The trigger controls the reset generation for the electronics, as well as notifying the on-line computer that a trigger has occurred.

The lowest level decision, known as level 0, must take place within one beam crossing period to avoid deadtime. The decision must be made by 590 nsecs after the beam crossing to allow time to reset storage capacitors in the sample-hold electronics before the next beam crossing. This is a serious limitation because the drift times in the outer drift cells are too large to allow their use in this decision. Therefore, the decision is based on the time sum from the trigger chamber as well as the signals from the TOF counters. Two parallel triggers are developed at this level. The first trigger, known as the '1 track' trigger, requires a single TOF counter as well as a single in-time cell pair from the trigger chamber. The TOF counter requirement in this trigger allows the event time to be accurately determined, and so a narrow time window of $\sim$ 30 nsecs can be used to reject out of time cosmic rays. The second trigger, known as the '2 track' trigger, requires two in-time cell pairs in the trigger chamber, but makes no TOF requirement. This trigger is forced to use a wider time window of $\sim$ 80 nsecs to account for the width of the time sum calculated from the trigger chamber. This width comes from a combination of drift velocity variations in the trigger chamber cells, and variations due to track curvature. The level 0 trigger usually runs at $\sim$ 3 KHz, producing a reduction of $\sim 10^3$ from the actual crossing rate.

If there is a level 0 trigger, then the normal electronics reset sequence is

delayed for one beam crossing period while the next decision level is considered. This decision uses the trigger chamber information from level 0 and extrapolates it through layers 3 and 5 in the outer drift chamber to form more complex track candidates in the (r, ϕ) plane. This track finding is done very quickly ($\sim$ 25 nsecs) by using programmable array logic to form triple coincidences, as shown in Fig. 2.7. In order for a layer 3 or 5 cell to participate in this process, it is necessary that two of the three possible sense wires have hits. The track candidates are counted and used to make the trigger decision. The '1 track' trigger requires the presence of one level 1 track, whereas the '2 track' trigger requires two such tracks. There is an additional level 2 trigger which searches for tracks in the z projection, but it was not required for $\psi(3097)$ running. The level 1 trigger typically runs at $\sim$ 3 Hz at the $\psi(3097)$.

Once there is a level 1 trigger, the reset sequence is inhibited, and the BADC processors start their digitization procedure. Each BADC is responsible for digitizing, formatting and correcting 500 – 2000 channels of analog information. This process typically takes about 15 msecs, and is carried out in parallel for all the detector systems. While the BADC's are digesting the analog data for the event, the on-line computer is interrupted. The on-line computer for this experiment is a VAX-780 processor which uses an intelligent I/O processor to implement a powerful CAMAC interface. This interface allows largely autonomous acquisition capability with very little CPU intervention. When the on-line computer is interrupted, it instructs the I/O processor to begin the event read out. The I/O processor first reads out the trigger information for the event, since it is available immediately. It then interrogates the BADC's responsible for the smaller detector systems and reads them out as they finish their tasks. Finally, after all the BADC's have been read out, the last operation performed is to re-enable the trigger to accept the next

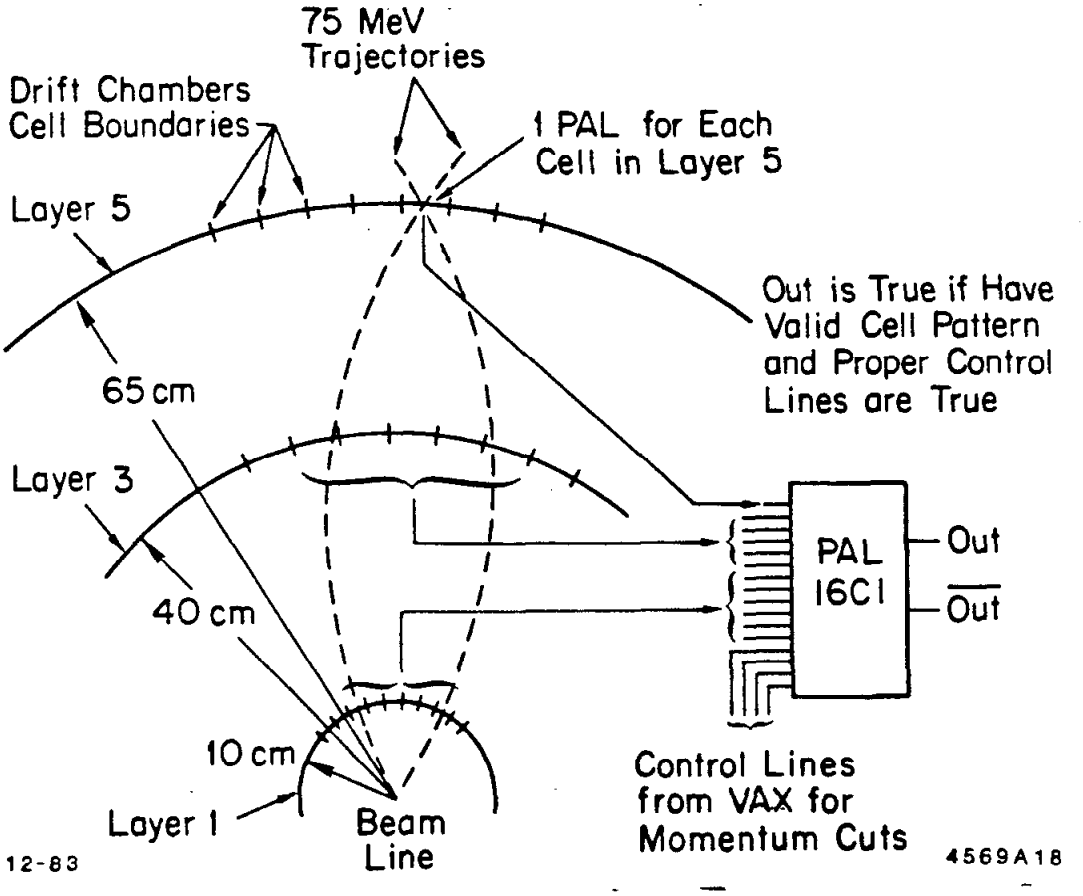

Figure 2.7. The Level 1 trigger logic. This figure indicates, in a schematic way, the formation of the drift chamber trigger decision.

event. The on-line computer then takes control again, finishes formatting the event and writes it out to tape.

This completes the immediate responsibility of the on-line computer, but in order to insure that the data is free of problems, a large analysis program is also executing. This program samples the acquired events as frequently as the available CPU time allows, generating displays, accumulating histograms, and generally entertaining the physicists on shift. In addition to these diagnostic tasks, the on-line computer is also used to perform frequent calibrations of the analog electronics. Such calibrations are performed several times per day, and the results are used to update the BADC correction constants and compensate for electronics drifts. This on-line calibration and correction is very useful for diagnostic purposes and also assures that the data which is recorded on magnetic tape will require a minimal amount* of off-line massaging before being fed to the reconstruction programs.

2.8 A Brief Chronology

In the beginning, there was a proposal. The proposal for the MARK III experiment was accepted in the Spring of 1978. Construction and checkout occupied several intervening years, and the detector was installed in the West Pit of SPEAR in the Summer of 1981. The Fall of 1981 was used for detector checkout with colliding beams at SPEAR, and the first real physics running commenced in the Spring of 1982. During this running period, a sample of $\sim 0.9 \times 10^6$ produced ψ's was acquired. At this time, there were several known problems with the detector, and there was very little analysis software available. During the Summer of 1982, many of the detector problems were repaired. There was an additional block of

* The major benefit is that short term variations are largely eliminated, allowing off-line calibration procedures to average relatively large blocks of stable data.

running in the Fall of 1982 at the $\psi'(3685)$ and the $\psi''(3770)$. A first consistent reconstruction of the Spring 1982 data became available in January 1983, bringing with it intriguing evidence for new results. Further detector modifications were performed, and then a struggle ensued to decide where to run in the Spring of 1983. The result was a split of running time between the $\psi(3097)$ and the $\psi''(3770)$. During this run, the detector performed very well, and an additional sample of 1.8×10^6 produced ψ's was acquired.

The result of this running history is two samples of ψ data, taken one year apart. Unfortunately, the first data sample was acquired when there were known detector deficiencies. These problems were largely confined to the drift chamber. They included:

1. Layer 1 had no pre-amplifiers, which meant that it was susceptible to noise and pulse height slewing.

2. Layer 1 had only the innermost two sub-layers instrumented.

3. Layer 2 did not have pre-amplifiers or cross-talk compensation resistors. This made it virtually useless for tracking.

4. The linear region of the MTAC time measurement did not cover the full collection period, producing suspicious measurements for small and large times.

5. The current division information in the drift chamber was very unreliable due to electronics problems.

These problems, along with minor problems with other detector elements, were corrected by the time of the Spring 1983 run.

The disparity between the detector performance for the smaller 1982 data sample and the 1983 data sample will haunt the subsequent analyses, especially in the cases where the statistics is too limited to perform proper cross-checks. In addition, the Monte Carlo has been optimized for the very functional 1983 detector, rather than the more idiosyncratic 1982 detector. This leads to a policy of using the 1983 data alone when good agreement with the Monte Carlo is required.

Before proceeding to the physics analyses, brief mention is made of the exact sizes of the data samples. This knowledge is required in order to obtain correct branching ratios. The normalization for the 1983 data has been carefully evaluated using the number of produced hadrons and the trigger efficiency.

Prior to the full reconstruction of the raw data, a filtering program is used to classify the events on the basis of drift chamber, TOF, shower counter and muon system information.[33] An attempt is made to correctly isolate cosmic ray events, beam gas events, di-muon events, Bhabha events, 'junk' events, and hadron events. These classifications have been laboriously checked by extensive hand-scanning of events. The result of this is an accurate determination of the number of detected hadronic ψ events. The triggering efficiency has also been studied, using a sample of $\psi'(3685)$ events. These events have the advantage of providing a source of tagged ψ events through the decay chain: $\psi' \rightarrow \pi^+\pi^-\psi$. The pions can be used to trigger the event, and one can ask how often the ψ would also have triggered the event. This technique could be slightly biased due to the fact that the ψ is not at rest in the detector, but this does not appear to be significant. Combining the trigger efficiency with the number of observed hadrons provides an estimate of the number of produced hadronic ψ's (it is a safe assumption that all the observed hadronic events are from the ψ). This result is then corrected for the branching ratios to

leptons to produce the estimate for the total number of ψ's:

$$n_\psi = (1.80 \pm 0.15) \times 10^6 \quad (1983).$$

The number of produced ψ's in 1982 has been extracted by using the ratio of detected $\psi \rightarrow \mu^+\mu^-$ events for the 1982 and 1983 data samples. This gives a ratio of 1 : 1.96, providing an estimate for the total number of produced ψ's of:

$$n_\psi = (2.70 \pm 0.25) \times 10^6 \quad (1982 + 1983).$$

Chapter 3. The $\psi \to \gamma\pi^+\pi^-$ Final State

3.1 INTRODUCTION

The radiative decay of the ψ to the $\pi\pi$ final state has been explored by several previous experiments. The dominant feature is the decay: $\psi \to \gamma f(1270)$. The production characteristics (*i.e.*, the population of the different polarization states) of this final state have been measured by the MARK II and Crystal Ball experiments,[23,22] and the results are in disagreement with QCD predictions. This question will be studied here as a prelude to further spin analyses to be carried out for the K^+K^- system. There are additional reasons to explore this final state in more detail. One of the possible clues for finding glueballs should be their $SU(3)$ flavor singlet decay pattern. The $\theta(1700)$ has been observed in the $\eta\eta$ and K^+K^- decay modes by the MARK II and Crystal Ball experiments, but they have only set limits on its observation in the $\pi\pi$ final state.[24,25] This suggests that it is worthwhile to investigate the $\theta(1700)$ in the $\pi^+\pi^-$ final state.

This chapter will first describe the $\psi \to \gamma\pi^+\pi^-$ event selection and backgrounds. An analysis of the $f(1270)$ mass region will be performed, and the production and decay amplitudes for the $f(1270)$ will be measured. In addition, a branching ratio will be extracted. Limits on the existence of other states are explored, leading to several interesting new results.

3.2 EVENT SELECTION FOR $\psi \to \gamma\pi^+\pi^-$

Photon Selection

The events were required to have $n_\gamma \leq 4$. The photons which were actually used in the kinematic fitting were required to be 'good' photons. This requirement means that: the angle between the photon and the nearest charged track, $\cos\theta_{\gamma\pi}$,

was required to be < 0.95, the number of layers hit in the shower counter was required to be ≥ 2, and the starting layer of the shower was required to be ≤ 7.

Charged Track Selection

The drift chamber cuts are very minimal. The tracks must be well measured in the drift chamber in order to perform subsequent fits to the events. This means that it is necessary that the track has a full error matrix from the precision helix fit in the drift chamber.

The number of kaons produced at the ψ is much smaller than the number of pions, so no particle identification requirement was made using the TOF information. This results in a higher efficiency and greater solid angle coverage. The kaons in the sample will be adequately rejected by kinematic fitting alone.

The muon system was used to reject $\gamma\mu^+\mu^-$ events. To avoid biases due to hadronic punch-through, events were rejected only if both tracks had some indication of a muon signal. The event was called a di-muon if one track had both layers in the muon system fire and the other track had at least one muon layer fire.

Other Cuts

Before performing a kinematic fit, $\gamma\pi^+\pi^-$ candidate events were selected using simple kinematic cuts. These cuts serve to filter out events which are inconsistent with the $\gamma\pi^+\pi^-$ hypothesis. Two variables are used: a 'missing neutral energy' variable U, and a 'missing p_t' variable $p^2_{t_\gamma}$. The U variable is defined to be:

$$U = E_{miss} - P_{miss},$$

where E_{miss} and P_{miss} are the missing momentum and energy calculated from the charged track momenta using the pion mass hypothesis. This variable is used

because its resolution is approximately independent of the missing momentum. The missing mass squared is: $U(E_{miss}+P_{miss})$, and it does not have this feature. A cut is made at $|U| < 0.2$ GeV, which corresponds to $\sim 3\sigma$ in the resolution. The sample remaining after such a cut will be dominated by the $\psi \to \pi^+\pi^-$, $\psi \to \pi^+\pi^-\pi^0$ and the $\psi \to \gamma\pi^+\pi^-$ final states.

To increase the rejection of events with extra photons, two additional cuts are made. The first involves the $p^2_{t_\gamma}$ variable. This variable was introduced by G. Trilling, and measures the agreement between the missing momentum recoiling against the charged tracks and the angles of the photon in the event. It uses the fact that the angle and magnitude of the missing momentum are well measured by the drift chamber, whereas only the angles of the photon are well measured by the shower counter. In general, the resolution in this variable is limited by the drift chamber missing momentum resolution and not by the shower counter angular resolution. This variable is defined to be:

$$p^2_{t_\gamma} = 4P^2_{miss}\sin^2\frac{\theta}{2},$$

where P_{miss} is the missing momentum recoiling against the charged tracks and θ is the angle between P_{miss} and the direction of the photon. This reduces to the form: $(P_{miss}\theta)^2$ for small values of θ, as expected for a 'p_t' variable. The $\theta/2$ factor provides additional rejection for the backward direction where the 'p_t' would otherwise vanish. The background from $\pi^+\pi^-\pi^0$ will be approximately flat in this variable for values up to $\sim m^2_{\pi^0}$, whereas the radiative signal events will be peaked at small values of $\lesssim 0.001$ GeV^2. The distribution of this variable for the candidate $\gamma\pi^+\pi^-$ events which have passed the U cut is shown in Fig. 3.1(a). Signal events were required to have $p^2_{t_\gamma} < 0.002$. This cut suppresses about $80-90\%$ of the $\pi^+\pi^-\pi^0$ background.

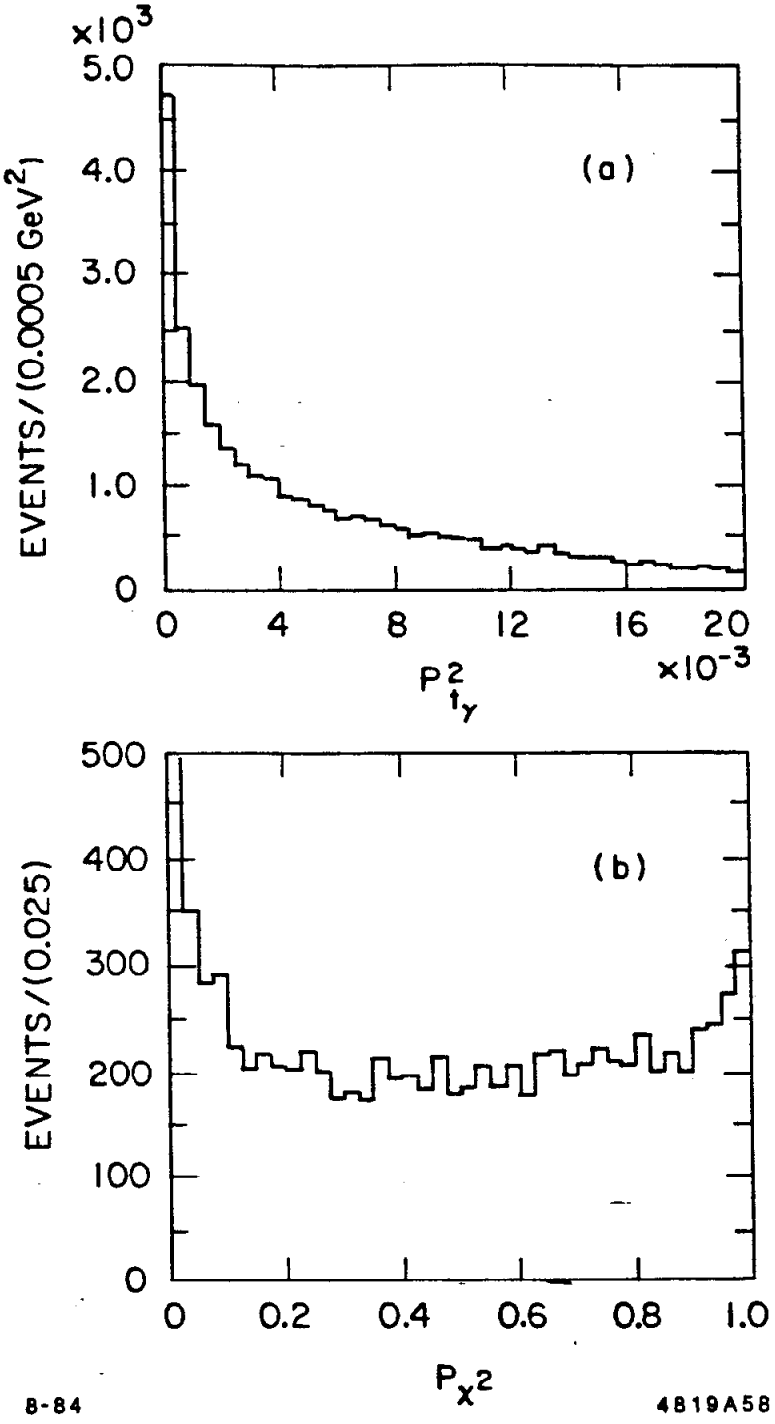

Figure 3.1. Kinematic variables for $\psi \rightarrow \gamma\pi^+\pi^-$. (a) shows the $p^2_{l_\gamma}$ distribution for events which have passed a loose U cut. (b) shows the kinematic fit confidence level, P_{χ^2}, after a $p^2_{l_\gamma}$ cut.

To obtain still further rejection, events containing more than one 'good' gamma were rejected. This is, in principle, a fairly dangerous cut, and it was actually applied after the kinematic fitting to allow more careful study of its effects. It could introduce a momentum dependence into the efficiency because the hadronic interaction cross-section in the shower counter is changing rapidly in the 0.3 – 1 GeV region. By eliminating events only if they have extra photons which are not close to charged tracks, this bias is largely removed. The effects of this cut have been studied and it has been found to remove ~ 5% of the signal events. This is a small effect when compared to the large number of background events which are removed.

Kinematic Fitting

In order to improve the resolution and increase the ability to reject background events, 4 constraint fits were done to impose energy and momentum conservation. The ability of the kinematic fit to discriminate between signal and background is very important for this analysis. It serves as a form of particle identification, making up for the absence of TOF cuts. It also serves to find the 'correct' photon for the event, if it is a single photon event. This is an important function because of the problem with extra 'fake' photons produced by hadronic interactions in the shower counter. In addition, the kinematic fit discriminates against events which contain extra photons, since they will not balance momentum.

Fits were performed using all permutations of the 'good' gammas in the event, and the fit with the smallest χ^2 was used for that event (this allowed a careful study of the cut, discussed previously, in which exactly one 'good' gamma was required). With a small number of 'real' photons in the event, this procedure will almost always isolate the correct photons and ignore the 'fake' photons. Two parallel hypotheses were examined, representing the signal of interest ($\psi \rightarrow \gamma\pi^+\pi^-$)

as well as the largest background ($\psi \rightarrow \gamma\gamma\pi^+\pi^-$). The P_{χ^2} distribution for the events passing the $p^2_{t_\gamma}$ cut is shown in Fig. 3.1(b). Signal events were required to have a confidence level ≥ 0.05. With this cut, there is very little kaon contamination, even without the TOF cuts. Further checks have been made to see that the pull distributions for all the fit variables look reasonable. These checks have been carried out on the large decay mode $\psi \rightarrow \rho\pi$. The results show that the mean and sigma of the pulls are typically within about 10% of the expected values of 0 and 1.

The mass distribution which results from these kinematic cuts is shown in Fig. 3.2. There is evidence for a $\rho^0(770)$ peak due to feed-through from the $\psi \rightarrow \rho^0\pi^0$ channel, an $f(1270)$ peak due to real radiative events, plus a great deal of background.

3.3 BACKGROUNDS

There are several potential background sources for the $\psi \rightarrow \gamma\pi^+\pi^-$ analysis. These sources are considered in this section, and an attempt is made to estimate their significance.

$\underline{\psi \rightarrow \gamma e^+ e^-}$

Since electrons radiate very easily, this background is potentially quite serious. To aid in rejecting this background, any events in which the energy deposited in the shower counter was greater than 1.1 GeV for each track were eliminated very early in the analysis. However, this is not the expected configuration for a $\psi \rightarrow \gamma e^+ e^-$ event which could populate the region of interest here. There are two possible configurations for these events, corresponding to initial state or final state radiation. The final state cross-section is enhanced by the presence of the ψ. This configuration consists of one electron track with the full elastic momentum of 1.55 GeV while the other track has a somewhat lower momentum.

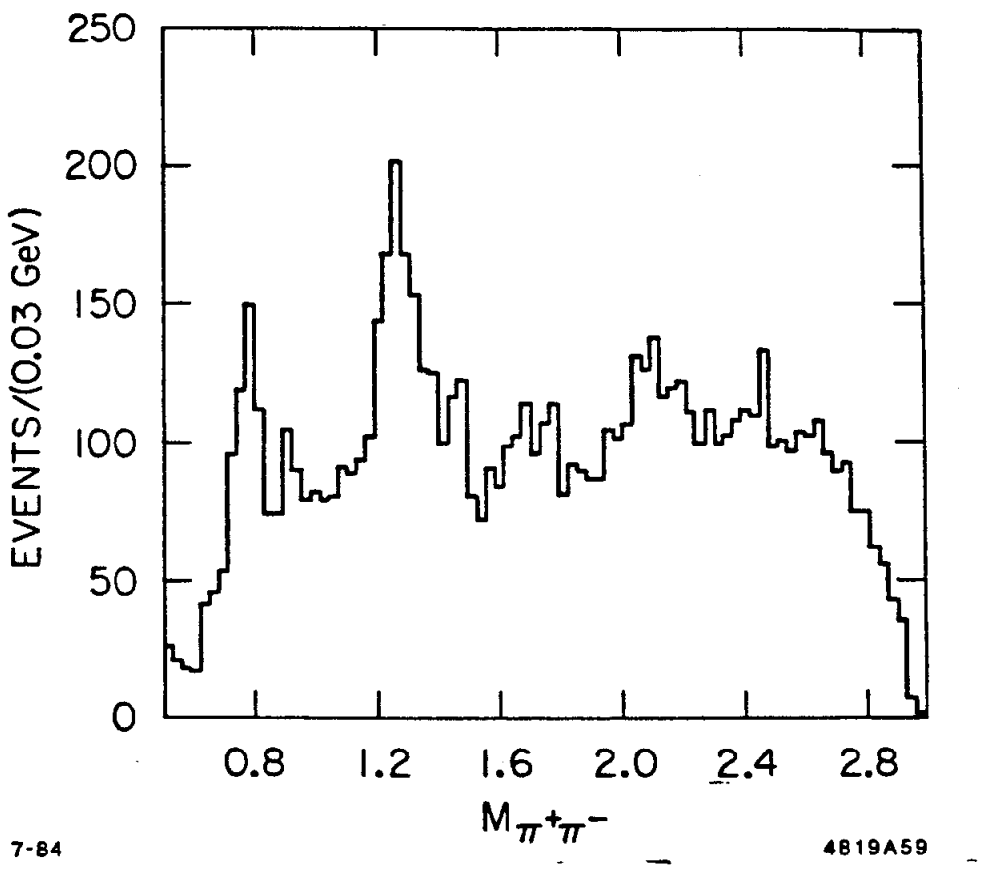

Figure 3.2. The $\pi^+\pi^-$ mass distribution. Events in this distribution were required to pass kinematic cuts.

In addition, events produced by the decay of the ψ will have a $1+\cos^2\theta$ angular distribution relative to the beam axis, rather than the much more strongly peaked distribution characteristic of Bhabha scattering. For these reasons, final state radiation dominates this background source.

There are two complementary ways of rejecting such a background. One uses the momenta measured in the drift chamber and the other uses the energy deposited in the shower counter. The energy deposited in the shower counter by the electron should have the characteristic properties of an electromagnetic shower. The pattern of energy deposit can be used as input to an electron/hadron separation algorithm. A very general technique, known as non-parametric partitioning, has been used to perform the separation with the least possible mis-identification. The algorithm developed by the MARK III offers a per track rejection of about 50:1 against electrons at 1 GeV. The second approach is to use the kinematics of the event. The electron mass is quite different from the pion mass, and a kinematic fit provides rejection against this background due to the different energies implied for the electron and pion hypotheses. Both of these techniques have been used in order to eliminate this background.

The electron/hadron separation algorithm provides us with an identification for each track, using the momentum, TOF and shower profile of the track as input. This information can be used in different ways to isolate a clean sample of $\psi \to \gamma\pi^+\pi^-$ events. A strict method is to require that neither track is consistent with the electron hypothesis. These 'anti-electron' cuts have an efficiency of:

$$\epsilon(\pi\pi) = (1-\epsilon_{\pi\to e})^2,$$

$$\epsilon(ee) = (\epsilon_{e\to\pi})^2,$$

where $\epsilon_{\pi\to e}$ is the mis-identification probability for a pion, *i.e.*, the probability that

a pion is called an electron. $\epsilon_{e\to\pi}$ is the corresponding probability for an electron to be called a pion. A less strict method is to require that either of the two tracks is a well-identified pion. These 'pion' cuts give an efficiency:

$$\epsilon(\pi\pi) = 1 - (1 - \epsilon_{\pi\to\pi})^2,$$

$$\epsilon(ee) = 1 - (1 - \epsilon_{e\to\pi})^2 \sim 2\epsilon_{e\to\pi},$$

where $\epsilon_{\pi\to\pi}$ is the identification probability, *i.e.*, the probability that a pion is called a pion. The algorithm used in this analysis has been optimized to minimize $\epsilon_{e\to\pi}$ for different momenta, with the result that:

$$\epsilon_{e\to\pi} \sim 0.02 - 0.05,\ \epsilon_{\pi\to e} \sim 0.15,\ \epsilon_{\pi\to\pi} \sim 0.85.$$

For the $\gamma\pi^+\pi^-$ final state, very few γe^+e^- events survive the 'pion' cut. This is checked by examining the distribution of events removed by applying the stricter 'anti-electron' cut after the 'pion' cut. The conclusion is that there is more than ample pion/electron separation available to eliminate this background. An estimate is that less than 5% of the remaining events are from the γe^+e^- final state.

$\underline{\psi \to \gamma\mu^+\mu^-}$

These events are all due to final state radiation. This is because the continuum cross-section for $e^+e^- \to \mu^+\mu^-$ is very small when compared to the cross-section at the ψ, and after initial state radiation the cross-section no longer benefits from the ψ enhancement. The difference between this case and the e^+e^- case is that only the QED annihilation diagram can contribute, whereas the e^+e^- case has an additional t-channel diagram which increases the cross-section. In addition, due to the larger muon mass, the total cross-section for the $\gamma\mu^+\mu^-$ final

state is smaller than that for the γe^+e^- final state, and the $\mu^+\mu^-$ mass distribution peaks strongly near the ψ mass. Even with no background rejection, there are a negligible number of $\mu^+\mu^-$ events below 2 GeV. For the higher mass region, the muon system is used to eliminate most of the remaining events. The conclusion is that this is a negligible background, contributing $\ll 1\%$ to the total sample of signal events.

$\underline{\psi \to \gamma K^+K^- \ / \ \psi \to \gamma\gamma K^+K^-}$

These final states are intrinsically smaller than the equivalent modes containing pions. In addition, there is a kinematic rejection because the mass of the pion is much smaller than that of the kaon. The combination of these factors results in a negligible background contribution from this source. This has been checked by generating Monte Carlo γK^+K^- events and measuring the probability for them to pass the event selection cuts. Of particular interest are the two largest signals in γK^+K^-, the $f'(1515)$ and the $\theta(1700)$. Monte Carlo samples of these two final states were generated using the full angular distributions (as described in a later chapter). The $f'(1515) \to K^+K^-$ events feed through into the $f(1270)$ mass region, and the Monte Carlo predicts that there should be ~ 5 such events in the total event sample. A similar investigation for the $\theta(1700) \to K^+K^-$ events shows that they feed through into the $1.5 - 1.7$ GeV region, and there should be approximately 15 such events present. In both cases, requiring that the TOF identification be consistent with the pion hypothesis at the 2.5σ level eliminates all of these events.

The Monte Carlo estimate was checked using the events in the $\gamma\pi^+\pi^-$ sample by requiring that the TOF identification be consistent with the kaon hypothesis. This is an attempt to isolate the γK^+K^- events in the $\gamma\pi^+\pi^-$ sample. The observed events are consistent with the Monte Carlo prediction. This provides the estimate that the γK^+K^- contamination is $< 1\%$ of the total event sample.

In addition, the effect on the mass distribution of making the pion TOF cuts was examined. The distribution was unchanged and there was no sign of structure in the events which were removed.

$\underline{\psi \rightarrow \pi^+\pi^-\pi^0/\rho\pi}$

This is a very large ψ decay mode, with about 20000 events observed in the total ψ sample. The difficulty arises for the case where the π^0 decays asymmetrically, producing a low energy photon and a high energy photon. This configuration is kinematically indistinguishable, for finite resolution, from the single photon topology because the low energy photon carries away a negligible momentum. Thus, despite all of the cuts that have been applied, $\psi \rightarrow \rho\pi$ remains the dominant source of background in this final state. Figure 3.3(a) shows the mass distribution for $\psi \rightarrow \pi^+\pi^-\pi^0$ events which have been kinematically fit to the $\psi \rightarrow \gamma\gamma\pi^+\pi^-$ hypothesis with an additional requirement that: $0.08 \leq m_{\gamma\gamma} \leq 0.19$ GeV. The ρ^0 mass peak is visible, and the broader peak at higher masses comes from the kinematic reflection of the $\rho^{\pm}\pi^{\mp}$ events. The Dalitz plot shows remarkably complete quasi-two body dominance of the three pion final state. Due to this dominance, all future discussion of this background refers to it as $\rho\pi$ rather than $\pi^+\pi^-\pi^0$. Further features of this background are its confinement to a small region of the total phase space, as seen in Fig. 3.3(b), and the parameter-free prediction for the mass and angular dependence of the events which is discussed in Appendix B.

3.4 THE $\pi^+\pi^-$ MASS SPECTRUM FROM $\psi \rightarrow \gamma\pi^+\pi^-$

The mass distribution obtained for the standard event selection cuts has been shown in Fig. 3.2. If the additional electron/hadron identification is used in the form of the looser 'pion' cut described previously, the mass distribution which is obtained is shown in Fig. 3.4(a), and the corresponding Dalitz plot is shown in

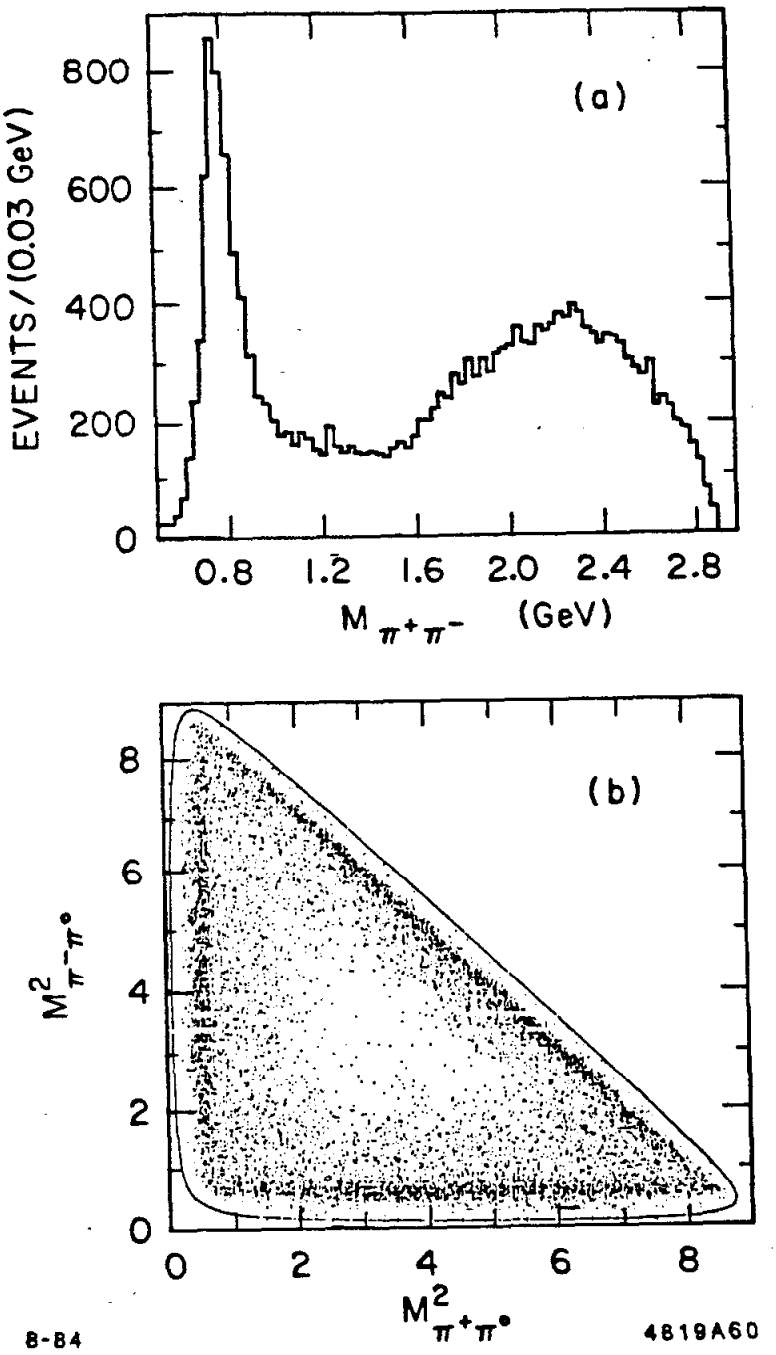

Figure 3.3. The distributions for $\psi \rightarrow \rho\pi$ events. (a) shows the $\pi^+\pi^-$ mass distribution for these events. (b) shows the Dalitz plot.

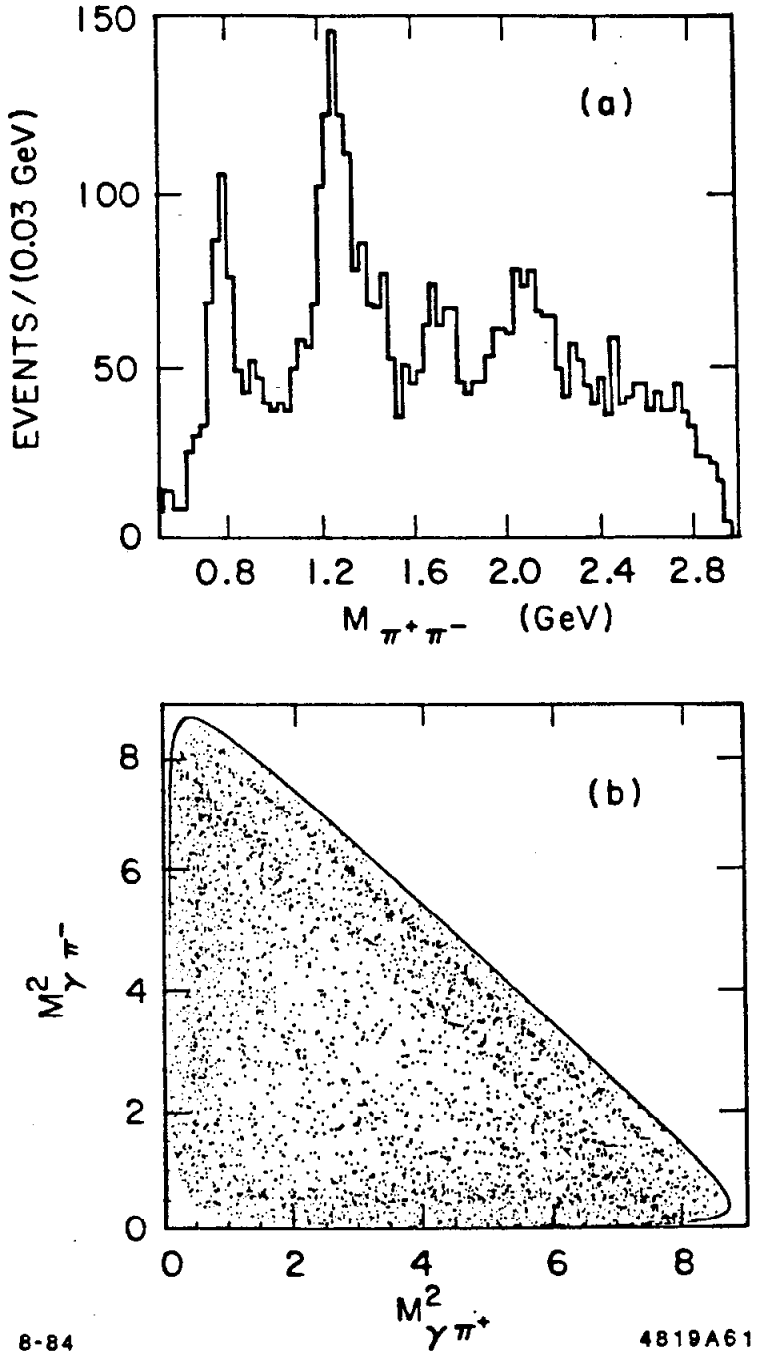

Figure 3.4. The $\pi^+\pi^-$ mass distribution after pion cuts. (a) is the mass plot. (b) is the Dalitz plot.

Fig. 3.4(b). In this plot, states with a fixed $\pi^+\pi^-$ mass will appear as diagonal bands. The previous section concluded that the background in this plot is almost totally due to $\psi \rightarrow \rho\pi$ events. This background is visible in the Dalitz plot in the form of bands at the edges of the plot. There are a number of events which lie outside the $\rho\pi$ bands, and which cannot be readily attributed to any background process. These events correspond to real $\gamma\pi^+\pi^-$ events.

A fit has been performed to the mass distribution shown in Fig. 3.4(a) to extract the $f(1270)$ parameters. This fit is somewhat biased because the large width of the $f(1270)$ is strongly correlated with the shape and magnitude of the background, and so the width cannot be reliably measured. Unfortunately, the world measurements of the $f(1270)$ width are also not very consistent. The Particle Data Book[34] quotes the value:

$$\Gamma = 0.179 \pm 0.020 \text{ GeV},$$

where the error has been inflated to account for the inconsistent measurements. Taking a weighted mean and sigma for the world measurements gives a confidence level of 0.001 (*i.e.*, this is the probability that the world measurements result from a common source). Given this uncertainty, two fits have been performed. One has the width fixed at 0.180 GeV, and the other allows the width to vary. The results are shown in Fig. 3.5, where a simple polynomial has been used to represent the background.

The results of these fits are:

$$m = 1.269^{+0.013}_{-0.013} \text{ GeV} \quad , \quad \Gamma \equiv 0.180 \text{ GeV},$$

$$m = 1.268^{+0.012}_{-0.012} \text{ GeV} \quad , \quad \Gamma = 0.139^{+0.055}_{-0.039} \text{ GeV},$$

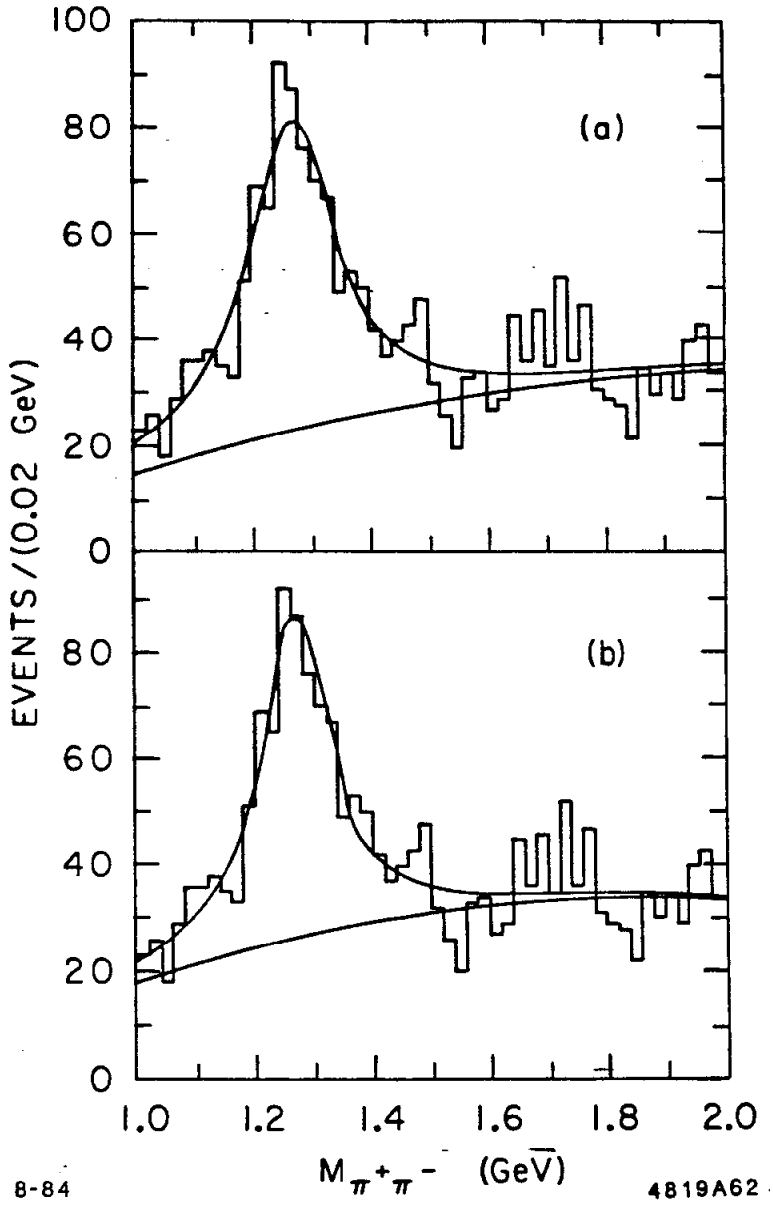

Figure 3.5. Fits to the $f(1270)$. (a) shows a fit with the $f(1270)$ width fixed. (b) shows a fit where the width was allowed to vary.

where the quoted errors represent the 2σ statistical errors from the fit. The fits are consistent with each other, but the narrower width corresponds to a smaller number of events in the peak, and hence to a branching ratio which is smaller by about 20%. In extracting the branching ratio for the $f(1270)$, the width will be fixed at 0.180 GeV.

To extract a branching ratio for the $f(1270)$, it is necessary to estimate the detection efficiency as well as to fit for the number of detected events. The efficiency has been estimated by generating Monte Carlo events with the correct mass, width and angular distributions for the $f(1270)$. The actual parameters used for the Monte Carlo generation were:

$$m = 1.270 \text{ GeV} \quad , \quad \Gamma = 0.180 \text{ GeV},$$

$$x = 0.88 \quad , \quad y = 0.04 \quad , \quad \varphi_x = \varphi_y = 0.$$

The helicity amplitude ratios (described in Appendix B) were taken from the measurement of Crystal Ball for the $\gamma\pi^0\pi^0$ final state,[22] rather than from the current analysis, because the $\gamma\pi^0\pi^0$ state does not suffer from the hadronic ($\rho\pi$) background problems inherent in the MARK III analysis. The efficiency is found to be:

$$\epsilon = 0.38 \pm 0.05.$$

The number of detected events has been measured using a fixed $f(1270)$ width as described previously. The result is:

$$n_f = 707 \pm 54 \text{ events},$$

where the error is purely statistical. This leads to the product branching ratio:

$$\text{BR}(\psi \to \gamma f(1270))\text{BR}(\text{f}(1270) \to \pi\pi) = (1.03 \pm 0.08 \pm 0.18) \times 10^{-3},$$

where the systematic error includes the uncertainties from the Monte Carlo efficiency calculation, the imperfectly known angular distributions, the number of produced ψ events and the ambiguity concerning the correct value of the width to use in the fit. Since the $f(1270)$ is an isoscalar, a factor of 3/2 has been used to correct for the unobserved $\pi^0\pi^0$ mode.

3.5 Polarization Analysis for $\psi \to \gamma f(1270)$

To measure the spin of the object X in the decay chain $\psi \to \gamma X$, $X \to 0^- + 0^-$, one needs to look at the angular distributions of the detected particles. In addition, even when the spin is known to be $J^P = 2^+$, as for the $f(1270)$, there are other quantities to be measured. The study of the angular distributions is simplified by the fact that, unlike the situation for hadronic production, the initial state is prepared for us in a very simple form. The ψ is produced as an incoherent mixture of $M = \pm 1$ states, where M is the spin projection of the ψ along the beam direction. This means that there are no unknown amplitudes for producing the ψ; the only unknown amplitudes are those associated with producing the X. There are three such unknown amplitudes for the case of the $f(1270)$, where $J^P = 2^+$.

The calculation of the production and decay angular distributions for this analysis involves an application of the helicity formalism. These calculations are carried out in detail in Appendix B, and the brave reader is referred to that section to satisfy any lingering curiosity. There are three angles which parameterize the production and decay process. The definitions used in this analysis are described in detail in Appendix B, but are summarized here:

θ_γ = the polar angle of the radiative photon in the lab,

θ_π = the polar angle of the positive pion in the X center of mass,

ϕ_π = the azimuthal angle of the positive pion in the X center of mass.

For $J = 2$, the X state can be produced with a helicity in the range of $[-2, 2]$. Parity invariance reduces the number of independent production amplitudes to three, labeled A_0, A_1 and A_2. These amplitudes are complex, and hence correspond to six independent real quantities. By taking ratios, as in Appendix B, these six quantities are reduced to four. These are chosen to be

$$(x, y, \varphi_x, \varphi_y): \quad xe^{i\varphi_x} \equiv \frac{A_1}{A_0} \quad , \quad ye^{i\varphi_y} \equiv \frac{A_2}{A_0}.$$

The next stage in the spin analysis is to perform an acceptance corrected fit to measure the values for the four parameters just described. This fitting procedure uses a maximum likelihood technique where the effects of acceptance are included in the likelihood function. The formalism is discussed in detail in Appendix C. The Monte Carlo acceptances for the three angles are shown in Fig. 3.6. These acceptances are histograms of accepted Monte Carlo events which were generated with flat distributions in the three angles. These events are used to perform the normalization integrations described in Appendix C.

After examining these acceptances, some general remarks can be made about the quality of information which can be obtained from the different angles. The factor which has the greatest impact on the acceptance is the limited solid angle available for well-measured charged tracks.

1. θ_γ - since this angle is defined in the detector frame it suffers from acceptance corrections, especially due to its correlation with the charged track directions. This effect is not easily visible in the phase space normalization, but it is more apparent when there are stronger correlations present. The result is that the acceptance is not very good in the region of large $|\cos\theta_\gamma|$, which is important in distinguishing a flat distribution from $1 + \cos^2\theta_\gamma$

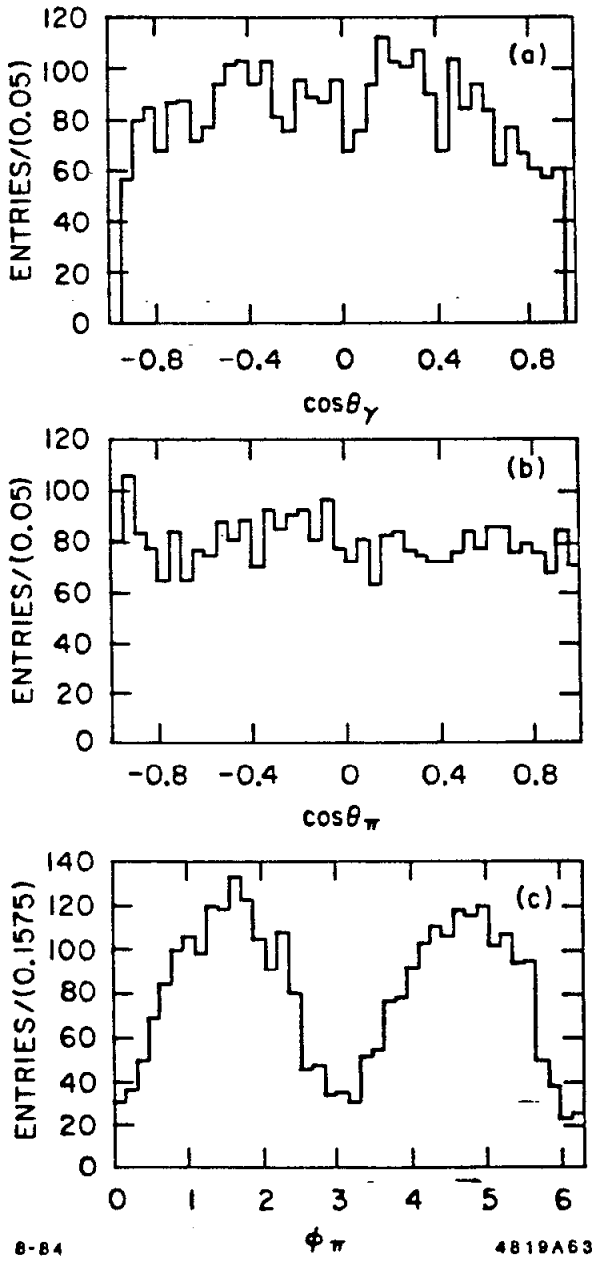

Figure 3.6. The Monte Carlo acceptance. The plots show the three angular distributions after acceptance cuts.

2. $\underline{\theta_m}$ - since this angle is defined in the X center of mass frame, it gets averaged over directions in the detector. The result is that the acceptance corrections are minimal. This angle carries the highest quality information about the spin of the X state.

3. $\underline{\phi_m}$ - since this angle is also defined in the center of mass, one might expect it to contain high quality information. Unfortunately, this is not true, and it receives very large acceptance corrections. This angle is Lorentz invariant because it is defined in a plane normal to the direction of the boost to the X center of mass system. Its interpretation in the lab frame is simple. It is the angle between the production plane (containing the beams and the radiative photon) and the decay plane (containing the pions and the radiative photon). One can imagine the production plane rotating about the beam axis and the decay plane rotating about the radiative photon axis. In this case, when the two planes coincide (at $\phi = 0, \pi, 2\pi$) it is very likely that one of the charged tracks will leave the detector through the endcaps. This is the source of the large holes in the acceptance for this angle, which render it virtually useless for the spin analysis.

A further complication for the polarization analysis is the presence of $\rho\pi$ background. Fortunately, the $f(1270)$ lies in a region of minimum background, between the $\rho^0\pi^0$ and the $\rho^\pm\pi^\mp$ feed-through. In order to correctly account for this background in the fitting procedure, an additional term is added to the total likelihood function. The likelihood function for the fit is then written as:

$$\mathcal{L} = (1-\delta)\mathcal{L}_{\gamma\pi\pi} + \delta\mathcal{L}_{\rho\pi} \qquad (3-1)$$

where $\mathcal{L}_{\gamma\pi\pi}$ is the $J = 2$ angular correlation function calculated in Appendix B, and δ represents the fraction of $\rho\pi$ contamination. This fitting procedure

should be somewhat less biased than a procedure which ignores the background. The background term contains no free parameters and has been calculated in Appendix B using the helicity formalism. The formula for the angular correlation function is:

$$W_{\rho\pi} = \sin^2\vartheta_{\pi'}\left[1+\cos^2\vartheta_{\pi}+\sin^2\vartheta_{\pi}\cos 2\varphi_{\pi'}\right],$$

ϑ_{π} = the lab polar angle of the pion not in the ρ,

$\vartheta_{\pi'}$ = the polar angle of the π in the ρ center of mass,

$\varphi_{\pi'}$ = the azimuthal angle of the π in the ρ center of mass.

The true likelihood should include interfering contributions from the three possible ρ states:

$$P_{\rho\pi} = \left|\frac{\rho^+\pi^- - \rho^-\pi^+ + \rho^0\pi^0}{\sqrt{3}}\right|^2,$$

where the minus sign is determined by constructing a $C = -$ eigenstate. This effect is ignored here since the region of the Dalitz plot where the interference is important is the region where the ρ bands overlap, i.e., where $\cos\vartheta_{\pi'} \sim \pm 1$. The matrix element is proportional to $\sin^2\vartheta_{\pi'}$, which vanishes in this region. The background likelihood is then written:

$$\mathcal{L}_{\rho\pi} = \left[\text{Breit} - \text{Wigner}_{\rho}(\pi\pi)\right]\left[W_{\rho\pi}(\vartheta_{\pi},\vartheta_{\pi'},\varphi_{\pi'})\right],$$

where the calculations are performed for the $\pi\pi$ combination which is closest to the ρ mass. The angles are calculated by using the missing 4-momentum recoiling against the $\pi^+\pi^-$ system as an estimate for the π^0 4-momentum.

A weakness of this fitting technique involves the relative normalization of the two components of the total likelihood in Eqn. (3-1). The usual technique is to normalize the likelihood function by numerically integrating over the input variables. To perform this integration correctly, one should write the $\rho\pi$ likelihood for the full $\gamma\gamma\pi^+\pi^-$ final state, and then perform an acceptance corrected

integration over the unobserved photon. However, there is only one unknown—the relative normalization, and so a simpler technique will be used. This approach takes an un-normalized form for the $\rho\pi$ likelihood and performs fits to Monte Carlo data containing a known mixture of $\rho\pi$ events and $\gamma\pi^+\pi^-$ events. The scale for δ is then adjusted until it agrees with the true Monte Carlo fraction. Once the scale is defined, the actual fit can be performed either with a fixed value for δ or with δ allowed to vary. The least biased technique is to fix δ to a value determined by some independent means. This eliminates the possibility of correlations between δ and the other fit parameters, and is the method used here.

The next issue is the selection of events to be included in the fit. The events are chosen to lie in a narrow mass region containing the $f(1270)$. The region is chosen as:

$$1.15 \leq m \leq 1.40 \text{ GeV}.$$

The analysis has been performed using the 1983 data sample alone, in order to avoid any problems involved with the acceptance for the 1982 detector. The events were required to have $|\cos\theta_{DC}| \leq 0.85$ and $|\cos\theta_{SC}| \leq 0.95$, where SC refers to the angle for a neutral track in the shower counter and DC refers to the angle for a charged track in the drift chamber. This insures agreement with the Monte Carlo acceptance calculations. The resulting event sample consists of 574 events.

The results of applying the likelihood procedure to this event sample are displayed in Fig. 3.7. The histograms are the data, and the curves represent a smoothed approximation to the Monte Carlo expectation for the results of the fit , as described in Appendix C. The fit result cannot be displayed directly because the acceptance function has never been explicitly evaluated. The fit appears to be a good representation of the data, although it should be remembered that the fit uses the correlated three dimensional angular information rather than just the three

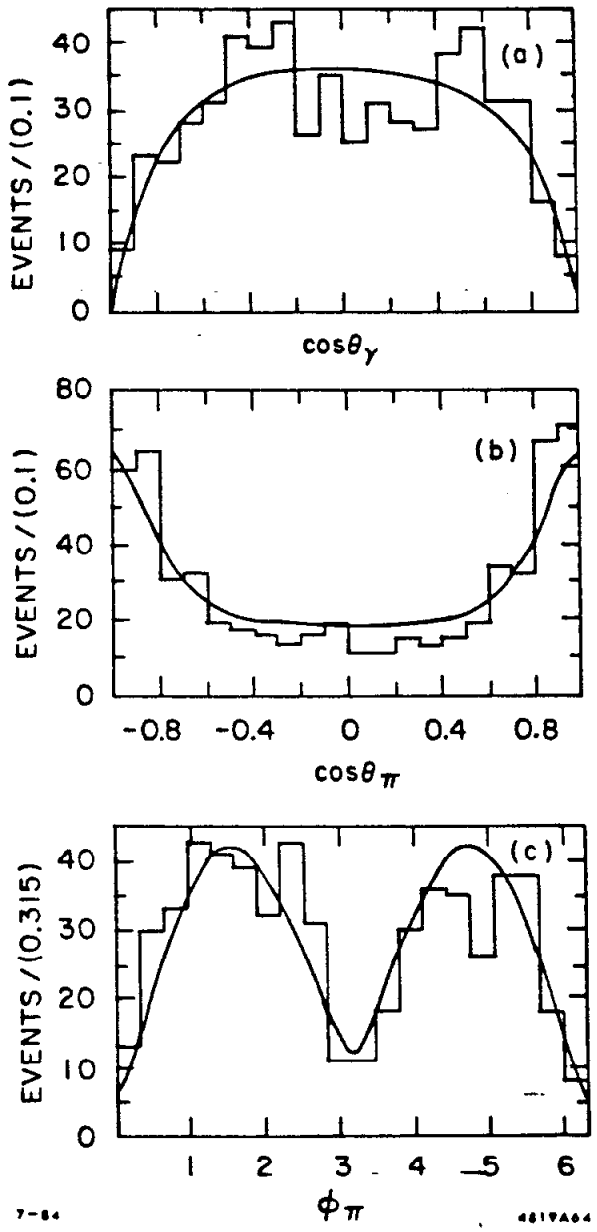

Figure 3.7. The results of the $f(1270)$ polarization fit. The curves represent the Monte Carlo expectation.

projections displayed here. The parameter values for this fit are:

$$x = 0.96 \pm 0.07 \quad , \quad \varphi_x = -0.5 \pm 0.7,$$

$$y = 0.06 \pm 0.08 \quad , \quad \varphi_y = -0.4 \pm 1.9,$$

where the quoted errors are statistical only. These results are consistent with a value of zero for both of the relative phases. This has been an assumption in the previous analyses of the $f(1270)$, and it is checked here for the first time. The large errors reflect the relatively minor influence of the relative phases on the fit results. Since the phases are consistent with zero, an additional fit was performed in which they were fixed to be zero. The results of this fit are:

$$x = 0.96 \pm 0.06 \quad , \quad \varphi_x \equiv 0,$$

$$y = 0.06 \pm 0.08 \quad , \quad \varphi_y \equiv 0.$$

The likelihood for this fit is insignificantly different from that of the variable phase fit.

To better convey the allowed regions for the x and y parameters, Fig. 3.8 shows a contour plot of the likelihood function for the variable phase fit. The phases have been left at their fit values, and the only other likely parameter values correspond to a sign change in x. It appears very difficult to move the value for y away from zero.

3.6 STUDY OF OTHER STATES

There are several states which would be expected to appear in the $\gamma\pi^+\pi^-$ channel.

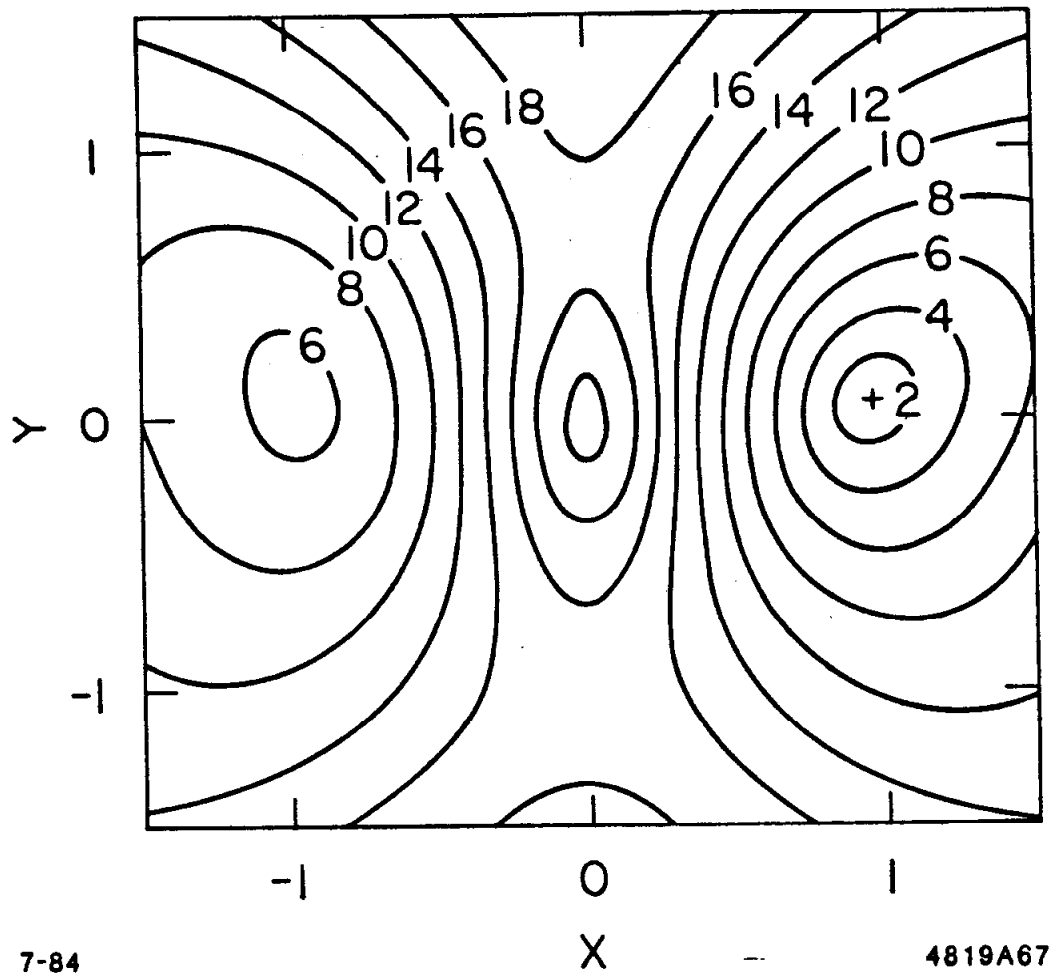

Figure 3.8. Contour plot of x versus y for the $f(1270)$ spin analysis. The contours correspond to changes in the likelihood of 2σ, and the + indicates the location of the minimum. The relative phases were fixed at their fit values for making this plot.

The $S^*(975)$

The low-lying 0^{-+} and 2^{++} isoscalar mesons are observed in radiative ψ decays with large branching ratios, but there is no indication of the 0^{++} mesons. The non-strange state, the $\epsilon(1300)$, is a very poorly defined object and no useful limit can be set on its existence. The $s\bar{s}$ 0^{++} isoscalar, the $S^*(975)$, lies just below K^+K^- threshold and thus appears as a narrow peak in the $\pi\pi$ mass spectrum. It is clearly observed in the hadronic decay $\psi \to \phi\pi\pi$. It is not observed in $\psi \to \gamma\pi^+\pi^-$ and a limit has been set by performing a maximum likelihood fit using a Breit-Wigner with the parameters:

$$m = 0.975 \text{ GeV} \quad , \quad \Gamma = 0.035 \text{ GeV}.$$

The result is:

$$\text{BR}(\psi \to \gamma \text{S}^*(975))\text{BR}(\text{S}^*(975) \to \pi\pi) < 7 \times 10^{-5} \quad 90\% \text{ C.L.}$$

The Higher Mass Structures

The mass distribution shown in Fig. 3.4(a) contains indications for the presence of additional structures above the $f(1270)$. The interpretation of these structures is not unambiguous, but a fit has been performed to indicate a possible (perhaps somewhat far-fetched) interpretation. The fit which has been performed includes three incoherent Breit-Wigners. The first one represents the $f(1270)$ and has its mass fixed at 1.270 GeV and its width fixed at 0.180 GeV. The second peak represents a possible $\theta(1700)$ signal. Its mass has been left free to allow comparison with the K^+K^- results, but its width (which is very poorly determined) is fixed at 0.130 GeV, as seen in the K^+K^- channel. The third Breit-Wigner represents the third structure in the mass distribution. This peak could correspond to an excited

$f(1270)$, either the $h(2040)$ with $J^P = 4^+$ or possibly the corresponding $J^P = 2^+$ state.

The results of this fit are shown in Fig. 3.9. The parameters which are found are:

$$m_2 = 1.713 \pm 0.015 \text{ GeV} \quad , \quad \Gamma_2 = 0.130 \text{ GeV},$$

$$m_3 = 2.086 \pm 0.015 \text{ GeV} \quad , \quad \Gamma_2 = 0.210 \pm 0.063 \text{ GeV},$$

where the errors are statistical only. The inclusion of additional peaks in the fit decreases the background level relative to that shown in Fig. 3.5, and hence increases the number of $f(1270)$ events found by the fit. Evaluating the corresponding branching ratio gives:

$$\text{BR}(\psi \rightarrow \gamma \text{f}(1270))\text{BR}(\text{f}(1270) \rightarrow \pi\pi) = (1.15 \pm 0.07 \pm 0.19) \times 10^{-3}.$$

The mass for the second peak is consistent with the $\theta(1700)$ mass measured in K^+K^-, and the fixed width, derived from the K^+K^- channel, is also fairly consistent with the $\pi^+\pi^-$ data. There is no compelling evidence that this is the $\theta(1700)$, but it seems rather problematic to set an upper limit for $\theta \rightarrow \pi\pi$ when there is a large peak in the same region. If one pursues the $\theta(1700)$ hypothesis somewhat further, it is possible to extract a branching ratio. Monte Carlo events have been generated using the $\theta(1700)$ parameters found in the K^+K^- system (see next several chapters):

$$m = 1.720 \text{ GeV} \quad , \quad \Gamma = 0.130 \text{ GeV},$$

$$x = -1.2 \quad , \quad y = -1.2.$$

The efficiency estimated for the cuts applied to Fig. 3.9 is:

$$\epsilon = 0.39 \pm 0.06.$$

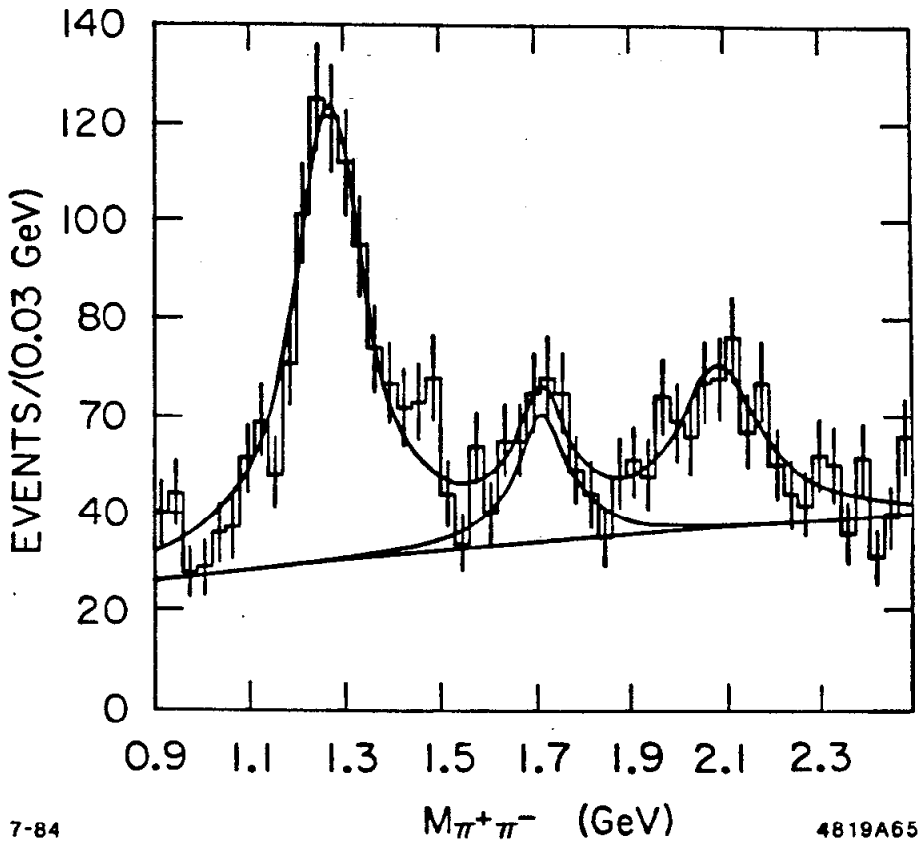

Figure 3.9. The $\pi^+\pi^-$ mass distribution with a three peak fit. The fit represents a possible interpretation for the visible structures and does not include interference effects.

This leads to the branching ratio:

$$\mathrm{BR}(\psi \to \gamma\theta(1700))\mathrm{BR}(\theta(1700) \to \pi^+\pi^-) = (1.6 \pm 0.4 \pm 0.3) \times 10^{-4},$$

where the systematic error includes estimates for uncertainties in the efficiency due to uncertainties about the true angular distributions.

To proceed further in testing the $\theta(1700)$ hypothesis, an attempt has been made to study the decay angular distributions. Unfortunately, there is too much background, both from the tail of the $f(1270)$ and from $\rho\pi$ events, to perform a full spin analysis. A simpler technique involves extracting the angular distribution of the signal events. The θ_π angle contains the highest quality information about the decay. To extract its distribution, the total event sample shown in Fig. 3.9 was divided into five bins in $|\cos\theta_\pi|$. Fits were performed to the mass distribution corresponding to each such bin to extract the number of observed events in each peak versus $\cos\theta_\pi$. The results are displayed in Fig. 3.10. The distribution found for the $f(1270)$ is shown in Fig. 3.10(a), and agrees well with the polarization analysis discussed previously. The distribution for the $\theta(1700)$ and the third peak are shown in Fig. 3.10(b) and Fig. 3.10(c), and appear consistent with being flat. As will be seen later, this distribution for the $\theta(1700)$ is quite similar to that observed in the $\mathrm{K^+K^-}$ channel.

The third peak has no obvious interpretation. Its parameters agree with those expected for the $h(2040)$, namely: $m = 2.040 \pm 0.020$ GeV and $\Gamma = 0.150 \pm 0.050$ GeV. However, $J^P = 4^+$ states are not expected to be strongly produced by a point-like source such as radiative ψ decays (it is difficult to produce a large angular momentum with a point-like production mechanism). Its angular distributions look similar to those of the $\theta(1700)$ and so the same efficiency will be

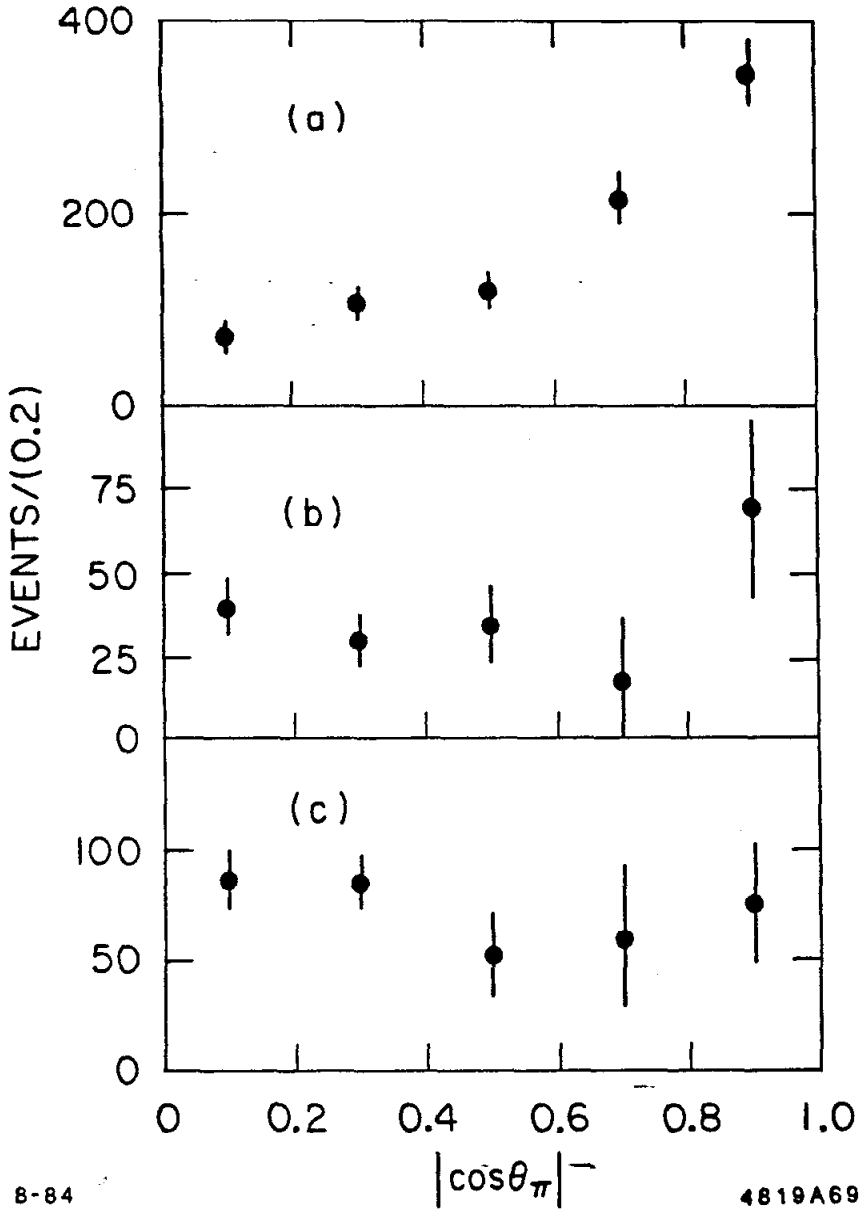

Figure 3.10. The extracted $\cos\theta_\pi$ distribution for the peaks. (a) is the number of events versus $\cos\theta_\pi$ for the $f(1270)$. (b) is for the $\theta(1700)$. (c) is for the third peak in the fit.

used in order to calculate a branching ratio. The result is:

$$BR(\psi \rightarrow \gamma X(2100))BR(X(2100) \rightarrow \pi^+\pi^-) = (3.0 \pm 0.5 \pm 0.6) \times 10^{-4}.$$

Since it is quite possible that all three resonances included in the fit displayed in Fig. 3.9 have $J^P = 2^+$, it seems appropriate to perform an additional fit in which the Breit-Wigners are allowed to interfere. The results of such a fit are displayed in Fig. 3.11(a). The envelope of the fit is shown, in addition to the contributions from the individual squared amplitudes. Although the envelope of the fit is almost identical, an immediate difference from the non-interfering fit is visible—the area contained in the $\theta(1700)$ contribution to the fit is much smaller for the interfering Breit-Wigner fit. This effect is due to the cross-terms which appear when the summed amplitudes are squared. The events contained in these cross-terms don't strictly belong to any one of the resonances in the fit, and hence they don't contribute to the measured branching ratios. This serves to indicate that a much more detailed analysis of this complex region is required. It is necessary to let the full helicity amplitudes for each resonance interfere with each other, rather than just modeling the interference in the mass plot. It is also necessary to introduce a more sophisticated model for the background since some of it may be coherent and some of it is incoherent. In the absence of such an analysis, the branching ratios derived earlier, particularly that of the $\theta(1700)$, represent more of an upper bound than a true measurement. The true $\theta(1700)$ branching ratio could be a factor of two or more smaller, depending on the model used to extract it.

Additional Checks

Several additional checks have been performed. A cut was made, requiring that the TOF identification for both charged tracks was consistent with the pion hypothesis at the 2.5σ level. After such cuts, there was no change in the observed

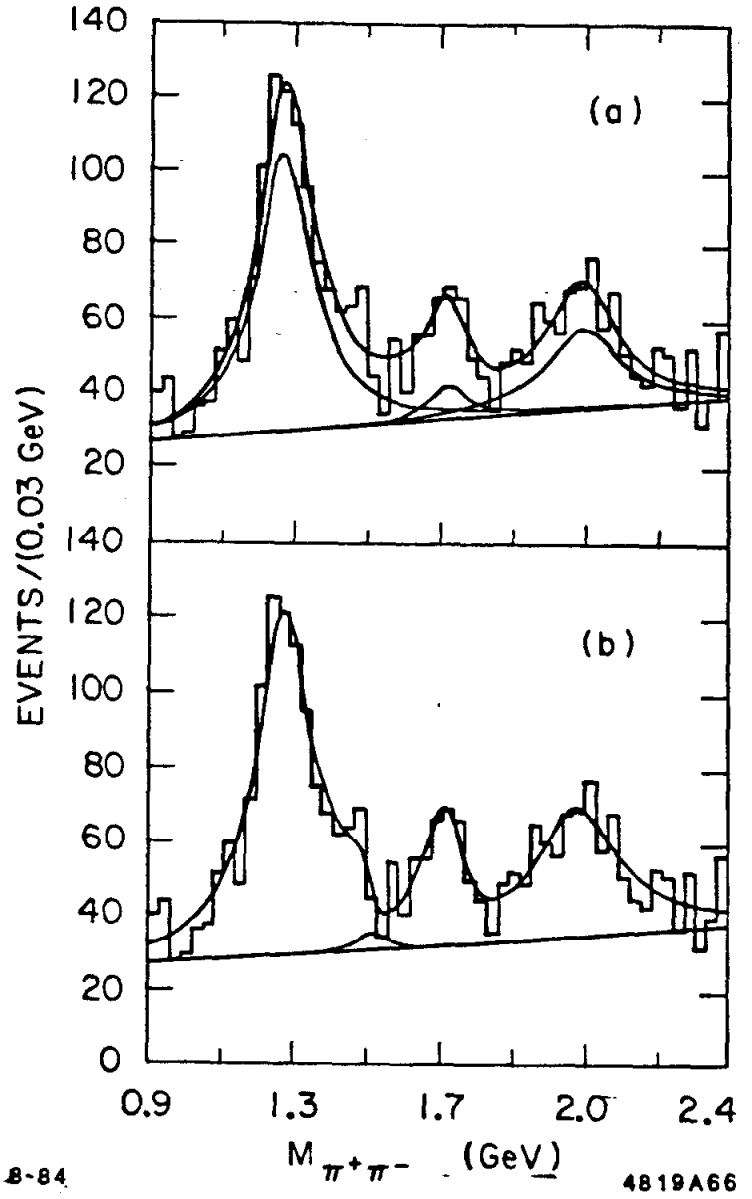

Figure 3.11. The $\pi^+\pi^-$ mass distribution with interfering fits. (a) shows a fit containing three Breit-Wigners representing the $f(1270)$, the $\theta(1700)$, and the $X(2100)$. (b) shows a fit containing four interfering Breit-Wigners. The additional peak corresponds to a possible signal for $f'(1515) \rightarrow \pi^+\pi^-$.

mass spectrum or in the measured branching ratios. This eliminates the possibility that the additional structures are associated with kaon feed through.

The other major background is $\psi \rightarrow \rho\pi$. Figure 3.3(b) indicates that its projection into the $m_{\pi^+\pi^-}$ plot is smooth. To check for problems, an additional cut was made in an attempt to remove much of this background. There are two aspects of the $\psi \rightarrow \rho\pi$ background which are useful in isolating these events. The first is the parameter-free prediction for the mass and angular dependence of the background, and the second is the limited region of phase space which is occupied by the background.

It is desirable to use as much information as possible in identifying the $\rho\pi$ events. The approach chosen uses the available angles and masses to calculate a 'probability' that a given event is a $\rho\pi$ event. This probability is just the $\rho\pi$ likelihood discussed in the previous section, and removing events which have a high $\rho\pi$ probability should be a very effective means to reduce the background. When this is done, the resulting spectrum still contains the same structures. The branching ratios measured for the $f(1270)$ and the $\theta(1700)$ are consistent with those found without the cut on the $\rho\pi$ probability, where in order to calculate the corresponding efficiencies, the full angular distributions have been modeled.

One final speculation has been investigated. In the previous studies of $\psi \rightarrow \gamma\pi\pi$ by MARK II and Crystal Ball there was a hint (not very significant) of structure on the high side of the $f(1270)$. This feature is also visible in Fig. 3.9. In addition, the decay $\psi \rightarrow \omega\pi^+\pi^-$ has been studied by MARK III. This mode has a very large quasi-two body decay mode: $\psi \rightarrow \omega f(1270)$, with about 2000 observed events. In this final state, there is no indication for structure on the high side of the $f(1270)$.

A possible explanation for this is shown in Fig. 3.11(b). In this figure, a fit

has been made to four interfering Breit-Wigners, including a possible contribution from $f'(1515) \to \pi^+\pi^-$. The mass and width of the $f(1270)$, $f'(1515)$, and $\theta(1700)$ have been fixed:

$$m_f = 1.270 \text{ GeV} \quad , \quad \Gamma_f = 0.180 \text{ GeV},$$

$$m_{f'} = 1.520 \text{ GeV} \quad , \quad \Gamma_{f'} = 0.080 \text{ GeV},$$

$$m_\theta = 1.720 \text{ GeV} \quad , \quad \Gamma_\theta = 0.130 \text{ GeV}.$$

The relative magnitude and phase of each Breit-Wigner amplitude was allowed to vary. The small peak in the $f'(1515)$ region corresponds to the squared amplitude for the $f'(1515)$ from the fit. This 'signal' corresponds to a product branching ratio of $\sim 3 \times 10^{-5}$. This can be translated into:

$$\frac{\text{BR}(\text{f}' \to \pi\pi)}{\text{BR}(\text{f}' \to \text{K}\bar{\text{K}})} \sim 0.05,$$

where the value for the f' product branching ratio to $\text{K}\bar{\text{K}}$ has been taken from the analysis of the K^+K^- channel presented in a later chapter. The 'signal' observed here is somewhat larger than expected, but the errors are correspondingly large. Such a signal would not be expected in the $\omega\pi^+\pi^-$ spectrum discussed above because $\psi \to \omega f'(1515)$ is OZI suppressed.

3.7 SUMMARY

The $\gamma\pi^+\pi^-$ final state has been analyzed. The $f(1270)$ is observed with a mass and width which agree well with the standard values. Due to the correlation between the $f(1270)$ width and the background shape, a fixed $f(1270)$ width has been used. The quoted branching ratio comes from a fit using three Breit-Wigners to describe the $f(1270)$ mass region since this appears to give the best description of the distribution. The results are:

$$m_f = 1.269 \pm 0.013 \text{ GeV}, \quad \Gamma_f = 0.180 \text{ GeV}$$

$$\text{BR}(\psi \to \gamma f(1270))\text{BR}(f(1270) \to \pi\pi) = (1.15 \pm 0.07 \pm 0.19) \times 10^{-3}$$

The best previous measurement of this branching ratio has been made by the Crystal Ball experiment[22] with the value:

$$(1.23 \pm 0.21 \pm 0.25) \times 10^{-3}.$$

The result presented here is in good agreement with this value.

A polarization analysis of the $f(1270)$ has been performed. The results shown below include estimated systematic effects in the fitting procedure, mostly associated with the large $\rho\pi$ background. These results are:

$$x = 0.96 \pm 0.12 \quad , \quad \varphi_x = -0.5 \pm 0.7$$

$$y = 0.06 \pm 0.13 \quad , \quad \varphi_y = -0.4 \pm 1.9$$

The best previous measurement of these parameters comes from the Crystal Ball experiment[22] with the values:

$$x = 0.88 \pm 0.11 \qquad y = 0.04 \pm 0.14.$$

This measurement was made for the $\pi^0\pi^0$ final state, and does not suffer from the large $\rho\pi$ background present in the current analysis. This measurement also did not include relative phases between the different helicity amplitudes (*i.e.*, $\varphi_x = \varphi_y = 0$ is assumed), but they don't appear to be significant in the current analysis. Again, the agreement is good.

A limit has been placed on the observation of the scalar state $S^*(975)$. The result is:

$$\mathrm{BR}(\psi \to \gamma \mathrm{S}^*(975))\mathrm{BR}(\mathrm{S}^*(975) \to \pi\pi) < 7 \times 10^{-5} \quad 90\% \text{ C.L.}$$

There is evidence for additional structure at high masses. This can be interpreted in terms of production of the $\theta(1700)$ and an additional broad resonance with a mass of ~ 2 GeV. The observed mass, width and $\cos\theta_\pi$ distributions for the "$\theta(1700)$" seen here are quite consistent with those observed in the $\mathrm{K^+K^-}$ channel, and so the $\theta(1700)$ interpretation appears well-founded. No clear interpretation exists for the higher mass resonance, but it could be an excited $f(1270)$, possibly the $h(2040)$. The branching ratio has been obtained for the $\theta(1700)$ by assuming the decay angular distributions are the same as those found in the $\mathrm{K^+K^-}$ channel. The results are:

$$m = 1.713 \pm 0.015 \text{ GeV} \quad , \quad \Gamma = 0.130 \text{ GeV},$$
$$\mathrm{BR}(\psi \to \gamma\theta(1700))\mathrm{BR}(\theta(1700) \to \pi^+\pi^-) = (1.6 \pm 0.4 \pm 0.3) \times 10^{-4}.$$

Previous studies of this final state by the MARK II experiment[24] resulted in the limit:

$$\mathrm{BR}(\psi \to \gamma\theta)\mathrm{BR}(\theta \to \pi\pi) < 3.2 \times 10^{-4} \quad 90\% \text{ C.L.}$$

This limit needs to be multiplied by 2/3 to compare with the current measurement (assuming $I = 0$), but there is no conflict.

The higher mass peak has the following properties:

$$m = 2.086 \pm 0.015 \text{ GeV} \quad , \quad \Gamma = 0.210 \pm 0.063 \text{ GeV},$$
$$\mathrm{BR}(\psi \to \gamma\mathrm{X}(2100))\mathrm{BR}(\mathrm{X}(2100) \to \pi^+\pi^-) = (3.0 \pm 0.5 \pm 0.6) \times 10^{-4}.$$

Chapter 4. The $\psi \to \gamma K^+K^-$ Final State

4.1 INTRODUCTION

Previous investigations of radiative ψ decays by the MARK II and Crystal Ball experiments have uncovered evidence for two unusual states, the $\iota(1440)$ and the $\theta(1700)$. These states do not fit conveniently into known $q\bar{q}$ multiplets, and further study is required to find out what kind of objects they really are. The $\iota(1440)$ appears to be a $J^P = 0^-$ state.[21] If this J^P assignment is correct, this state cannot decay into K^+K^-, and so nothing can be learned about it here. The $\theta(1700)$ has been observed in the K^+K^- final state, and will be discussed in more detail

The previous observations of the $\theta(1700)$ have left us with a very incomplete understanding of this state. The state was first observed by the Crystal Ball experiment[25] in the $\eta\eta$ mode, using 2.2×10^6 produced ψ's. They have used this mode to perform a spin analysis, with the result that $J^P = 2^+$ is favored at the 95% C.L. The statistics for this analysis were very poor, and no allowance was made for the possible presence of $f'(1515)$ contamination. This makes the J^P assignment less than totally convincing.

The MARK II experiment[24] later observed the $\theta(1700)$ in the K^+K^- mode. Their analysis was able to distinguish the $\theta(1700)$ from the nearby $f'(1515)$ signal. Unfortunately, their total event sample was 1.3×10^6 produced ψ's, and only 0.43×10^6 had fully functional electromagnetic calorimetry. This did not leave a large enough sample of clean events to perform an unambiguous spin analysis.

With the larger number of events available to the MARK III experiment, the $f'(1515)/\theta(1700)$ region can be studied in greater detail. The spins and production characteristics for both the $f'(1515)$ and the $\theta(1700)$ can be studied.

In addition, it appears that both the $\iota(1440)$ and the $\theta(1700)$ decay predominantly into final states which are rich in strange quarks. This offers the hint that such final states are worth the effort of continued examination; perhaps other new phenomena will emerge.

The current chapter will offer a brief overview of the γK^+K^- final state. The subsequent chapters will describe the analysis of the interesting mass regions in excruciating detail.

4.2 Kinematics and Event Selection

Before proceeding to the details of the event selection procedure, it is worthwhile to discuss the kinematics of the γK^+K^- final state. The most significant feature to consider is the charged kaon lifetime: $c\tau = 3.71$ meters. Very often, these kaons will decay in the detector. The charged kaons decay most of the time to $\mu^\pm\nu$ and $\pi^\pm\pi^0$, and the decay vertex is very difficult to reconstruct. This means that in order to reconstruct the event properly, the kaon must have a large flight path through the detector before it decays. The characteristic decay length in the detector is:

$$R_D = \beta\gamma c\tau = \frac{p_K}{m_K} c\tau,$$

and since $c\tau$ is similar to the size of the detector, the number of kaons which decay inside the detector depends very strongly on their momentum.

To make this statement more quantitative, the detection efficiency for single kaons as a function of momentum has been studied using Monte Carlo events. The kaon track was required to have a good helix fit in the drift chamber and to be consistent with the kaon hypothesis at the 2.5σ level in the TOF system. The TOF cut has a large effect on the efficiency. It tends to remove tracks which have a decay kink in the drift chamber, since they will not hit the proper TOF counter.

The results of this study are summarized in Fig. 4.1. This figure indicates that the efficiency for detecting kaons falls rapidly below 500 MeV, and is negligible below 200 MeV.

To understand the implications of this efficiency for the γK^+K^- final state, it is necessary to calculate the kaon momentum spectrum as a function of the K^+K^- mass. It is straight-forward to calculate the minimum and maximum kaon momenta in the detector for different K^+K^- masses. The results of such a calculation are displayed in Fig. 4.2. This figure indicates that the maximum momentum does not change greatly over this mass region, but the minimum momentum does. The vanishing minimum momentum that occurs at $m_{KK} \sim 1.35$ GeV is the result of a kinematic cross-over which takes place when the velocity of the K^+K^- system is equal to the velocity of the kaons in the K^+K^- center of mass. This occurs when:

$$m_{KK}^2 = \frac{m_\psi^2 m_K}{m_\psi - m_K},$$

and corresponds to a change in the event topology. Below the critical m_{KK}, the K^+K^- system has a large enough momentum that even a kaon moving backward in the K^+K^- center of mass is boosted forward in the lab. Above the critical m_{KK}, a kaon going backward in the center of mass has enough momentum that it continues going backwards in the lab. At the cross-over point, a kaon going backward in the center of mass comes to rest in the lab. This kinematic effect interacts with the kaon detection efficiency to produce a reduction in the overall efficiency in the 1.4 GeV mass region. This is significant for the $f'(1515)$ branching ratio measurement as well as for the $f'(1515)$ spin analysis. Armed with an understanding of the kinematics of the γK^+K^- final state, we can begin the event selection process.

The topology of this final state is quite simple, and the corresponding event selection is also simple.

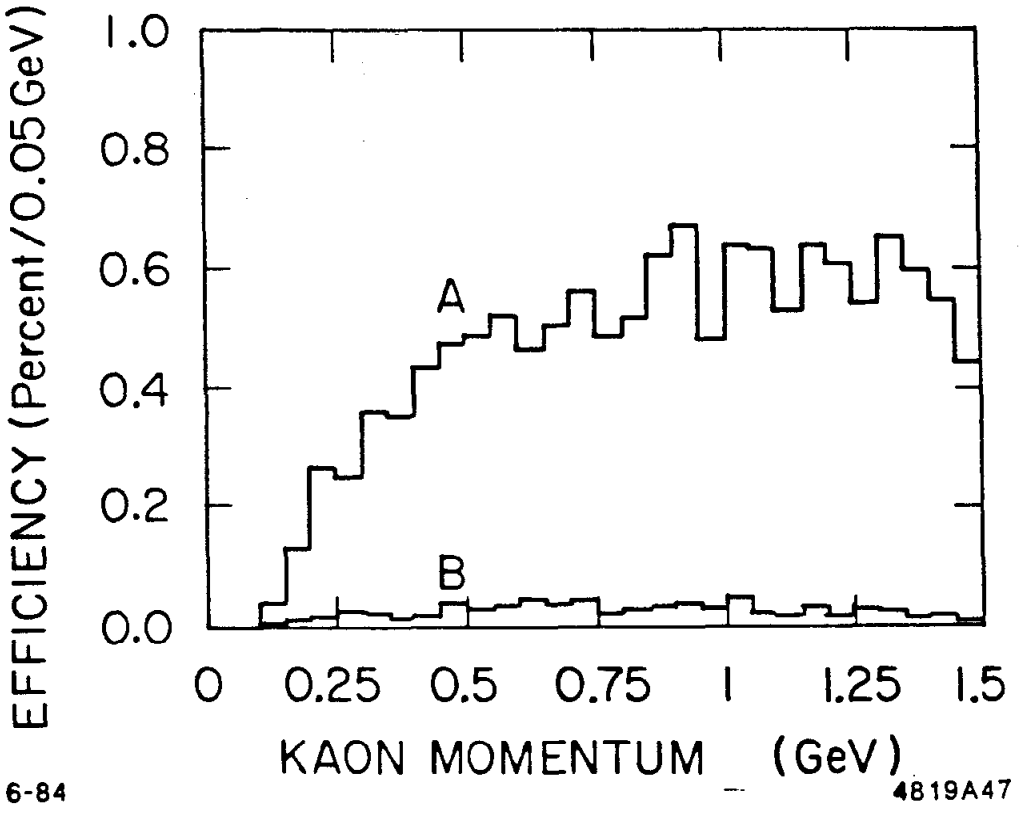

Figure 4.1. Single track kaon efficiency versus momentum. Curve (A) corresponds to non-decaying kaons and curve (B) corresponds to kaons which decayed in the drift chamber volume.

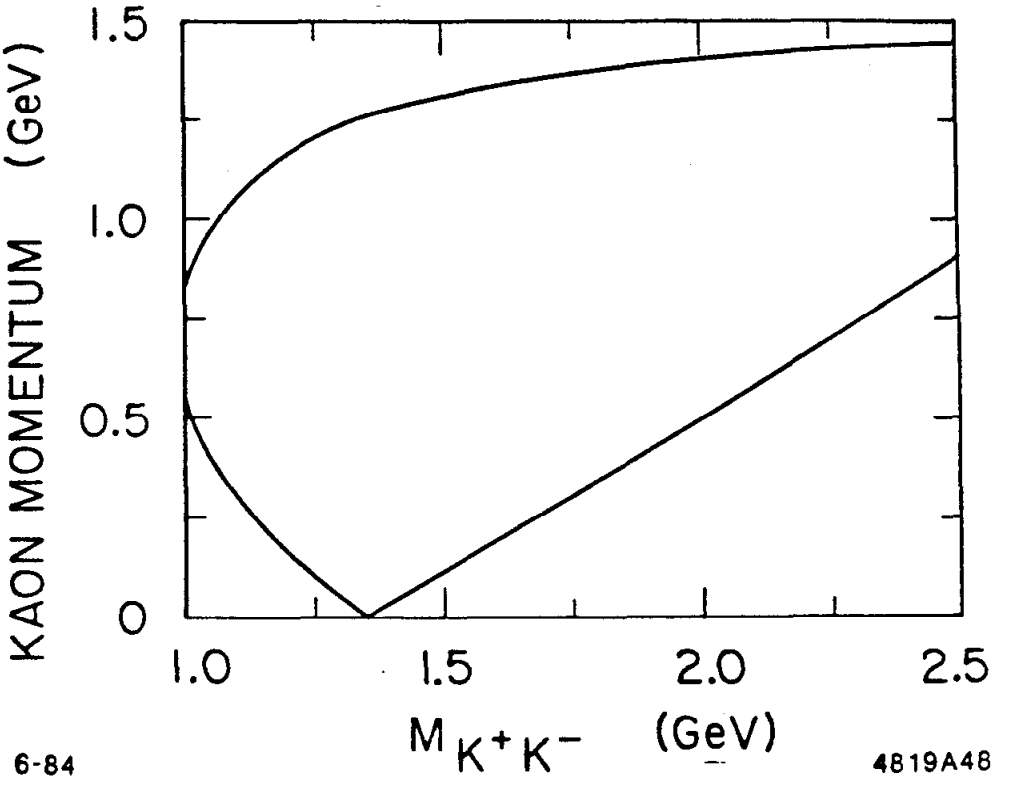

Figure 4.2. The minimum and maximum kaon momenta versus m_{KK}.

Photon Selection

The events were required to have $n_\gamma \leq 4$. The photons which were actually used in the kinematic fitting were required to be 'good' photons. This requirement means that: the angle to the nearest charged track, $\cos\theta_{\gamma-K}$, was required to be $< .95$, the number of layers hit in the shower counter was required to be ≥ 2, and the starting layer of the shower was required to be ≤ 7. No cut was imposed on the number of such 'good' gammas in the event.

No cut is made on the position of the photon in the detector, and, in particular, the endcap/barrel boundary region is not eliminated. Although the photon energy is poorly measured in this region, the photon position measurement is not strongly affected. Since the energy resolution is poor to begin with, the results of the kinematic fit are also not strongly affected.

Charged Track Selection

There are two types of criteria relevant for the charged track selection. The tracks must be well measured in the drift chamber, and they must be identified as being consistent with kaons in the TOF system. The drift chamber cuts are very minimal. In order to perform subsequent fits to the events, it is necessary that the track has a full error matrix from PARCS, the precision helix fitting routine for the drift chamber. Because of the restricted solid angle imposed by the TOF requirement for each track, no further cuts were made on DC track quality.

The TOF identification for the tracks is somewhat more difficult. Figure 4.2 indicates that the maximum kaon momentum is always above 1 GeV. The ability of the TOF system to separate kaons from a pion background at momenta above 1 GeV is very limited. For this reason, the only requirement for the initial selection was that each track was consistent with the kaon hypothesis at the 2.5σ

level. This corresponds, assuming the errors are correct, to a weight ≥ 0.05, where the weight is defined to be:

$$e^{-\chi^2/2} \quad \text{and} \quad \chi^2 = \left(\frac{t_{meas} - t_{pred}}{\sigma_t}\right)^2.$$

Although the TOF separation is not good for high momentum tracks, there are two reasons why the situation is not as bad as it might seem. First, whenever one track is poorly identified due to its high momentum, the other track is better identified due to its lower momentum. This means that the ability to identify the K^+K^- pair using the TOF information alone is quite good. Second, the drift chamber provides complementary particle identification via the kinematic fit. It is the combination of the TOF information and the kinematic fitting which provides a clean sample of charged kaons at the relatively high momenta present in this final state. The kaon consistency cut, in combination with a kinematic fit, is sufficient to isolate a clean sample of events with m_{KK} below about 2 GeV. For events with higher masses, the power of the kinematic fit to reject non-kaon background events is reduced. This can be intuitively understood in the following way. The error imposed by changing the mass of the charged tracks in the kinematic fit does not affect the momentum balance of the event, since the charged track momenta are actually measured. What is changed is the total energy of the event. If the momenta of the tracks are large, the energy of a given track is dominated by its momentum rather than by its mass. In this case, the wrong mass hypothesis produces a smaller energy change, and is not as easy to eliminate.

In order to proceed further towards a clean sample, it is necessary to make the additional requirement that the tracks are not consistent with the pion hypothesis. This is done by requiring that the relative TOF weight: π weight/K weight, is less than one for both charged tracks. This cut does introduce a slight momentum dependence in the efficiency for kaons with momenta above

1 GeV. However, the overall efficiency for the K^+K^- system is almost independent of the individual kaon momenta, since when one K has a high momentum, the other has a low momentum.

Kinematic Fitting

Kinematic fits were performed to impose energy and momentum conservation. These fits provide an improvement in the resolution and also aid in rejecting background events. Fits were performed using all permutations of the 'good' gammas in the event, and the fit with the smallest χ^2 was used for that event. Two parallel hypotheses were examined, representing the signal of interest ($\psi \rightarrow \gamma K^+K^-$) as well as the largest background ($\psi \rightarrow \gamma\gamma K^+K^-$).

K Decays

The previous discussion of kaon decays described the single track efficiency. Now that the event selection procedure has been established, it is useful to examine the influence of kaon decays on the results. In order to study this, Monte Carlo events have been generated over the $1 - 2$ GeV mass region with a phase space distribution. Figure 4.3(a) shows a distribution for events in which one of the two kaons decayed inside the drift chamber volume. The quantity plotted is the radius at which the kaon decay occurred. Two interesting results are obtained. The first is that $\sim$ 5% of the events which pass the selection cuts actually contain a decaying kaon. The second result is that the radius at which the kaon decay occurs is large. For reference, some drift chamber radii are: $L3 \sim .40\ m$, $L5 \sim .67\ m$, and $L7 \sim .94\ m$. Clearly, events with an early kaon decay are too poorly measured to survive the selection procedure. Fig. 4.3(b) shows the kinematic fit P_{χ^2} for these events. It is flat, and indicates that no serious measurement errors exist for these events. In addition, the Monte Carlo indicates that the mass resolution for these events is identical to that for events without decaying kaons. This leads to

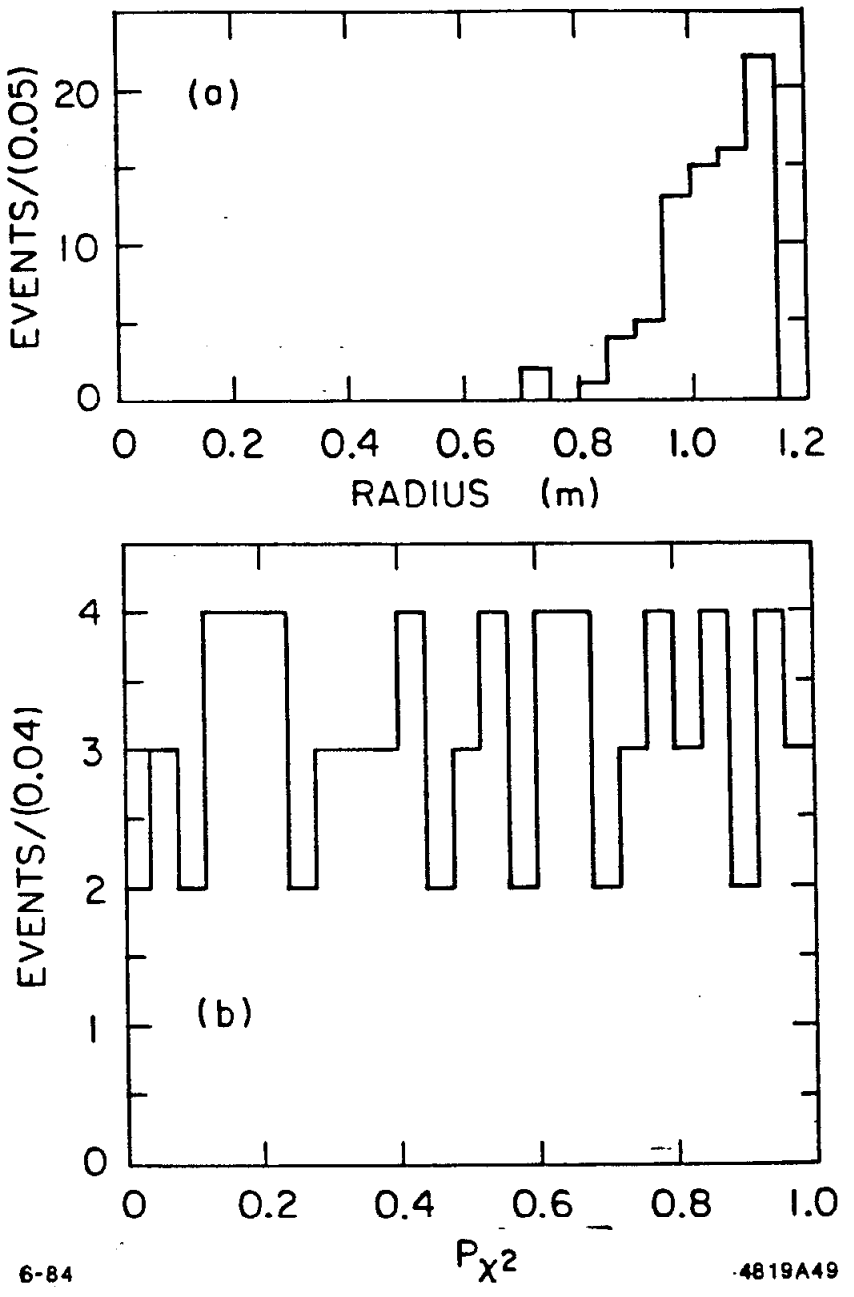

Figure 4.3. Distributions for Monte Carlo events containing kaon decays. The events in these plots contain at least one kaon which decayed in the drift chamber volume. (a) shows the radius (in meters) at which the kaon decay occurred for events which have passed the γK^+K^- event selection cuts. (b) shows the kinematic fit P_{χ^2} for these events.

the conclusion that the presence of kaon decays serves to lower the efficiency for detecting an event, but it *does not* affect the mass resolution or the kinematic fit P_{χ^2} distribution for those events which pass the selection criteria.

4.3 THE $\psi \to \gamma K^+K^-$ SIGNALS

The distribution of events which is obtained after making the event selection cuts is shown in Fig. 4.4. The charged tracks were both required to be consistent with the kaon hypothesis and not consistent with the pion hypothesis. If the anti-pion cut were removed, the background above a mass of 2 GeV would be unacceptably large.

This distribution shows evidence for the $f'(1515)$ and the $\theta(1700)$ peaks, seen previously by MARK II, and shows further evidence for a remarkably narrow structure at ~ 2.2 GeV. This peculiar object has been christened the $\xi(2220)$. The name is derived from the word $\xi\acute{\epsilon}\nu o\varsigma$, which is a Greek adjective for something strange or extra-ordinary,[35] as well as a letter which, due to its sibilant character, has not been recently used in the naming of particles. The detailed analysis of the $f'(1515)/\theta(1700)$ region and the $\xi(2220)$ region will be discussed in the following chapters. In preparation for that discussion, we briefly describe the possible backgrounds for the events shown in Fig. 4.4.

4.4 BACKGROUNDS

There are a number of potential background sources for $\psi \to \gamma K^+K^-$. These backgrounds fall into two general classes. One class, in which the charged particles are not kaons, can be largely eliminated by simple cuts since the detector provides high quality information. The second class, in which there are extra photons in the event, is much more difficult to eliminate—especially when these photons have a low energy. This is especially true for radiative decays, since the

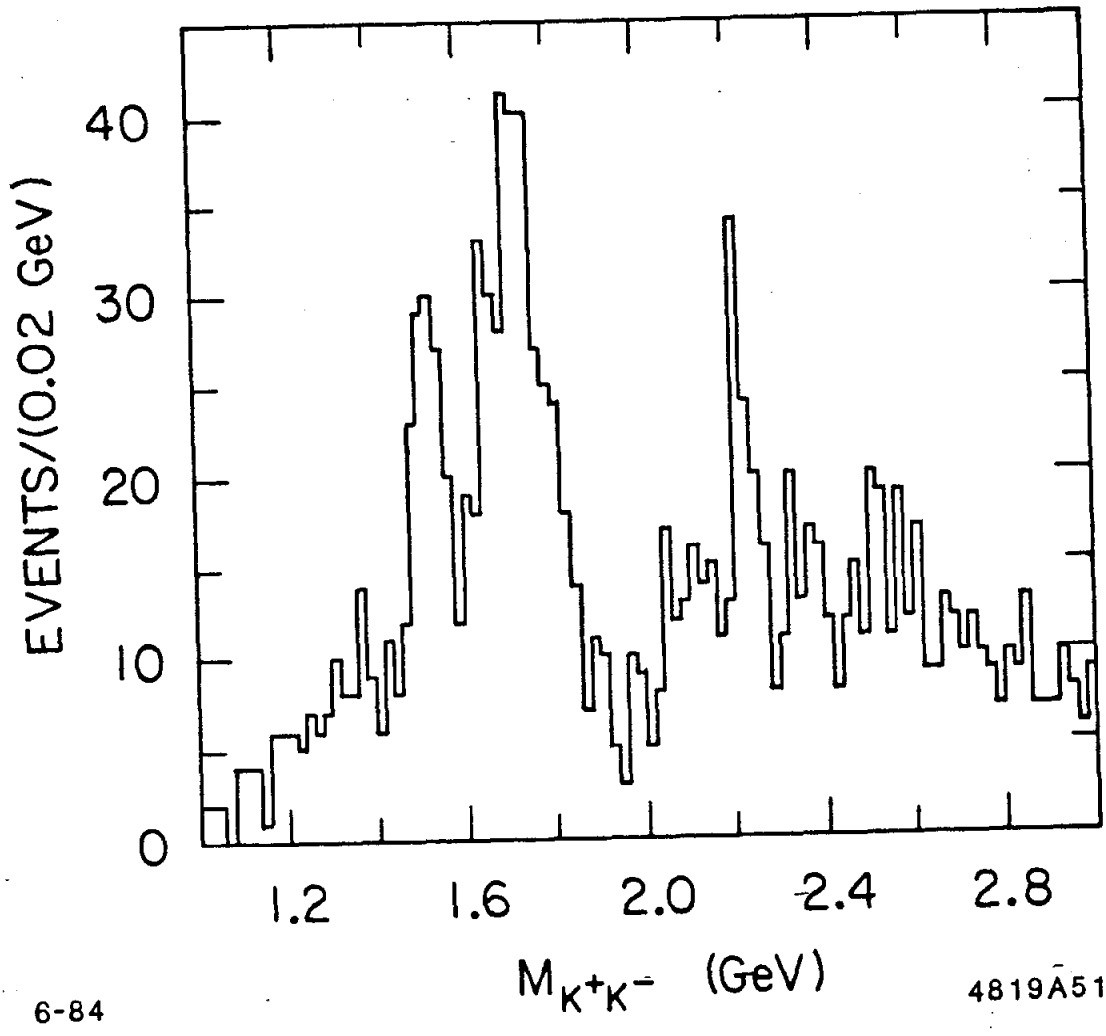

Figure 4.4. The $\psi \rightarrow \gamma K^+K^-$ mass distribution.

backgrounds with one extra photon arise from the larger direct decays of the ψ. The background sources will be examined, one at a time, for the full mass region. Background estimates will be made for the two regions of interest: the low mass region with $1.0 \leq m_{KK} \leq 2.0$ GeV and the high mass region with $2.0 \leq m_{KK} \leq 2.5$ GeV. For reference in the following discussions, the total sample contained in Fig. 4.4 numbers 1337 events.

The background levels may be estimated in two different ways, both of which have potential pitfalls. One technique involves generating Monte Carlo background events. These background events are passed through the standard event selection and the efficiency for them to appear in the signal region is calculated. The efficiency is combined with the total number of such events expected, and provides the background estimate. This technique will tend to underestimate the background levels, because the event selection will choose unusual events which agree with the incorrect (signal) hypothesis. A Monte Carlo simulation usually generates too few of these pathological events, since they may not be the result of Gaussian measurement errors.

The other technique for estimating background levels involves using real data. One isolates a sample of background events using loose cuts and then passes them through the event selection used for the signal. This technique suffers from the complication that signal events (which will be a background for the background ...) will feed through into the background estimate. It also has the same problem as the Monte Carlo estimate—once a clean background sample is selected, the resulting events are less likely to be pathological and hence less likely to agree with the incorrect (signal) hypothesis. Both of these techniques will be used, when it is possible, to provide a more reliable background estimate.

$\underline{\psi \to \gamma e^+ e^-}$

This background has been discussed in detail in the preceding chapter on $\psi \to \gamma\pi^+\pi^-$. It is strongly suppressed by kinematic fitting, since the mass difference between the electron and the kaon is large. The kinematic suppression was checked by looking for the characteristic pattern of electromagnetic energy deposit in the shower counter that would be expected for electrons. For the mass region below 2.5 GeV, there were three events in which one track had a shower energy above 1 GeV and the other track had a shower energy above 0.5 GeV. This suggests that at most ~ 5 events in the $1 - 2.5$ GeV mass region arise from this background source, and it is negligible.

$\underline{\psi \to \gamma\mu^+\mu^-}$

The rejection of these events by the muon system is very poor in this mass region. The presence of kaon punch-through and kaon decays does not permit making very tight anti-muon cuts, and so the contribution of the muon system to rejecting this background will be ignored. In that case, the rejection of the background comes from kinematics alone. These events are all due to final state radiation. This is due to the fact that the continuum cross-section for $e^+e^- \to \mu^+\mu^-$ is very small when compared to the cross-section at the ψ. It is important to note that these events have a mass distribution which is strongly peaked at high mass. This is because the muon is sufficiently heavy that it doesn't radiate a large photon very often. To check the contribution from this background, Monte Carlo events were generated using a QED radiative event generator.[36] These events were produced with the correct mass distribution and total cross-section. They were then passed through the standard γK^+K^- event selection. The result is that the efficiency with which these events pass the γK^+K^- selection procedure is $\epsilon \lesssim 0.001$, which corresponds to a background from this source of ~ 1 event in the mass region

below 2.5 GeV.

$\underline{\psi \rightarrow \gamma\pi^+\pi^-}$

The major feature in this final state is the $f(1270)$ resonance. One might worry about the possibility of events from the process $\psi \rightarrow \gamma f(1270)$ with $f(1270) \rightarrow \pi^+\pi^-$ passing the γK^+K^- event selection cuts and appearing in the $f'(1515)$ region. This has been checked using Monte Carlo events generated with the correct $f(1270)$ characteristics. The efficiency for passing these events through the γK^+K^- cuts is found to be:

$$\epsilon \sim 1 \times 10^{-3}$$

for the case where the charged tracks were required to pass a kaon consistency cut, but not an anti-pion cut. This means that there should be ~ 3 such events in the γK^+K^- sample. This estimate may be overly optimistic, since the Monte Carlo does not correctly simulate all the tails of the distributions properly. In order to check this and also to check the feed-through in the high mass region, the $\gamma\pi^+\pi^-$ event sample was passed through the γK^+K^- event selection procedure. The result is similar to the Monte Carlo estimate. There were ~ 5 events below 2 GeV in mass after the kinematic fit and the kaon consistency cut. A larger number of events feed through above 2 GeV. This feed through was substantially reduced with the addition of the anti-pion TOF cut. The result is that ~ 15 events remain in the $2 - 2.5$ GeV mass region. This background in the higher mass region is mostly associated with the $\psi \rightarrow \rho\pi$ decay mode which is discussed in the next section.

$\underline{\psi \rightarrow \pi^+\pi^-\pi^0/\rho\pi}$

The $\pi^+\pi^-\pi^0$ final state is almost totally dominated by the $\rho\pi$ resonant state, as indicated previously. This is a very large branching ratio for the ψ, and

a total of 20000 such events have been detected. The size of this branching ratio makes it important that the rejection is very good. To understand the effects of this background, Monte Carlo events were generated with the correct angular distributions, and passed through the γK^+K^- event selection. The $\rho^0\pi^0$ final state is very strongly suppressed by the combination of TOF and kinematic fitting. This is because the charged tracks have a relatively soft momentum spectrum, making both TOF and kinematic discrimination more effective. The Monte Carlo estimate is that < 5 $\rho^0\pi^0$ events will appear as background in the mass region below 2 GeV. The $\rho^\pm\pi^\mp$ background is more difficult to reject. Most of the events which survive the event selection process are above a mass of 2.5 GeV. The Monte Carlo estimate is that ~ 15 $\rho^\pm\pi^\mp$ events feed through into the $2-2.5$ GeV region of the mass plot.

These Monte Carlo estimates have been partially checked by studying the feed-through of $\rho^\pm\pi^\mp(\pi^+\pi^-\pi^0)$ events into the $K^{*\pm}K^\mp(K^+K^-\pi^0)$ signal. The contamination is estimated by making a series of increasingly stringent $K^+K^-\pi^0$ event selection cuts, and studying several distributions for the events that pass and fail these cuts. The distributions for the real data are compared with those found for Monte Carlo events. For loose event selection cuts, the data has a great deal of contamination and looks different from the Monte Carlo. As the cuts are tightened, the data and the Monte Carlo start to agree. The contamination estimates for various selection cuts which are derived agree reasonably well (within $\sim 50\%$) with the Monte Carlo technique used previously. This suggests that the $\rho\pi$ background is also not a significant source of events.

$\underline{\psi \to K^+K^-\pi^0/K^{*\pm}K^\mp}$

This background is dominated by the resonant two body final state $K^{*\pm}K^\mp$, as shown in Fig. 4.5. This figure contains events which have been kinematically fit to the $\gamma\gamma K^+K^-$ hypothesis. An additional cut has been made,

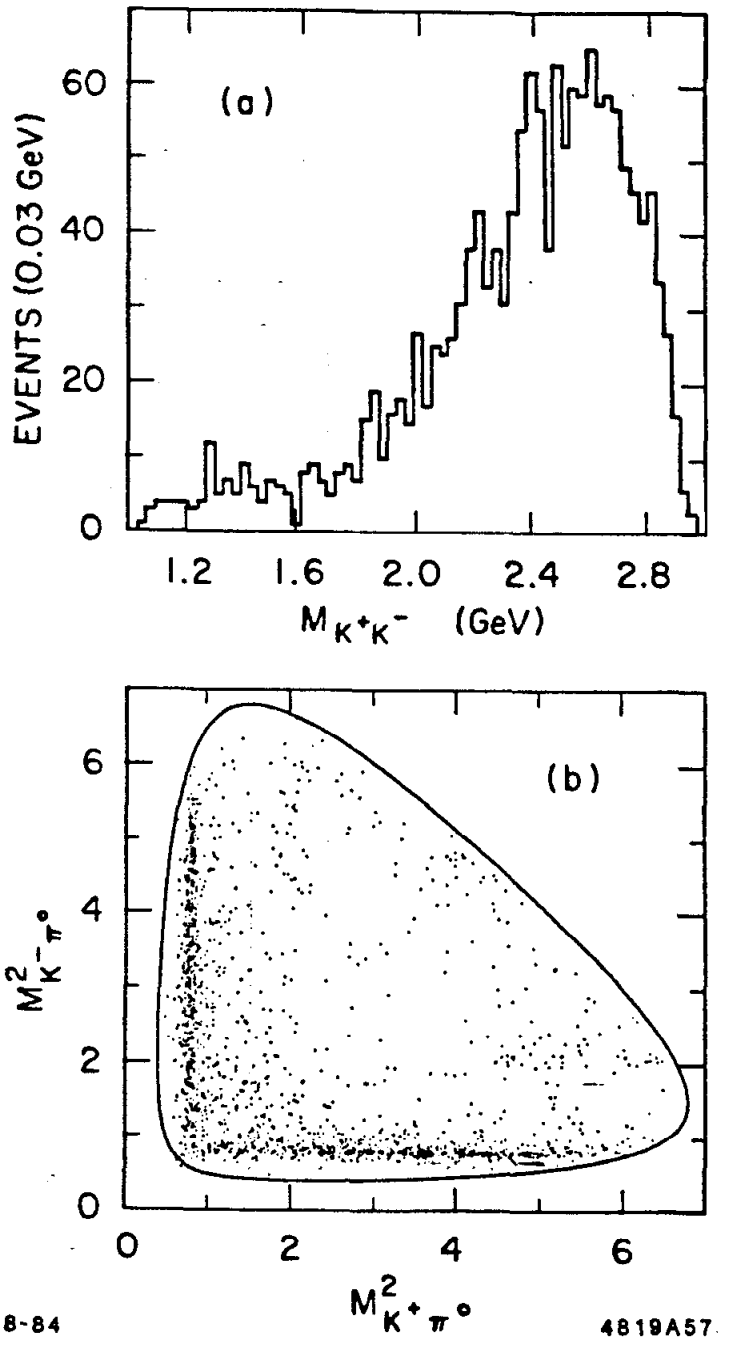

Figure 4.5. The distributions for $K^+K^-\pi^0$ events. (a) shows the mass for the two kaons. (b) shows the Dalitz plot.

requiring $m_{\gamma\gamma}$ to be consistent with the π^0 mass. These events are difficult to distinguish from the γK^+K^- signal events, and this final state provides the only serious source of background. Fortunately, the analysis of the region below 2 GeV in mass is not strongly affected by this background. This is indicated by the distribution shown in Fig. 4.5(b). Most of these events have a K^+K^- mass above 2 GeV. The contribution of $K^+K^-\pi^0$ events in the $1-2$ GeV region is estimated to be ~ 30 events. This is roughly 5% of the total signal in this mass region, and so does not constitute a large background. We are left with a large background from $\psi \rightarrow K^{*\pm}K^{\mp}$ in the $2-2.5$ GeV region. The shape of the background, as well as the number of such events observed in the 2 to 2.5 GeV region, has been estimated by generating the correct number of $K^{*\pm}K^{\mp}$ events, and then passing them through the γK^+K^- analysis chain. The estimate from the Monte Carlo is that ~ 120 events in the 2 to 2.5 GeV region are from this background source, which accounts for $\sim 1/2$ of the total number of events observed in this region. This background will be discussed in more detail in the chapter on the $2-2.5$ GeV mass region.

Chapter 5. The Low Mass Region in $\psi \rightarrow \gamma K^+K^-$

5.1 Event Selection

The event selection has been described previously and is summarized here. A loose kaon requirement is made—both tracks must have TOF measurements which are consistent with the kaon hypothesis at the 2.5σ level. This cut is sufficient to provide a clean sample of events, since the pion backgrounds peak at higher masses. A kinematic fit is performed in order to improve resolutions and eliminate backgrounds. The confidence level for the kinematic fit is required to be: $P_{\chi^2} \geq 0.02$.

This set of cuts produces the mass distributions shown in Fig. 5.1(a) for the 1983 data sample, and Fig. 5.1(b) for the combined 1982 and 1983 data sample. These samples are displayed separately because different aspects of the analysis will use one or the other of the samples. The 1983 sample will be used when precise agreement with the Monte Carlo is required, since only the 1983 detector is well modeled by the Monte Carlo. This is necessary for the spin analysis and the branching ratio measurements. The combined sample will be used when there is no reason to ignore the 1982 data sample. It should be noted that, in contrast to the higher mass region, there is no significant difference between the results derived from the two different samples.

Two states are apparent in the mass plot. The lower peak has the correct mass to be identified with the $f'(1515)$ tensor meson. The upper peak has a mass which is in approximate agreement with the $\theta(1700)$. The statistics is sufficient to see a Breit-Wigner line shape for both states, and the separation between the states is clear.

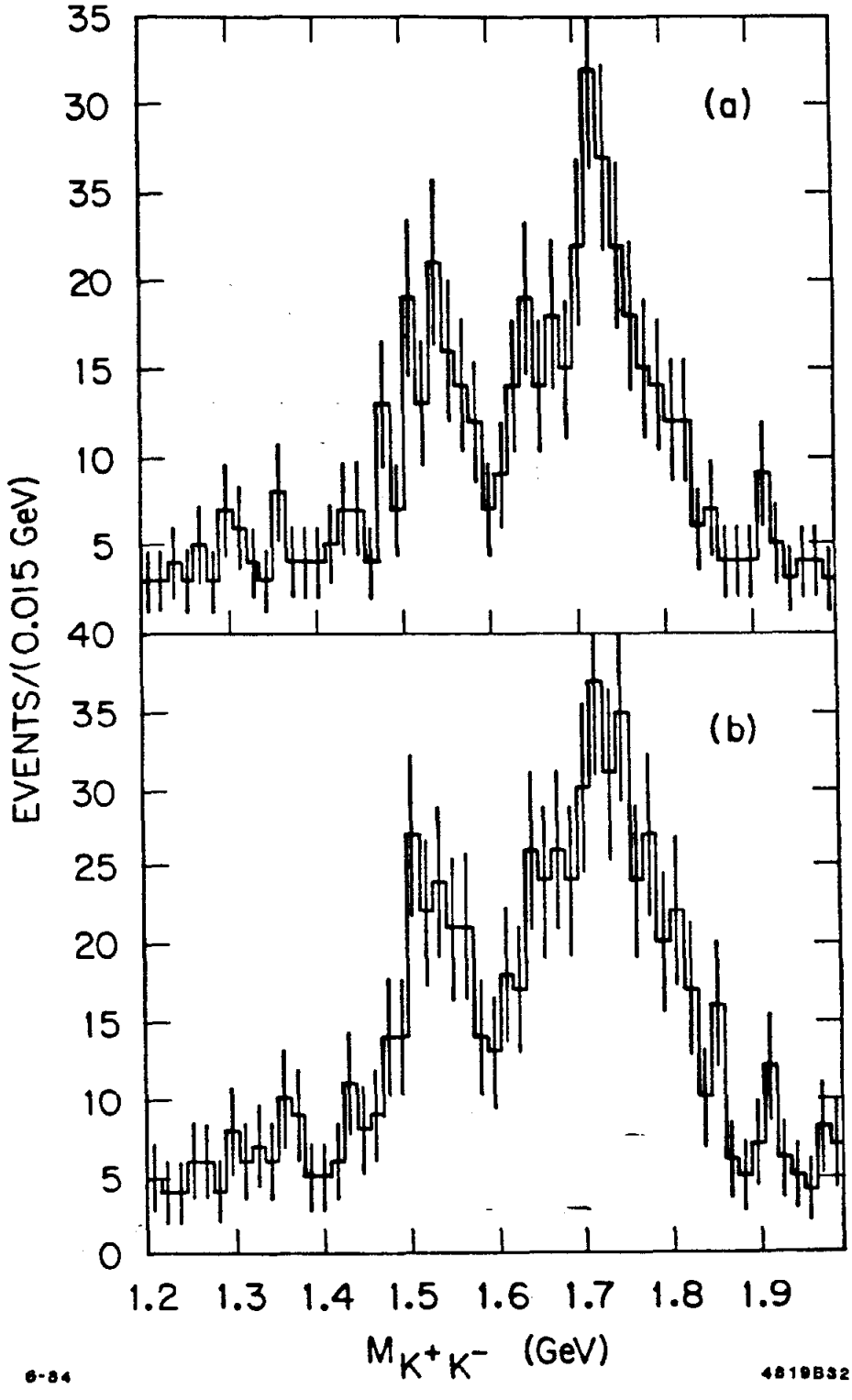

Figure 5.1. The K^+K^- mass distribution for the 1-2 GeV region. (a) shows the 1983 data sample alone. (b) shows the combined 1982 and 1983 data sample.

5.2 BACKGROUNDS

The preceding chapter indicates that the background level in this mass region, for these cuts, is very low. The principal source of background appears to be $K^+K^-\pi^0$ events. This background is estimated to contribute ~ 30 events in the $1.2 - 2.0$ GeV mass region. This represents $\lesssim 5\%$ of the total signal in this region, and will be neglected in future discussions.

5.3 ANALYSIS STRATEGIES FOR THE $f'(1515)/\theta(1700)$ REGION

The low mass region in $\psi \to \gamma K^+K^-$ appears to be quite complex. There are at least two observed resonances, and a third resonance, the $f(1270)$, is expected to be present at a low level. The two observed resonances overlap, with the consequent problem of interference. It is possible that the $\theta(1700)$ is not one state, but actually two overlapping states. There is a further possibility of a sizeable γK^+K^- continuum which could, in analogy with the Born production of pion pairs[37] in $\gamma\gamma \to \pi^+\pi^-$, interfere with the resonances. In the face of such a diverse range of possibilities, there are numerous models or fitting procedures which can be used to try to understand this region.

The measured quantities to be included in the analysis are chosen to be the mass of the kaon pair (m_{KK}), and the three production and decay angles defined previously ($\cos\theta_\gamma$, $\cos\theta_K$ and ϕ_K). A complete description of the physics in this region should depend only on these quantities. This can be demonstrated by a counting argument. For a 3-body final state there are 12 unknowns, corresponding to the components of the three 4-vectors. These can be chosen as follows:

3 known 1-body masses,

4 known components of the total 4-vector of the system,

5 additional variables.

These five additional variables have natural definitions in the helicity formalism. They can be chosen to be:

1 2-body mass,

1 (θ, ϕ) pair for the recoil against the 2-body system,

1 (θ, ϕ) pair for the decay of the 2-body system.

Of the four angles described here, only three are meaningful in this analysis. The azimuthal angles may be re-written as two linear combinations of the original angles. One combination is the difference, which contains useful information. The other combination is the sum, which is not interesting because the beam has no polarization component perpendicular to its direction of motion, and hence there is a rotational symmetry about the beam axis. We are left with the 2-body mass and three angles as the complete set of variables.

A sequence of increasingly complex models will be applied to attempt to untangle the resonant structures which may be present. The first analysis to be performed uses a model which ignores the angular distributions, as well as any acceptance corrections, and just parameterizes the distribution of events in the mass plot. This provides measurements of masses and widths, using the maximum likelihood fit technique described in Appendix A. The next analysis involves fits to the angular distributions in the $f'(1515)$ and the $\theta(1700)$ regions, including all the acceptance corrections, and ignoring the details of the mass distribution. This provides a measurement of the J^P of the resonances as well as their production amplitudes. Once the Breit-Wigner parameters, along with the J^P, x, and y are known, it becomes possible to measure the branching ratios by correctly modeling the true final state distributions. Finally, an attempt has also been made to fit both the mass and angular distributions simultaneously in order to explore the possibility of sub-structure in the $\theta(1700)$. The available statistics is insufficient for an analysis

of this complexity, and the results are inconclusive; no detailed discussion of this analysis is included.

5.4 Mass Plot Analysis for the $f'(1515)/\theta(1700)$ Region

The simplest procedure for extracting the masses and widths for the $f'(1515)$ and the $\theta(1700)$ is to fit the mass plot to a polynomial background plus a sum of two incoherent Breit-Wigners. The polynomial background can be left free, or its shape can be fixed to be the shape expected for γK^+K^- 3-body phase space. For the purposes of this section, the background has been chosen as 3-body phase space. This provides a reasonably accurate description of the data, as well as simplifying the comparison of different resonance hypotheses which would otherwise be free to distort the background shape in non-physical ways. The results of a fit using two incoherent Breit-Wigners with a phase space background are displayed in Fig. 5.2(a). The parameters obtained are:

$$m_{f'} = 1.527 \pm 0.008 \text{ GeV}, \quad \Gamma_{f'} = 0.087 \pm 0.037 \text{ GeV},$$

$$m_{\theta} = 1.721 \pm 0.007 \text{ GeV}, \quad \Gamma_{\theta} = 0.132 \pm 0.020 \text{ GeV},$$

where the quoted errors are statistical only. These fits have been performed using both a non-relativistic Breit-Wigner and a relativistic Breit-Wigner (although without including the effect of an energy dependent width). The results from the two cases differ by only a few MeV. For simplicity, the values discussed in the remainder of this chapter use non-relativistic Breit-Wigners.

This procedure seems to describe the data relatively well, but it is not the most general representation of the possible physics. An obvious generalization involves letting the two Breit-Wigners interfere with each other. For the situation here, one can define a simple model in which there are two different resonant

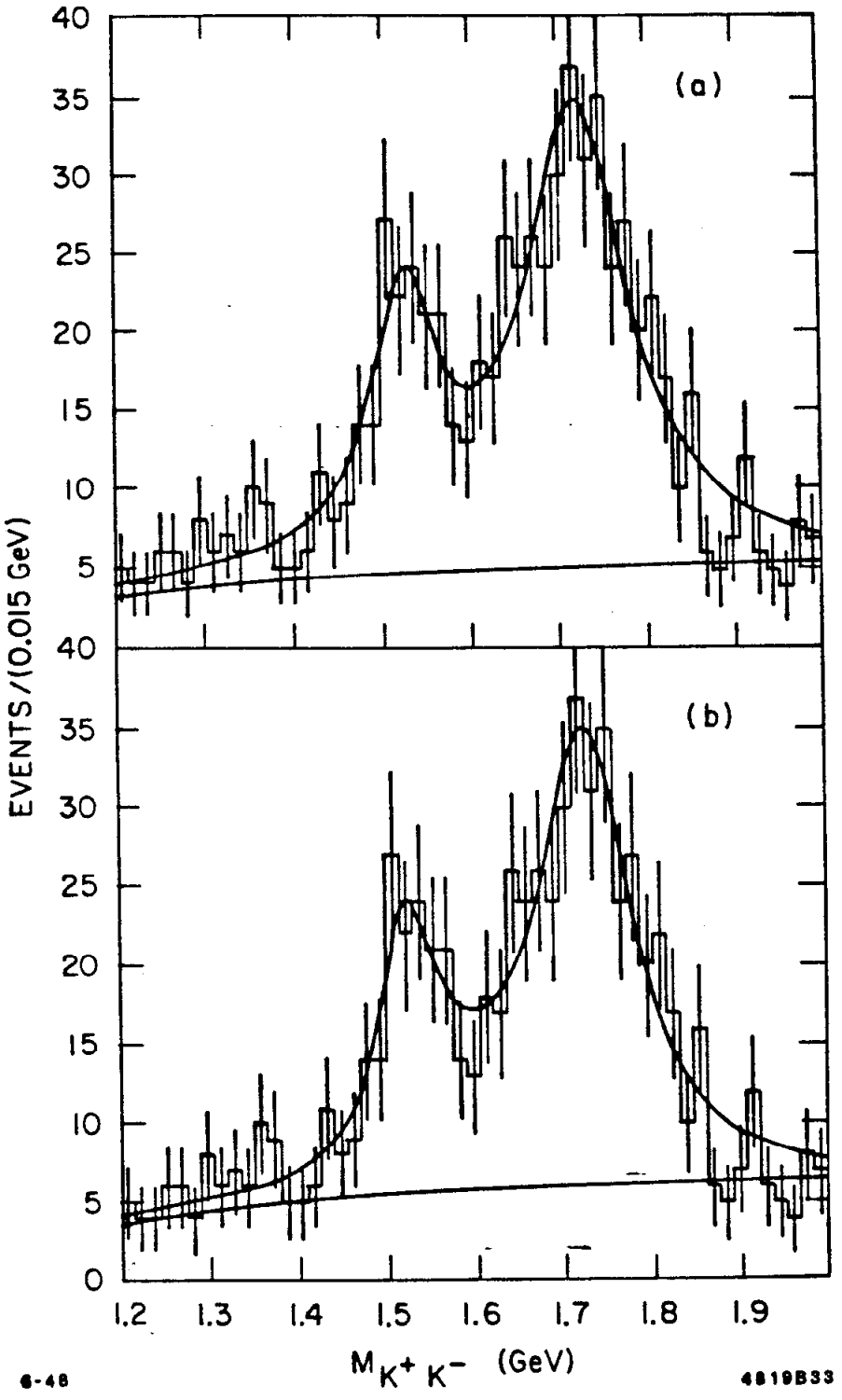

Figure 5.2. Fits to the $f'(1515)/\theta(1700)$ mass distribution. (a) shows a fit which includes two incoherent Breit-Wigner probabilities. (b) shows a fit which includes two coherent Breit-Wigner amplitudes.

amplitudes for producing the same final state. The cross-section is then of the form:

$$\frac{d\sigma}{dm} \sim \int |A_1(m,\Omega) + A_2(m,\Omega)|^2 \, d\Omega.$$

The interference effects arise from the cross-term:

$$\sim \int Re\,[A_1(m,\Omega)^* A_2(m,\Omega)]\, d\Omega.$$

If the resonant states don't overlap in mass, then the cross-term clearly vanishes for every value of the mass. If the resonances do overlap, the cross-term will still vanish for states with different J values. This is because the amplitudes are orthogonal when integrated over the angles, and is discussed in more detail in Appendix B. It leads to the conclusion that, if the angular acceptance is sufficiently good, only states with the same values for J will interfere in the mass plot. The possibility of significant interference between the $f'(1515)$ and the $\theta(1700)$ has been discussed for the MARK II data.[38] In that case, there was some evidence for a large dip between the $f'(1515)$ and the $\theta(1700)$. The effect of the interference for the $f'(1515)/\theta(1700)$ system is easily calculated if one considers only the mass dependent part of the amplitudes. The cross-section involves the sum of two Breit-Wigner probabilities plus an additional cross-term which can be written (assuming non-relativistic Breit-Wigners) as:

$$\frac{\left[(m-m_{f'})(m-m_\theta)+\Gamma_{f'}\Gamma_\theta\right]\cos\varphi + \left[(m-m_{f'})\Gamma_\theta-(m-m_\theta)\Gamma_{f'}\right]\sin\varphi}{\left[(m-m_{f'})^2+\Gamma_{f'}^2\right]\left[(m-m_\theta)^2+\Gamma_\theta^2\right]}.$$

This cross-term is a function of two parameters: the mass m and the relative phase φ, and different effects will be observed for different relative phases. There are three extreme cases which are of interest: the cross-term is large and negative, the cross-term is large and positive, or the cross-term is negligible. The most sensitive

mass region for studying this cross-term is the dip at a mass of 1.6 GeV, which occurs between the $f'(1515)$ and the $\theta(1700)$ peaks. If m is fixed to be 1.6 GeV, then one can easily solve for the relative phase which produces the extreme cases above. Note that the value for the phase which corresponds to a particular case, *e.g.*, a vanishing cross-term, depends on the mass. This means that there is no value for the phase which will cause the cross-term to vanish for all masses, and hence the incoherent fit is not a limiting case of the coherent fit. The phases which produce the extreme cases for the dip region are listed below:

maximum positive cross-term	$\varphi \sim 3\pi/4$
maximum negative cross-term	$\varphi \sim -\pi/4$
vanishing cross-term	$\varphi \sim \pi/4$

Fits in which the phase has been fixed at these three extreme values have been performed. The remaining parameters were allowed to vary, and the results are shown in Fig. 5.3 and summarized in Table 5.1. The qualitative features are fairly simple. For the case with large destructive interference between the $f'(1515)$ and the $\theta(1700)$, Fig. 5.3(a), there is constructive interference above and below the resonances. The masses found for the resonances are pulled closer together, and the fraction of background is forced to be smaller. For the case of constructive interference between the peaks, Fig. 5.3(c), the effects are just the opposite. For the case with a vanishing cross-term, Fig. 5.3(b), the results correspond fairly closely to those observed for the incoherent fit. In both of the cases with large interference effects, the interfering fits are, in general, worse than the incoherent fit, but they are better in certain respects. The fit with destructive interference between the peaks appears to describe the dip region better than the incoherent fit does. It also involves a very large value for the $f'(1515)$ mass. The fit with constructive interference between the peaks appears to describe the leading edge of the $f'(1515)$

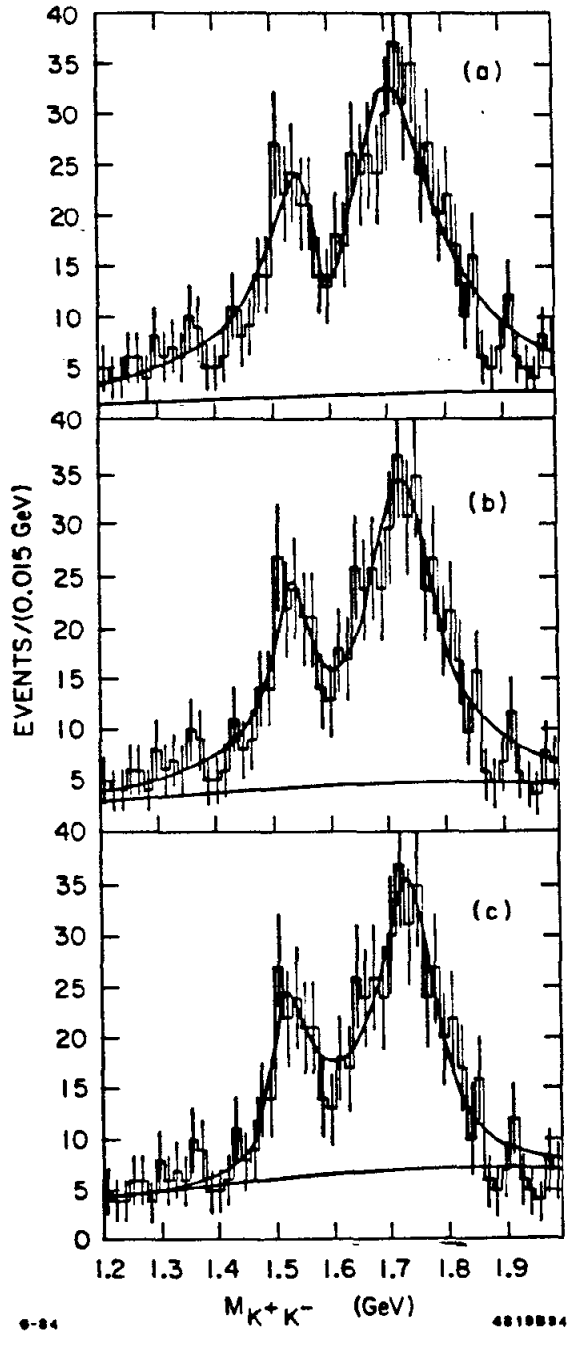

Figure 5.3. Interfering fits to the $f'(1515)/\theta(1700)$. (a) Destructive interference between the peaks. (b) Vanishing interference between the peaks. (c) Constructive interference between the peaks.

Table 5.1. A summary of fits to the $f'(1515)/\theta(1700)$ mass distribution. The 'χ^2' used here is calculated by taking the difference between the fit function and the histogram bin contents, and using Gaussian statistics for the errors. The errors on the fit parameters are statistical only.

	$m_{f'}$	$\Gamma_{f'}$	m_θ	Γ_θ	φ	'χ^2'/'DOF'
incoherent	1.527	0.087	1.721	0.132		39.2/47
fit	±0.008	±0.037	±0.007	±0.020		
coherent	1.518	0.082	1.727	0.129	1.6	39.2/46
fit	±0.015	±0.016	±0.011	±0.022	±0.9	
	1.564	0.080	1.691	0.194	−0.785	45.3/47
	±0.006	±0.026	±0.006	±0.031		
coherent	1.534	0.087	1.719	0.141	0.785	39.5/47
fits	±0.008	±0.020	±0.007	±0.022		
	1.512	0.078	1.736	0.115	2.36	40.2/47
	±0.007	±0.018	±0.008	±0.014		

somewhat better than the incoherent fit does. Unfortunately, it is not possible to reap all of these benefits from a single fit.

A fit has also been performed in which the phase was allowed to vary. The result for this fit is shown in Fig. 5.2(b). The parameters are:

$$m_{f'} = 1.518 \pm 0.015 \text{ GeV}, \quad \Gamma_{f'} = 0.082 \pm 0.016 \text{ GeV},$$

$$m_\theta = 1.727 \pm 0.011 \text{ GeV}, \quad \Gamma_\theta = 0.129 \pm 0.022 \text{ GeV},$$

$$\varphi = 1.6 \pm 0.9 \text{ radians}.$$

This is consistent with the case in which maximum constructive interference occurs between the two peaks. It seems to be virtually indistinguishable from the incoherent fit.

The cases for which the interference phase was fixed indicate that there are certain aspects of the data which are better represented by interfering Breit-Wigners, but that there is no general improvement over the non-interfering fit. The fit in which the phase is left free prefers a value for this phase which corresponds to an overall shape very much like that of the non-interfering fit. This leads one to the tentative conclusion that there is no significant evidence for interference effects in this mass region since such interference does not offer a better description of the mass distribution.

5.5 Spin Analysis for the $f'(1515)/\theta(1700)$ Region

The next logical step in understanding this mass region is to perform a spin analysis using the production and decay angular distributions. The calculation of the production and decay angular distributions for this case has already been described in a previous chapter on the $f(1270)$, but the analysis to be performed here will have a slightly different flavor. In the present case, the spin will not be assumed, but fits will be performed to several hypotheses in order to find the correct spin assignment. First, we consider which J^P hypotheses to use for this mass region.

The allowed quantum numbers for X in the decay sequence $\psi \rightarrow \gamma X$, $X \rightarrow 0^- + 0^-$ are severely limited. For a boson/anti-boson system: $C(B\bar{B}) = (-1)^{l+s}(B\bar{B})$, where l is the relative angular momentum of the B and the $\bar{B}$ and s is the total spin of the $B\bar{B}$ system. In addition, $P = (-1)^l$. Since B has spin 0, $s = 0$, $J = l$ and $P = C = (-1)^J$. This means that J must be even, and so the allowed states are:

$$J^{PC} = 0^{++},\ 2^{++},\ 4^{++} \ldots$$

In the analysis of the $f'(1515)$ and the $\theta(1700)$, only $J^P = 0^+$ and 2^+ will be considered. In the analysis of the $\xi(2220)$, $J^P = 4^+$ will also be considered. These

choices are suggested by current meson spectroscopy data which tells us that the recurrences on the $f(1270)$ Regge trajectory (which is the leading trajectory) are: the $h(2040)$ with $J^P = 4^+$, and the $r(2510)$ with $J^P = 6^+$. Since the states on the leading trajectory are, presumably, the lightest states with this J^P (except for the Pomeron trajectory, which should have 1/2 the slope of a normal hadron trajectory, and which may be associated with glueballs in some way...), we conclude that both the $J^P = 4^+$ hypothesis for the $\theta(1700)$ and the $J^P = 6^+$ hypothesis for the $\xi(2220)$ are unlikely.

For the $J = 0$ case, the angular distribution is completely determined. For $J \geq 2$, the X state can be produced with a helicity in the range of $[-2, 2]$, and there are four free parameters:

$$(x, y, \varphi_x, \varphi_y),$$

which are described in more detail in Appendix B. These parameters are *a priori* unknown, and allow the angular distributions for states with $J \geq 2$ to vary greatly in shape. The ability to separate different values of the spin is compromised by this uncertainty. For some values of x and y, states with $J \geq 2$ will have a highly peaked distribution in $\cos\theta_K$ which allows them to be distinguished from $J = 0$ states. However, if the $\cos\theta_K$ distribution is approximately flat, it is very difficult to distinguish different spins without high statistics. A further comment is in order about the relative importance of the phases φ_x and φ_y. As is shown in Appendix B, these phases appear only in the off-diagonal terms in the angular correlation function. These terms also contain $\cos\phi_K$ or $\cos 2\phi_K$ factors, which integrate to zero when averaged over ϕ_K. This means that the influence of the relative phases is not felt in the $\cos\theta_\gamma$ or $\cos\theta_K$ distributions directly, but only in the heavily acceptance corrected ϕ_K distribution and in the two dimensional correlations between the other angles. For these reasons, the phases have a minor

impact on the fit as a whole, and so they are very poorly determined.

The next stage in the spin analysis is to perform an acceptance corrected fit to measure the values for the unknown helicity amplitudes. This fitting procedure uses a maximum likelihood technique where the effects of acceptance are included in the likelihood function. The formalism is discussed in detail in Appendix C. The factor which has the greatest impact on the acceptance is the limited solid angle available for identified charged tracks.

The spin analysis is performed separately for the $f'(1515)$ and the $\theta(1700)$ mass regions, where these regions are defined to be:

$$f'(1515) \ : \ 1.45 \text{ GeV} \leq m \leq 1.60 \text{ GeV},$$

$$\theta(1700) \ : \ 1.60 \text{ GeV} \leq m \leq 1.85 \text{ GeV}.$$

The fits are performed using the 1983 data alone, in order to avoid any subtleties in understanding the acceptance for the 1982 detector. Additional cuts were made on the track angles to insure agreement with the Monte Carlo acceptances. The requirements are:

$$|\cos\theta_{SC}| \leq 0.95 \quad , \quad |\cos\theta_{DC}| \leq 0.75,$$

where SC refers to the angle for a neutral track in the shower counter and DC refers to the angle for a charged track in the drift chamber. The final event sample contains 103 events in the $f'(1515)$ region and 239 events in the $\theta(1700)$ region. The two observed resonances are too close in mass to be fully isolated from each other. Using the previous incoherent Breit-Wigner fit as a guide, the $\theta(1700)$ contamination in the $f'(1515)$ region is estimated to be $\sim 20\%$, and the $f'(1515)$ contamination in the $\theta(1700)$ region is estimated to be $\sim 5\%$. It is evident that, especially for the $f'(1515)$, the contamination in the overlap region is quite large. The influence of

this contamination will be studied by performing fits over sub-intervals of these two regions.

Before proceeding with the fitting, it is important to understand the acceptance of the detector in the mass regions to be fit. Due to kinematical effects, as well as the presence of kaon decays, the acceptance is not completely uniform in the low mass region. This is indicated in Fig. 5.4. There are two effects which are important. For the $\cos\theta_\gamma$ angle shown in Fig. 5.4(a), when the mass is low, the two kaon tracks are boosted forward and are nearly collinear with the photon. This introduces a strong correlation between the limited charged track acceptance and the otherwise complete photon acceptance. This effect is visible as a drastically reduced acceptance for $|\cos\theta_\gamma| \geq .75$ at masses below 1.5 GeV. The other effect stems from the kaon momentum spectrum discussed in the preceding chapter. Near the kinematic cross-over point at $m \sim 1.35$ GeV, there are a large number of very low momentum kaons associated with $|\cos\theta_K| \sim 1$. The detection efficiency for such kaons is poor, since they have a high probability for decay in flight. This manifests itself as a hole in the acceptance for $m \sim 1.35$ GeV and $|\cos\theta_K| \geq .8$. These acceptance corrections make the angular distribution analysis somewhat more difficult, especially for the $f'(1515)$ region. They give a mass dependence to the acceptance which needs to be accounted for in the fitting procedure. This is done by generating a Monte Carlo normalization sample which is uniformly distributed in the angles, but has the correct Breit-Wigner mass distribution for the resonance which is being analyzed. Using this technique, the mass dependent acceptance should be correctly modeled.

The resulting Monte Carlo acceptances are displayed for the $f'(1515)$ region and for the $\theta(1700)$ region in Fig. 5.5. In the $f'(1515)$ region, the previously discussed inefficiencies in the $\cos\theta_\gamma$ and the $\cos\theta_K$ variables are evident. For the

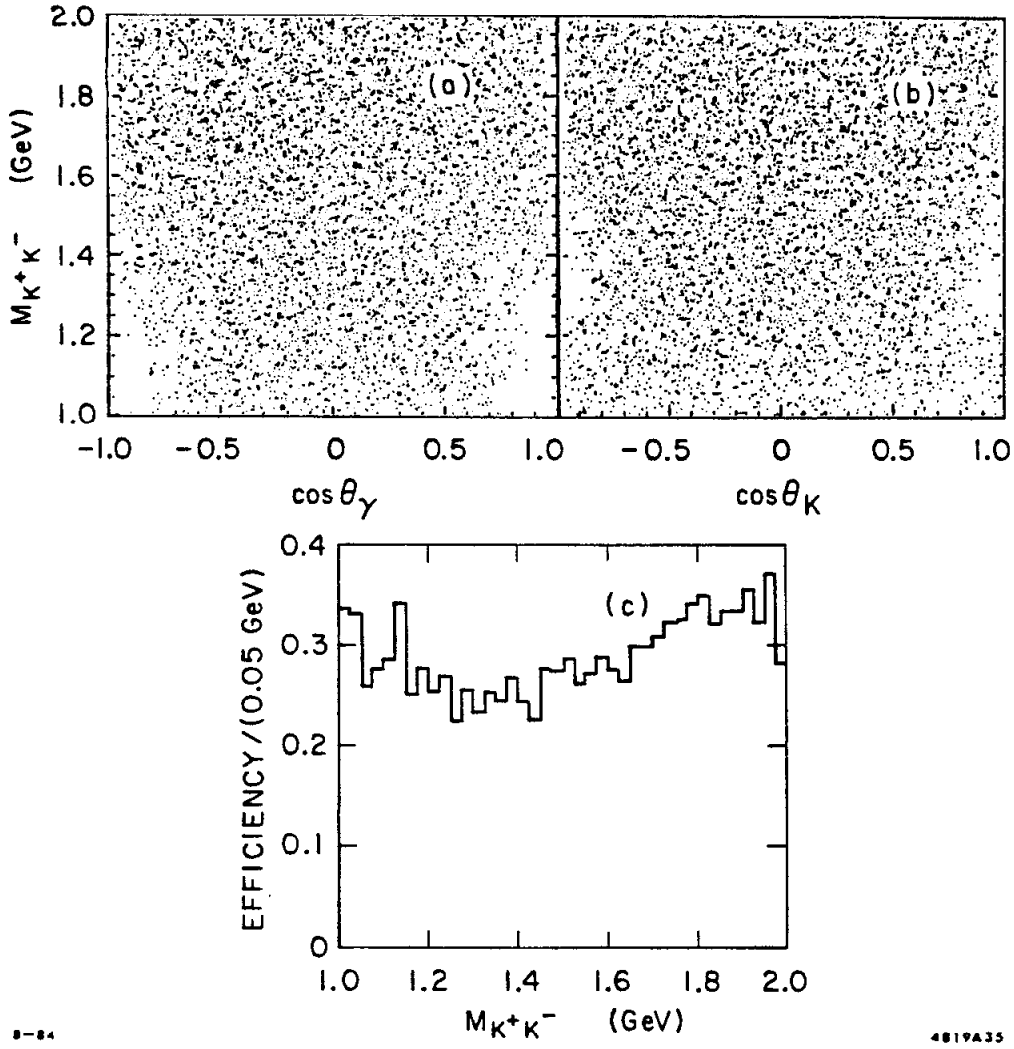

Figure 5.4. The angular acceptance for the low mass region. The plots are for events generated uniformly in angle with a phase space distribution in the mass. (a) This is the acceptance for $\cos\theta_\gamma$ as a function of m_{KK}. (b) This is the acceptance for $\cos\theta_K$ as a function of m_{KK}. (c) This is the overall efficiency as a function of m_{KK}.

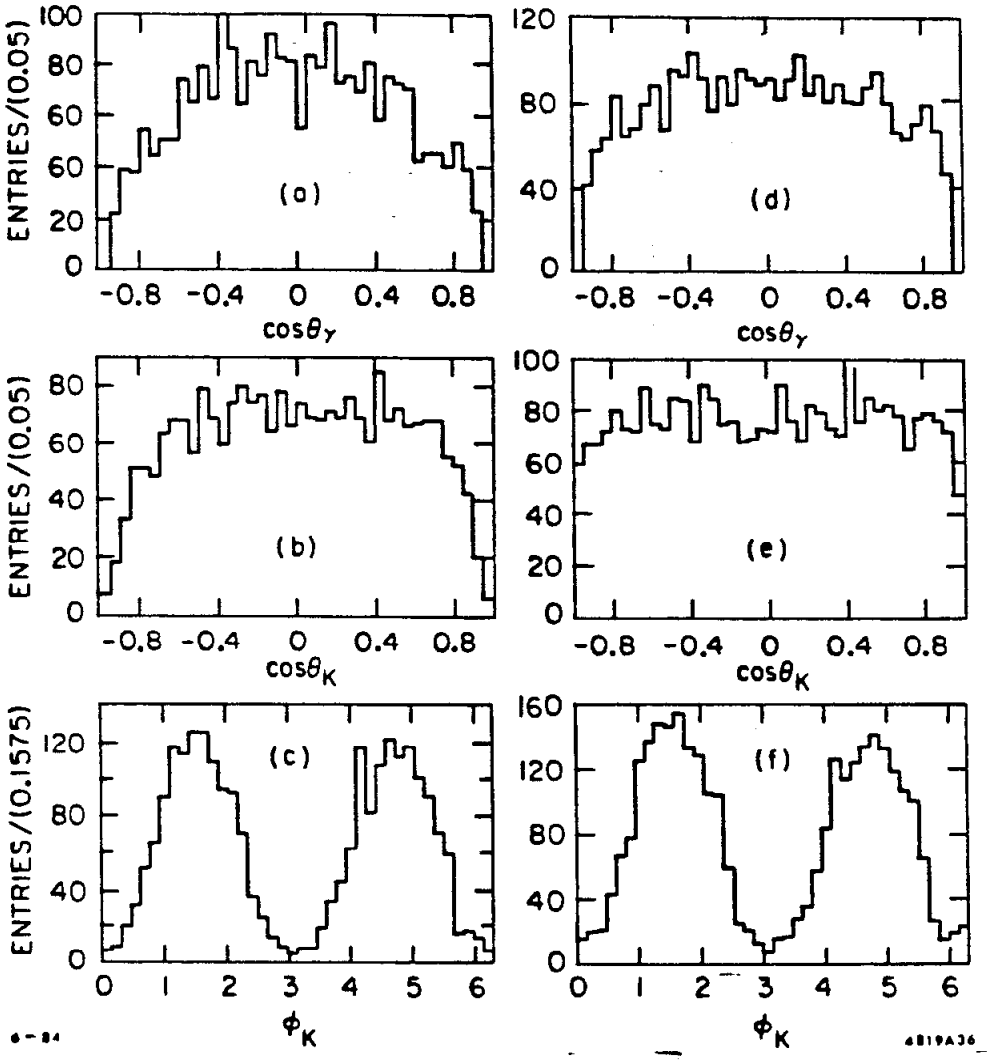

Figure 5.5. The acceptances for the $f'(1515)/\theta(1700)$ spin analysis. (a), (b), and (c) are the distributions for the $f'(1515)$ region. (d), (e), and (f) are the distributions for the $\theta(1700)$ region.

Table 5.2. The $f'(1515)$ spin analysis results. The upper group of fits were performed over the full mass region, which has more events but also has more contamination from the $\theta(1700)$. The lower group of events has fewer events, but should have much less $\theta(1700)$ contamination.

Full $f'(1515)$ region $1.45 \leq m \leq 1.60$ 103 Events	Fit $J = 0$	$ln\mathcal{L} = -257.5$
	Fit $J = 2$ (fixed phases)	$ln\mathcal{L} = -237.3$ $x = 0.65 \pm 0.09$, $\varphi_x = 0.$ $y = -0.03 \pm 0.11$, $\varphi_y = 0.$
	Fit $J = 2$ (variable phases)	$ln\mathcal{L} = -235.9$ $x = 0.63 \pm 0.09$, $\varphi_x = 1.3 \pm 0.6$ $y = 0.17 \pm 0.15$, $\varphi_y = 2.6 \pm 0.9$
Partial $f'(1515)$ region $1.450 \leq m \leq 1.525$ 43 Events	Fit $J = 0$	$ln\mathcal{L} = -84.2$
	Fit $J = 2$ (variable phases)	$ln\mathcal{L} = -81.6$ $x = 0.85 \pm 0.23$, $\varphi_x = 1.1 \pm 0.8$ $y = -0.4 \pm 0.3$, $\varphi_y = 1.3 \pm 1.0$

$\theta(1700)$ region, there is a small effect visible in the $\cos\theta_\gamma$ variable. After this brief discussion of acceptance, we proceed to perform the spin analysis on the two interesting regions.

The results for the spin analysis of the $f'(1515)$ region are summarized in Table 5.2. The fit procedure has been performed under a variety of conditions. The first group of fits were performed over the full $f'(1515)$ region. A fit to $J = 2$ was performed with the relative phases of the helicity amplitudes fixed at zero, as well as a fit in which they were left free. A second group of fits were performed using a smaller event sample, which should contain less background from the $\theta(1700)$ region. The results for this second group are similar to the larger statistics results for the full mass region, and the results for the full region will be discussed in more detail. These fit results are displayed in Fig. 5.6. The curves represent an indirect attempt

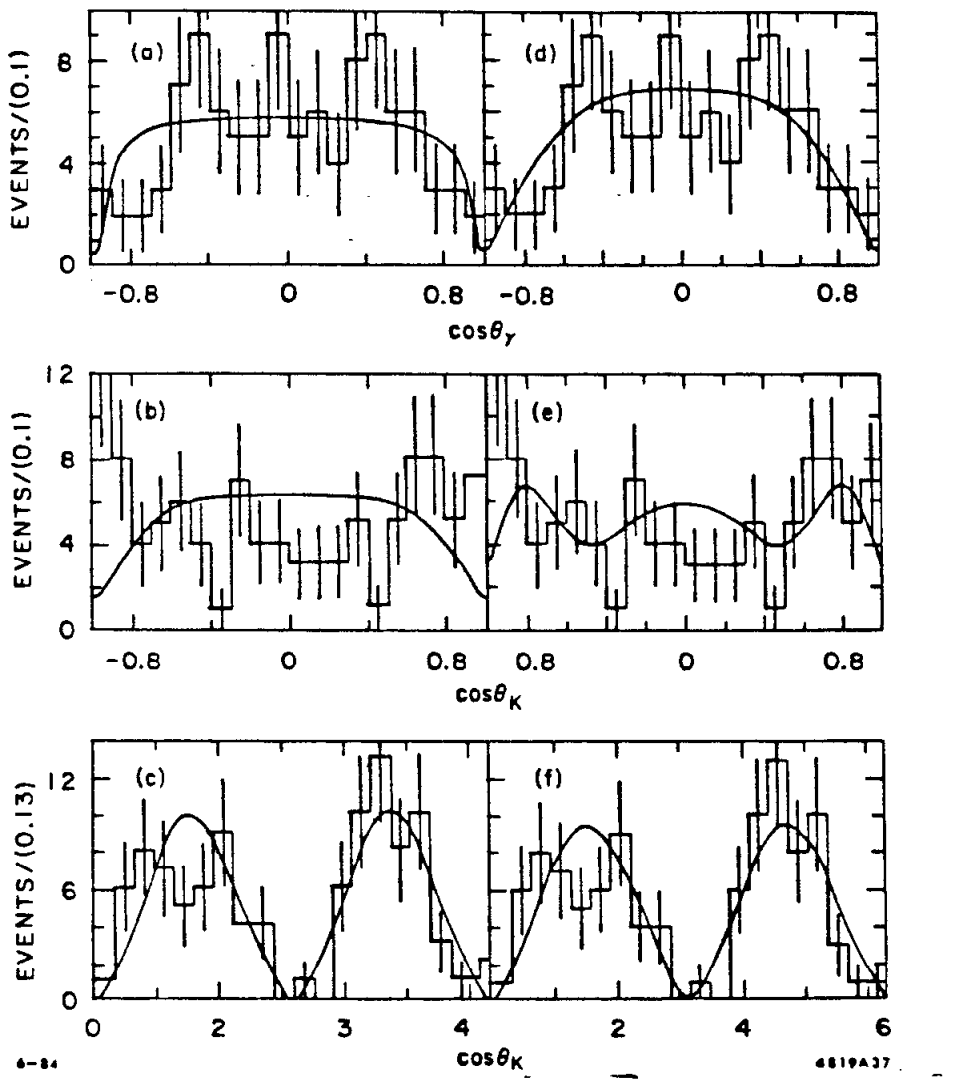

Figure 5.6. The fit results for the $f'(1515)$ spin analysis. The histograms display the events used in the fit. (a), (b), and (c) indicate the fit results for the $J = 0$ fit. (d), (e), and (f) indicate the fit results for the $J = 2$ fit.

to display the expected fit result for a particular projection of the three dimensional correlation function. The curves are a smoothed fit to Monte Carlo events which have been weighted by the actual fit results, as described in Appendix C. This indirect technique is necessary because the acceptance function is never explicitly evaluated, but appears only in the form of a normalization integral.

It is evident that the acceptance effects are large for this mass region since the $J = 0$ $\cos\theta_\gamma$ distribution before acceptance is $1 + \cos^2\theta_\gamma$, whereas after acceptance it appears approximately flat. The fit to $J = 2$ appears, in projection, to be slightly better than the fit to $J = 0$. (Strictly speaking the $J = 0$ case is a 'calculation' not a 'fit', since there are no free parameters for this case, but the nomenclature will be retained for the sake of brevity.) Neither fit describes the excess of events near $\cos\theta_K = -1$ very well. For the $J = 0$ case, there should be no excess. For the $J = 2$ case, there should be an excess which is rendered invisible by the acceptance corrections. In this case, a small number of events at higher mass, where the acceptance is much better, can produce the observed excess.

In addition, the likelihood is much better for the $J = 2$ fit than for the $J = 0$ fit. A direct comparison of these likelihoods cannot be rigorously made because the two hypotheses which are being compared are not members of the same continuous family.[39] The likelihood ratio is still a reasonable test statistic to use, although it loses a simple interpretation in terms of confidence levels. A simple, non-rigorous estimate of the significance proceeds by analogy with a test used for simple (*e.g.*, no free parameters) hypotheses. One defines a relative probability:

$$\lambda = \frac{\mathcal{L}(J=0)}{\mathcal{L}(J=2)} \sim e^{-21.6} = 4 \times 10^{-10}.$$

This estimate does not take into account the different number of free parameters for the two cases. A slightly better estimate (not rigorous unless one hypothesis is

a limiting case of the other) takes the parameters into account by defining:

$$\chi^2 = -2ln\left[\frac{\mathcal{L}(J=0)}{\mathcal{L}(J=2)}\right] \sim 43.$$

The claim is that this variable should be distributed like a χ^2 variable for four degrees of freedom, since there are four more variables in the $J = 2$ fit than there are in the $J = 0$ fit. This would imply that $J = 0$ is rejected at the 10^{-6} level.

A more believable means of evaluating the significance of the fit results involves performing an ensemble of Monte Carlo experiments using pure samples consisting of the number of events actually observed. This technique is described in more detail in Appendix C. It provides two distinct benefits. The first is a check that, if one had a pure sample, generated with known characteristics, it would be measured correctly by the fitting procedure. This checks for systematic biases in the fitting procedure and gives a 'goodness-of-fit' by indicating how likely it would be to measure the observed results for the correct hypothesis. The second benefit comes from fitting events generated according to the wrong hypothesis. This provides an indication of how likely it would be to measure the observed results for the incorrect hypothesis, and hence gives an estimate of the power of the fit in discriminating against alternate hypotheses.

For the $f'(1515)$ region, two ensembles of Monte Carlo experiments have been performed. The first used events generated with $J^P = 0^+$, the second used events generated with $J^P = 2^+$ and $x = 0.67$, $y = 0$, $\varphi_x = \varphi_y = 0$. The latter values were chosen as a representative set of parameters from the $J = 2$ fit to the real events. The results of performing 100 Monte Carlo experiments, each containing 103 events in the $f'(1515)$ mass region, are displayed graphically in the following figures. Figure 5.7 is a comparison of the likelihoods for the different ensembles of experiments. The $J^P = 2^+$ Monte Carlo results shown in Fig. 5.7(c) and Fig. 5.7(d)

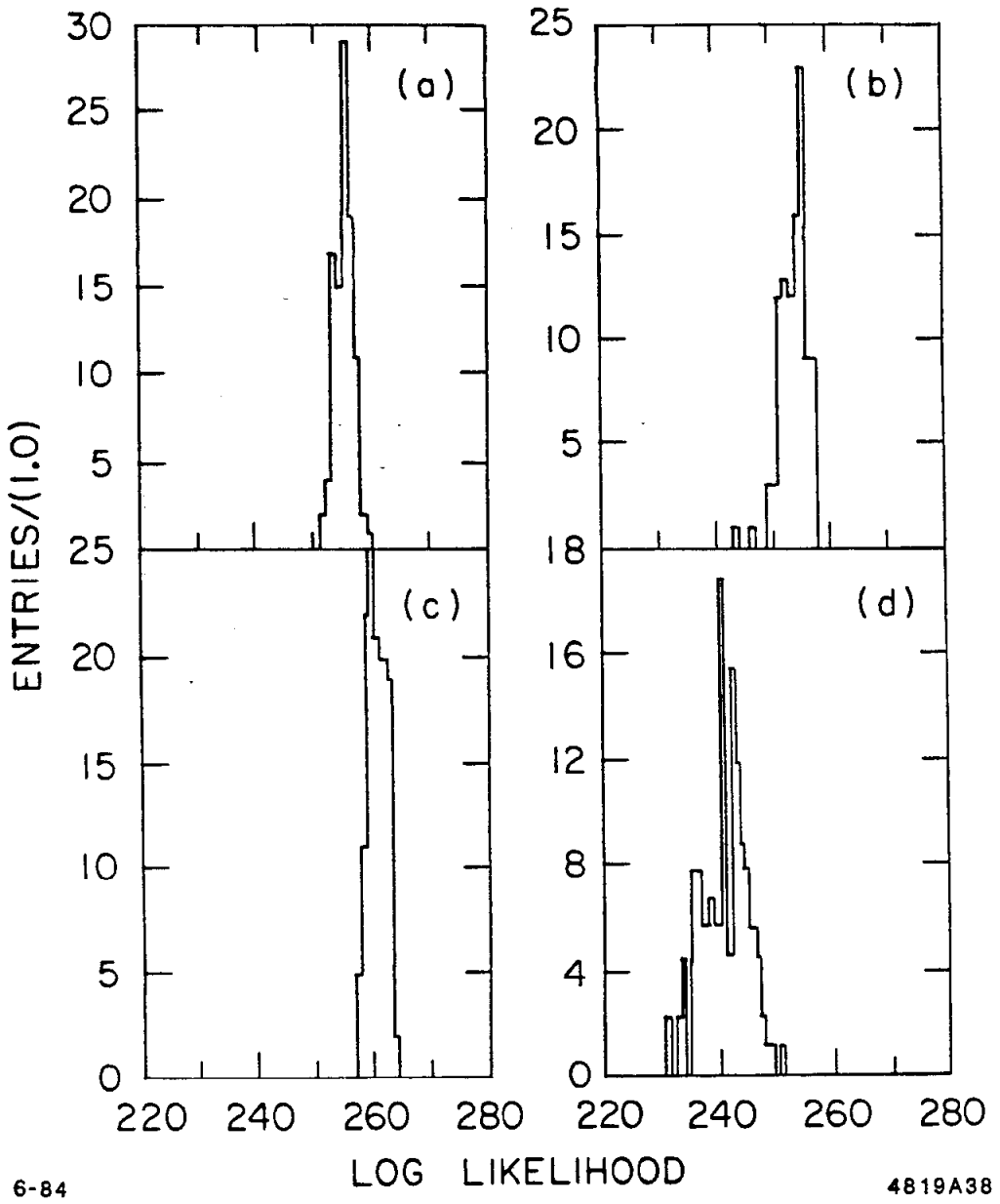

Figure 5.7. The likelihood distributions for $f'(1515)$ Monte Carlo experiments. Each plot shows the distribution of $-ln\mathcal{L}$ for 100 Monte Carlo experiments using 103 events. (a) has the input events generated with $J = 0$ and then fit to a $J = 0$ hypothesis. (b) has the input events generated with $J = 0$ and then fit to a $J = 2$ hypothesis. (c) has the input events generated with $J = 2$, $x = 0.67$, $y = 0$ and then fit to a $J = 0$ hypothesis. (d) has the input events generated with $J = 2$, $x = 0.67$, $y = 0$ and then fit to a $J = 2$ hypothesis. For reference, the fits to the real events gave:

$$J = 0 : \quad -ln\mathcal{L} = 257.5 \quad \text{and} \quad J = 2 : \quad -ln\mathcal{L} = 235.9.$$

agree well with the fit to the real data, whereas the $J^P = 0^+$ Monte Carlo results shown in Fig. 5.7(a) and Fig. 5.7(b) do not. The likelihood for the $J = 2$ fit is much worse for the Monte Carlo experiments than for the real data. This provides strong evidence that the $J^P = 2^+$ hypothesis is correct, and that the $J^P = 0^+$ hypothesis is incorrect. A study with a larger number of experiments provides a rough estimate that the relative probability for the $J^P = 0^+$ hypothesis is $\leq 10^{-3}$.

The second figure, Fig. 5.8, shows the distributions of measured parameters for $J = 2$ fits to $J = 2$ Monte Carlo events. This allows an exploration of systematic problems in measuring the parameters for the $J^P = 2^+$ hypothesis. One can ask the question: are the measured values what one would expect for a parent distribution with $x = 2/3$, $y = 0$ and $\varphi_x = \varphi_y = 0$?? Figure 5.8 indicates that the answer appears to be yes, and is summarized in the following discussion. The x parameter is measured with no indication of systematic error. The φ_x parameter is poorly measured, but is consistent with the $\varphi_x = 0$ parent distribution. The y parameter has a bi-modal distribution in the Monte Carlo experiments. This corresponds to two different fit results: $y \sim 0.2$, $\varphi_y \sim \pi$ and $y \sim -0.2$, $\varphi_y \sim 0$. These fit results are identical, and indicate a double-valued property of the fit. A single-valued range for the fit parameters would be: $y \geq 0$ and $\varphi \in [-\pi, \pi]$. This restriction was not imposed on the fit in order to prevent the fitter from falling into local minima. Taking this idiosyncrasy into account, the measured values for y and φ_y are consistent with a parent distribution which has $y = 0$ and $\varphi_y = 0$, and indicate that there appears to be a bias in the fit procedure which shifts the fit value of y slightly. This shift is probably due to the large acceptance corrections which are present in the ϕ_K distribution. In addition, the observed widths of the Monte Carlo distributions shown in Fig. 5.8 agree well with the calculated errors from the fit to the real data.

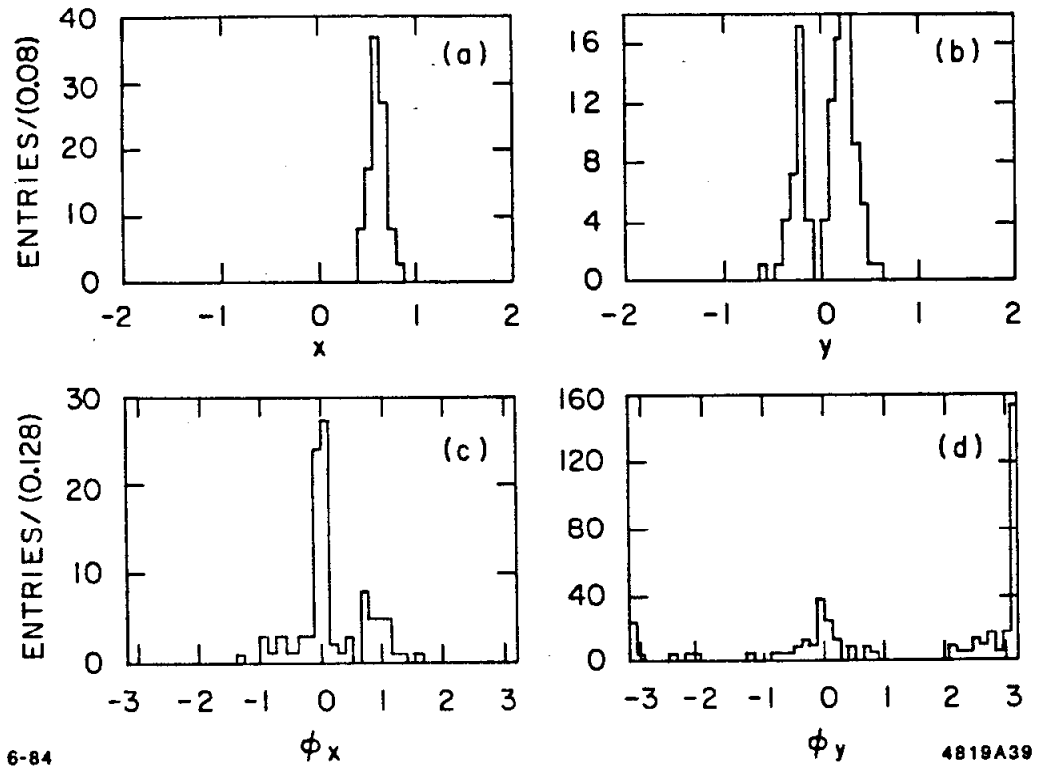

Figure 5.8. The parameter distributions for $f'(1515)$ Monte Carlo experiments. These distributions are the result of performing $J = 2$ fits to 100 Monte Carlo experiments using 103 event samples. The input events were generated with: $J = 2$, $x = 0.67$, $y = 0$, $\varphi_x = \varphi_y = 0$. For reference, the fits to the real events gave:

$$x = 0.63 \pm 0.09,\ y = 0.17 \pm 0.15\ ,\varphi_x = 1.3 \pm 0.6,\ \varphi_y = 2.6 \pm 0.9.$$

The conclusion for the $f'(1515)$ analysis is that the state has $J^P = 2^+$, which was already well established, and has helicity amplitude ratios with $x \sim 2/3$ and $y \sim 0$. The corresponding phases are consistent with zero, although this is not a very significant statement. The production amplitudes for the $f'(1515)$ are measured here for the first time, and agree qualitatively with those found for the $f(1270)$ tensor meson in a previous chapter. To indicate the allowed values for x and y in a more graphic manner, a contour plot of the likelihood function has been made for the $f'(1515)$ region. Figure 5.9 shows the likelihood contour plot for a fit in which the phases have been left at the minimum values shown in Table 5.2, and only x and y have been varied. It is apparent that there is a sign ambiguity in x and that y needs to lie close to zero.

The analysis of the $\theta(1700)$ region proceeds in an identical manner to the analysis of the $f'(1515)$ region. The results of the spin analysis are summarized in Table 5.3. The results for fits to the full $\theta(1700)$ region are listed, along with the results for fits performed in a sub-interval with less potential $f'(1515)$ contamination. The results for the two groups of fits are consistent, and the fit to the full region will be discussed in detail. The data is plotted, along with the fit results, in Fig. 5.10. Once again, the three projections indicate that the $J = 2$ fit is a better description of the data. The likelihood indicates the same trend, but not as strongly as for the $f'(1515)$ fits. Using the same non-rigorous estimates for the significance of these results gives:

$$\lambda = \frac{\mathcal{L}(J=0)}{\mathcal{L}(J=2)} \sim e^{-8.4} = 2 \times 10^{-4},$$

and:

$$\chi^2 = -2ln\left[\frac{\mathcal{L}(J=0)}{\mathcal{L}(J=2)}\right] \sim 17.$$

Assuming a χ^2 distribution for 4 DOF gives a confidence level of about 2×10^{-3}.

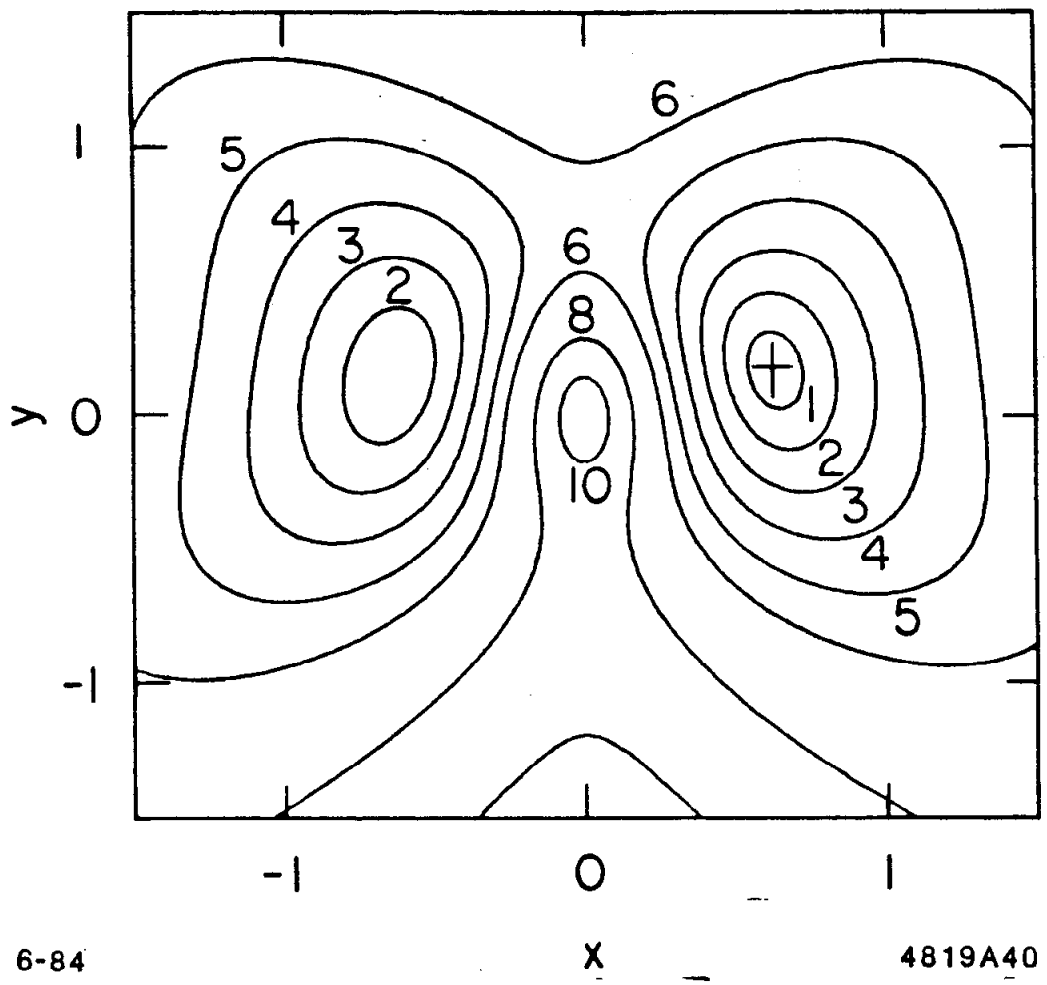

Figure 5.9. Contour plot of x versus y for the $f'(1515)$ spin analysis. The contours correspond to changes in the likelihood of 1σ, and the + indicates the location of the minimum. The relative phases were fixed at their fit values for making this plot.

Table 5.3. The $\theta(1700)$ spin analysis results. The upper group of fits were performed over the full mass region, which has more events but also has more contamination from the $f'(1515)$. The lower group of events has fewer events, but should have much less $f'(1515)$ contamination.

Full $\theta(1700)$ region $1.60 \leq m \leq 1.85$ 239 Events	Fit $J = 0$	$ln\mathcal{L} = -644.9$
	Fit $J = 2$ (fixed phases)	$ln\mathcal{L} = -636.7$ $x = -1.07 \pm 0.16$, $\varphi_x = 0.$ $y = -1.10 \pm 0.16$, $\varphi_y = 0.$
	Fit $J = 2$ (variable phases)	$ln\mathcal{L} = -636.5$ $x = -1.07 \pm 0.16$, $\varphi_x = 0.6 \pm 0.6$ $y = -1.09 \pm 0.15$, $\varphi_y = -0.1 \pm 0.5$
Partial $\theta(1700)$ region $1.675 \leq m \leq 1.850$ 177 Events	Fit $J = 0$	$ln\mathcal{L} = -438.8$
	Fit $J = 2$ (variable phases)	$ln\mathcal{L} = -432.9$ $x = -1.14 \pm 0.20$, $\varphi_x = 0. \pm 1.1$ $y = -1.28 \pm 0.20$, $\varphi_y = 0. \pm 0.9$

Both of these strongly favor the $J^P = 2^+$ hypothesis.

The most important feature of the projections is the non-flat distribution in $\cos\theta_K$. This distribution receives very uniform acceptance corrections, since it is a true center of mass angle and averages over detector acceptance. This distribution is described fairly well by the $J = 2$ fit, and very poorly by the $J = 0$ fit. This can be made more quantitative by calculating a 'χ^2' using the difference between the histogram bin contents and the expected value from the fit, and using Gaussian statistics for the errors. The results are that: $\chi^2 = 57.9/20$ bins for the $J = 0$ fit, and $\chi^2 = 24.7/20$ bins for the $J = 2$ fit. If one evaluates the corresponding confidence levels, assuming a true χ^2 distribution and 20 DOF, the results are that $J = 0$ has a confidence level of 1.5×10^{-5}, and $J = 2$ has a confidence level of 0.21.

For the $\theta(1700)$ region, two ensembles of Monte Carlo experiments were

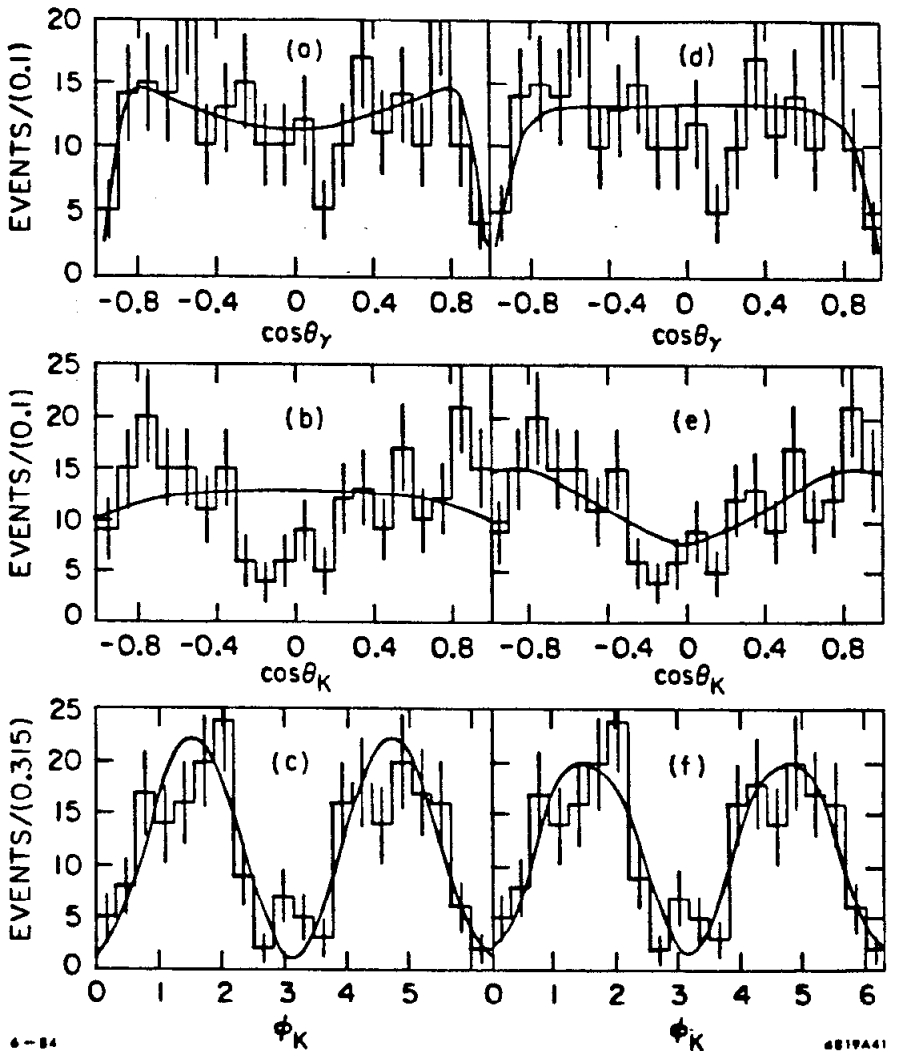

Figure 5.10. The fit results for the $\theta(1700)$ spin analysis. The histograms display the events used in the fit. (a), (b), and (c) indicate the fit results for the $J = 0$ fit. (d), (e), and (f) indicate the fit results for the $J = 2$ fit.

also performed. The first used events generated with $J^P = 0^+$, and the second used events generated with $J^P = 2^+$ and $x = -1.2$, $y = -1.2$, $\varphi_x = \varphi_y = 0$. The results of performing ensembles of 100 Monte Carlo experiments, each containing 239 events in the $\theta(1700)$ region, are shown in the following figures. Figure 5.11 shows the likelihood distributions for the different cases. In contrast to the $f'(1515)$, this situation is more ambiguous. The observed likelihood for the $J = 0$ fit agrees better with the $J^P = 0^+$ hypothesis, shown in Fig. 5.11(a), than with the $J^P = 2^+$ hypothesis, shown in Fig. 5.11(c). The observed likelihood for the $J = 2$ fit does not agree very well with either hypothesis. This fit has a likelihood which is somewhat worse than what one would expect for a pure $J^P = 2^+$ state, shown in Fig. 5.11(d), and somewhat better than what one would expect for a pure $J^P = 0^+$ state, shown in Fig. 5.11(b). It should be added that the presence of additional contamination should produce a likelihood which is worse than that of a pure sample, and it should be difficult to produce a likelihood which is better than that of a pure sample.

There is additional information to be found by looking at the values for the fit parameters. For $J = 2$ fits to $J = 0$ Monte Carlo events, the values resulting from the ensemble of Monte Carlo experiments are shown in Fig. 5.12. It is evident that the values measured for x and y in the real data do not agree with the values expected if the $\theta(1700)$ were really a $J^P = 0^+$ state. For $J = 2$ fits to $J = 2$ events, the values resulting from the Monte Carlo experiments are shown in Fig. 5.13. These distributions agree quite well with the measured values, and indicate that the $\theta(1700)$ is very consistent with the $J^P = 2^+$ parent distribution.

The conclusion of this analysis is that the $\theta(1700)$ is a $J^P = 2^+$ state. The evidence is three-fold:

1. The likelihood ratio for the fits to the two spin hypotheses prefers $J = 2$ to $J = 0$. This is difficult to make quantitative, but suggests a relative

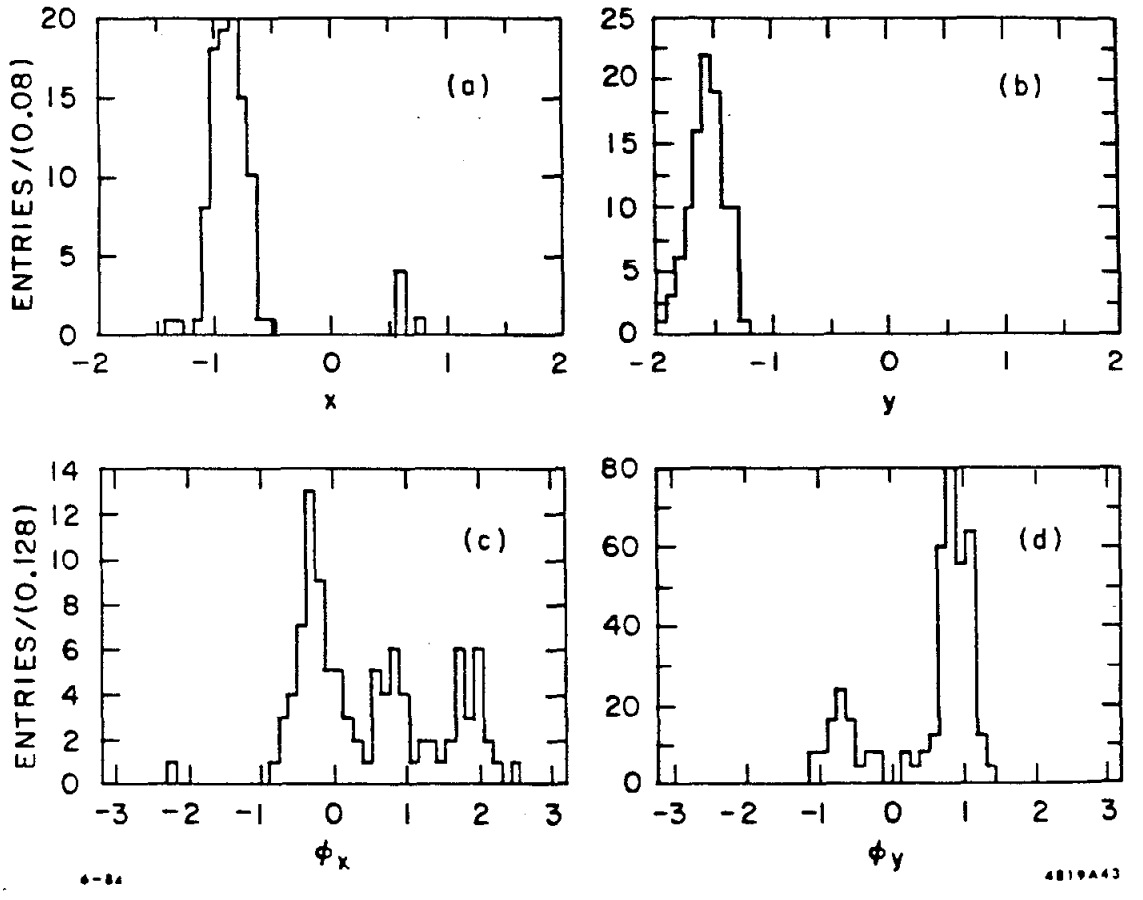

Figure 5.12. The parameter distributions for $\theta(1700)$ Monte Carlo experiments. These distributions are the result of performing $J = 2$ fits to 100 Monte Carlo experiments using 239 event samples. The input events were generated with: $J = 0$. For reference, the fits to the real events gave:

$$x = -1.07 \pm 0.16,\ y = -1.09 \pm 0.15\ , \varphi_x = 0.6 \pm 0.6,\ \varphi_y = -0.1 \pm 0.5.$$

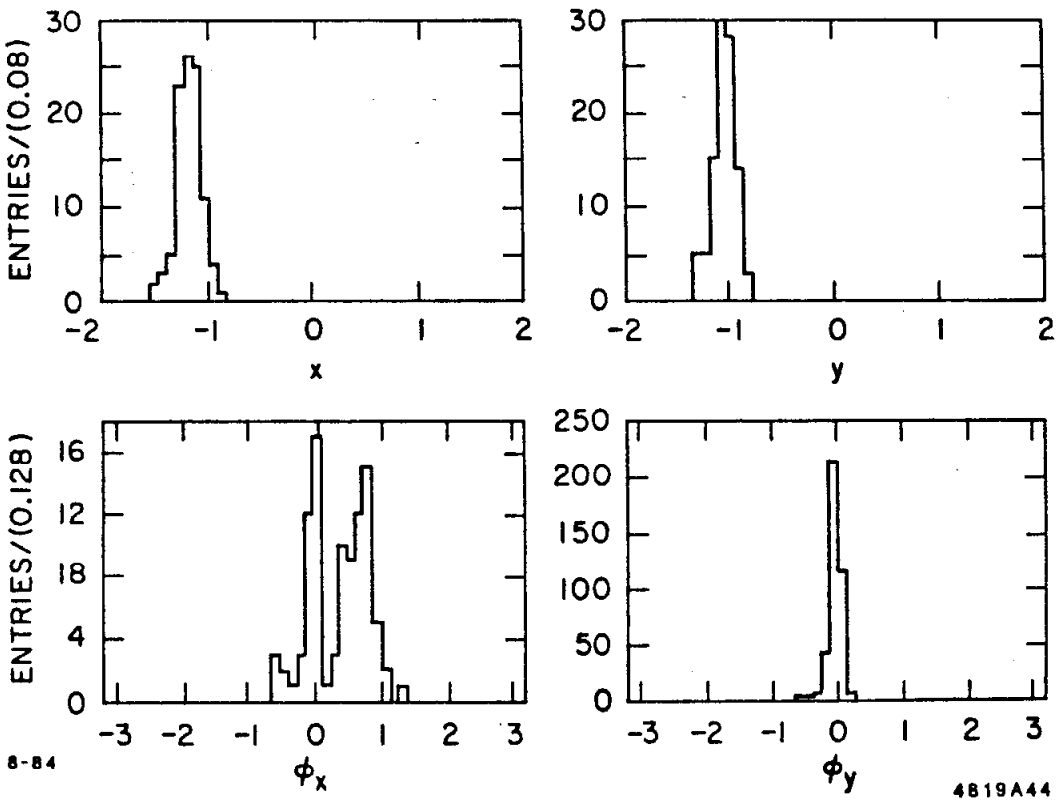

Figure 5.13. The parameter distributions for $\theta(1700)$ Monte Carlo experiments. These distributions are the result of performing $J = 2$ fits to 100 Monte Carlo experiments using 239 event samples. The input events were generated with: $J = 2$, $x = -1.2$, $y = -1.2$, $\varphi_x = \varphi_y = 0$. For reference, the fits to the real events gave:

$$x = -1.07 \pm 0.16,\ y = -1.09 \pm 0.15\ ,\varphi_x = 0.6 \pm 0.6,\ \varphi_y = -0.1 \pm 0.5.$$

probability for $J = 0$ of $\sim 10^{-3}$.

2. The χ^2 for the $\cos\theta_K$ projection strongly favors $J = 2$. This suggests a relative probability for $J = 0$ of $\sim 10^{-4}$.

3. The Monte Carlo experiments, although indicating that the $J = 2$ likelihood should be larger, also indicate that the measured values for x and y are not consistent with $J = 0$. This suggests a relative probability for $J = 0$ of $\sim 10^{-3}$.

It is difficult to turn this evidence into a quantitative statistical statement. Using the rough estimates above, it is reasonable to claim that the $J^P = 0^+$ hypothesis has a relative probability which is $\leq 10^{-3}$. To indicate the allowed values for the x and y parameters for the $J = 2$ fit, a likelihood contour plot has again been constructed. Figure 5.14 shows this plot, and it is evident that there are no other values for x and y which have an appreciable probability. A comparison of the contour plots for the $f(1270)$ region, Fig. 3.8, the $f'(1515)$ region, Fig. 5.9, and the $\theta(1700)$ region, Fig. 5.14, provides a very graphic demonstration of the similar characteristics of the $f(1270)$ and the $f'(1515)$ as well as the different characteristics of the $\theta(1700)$. The question of why the $J = 2$ fit has a smaller likelihood than would be expected remains unanswered. It may be indicative of background contamination, or possibly the presence of another state in the same mass region.

5.6 Branching Ratios for the $f'(1515)/\theta(1700)$ Region

With an understanding of the detailed properties of the $f'(1515)$ and the $\theta(1700)$, the information necessary to estimate the branching ratios is available. The number of events attributed to each resonance will be taken from the incoherent Breit-Wigner fits to the mass distribution. This fit describes the data well, and avoids the difficulty of defining the number of events for a Breit-Wigner fit with

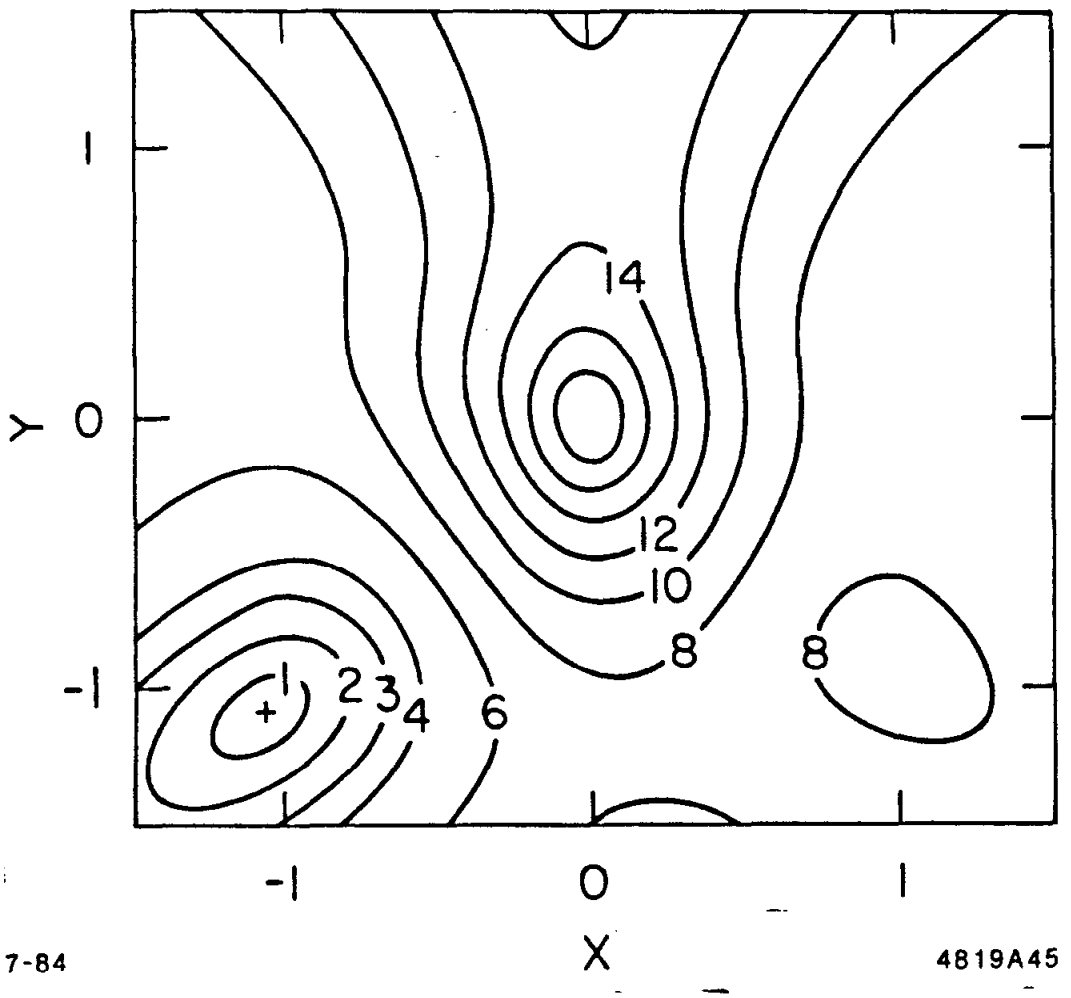

Figure 5.I4. Contour plot of x versus y for the $\theta(1700)$ spin analysis. The contours correspond to changes in the likelihood of 1σ, and the + indicates the location of the minimum. The relative phases were fixed at their fit values for making this plot.

interference.* Due to the subtleties of modeling the 1982 detector discussed previously, the branching ratio measurement uses the 1983 data sample alone. This produces slightly different resonance parameters than does the fit to the combined data sample, but the differences are not significant. Additional cuts are also placed on the angles of the tracks in the detector to insure that the Monte Carlo correctly models the detector efficiency. The results are:

$$m_{f'} = 1.540 \pm 0.010 \text{ GeV}, \quad \Gamma_{f'} = 0.090 \pm 0.040 \text{ GeV}, \quad N_{f'} = 87 \pm 20 \text{ Events},$$

$$m_\theta = 1.722 \pm 0.007 \text{ GeV}, \quad \Gamma_\theta = 0.101 \pm 0.019 \text{ GeV}, \quad N_\theta = 192 \pm 25 \text{ Events}.$$

In order to calculate a branching ratio, it is also necessary to evaluate the detection efficiency. This has been done by generating an event sample which mimics the real data sample as closely as possible. The $f'(1515)$ efficiency has been measured by using events generated with the following parameters:

$$m = 1.520 \text{ GeV}, \quad \Gamma = 0.075 \text{ GeV},$$

$$J = 2, \quad x = 0.67, \; y = 0.0, \; \varphi_x = \varphi_y = 0.$$

After passing these events through the standard event selection procedure the resulting detection efficiency was measured to be:

$$\epsilon_{f'} = 0.160 \pm 0.024.$$

---

* For the interfering fit, the contributions are:

$$\frac{d\sigma}{dm} \sim |A_{f'}|^2 + |A_\theta|^2 + 2Re[A_{f'} A_\theta^*].$$

The branching ratios are proportional to $|A_{f'}|^2$ and $|A_\theta|^2$. The coherent fit results indicate that the ratio $|A_{f'}|^2/|A_\theta|^2$ is smaller than the corresponding ratio for the incoherent fit, but not by a significant amount.

A similar procedure has been used for the $\theta(1700)$ detection efficiency. The Monte Carlo events were generated with the following parameters:

$$m = 1.725 \text{ GeV}, \quad \Gamma = 0.120 \text{ GeV},$$

$$J = 2, \quad x = -1.2, \; y = -1.2, \; \varphi_x = \varphi_y = 0.$$

The resulting detection efficiency was measured to be:

$$\epsilon_\theta = 0.222 \pm 0.033.$$

The large difference between the $f'(1515)$ detection efficiency and the $\theta(1700)$ detection efficiency is due to the acceptance effects which were discussed previously, and displayed in Fig. 5.4.

These efficiencies, when combined with the number of ψ's which were produced during the 1983 run and the number of observed events, yield the following branching ratios:

$$\text{BR}(\psi \to \text{f}'(1515))\text{BR}(\text{f}'(1515) \to \text{K}^+\text{K}^-) = (3.0 \pm 0.7 \pm 0.6) \times 10^{-4},$$

$$\text{BR}(\psi \to \theta(1700))\text{BR}(\theta(1700) \to \text{K}^+\text{K}^-) = (4.8 \pm 0.6 \pm 0.9) \times 10^{-4}.$$

The radiative decay $\psi \to \gamma f(1270)$ has a relatively large branching ratio. The $f(1270)$ has a small branching ratio to $\text{K}\bar{\text{K}}$, due to the nearly ideal mixing of the tensor nonet. Although this branching ratio is small, it is possible that a signal may be visible in the K^+K^- final state. The branching ratio is quoted by the Particle Data Book[34] to be: $\text{BR}(\text{f} \to \text{K}\bar{\text{K}}) = 2.9 \pm 0.2\%$. This result comes from an average of several partial wave analysis experiments which must consider the interference of the $f(1270)$ with the other tensor mesons: $A_2(1310)$ and $f'(1515)$. The extraction of $\text{BR}(\text{f} \to \text{K}\bar{\text{K}})$ is very difficult and Montanet[40] quotes a range of $2 - 7\%$ in

an extensive review of the tensor nonet. This range will be used for the present discussion. Using the Particle Data Book value for $BR(f \to \pi\pi) = 83.1 \pm 1.9\%$, one finds that:

$$\frac{BR(f \to K^+K^-)}{BR(f \to \pi\pi)} \sim 0.01 - 0.04.$$

This can be combined with the measured rate for the product branching ratios for the $f(1270)$ and the $f'(1515)$ to give the estimate:

$$BR(\psi \to \gamma f)BR(f \to K^+K^-) \sim (0.05 - 0.20) \times BR(\psi \to \gamma f')BR(f' \to K^+K^-).$$

This is a very small branching ratio, and there is no evidence for such an $f(1270)$ signal in the K^+K^- mass plot. Nevertheless, a fit has been performed to test for the presence of the $f(1270)$. Figure 5.15 shows the mass plot, fit to three non-interfering Breit-Wigner probabilities plus a phase space background. The $f(1270)$ parameters were fixed to be: $m_f = 1.270$ GeV, $\Gamma_f = 0.180$ GeV. The fit shows that a small $f(1270)$ contribution can easily be accommodated in the plot. The relative areas for the resonances are:

$$\frac{n_f}{n_{f'}} = 0.31 \pm 0.15.$$

Since the spin analyses performed in the preceding sections indicate that the angular distributions for the $f(1270)$ and the $f'(1515)$ are approximately the same, the detection efficiencies for the two states will also be approximately the same, and so the ratio of branching ratios is about 1/3. This ratio is somewhat larger than the estimate made above, but does not in itself constitute evidence for the presence of the $f(1270)$ in this final state. In addition, the decay angular distributions would not easily accommodate such a large $f(1270)$ signal. It is more likely that any signal which is present is at least a factor of $2 - 3$ smaller than that shown in Fig. 5.15.

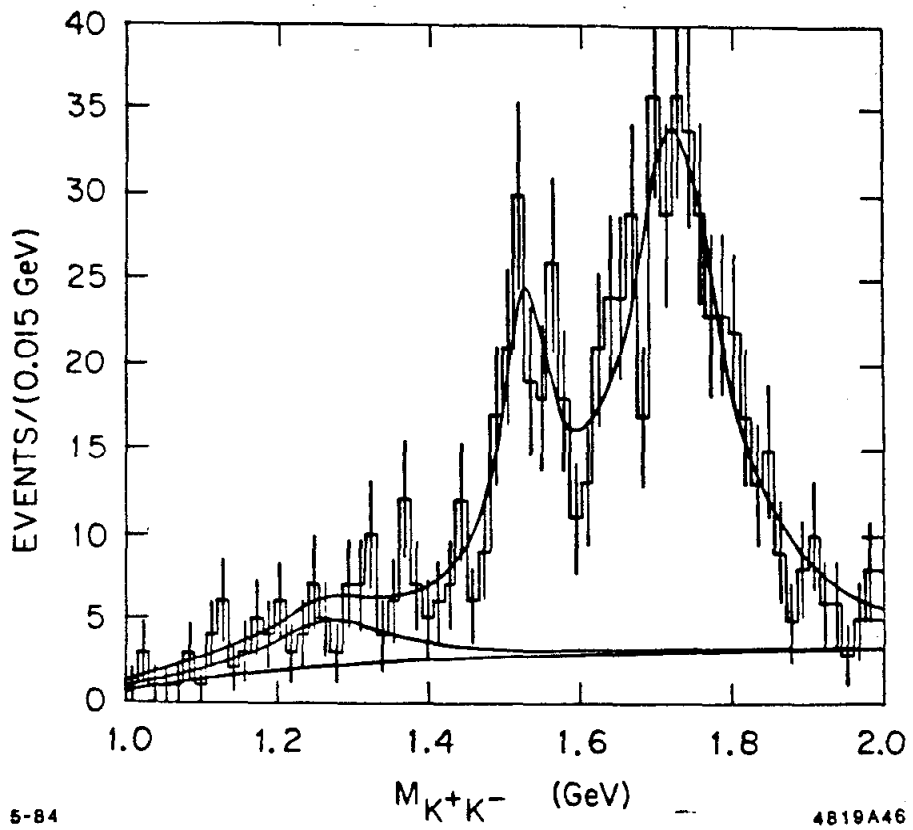

Figure 5.15. Fit to the $f(1270)$ in the K^+K^- mass distribution. The fit contains three incoherent Breit-Wigner probabilities and a phase space background.

5.7 SUMMARY

A plethora of results have been discussed in the preceding sections of this chapter, and it is useful to summarize the measurements which have been made. The values quoted below represent the best measurements for these quantities. Systematic errors have been included when it was appropriate to do so.

The masses and widths are taken from the incoherent fit to the combined 1982 and 1983 data sample. They are measured to be:

$$m_{f'} = 1.525 \pm 0.010 \pm 0.010 \text{ GeV}, \quad \Gamma_{f'} = 0.085 \pm 0.035 \text{ GeV}$$
$$m_{\theta} = 1.720 \pm 0.010 \pm 0.010 \text{ GeV}, \quad \Gamma_{\theta} = 0.130 \pm 0.020 \text{ GeV}$$

These values agree well with the standard values[34] for the $f'(1515)$: $m_{f'} = 1.520 \pm 0.010$ GeV and $\Gamma_{f'} = 0.075 \pm 0.010$ GeV. They also agree with the MARK II results[24] for the $\theta(1700)$: $m_{\theta} = 1.700 \pm 0.030$ GeV and $\Gamma_{\theta} = 0.156 \pm 0.020$ GeV.

The spin analyses give measurements for the J^P as well as for the helicity amplitude ratios. The results are taken from the fits in which the full mass region was used and the relative phases were allowed to vary. Systematic errors have been introduced to account for biases indicated by the Monte Carlo experiments, and have been added in quadrature with the statistical errors. The relative phases for the $f'(1515)$ fit are quoted as consistent with zero, as indicated by the Monte Carlo experiments. The results are as follows:

$J^P(f') = 2^+$ with $\sim 99.9\%$ C.L.

$x = 0.63 \pm 0.10,\ \varphi_x \sim 0$

$y = 0.17 \pm 0.20,\ \varphi_y \sim 0$

$J^P(\theta) = 2^+$ with $\sim 99.9\%$ C.L.

$x = -1.07 \pm 0.20,\ \varphi_x = 0.6 \pm 0.8$

$y = -1.09 \pm 0.25,\ \varphi_y = -0.1 \pm 0.5$

The branching ratio measurements are performed using a full Monte Carlo simulation of the mass and angular distributions. The results are taken from the incoherent fit to the 1983 data sample. This gives:

$$BR(\psi \to f'(1515))BR(f'(1515) \to K\bar{K}) = (6.0 \pm 1.4 \pm 1.2) \times 10^{-4}$$

$$BR(\psi \to \theta(1700))BR(\theta(1700) \to K^+K^-) = (4.8 \pm 0.6 \pm 0.9) \times 10^{-4}$$

The only previous measurements of these rates were made with much lower statistics by MARK II.[24] The value for the $f'(1515)$ branching ratio presented here is somewhat larger than the previous MARK II measurement of $(1.8 \pm 0.6 \pm 1.0) \times 10^{-4}$. The value for the $\theta(1700)$ branching ratio presented here agrees fairly well with the previous MARK II measurement of $(6.0 \pm 0.9 \pm 2.5) \times 10^{-4}$.

Chapter 6. The High Mass Region in $\psi \rightarrow \gamma K^+K^-$

6.1 Event Selection

The event selection for the high mass region has been described previously. The gammas used were required to be 'good' gammas and the charged tracks were both required to be kaons. An anti-pion cut was made as well as a kaon consistency cut, as described in the introductory γK^+K^- chapter. Kinematic fitting was performed to impose energy and momentum conservation. Fits were performed using all permutations of the 'good' gammas in the event, and the fit with the smallest χ^2 was used for that event. The resulting improvement in resolution is essential for the analysis, since the raw mass resolution at the $\xi(2220)$ is $\sigma_m \sim 30$ MeV while the fitted mass resolution is $\sigma_m \sim 10$ MeV. The additional purpose for using the kinematic fit procedure is the elimination of backgrounds. The drift chamber provides particle identification information which is complementary to the TOF information via the kinematic fit. It is the combination of the TOF information and the kinematic fitting which provides a clean sample of charged kaons at the relatively high momenta present in this final state.

The P_{χ^2} distribution (the confidence level for the kinematic fit) for the $\xi(2220)$ region is shown in Fig. 6.1. It is apparent that the distribution, which should be flat for events satisfying the correct hypothesis, has some problems. Roughly half the events in the $\xi(2220)$ signal region have $P_{\chi^2} < 0.2$. This could be due to the presence of background events in the $\xi(2220)$ region. Table 6.1 indicates the number of signal events (extracted by fitting the mass spectrum) versus the P_{χ^2} cut. This table shows that the non-flat P_{χ^2} distribution is present in the signal itself and cannot be accounted for by background events. This non-ideal distribution was originally attributed to the influence of kaon decays. Unfortunately, this explanation

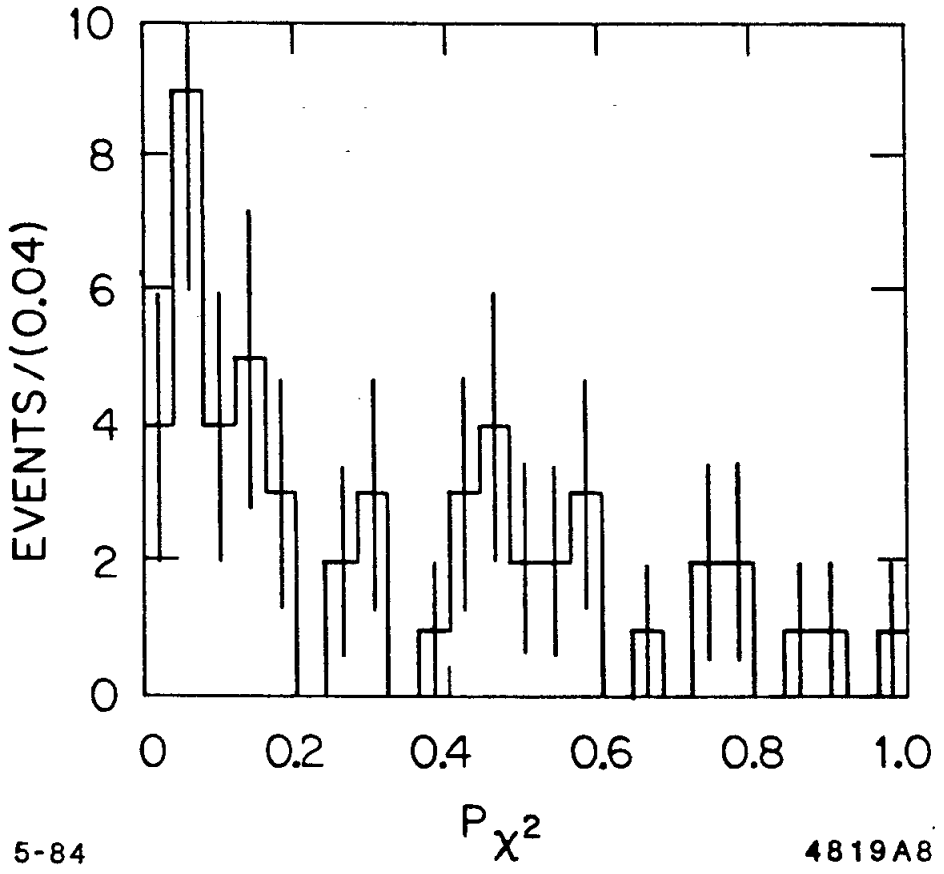

Figure 6.1. The P_{χ^2} distribution for the $\xi(2220)$ events. This distribution shows some indication for a non-ideal behavior.

Table 6.1. The $\xi(2220)$ signal versus P_{χ^2} cuts. The results are derived by performing Breit-Wigner fits over the $2 - 2.5$ GeV region, using those events which pass the given P_{χ^2} cut. The 1983 data sample is used.

P_{χ^2} Cut	Fraction of Total Events Found in the Peak	Number of Signal Events in the Peak
10^{-7}	0.066 ± 0.030	38.7 ± 17.6
0.001	0.097 ± 0.023	32.5 ± 7.7
0.002	0.096 ± 0.038	30.6 ± 12.1
0.005	0.089 ± 0.024	26.3 ± 7.1
0.01	0.100 ± 0.026	27.8 ± 7.2
0.02	0.114 ± 0.039	28.4 ± 9.7
0.05	0.124 ± 0.043	26.3 ± 9.1
0.1	0.135 ± 0.045	23.6 ± 7.9
0.2	0.122 ± 0.060	17.1 ± 8.4
0.5	0.115 ± 0.052	9.1 ± 4.1

($P_{\chi^2} = 10^{-7} \leftrightarrow \chi^2 = 50$)

has proven to be incorrect. Further study has indicated that the P_{χ^2} distribution is not influenced by kaons decaying in flight, since they fail the analysis cuts. The current Monte Carlo generates a P_{χ^2} distribution which is quite consistent with being flat, and the significance of the non-ideal P_{χ^2} distribution in the data is not clear. None of the pull distributions indicate a problem with any particular variable in the fit. After examining the K^+K^- mass distribution, a cut that $P_{\chi^2} \geq 0.02$ was chosen for use in the final event selection. This set of cuts produced the mass distribution and the Dalitz plot shown in Fig. 6.2. It should be noted that the cuts used to produce this plot are quite simple and obvious—they were not artificially tuned to enhance the result.

As an additional check, all of the events passing the final event selection

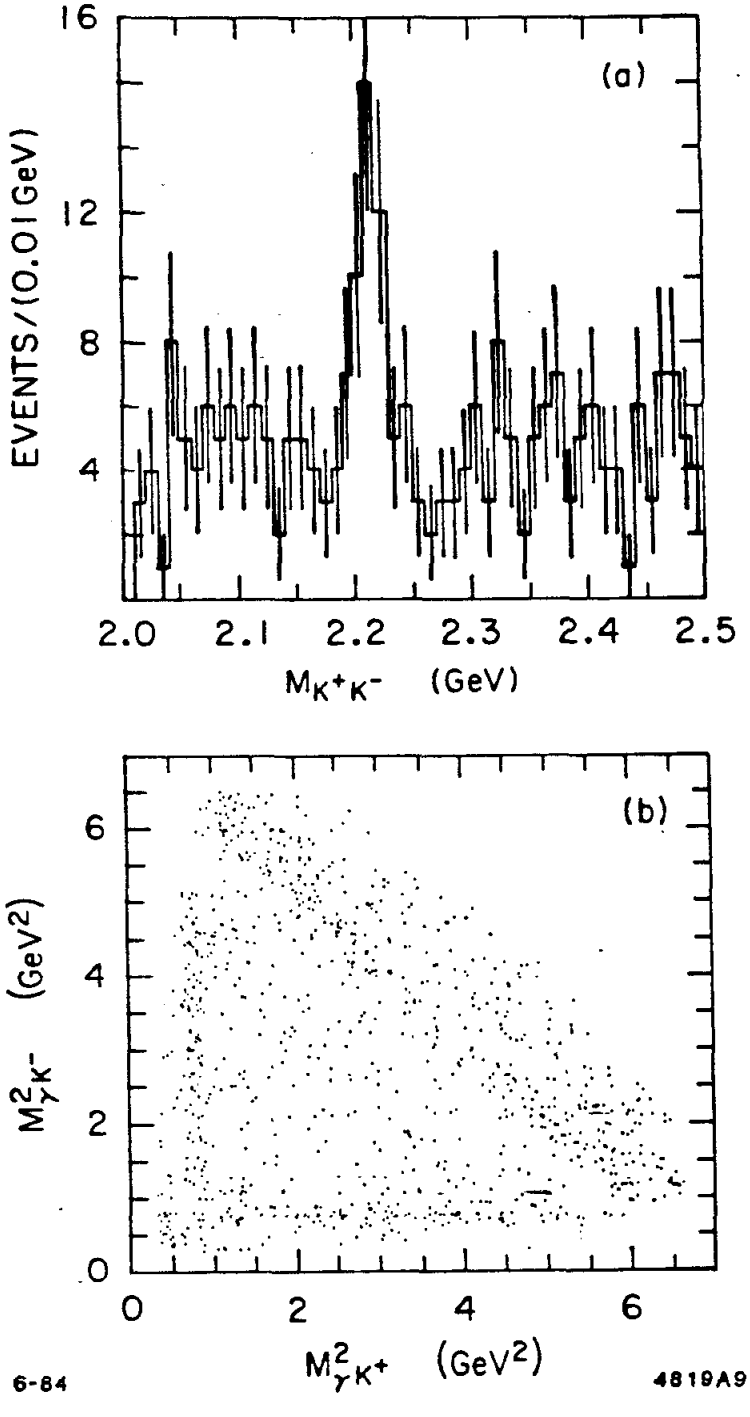

Figure 6.2. The final result for the 1983 data. The standard cuts have been made.

in the 2 to 2.5 GeV region have been hand-scanned using one event displays. They were checked for indications of detector problems or reconstruction errors; none were found. An attempt was made to classify the events as to their quality, but this was abandoned as being too subjective. A typical event contained in the $\xi(2220)$ peak is shown in Fig. 6.3.

The results discussed up to this point have included events from the 1983 run only. Applying the standard cuts to the 1982 run produces the mass distribution and the Dalitz plot shown in Fig. 6.4. It should be noted that Fig. 6.2 and Fig. 6.4 do not have the peak in the same location. Two different approaches to the subsequent analysis can be taken, depending on the interpretation given to the discrepancy. One school of thought is to ignore the 1982 data as *blemished and debased* and quote results based on the 1983 data alone. The other school of thought is, in the absence of compelling evidence to the contrary, to assume the 1982 data is *healthy and pristine* and include it in the subsequent analyses. Since neither approach appears very satisfactory, we will pursue both paths through the next sections. This vacillation will eventually be abandoned but only after great trauma, to be experienced more fully in the section on *Problems*.

If one ignores the difficulties and combines the two data samples, the mass distribution and Dalitz plot which are obtained are shown in Fig. 6.5.

6.2 BACKGROUNDS

The backgrounds for this final state have already been discussed in a cursory manner in the preceding chapter which presented an overview of γK^+K^-. It was concluded that the only significant background for this mass region came from the process $\psi \rightarrow K^+K^-\pi^0$. This background will now be discussed in more detail.

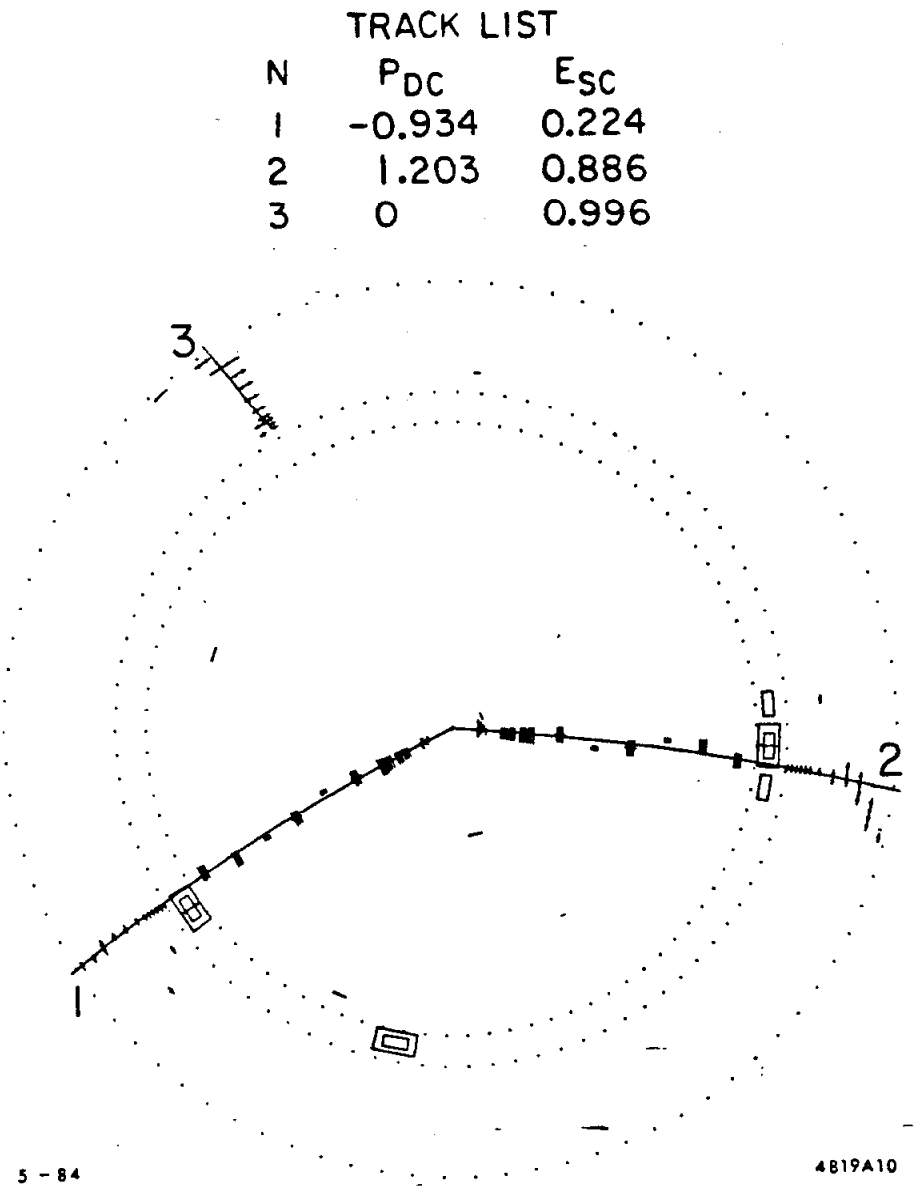

Figure 6.3. A typical one-event display for a $\xi(2220)$ event. The mass for this event is 2.217 GeV.

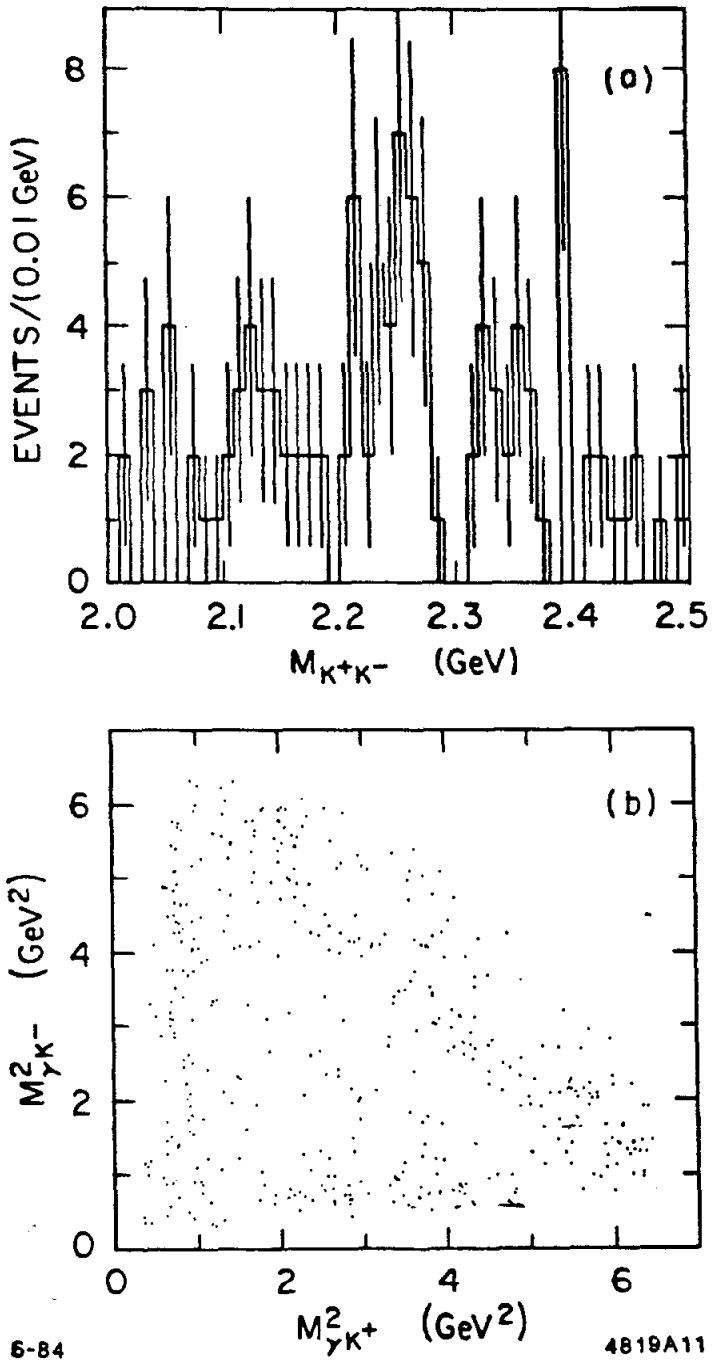

Figure 6.4. The final result for the 1982 data. The standard cuts have been made.

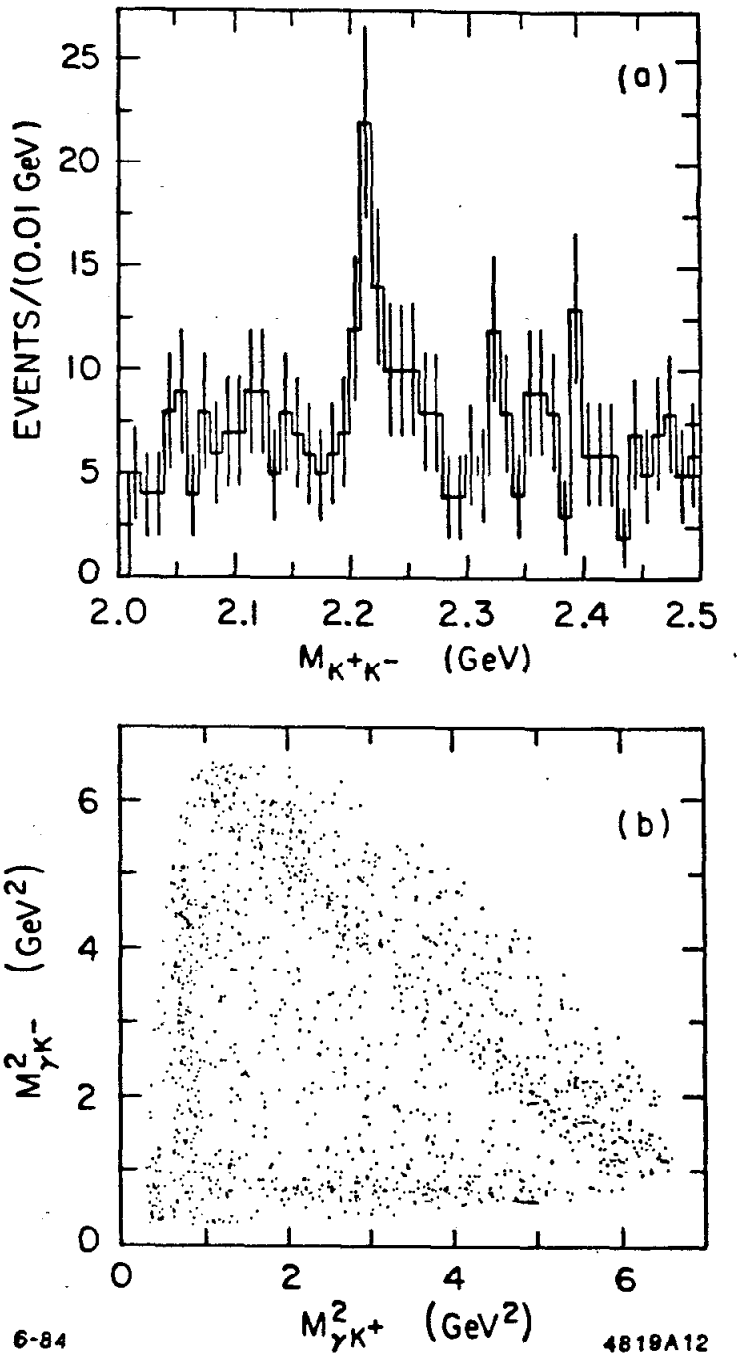

Figure 6.5. The final result for the 1982 and 1983 data. The standard cuts have been made.

The $K^+K^-\pi^0$ final state is dominated by the resonant two body final state $K^{*\pm}K^{\mp}$. Because of this quasi-two body dominance, the Monte Carlo studies which have been performed use $\psi \rightarrow K^+K^-\pi^0$ events which have been generated as $\psi \rightarrow K^{*\pm}K^{\mp}$. The process $\psi \rightarrow K^+K^-\pi^0$ has a fairly large branching ratio, and there are $\sim$ 1500 observed events. A typical $K^{*\pm}K^{\mp}$ background event which has passed the γK^+K^- event selection is shown in Fig. 6.6. This event contains a second photon with very low energy. Figure 6.7 shows the fit energy distribution for the photon which has the lower energy in $K^+K^-\pi^0$ events. There are many events which have a very low energy photon, corresponding to the case where the π^0 decays asymmetrically. This configuration provides a set of events which are, with finite resolution and inefficiency for low energy photons, kinematically indistinguishable from the signal events, since the missing energy and momentum are consistent with zero. This means that they cannot be separated from the signal events on the basis of a kinematic fit χ^2. The $p^2_{l_\gamma}$ variable could provide better rejection against the missing photon than the kinematic fit χ^2 because it was constructed to be very sensitive to such a missing photon, whereas the χ^2 is diluted by trying to satisfy other constraints. However, the cut $p^2_{l_\gamma} < 0.002$ has been tried and it does not significantly improve the background rejection. In addition, there is a great deal of ambiguity about the number of low energy photons present in an event, so cuts on the number of photons detected will not be helpful.

We are left with a large background from $\bar{\psi} \rightarrow K^{*\pm}K^{\mp}$. Fortunately for this analysis, this background is very smooth when it is projected into m_{KK}, as shown in a previous chapter. The estimate from the Monte Carlo is that $\sim$ 120 events in the 2 to 2.5 GeV region are from $\psi \rightarrow K^+K^-\pi^0$ background.

Several techniques have been tried to reduce the number of $K^+K^-\pi^0$ background events. None of them offered a significant improvement in the signal

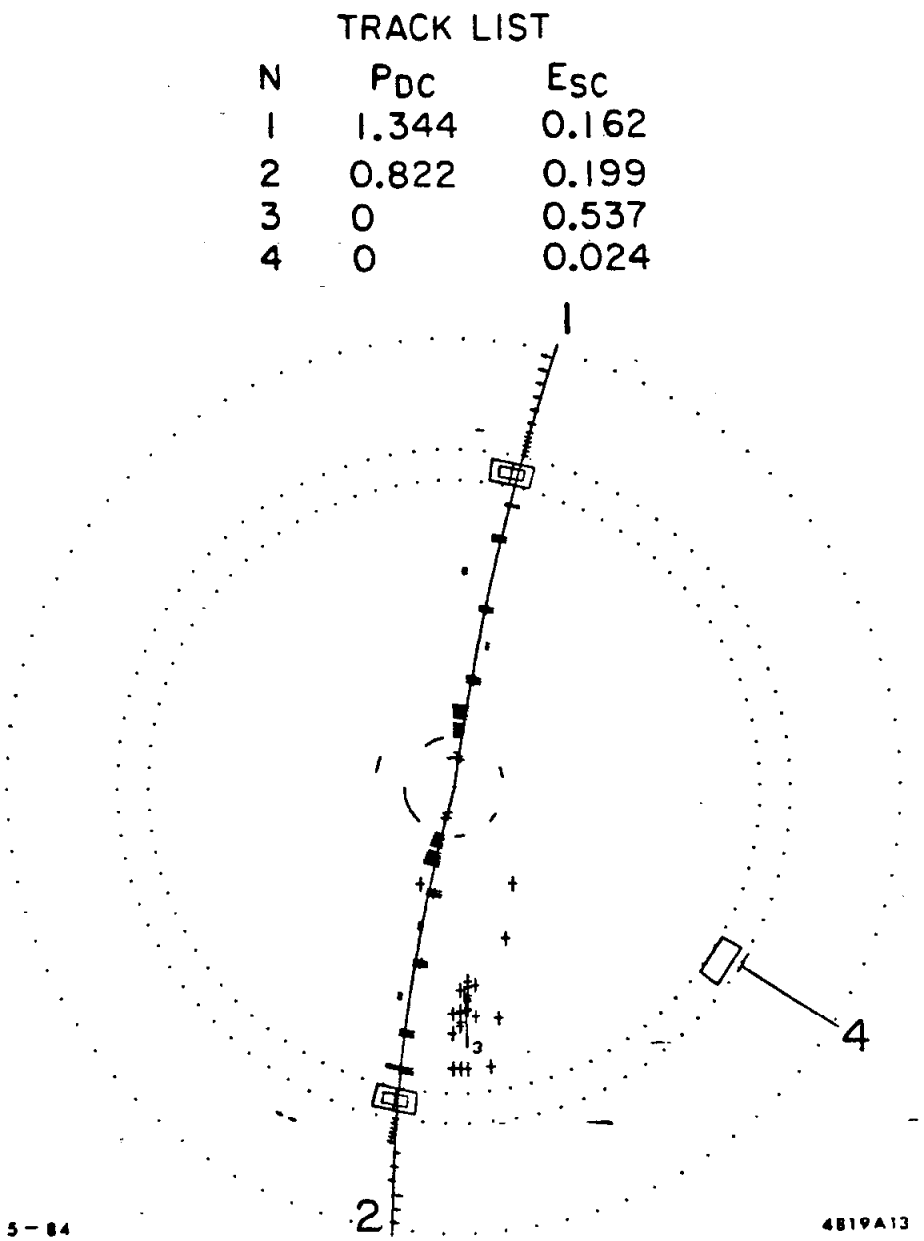

Figure 6.6. A typical one-event display for a $K^+K^-\pi^0$ background event. The masses for this event are: $m_{KK} = 2.316$ GeV, $m_{\gamma\gamma} = 0.131$ GeV and $m_{K^-\gamma\gamma} = 0.922$ GeV.

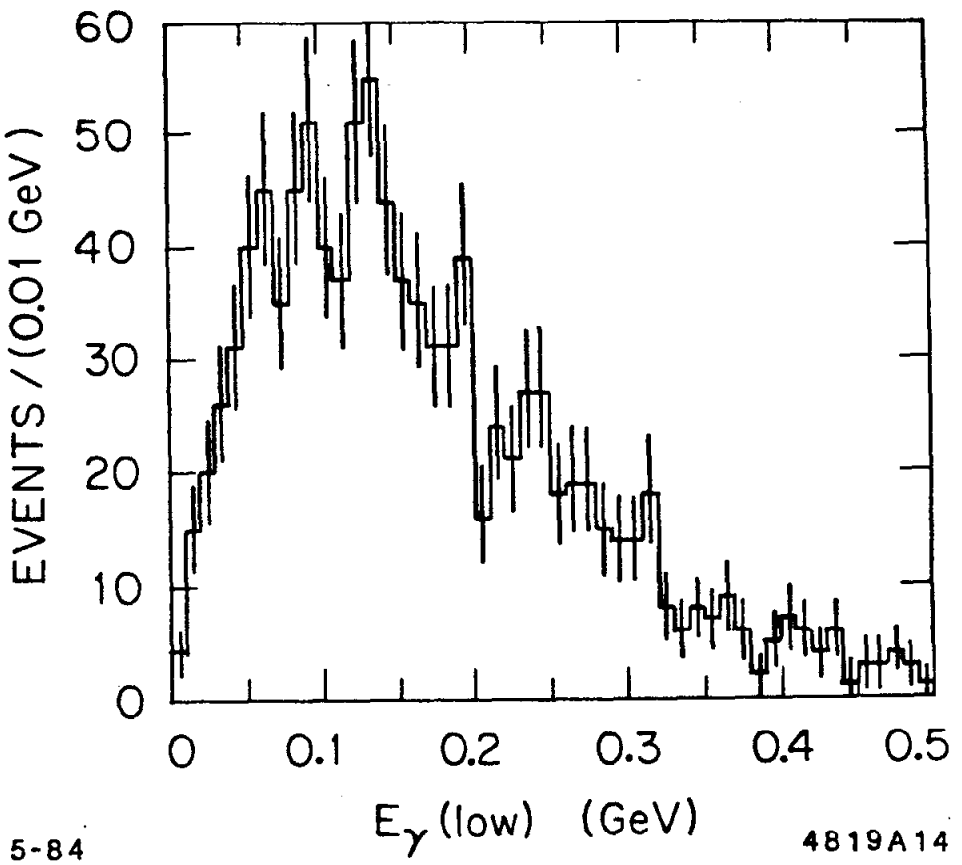

Figure 6.7. Photon energy distribution for $K^+K^-\pi^0$ events. The fitted energy for the lowest energy photon is shown. The events have been 4-C fit to the $K^+K^-\gamma\gamma$ hypothesis.

quality, and so they were not used in the subsequent analysis.

One technique was to simply cut on the P_{χ^2} for a parallel kinematic fit to the hypothesis $\psi \rightarrow \gamma\gamma K^+K^-$, where both of the gammas used in the fit were required to be 'good' gammas. The fit chosen was the best one for the event and did not necessarily include the same photons as the single gamma fit. The resulting mass distributions are shown in Fig. 6.8. This technique seems to produce a somewhat cleaner signal without losing many events. A more aggressive attempt was made by dropping the requirement that the gammas used in the parallel fit were 'good' gammas. This was tried because many of the $K^+K^-\pi^0$ events which fit the γK^+K^- hypothesis have very feeble second gammas, and they fail the 'good' gamma cuts. This technique eliminates many signal events because of the large number of fits which use fake low energy gammas.

A slightly different approach is to use the variable $m_{\gamma\gamma}$ from the best 4-C fit to the hypothesis $\gamma\gamma K^+K^-$, where the gammas in the fit are not required to be 'good' gammas. This should not be as harsh as the P_{χ^2} cut used previously, since it requires that $m_{\gamma\gamma}$ is close to the π^0 mass. The mass distribution which remains after removing events near the π^0 mass is shown in Fig. 6.9. There is a very broad π^0 peak in the $m_{\gamma\gamma}$ mass distribution which is caused by the poor measurement of this mass for events which contain a very asymmetric π^0 decay. The cut removes many signal events because they will use a 'fake' photon of low energy and appear as background under this broad π^0 peak.

A final attempt was made by performing 2-C fits, with one gamma missing, to the hypothesis $\psi \rightarrow K^+K^-\pi^0$, $\pi^0 \rightarrow \gamma(\gamma)$. This did not prove to be very successful because of the restricted topology of the $K^+K^-\pi^0$ events which pass the γK^+K^- cuts. These events have a very asymmetric π^0 decay, so the missing photon will have a very low energy and the 2-C fit can squeeze such a photon

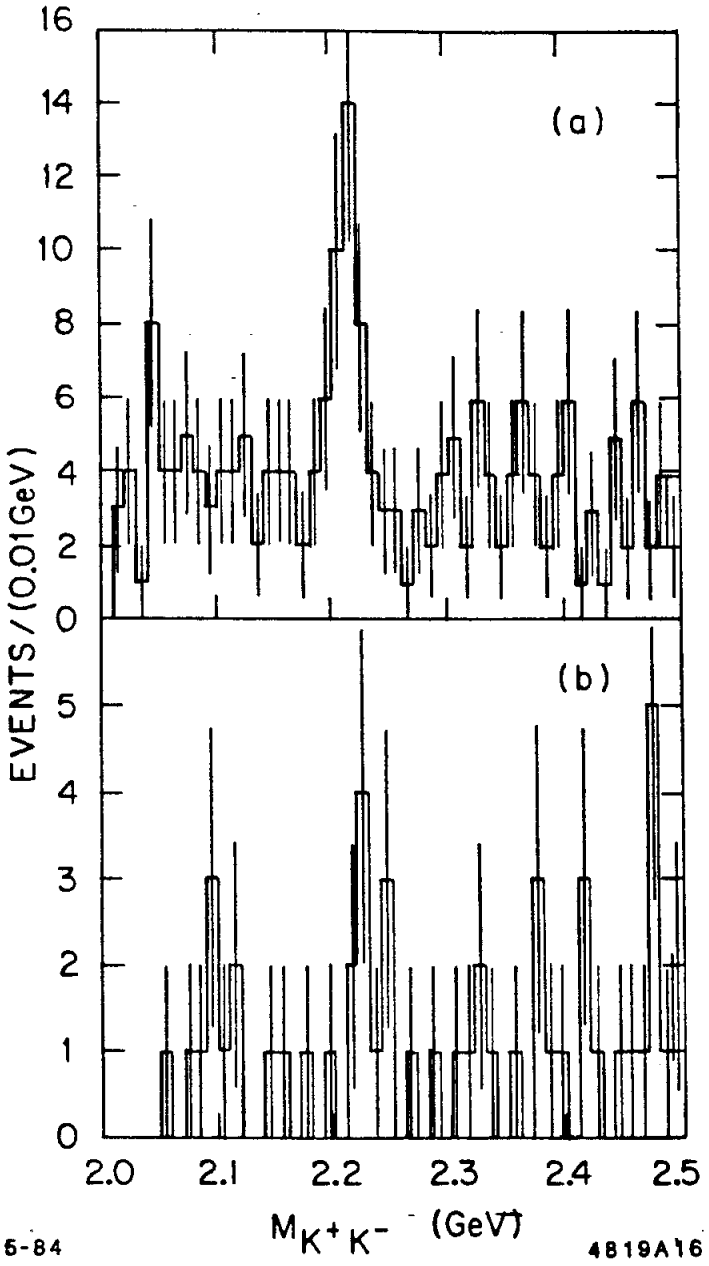

Figure 6.8. The effect of cutting against the two gamma P_{χ^2}. (a) shows the effects of a requirement that $P_{\chi^2}(\gamma\gamma) \leq 0.05$. (b) shows the distribution of events removed by the preceding cut. The gammas used in the 4-C fit were required to be 'good' gammas.

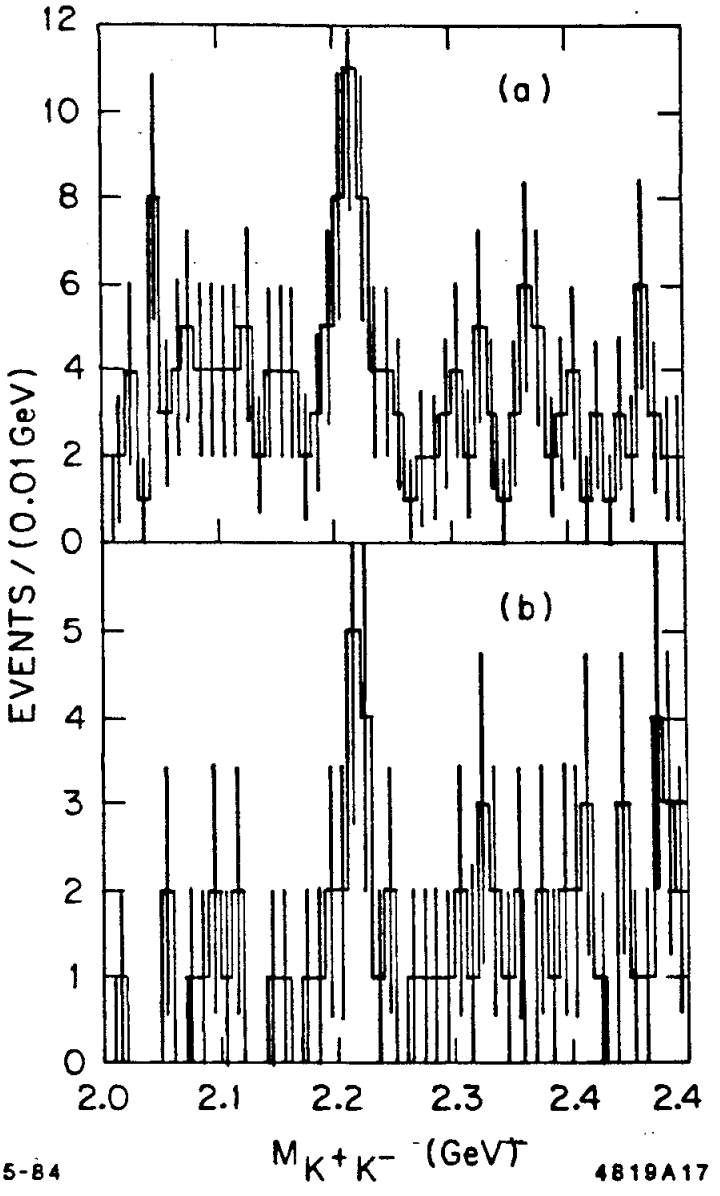

Figure 6.9. The effect of cuts against the two gamma mass. (a) shows the effects of a requirement that $m_{\gamma\gamma}$ was not in the π^0 region. (b) shows the distribution for events removed by the preceding cut. The gammas used in the 4-C fit were not required to be 'good' gammas.

almost anywhere. The errors on the position and energy of the missing photon are sufficiently large that it can not be determined whether such a photon could have remained unobserved in the event.

In summary, a rough breakdown of the sources of the events shown in Fig. 6.2 is as follows:

~ 120 $K^+K^-\pi^0$

~ 10 $\rho\pi$

~ 10 other

~ 80 γK^+K^- continuum (*i.e.*, non-resonant)

~ 30 $\xi(2220)$ signal

This will be of interest in considering backgrounds for the spin analysis performed on the $\xi(2220)$.

There are two conclusions to be drawn from the $K^+K^-\pi^0$ discussion. The first is that the $\xi(2220)$ signal is certainly *not* all due to $K^+K^-\pi^0$ events. The second is that none of the additional cuts tried here were very helpful in concentrating the $\xi(2220)$ event sample, indicating the difficult nature of the backgrounds as well as the poor statistics.

6.3 Measurement of the Parameters of the $\xi(2220)$

The Measurement of the Mass

The procedure for extracting the mass involves performing a maximum likelihood fit to the individual events using a polynomial background plus a Breit-Wigner convoluted with a Gaussian resolution function. The formalism for this fit is described in Appendix A. The resulting values for the mass are:

$$m = 2.217 \pm 0.003 \pm 0.010 \quad 1983$$

$$\boxed{m = 2.218 \pm 0.003 \pm 0.010 \quad 1982 \text{ and } 1983}$$

where the first error is statistical and the second error represents an estimate of the systematic error for the 1983 data. The fits which correspond to these measurements are shown in Fig. 6.10.

The systematic error has been computed in two different ways. One is deductive and proceeds by enumerating the possible sources for errors and estimating their contributions. This has been done by studying the interaction of the kinematic fit with possible measurement errors. Using Monte Carlo data, each one of the drift chamber or shower counter measurements was systematically shifted and the resulting changes in m_{KK} and the pull distributions were tabulated. The result of this study is that it is very unlikely that a combination of systematic errors in the momentum or energy scales could shift m_{KK} by as much as 10 MeV without producing drastic changes in the pull distributions.

A more empirical approach to estimating the systematic error is to examine the agreement between measurements in other final states and well established masses. The list of masses which are correctly and accurately measured is fairly long, including the following: K_s, η, η', ω and ϕ. In general, the measurement of a mass depends on the momenta and angles of the decay products and the errors in measuring these lower masses are smaller than for the $\xi(2220)$. Attempting to scale the errors up suggests that it would be difficult to have a systematic error much larger than $\sim$ 10 MeV.

The Measurement of the Width

The measurement of the width of the $\xi(2220)$ is somewhat more difficult. The maximum likelihood fit described previously is used to extract a residual Breit-Wigner width after the detector resolution is taken into account. Several models have been used for the detector resolution function. The simplest model is to use a single Gaussian with a sigma determined from the Monte Carlo. This model assumes

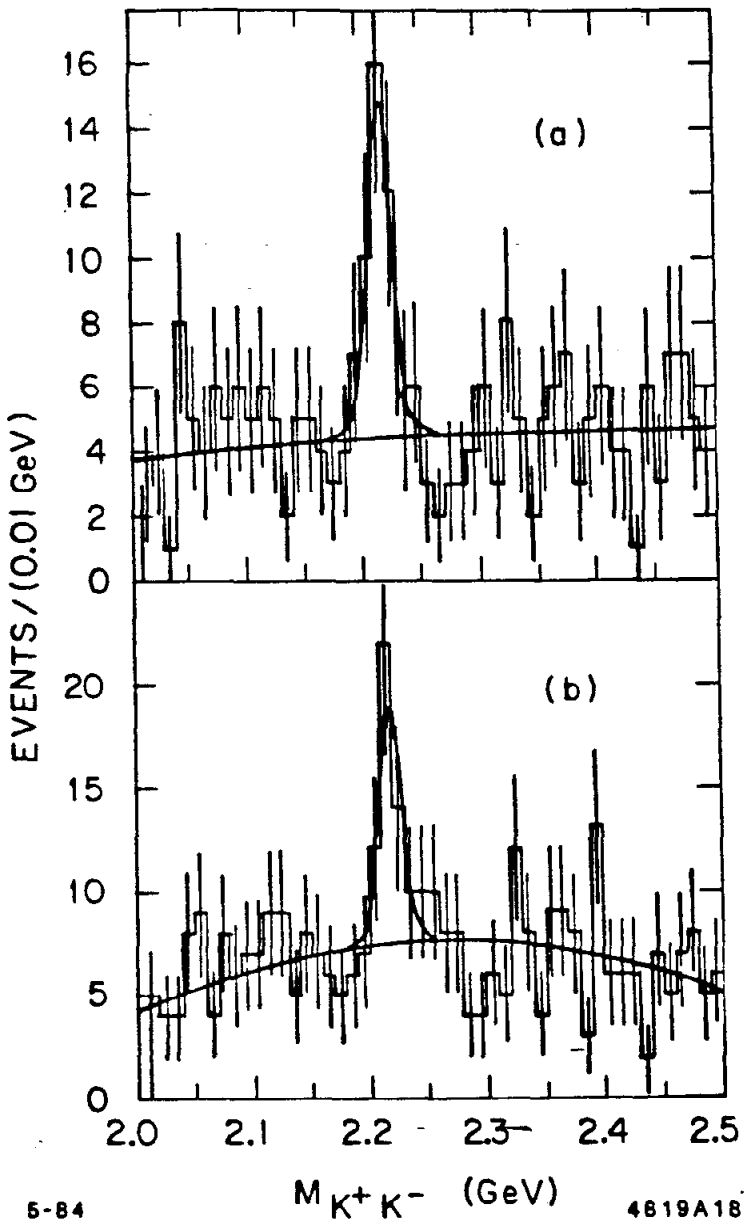

Figure 6.10. The fit results for the high mass region. (a) shows the fit result for the 1983 sample. (b) shows the result for the 1982 and 1983 sample.

that the mass resolution depends only on the value of the mass in question. In fact, this resolution also depends on the kaon momenta. This means that the shape of a narrow state is a super-position of Gaussians, and has a sharper peak and larger tails than a single Gaussian would. Despite this inadequacy in the simple model, it has proved possible to extract a width from Monte Carlo data with reasonable accuracy. Widths in the range of 1 to 15 MeV were generated with large statistics and were then fit using this procedure. The resulting extracted values of the width indicated that this simple resolution model introduced a systematic error which was less than 3 MeV.

A more complex model of the resolution was also used, in which the resolution was assumed to be Gaussian but the sigma was different for each event. This was done by using the estimated error on the mass provided by the kinematic fit. This technique increases the fitting time by two orders of magnitude because a numeric integration must be done to normalize the likelihood for each event. Such fits were performed, and gave a result which was compatible with that obtained using the simple model.

The values obtained by performing the fits using the simple resolution model gave a most probable value for the width in the range of 0 to 5 MeV for values of sigma in the resolution function which varied from 7 to 10 MeV. This range in resolution represents a plausible range for the real detector. The value of 10 MeV has been used in the subsequent analysis because it was the value predicted by the Monte Carlo. This is also the resolution which was used in the fits displayed in Fig. 6.10(a) and 6.10(b). The most probable value of the width, using this resolution, is zero for both of the fits displayed in Fig. 6.10.

Since the most probable value for the width is so small, and the number of events is also small, the correct approach is to quote an upper limit on the

width. The goal is to set a 95% C.L. upper limit using the results of the maximum likelihood fit. The standard approach to setting such a limit is to take the likelihood function and change the parameter of interest, re-maximizing with respect to the other parameters at each step, until a change in $ln\mathcal{L}$ of 2 is found ($ln\mathcal{L}$ is the log of the likelihood function). In the case of a parabolic $ln\mathcal{L}$ function, this corresponds to a change of 2σ, which corresponds to 95% C.L. for normal statistics. The association of a 95% C.L. with a $ln\mathcal{L}$ change of 2 is somewhat suspect here because the width cannot be less than zero and so the likelihood function has a boundary. A more general technique consists of numerically integrating the likelihood function, re-minimizing at each point of the integration, and finding an interval for the width which encompasses 95% of the total probability content. This is the approach that has been used, and it gives a larger upper limit than the standard technique. The values obtained are:

$$\Gamma \leq 0.030 \text{ GeV} \quad 95\% \text{ C.L.} \quad 1983$$

$$\boxed{\Gamma \leq 0.040 \text{ GeV} \quad 95\% \text{ C.L.} \quad 1982 \text{ and } 1983}$$

The contribution of the uncertainties in the resolution function to this limit are small because for such a large width, the additional contribution of the Gaussian is very small. Figure 6.11(a) shows the likelihood function and Fig. 6.11(b) shows a curve with a width equal to the limit value. It is evident that the limit is quite conservative.

The Statistical Significance and the Branching Ratio

Before proceeding to the branching ratio, it is worthwhile to discuss the statistical significance of the observation of the $\xi(2220)$. There are several techniques for estimating this significance, depending on the exact hypothesis that is being tested. The standard technique used by high energy physicists is to ask the question: how likely is it that the observed signal is a background fluctuation?

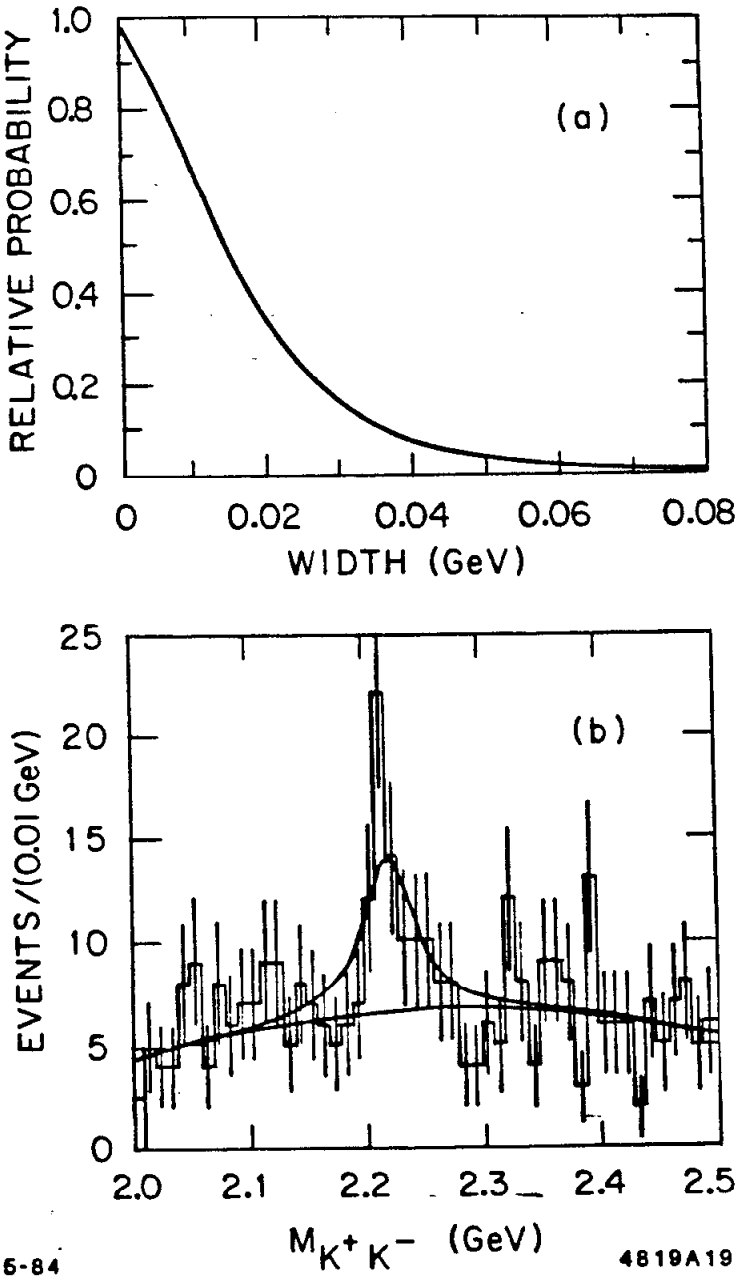

Figure 6.11. The width limit for the $\xi(2220)$. (a) shows the normalized likelihood function for the limit which has been set using the 1982 and 1983 data. (b) shows a curve which corresponds to the 95% C.L. upper limit for this data.

This can be quantified by using the estimator:[41]

$$d = \frac{N - \hat{B}}{\sqrt{\hat{B} + V(\hat{B})}},$$

where N is the total number of events, $\hat{B}$ is the estimate of the number of background events, and $V(\hat{B})$ is the variance on the estimate of the number of background events. The variable d is then the number of 'standard deviations' of the effect,i.e., it is a normal variable with a mean of 0 and a sigma of 1. The values obtained for the 1983 data are: $N = 54$, $\hat{B} = 21$,and $V(\hat{B}) \sim \hat{B}/4$. This gives $d \sim 6.5\sigma$.

A second way to look at this question is to ask: how likely is it that there is no signal? This can be quantified by varying the area of the signal to zero, re-maximizing in the other parameters and looking at the change in $ln\mathcal{L}$. The results of applying this technique to the samples in question are:

$$\delta(ln\mathcal{L}) = 12.3 \quad \Rightarrow \quad \text{a significance of } 5\sigma \quad (1983)$$

$$\boxed{\delta(ln\mathcal{L}) = 10.7 \quad \Rightarrow \quad \text{a significance of } 4.6\sigma \quad (1982 \text{ and } 1983)}$$

where the significance is related to the change in likelihood by the standard formula:

$$n_\sigma = \sqrt{2\delta(ln\mathcal{L})}$$

. There are two additional pieces of evidence that this state is not a background fluctuation. The first comes from comparing the decay angular distributions in the $\xi(2220)$ region with those observed in a slightly higher mass region. These distributions will be discussed in the section on *Spin Analysis*. The second comes from the related final state $\psi \rightarrow \gamma K_S K_S$, and will be discussed in the next chapter.

The branching ratio measurement is performed using the 1983 data only, in order to avoid any subtleties in modeling the 1982 detector. Since the production and decay angular distributions for this state are not known, it is necessary to

estimate the effect of this uncertainty on the detection efficiency. Most of this effect comes from the dependence of the efficiency on the kaon momentum spectrum. In estimating the change in efficiency, two extreme cases were used. The first is a phase space production and decay which has a flat momentum spectrum. The second was a $J = 2$ production and decay with helicity amplitude ratios $x = 1.0$ and $y = 0.0$ (this will be discussed more fully in the next section). This case has a kaon momentum spectrum which is strongly peaked near the endpoints. For these cases, the Monte Carlo efficiency is estimated to be:

$$\epsilon_{PS} = 0.32 \pm 0.02,$$

$$\epsilon_{J=2} = 0.25 \pm 0.02.$$

The actual efficiency which will be used to calculate the branching ratio corresponds to intermediate production and decay angular distributions which more closely resemble the data. The case used was $J = 2$ with helicity ratios $x = 1.0$ and $y = 1.0$. The value obtained for the efficiency is $\epsilon = 0.28 \pm 0.02$. A large systematic error has been assigned to account for the variations described above. The total systematic error is estimated to be:

$\pm 10\%$	ψ flux uncertainty
$\pm 20\%$	ϵ uncertainty due to angular distributions
$\pm 10\%$	ϵ uncertainty from other effects
$\pm 25\%$	total

The results of the maximum likelihood fit give:

28.5 ± 9.8 events 1983

28.7 ± 9.4 events 1982 and 1983

This gives the branching ratio:

$$\mathrm{BR}(\psi \to \gamma\xi(2220))\mathrm{BR}(\xi(2220) \to \mathrm{K^+K^-}) = (5.7 \pm 1.9 \pm 1.4) \times 10^{-5} \quad 1983$$

6.4 SPIN ANALYSIS OF THE $\xi(2220)$

This analysis proceeds in much the same manner as the analysis of the $f'(1515)$ and $\theta(1700)$ region discussed previously. In the current analysis, J values of 0, 2 and 4 will be considered. Once again, there are three angles which parameterize the production and decay process. The number of independent production amplitudes is still three, labeled A_0, A_1 and A_2. A standard approximation is to assume that the three amplitudes all have the same phase. It is argued in Appendix B that this approximation is probably accurate and has minimal consequences. It is made here in order to reduce the number of free parameters. These parameters can now be written as real ratios:

$$x \equiv \frac{A_1}{A_0} \quad , \quad y \equiv \frac{A_2}{A_0} \, ,$$

without the additional phase parameters. An acceptance corrected fit is performed to measure the values for the unknown helicity amplitudes. This fitting procedure uses a maximum likelihood technique where the effects of acceptance are included in the likelihood function. The formalism is discussed in detail in Appendix C. The Monte Carlo acceptance for the three angles is shown in Fig. 6.12. These plots are histograms of accepted Monte Carlo events which were generated with flat distributions in the three angles. The mass distribution for these events was generated in agreement with the measured mass and width for the $\xi(2220)$. These events are used to perform the normalization integrations described in Appendix C. The acceptances in this mass region are relatively free from the influence of kaon decays, because there are very few low momentum kaons in this mass region.

The events used in the fit are selected to be in the signal region:

$$2.195 \leq m_{KK} \leq 2.235 \text{ GeV}$$

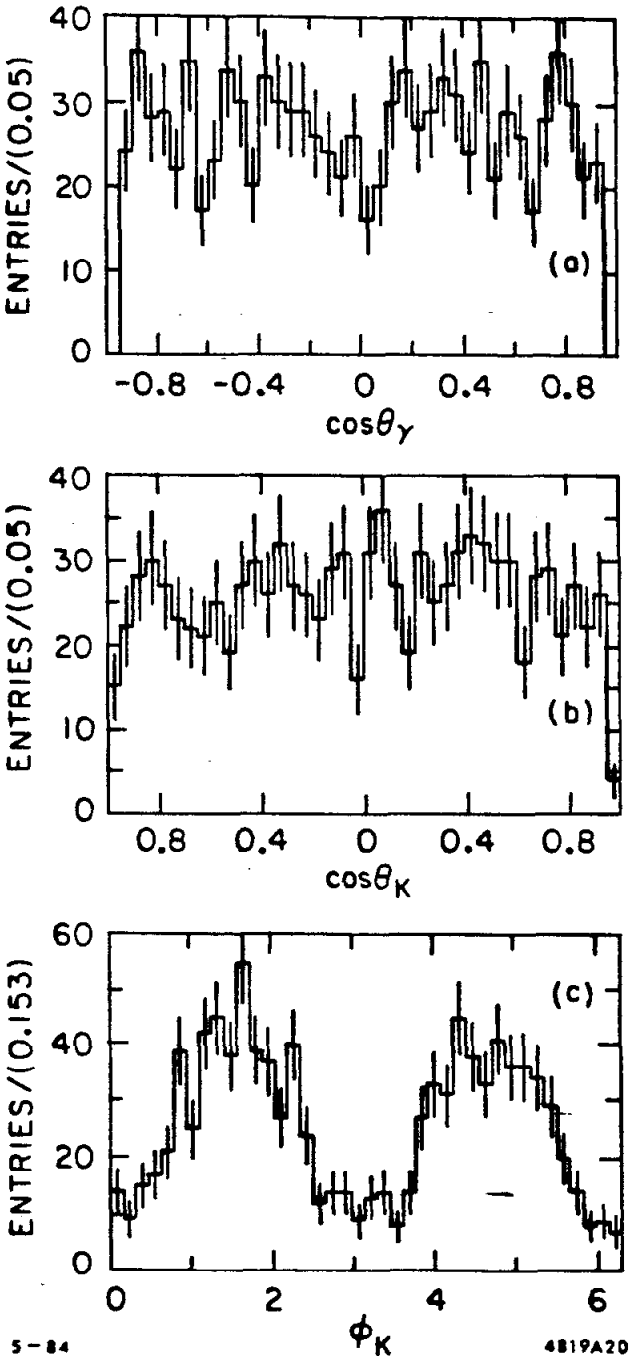

Figure 6.12. The Monte Carlo angular acceptances for the $\xi(2220)$. The plots show the three angular distributions after event selection and fiducial cuts.

in the 1983 data. A fiducial region is defined in the detector to insure agreement with the Monte Carlo acceptance calculations. The region is defined by: $|\cos\theta_{SC}| \leq 0.95$ and $|\cos\theta_{DC}| \leq 0.75$. There are 38 events remaining after these cuts. Their projected angular distributions are shown in Fig. 6.13(a), (b), and (c).

A very significant feature of this analysis is the large amount of background which is present. It is estimated that the different sources for the events in this analysis are as follows:

$\sim$ 24 events	$\xi(2220)$ signal,
$\sim$ 9 events	$K^{*\pm}K^{\mp}$ background,
$\sim$ 5 events	γK^+K^- non-resonant.

The $K^{*\pm}K^{\mp}$ background events cause the greatest difficulty. The one angle which carries the highest quality information (θ_K) is also the most strongly affected by this background source. This can be shown in two different ways. Fig. 6.13(d), (e), and (f) show the angular distributions for events in a mass region adjacent to the $\xi(2220)$ signal. A mass interval of 2.300 to 2.395 was chosen which contained the same number of events as the signal region. This asymmetric region was chosen because the mass region below the $\xi(2220)$ signal seems to have different angular distributions than the 2.3 – 3.0 GeV region (which could be associated with the broad state observed in $\gamma\pi^+\pi^-\ldots$). The plot of $\cos\theta_{\bar{K}}$ shows the highly peaked structure of the sidebands, which is due to the $K^{*\pm}K^{\mp}$ background. A comparison of Fig. 6.13(a) with Fig. 6.13(b) shows a change in the shape of the $\cos\theta_K$ angular distribution on and off the $\xi(2220)$. This is further evidence that the signal is not a background fluctuation. The approximate shape of the background can be understood from the Dalitz plot. An object with fixed m_{KK} appears as a diagonal band in the Dalitz plot. The ends of such a band correspond to collinear event configurations with $\cos\theta_K \sim \pm 1$. These endpoints are also the regions populated

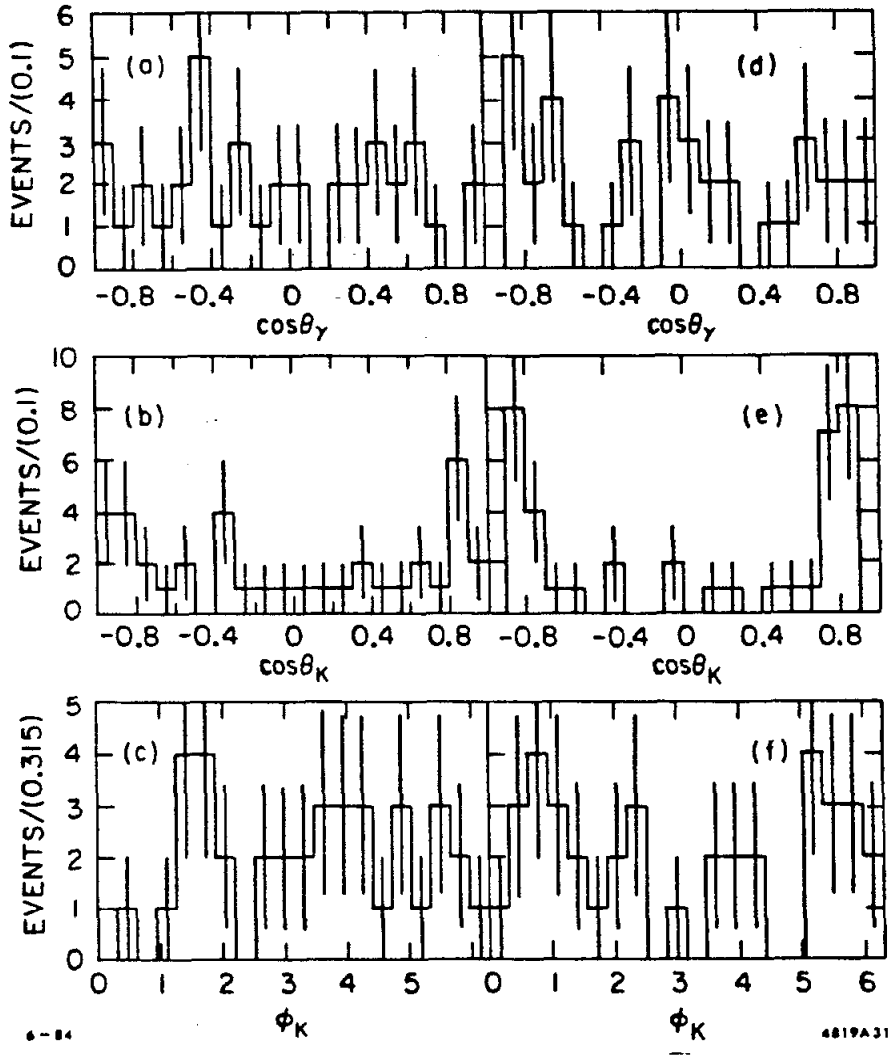

Figure 6.13. The angular distributions for the $\xi(2220)$ signal and sideband. (a), (b), and (c) show the three angular distributions for the $\xi(2220)$ signal events. (d), (e), and (f) show the three angular distributions for the $\xi(2220)$ sideband. The size of the sideband region was chosen so that it contained the same total number of events as the signal region.

by the $K^{*\pm}K^{\mp}$ background bands, which run horizontally and vertically in the Dalitz plot. The configuration with $|\cos\theta_K| = 1$ corresponds to the boundary of the Dalitz plot which occurs at the minimum $K\pi$ mass allowed by kinematics. The peak due to the K^* resonance appears at a value of $|\cos\theta_K| \sim 0.9$. This is less than one because the K^* resonance is more massive than the minimum kinematically allowed $K\pi$ mass.

Further evidence of the difficult background problem is shown in Fig. 6.14, which is a comparison between the $\cos\theta_K$ distribution for the $\xi(2220)$ events and for events which are kinematically fit to the $K^+K^-\pi^0$ hypothesis and have $2.1 \leq m_{KK} \leq 2.3$. It is clear that this background peaks in the region of interest. If one removes the ~ 9 events from the $\xi(2220)$ plot which correspond to the expected $K^{*\pm}K^{\mp}$ background shown in Fig. 6.14, the remaining distribution will be relatively flat. A flat distribution in this variable is consistent with any J^P hypothesis.

The preceding discussion has foreshadowed the result of the full spin analysis. It will prove inconclusive and result in the non-measurement of the J^P of the $\xi(2220)$. In spite of this discouraging situation, the actual spin analysis has been performed by attempting to include the $K^{*\pm}K^{\mp}$ background in the spin fit.

The likelihood function for the fit is generalized to be of the form:

$$\mathcal{L} = (1-\delta)\mathcal{L}_{\gamma K^+K^-} + \delta\mathcal{L}_{K^{*\pm}K^{\mp}}.$$

Using this form, the contribution of the $K^{*\pm}K^{\mp}$ background should be taken into account and $\mathcal{L}_{\gamma K^+K^-}$ should be sensitive to the angular distributions of the remaining events. The background term contains no free parameters and has been calculated in Appendix B using the helicity formalism. The formula for the angular correlation function is:

$$W_{K^{*\pm}K^{\mp}} = \sin^2\vartheta_{\pi^0}\left[1 + \cos^2\vartheta_K + \sin^2\vartheta_K\cos 2\varphi_{\pi^0}\right],$$

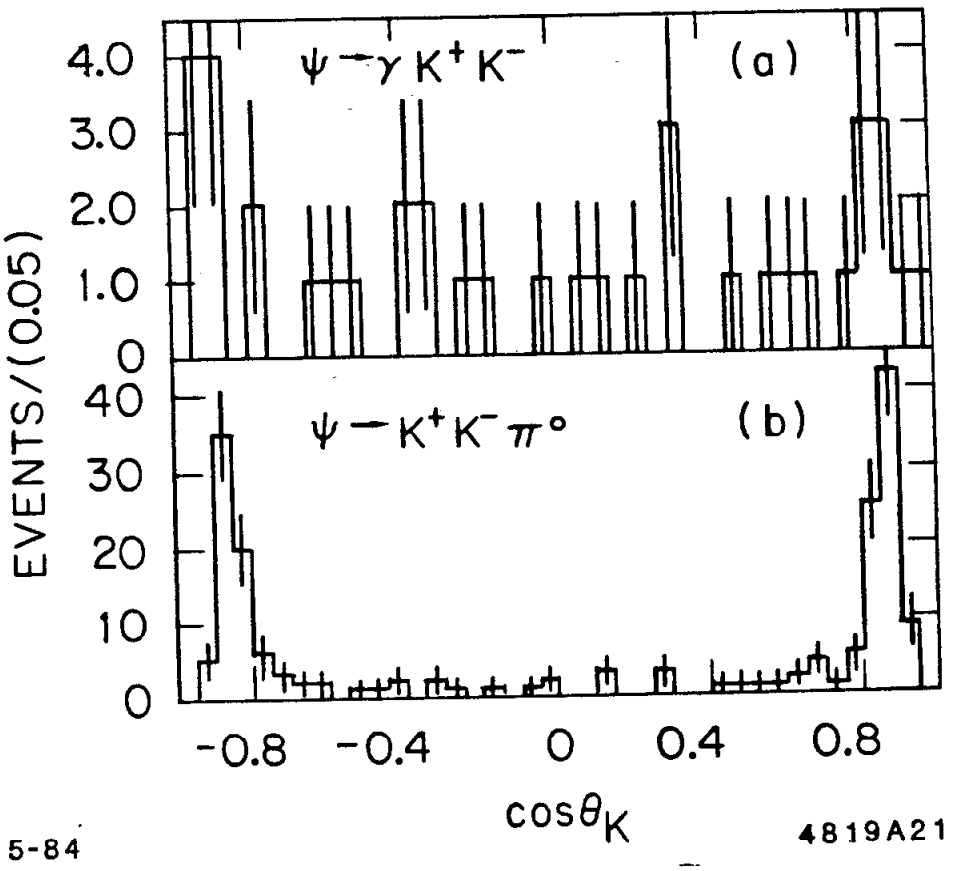

Figure 6.14. A comparison between $K^+K^-\pi^0$ background events and signal events. The events in the top plot are the signal, the events in the bottom are 4-C fitted $K^+K^-\pi^0$ events.

ϑ_K = the lab polar angle of the K not in the K^*,

ϑ_{π^0} = the polar angle of the π^0 in the K^* center of mass,

φ_{π^0} = the azimuthal angle of the π^0 in the K^* center of mass.

The true likelihood should include interfering contributions from the two possible K^* states:

$$P_{\mathrm{K}^{*\pm}\mathrm{K}^{\mp}} = \left| \frac{K^{*+}K^- - K^{*-}K^+}{\sqrt{2}} \right|^2 ,$$

where the minus sign is determined by constructing a $C = -$ eigenstate. This effect is ignored here since the region of the Dalitz plot where the interference is important is the region where the K^* bands overlap, *i.e.*, where $\cos\vartheta_{\pi^0} \sim \pm 1$. The matrix element is proportional to $\sin^2\vartheta_{\pi^0}$, which vanishes in this region. The background likelihood is then written:

$$\mathcal{L}_{\mathrm{K}^{*\pm}\mathrm{K}^{\mp}} = \left[\mathrm{Breit-Wigner}_{K^*}(K\pi^0)\right] \left[W_{\mathrm{K}^{*\pm}\mathrm{K}^{\mp}}(\vartheta_K, \vartheta_{\pi^0}, \varphi_{\pi^0})\right] ,$$

where the calculations are performed for the $K\pi^0$ combination which is closest to the K^* mass. The angles are calculated by using the missing 4-momentum recoiling against the $\mathrm{K}^+\mathrm{K}^-$ system as an estimate for the π^0 4-momentum. The relative normalization of the two components of the likelihood function has been adjusted to produce the correct values for the fraction δ when fitting Monte Carlo data. The behavior of the fitting procedure has been partially accounted for by comparing the observed results with a Monte Carlo data set which contains a mixture of $\xi(2220)$ signal events and $\mathrm{K}^{*\pm}\mathrm{K}^{\mp}$ background events. The comparison was made in the manner described in Appendix C, using the expected likelihood distributions from an ensemble of Monte Carlo experiments. The Monte Carlo results have been obtained for several sets of input angular distributions and fit hypotheses. The choice of $x = 1.0$ and $y = 0.0$ for the $J = 2, 4$ Monte Carlo samples represents an optimal case for a spin measurement, where the expected angular distributions look much different from those for $J = 0$.

Table 6.2. A summary of Monte Carlo spin fits for the $\xi(2220)$. These are the results of fits to Monte Carlo experiments using a fit procedure which includes $K^{*\pm}K^{\mp}$ background. The unlabeled numbers are $ln\mathcal{L}$ from the fit.

	Generate $J=0$	Generate $J=2$	Generate $J=4$
Fit $J=0$	-52.5 ± 4.3	-51.4 ± 4.3	-48.9 ± 4.5
Fit $J=2$	-52.9 ± 4.4 $x = 0.8 \pm 0.7$ $y = 1.1 \pm 0.4$	-45.8 ± 4.6 $x = 1.3 \pm 0.4$ $y = -0.2 \pm 0.5$	-46.0 ± 5.0 $x = 0.9 \pm 0.6$ $y = 0.1 \pm 0.4$
Fit $J=4$	-53.9 ± 5.1 $x = 1.0 \pm .5$ $y = 0.2 \pm 0.9$	-46.7 ± 5.4 $x = 1.2 \pm 0.4$ $y = 0.8 \pm 0.5$	-43.9 ± 5.3 $x = 1.4 \pm 0.3$ $y = 0.8 \pm 0.6$

A compilation of the results obtained from performing Monte Carlo experiments using this fit technique is shown in Table 6.2. This table shows the pattern which emerges from performing 100 Monte Carlo experiments on samples containing 38 events. Each entry summarizes one of the ensembles of 100 experiments, where the quoted error corresponds to the standard deviation for the ensemble of experiments. In constructing Table 6.2, the fraction δ was fixed at a value of 0.3. If this parameter is allowed to vary, it will introduce biases when fitting the wrong hypothesis. If the $J = 0$ hypothesis is tried on $J = 2, 4$ Monte Carlo data which is not flat in $\cos\theta_K$, then δ will increase to compensate for this. Conversely, for the $J = 4$ hypothesis, the angular distributions can be distorted to look like the background and δ will decrease and let some of the background be fitted as signal. It is also worth noting that when the Monte Carlo data is fit with the correct hypothesis, the fit is able to extract approximately correct values for x and y, and that the distributions for the expected likelihoods are very broad, indicating that the ability to isolate the correct hypothesis is very limited.

Table 6.3. A summary of spin fits to the $\xi(2220)$ signal region. The table displays the results of various spin fits to the $\xi(2220)$ using a fit procedure which includes $K^{*\pm}K^{\mp}$ background.

Fit $J = 0$	$ln\mathcal{L} = -51.9$
Fit $J = 2$	$ln\mathcal{L} = -50.1$ $x = 0.6 \pm 0.4$, $y = -0.9 \pm 0.3$
Fit $J = 4$	$ln\mathcal{L} = -55.1$ $x = 1.0 \pm 0.3$, $y = -0.3 \pm 0.4$

The values which result from applying this fit procedure to the data are shown in Table 6.3. For the $J = 0$ hypothesis, since it depends only on the angle $\cos\theta_\gamma$, the $ln\mathcal{L}$ is about the same for the different input distributions. For the $J = 2$ hypothesis, it appears that there is a limited ability to separate $J = 0$ inputs from $J = 2, 4$ inputs.

A naive estimate of the significance of these results would use the test statistic:

$$\text{“}\chi^{2}\text{”} = -2\ln\lambda \quad , \quad \lambda = \frac{\mathcal{L}(J=0)}{\mathcal{L}(J=2,4)}.$$

This statistic should be distributed like a χ^2 variable for 2 DOF, since that is the difference in the number of parameters for the two hypotheses. This gives $\text{“}\chi^{2}\text{”} \sim 2$ which corresponds to a $\sim 60\%$ C.L. In applying the full Monte Carlo hypothesis test, one would be tempted to fit the results in Table 6.3 into the pattern seen in Table 6.2 by claiming that they were very consistent with $J = 0$ and less consistent with $J = 2, 4$. This apparent pattern is indicative of the fact that the values $x \sim 1$ and $y \sim 0$ appear not to be the best values for the data.

The expected distributions for the θ_K angle are shown in Fig. 6.15. They indicate the minor differences expected in this distribution when such a pernicious background is also present. There are no overwhelming conclusions, but some tentative observations can be offered. The data is consistent with any of the

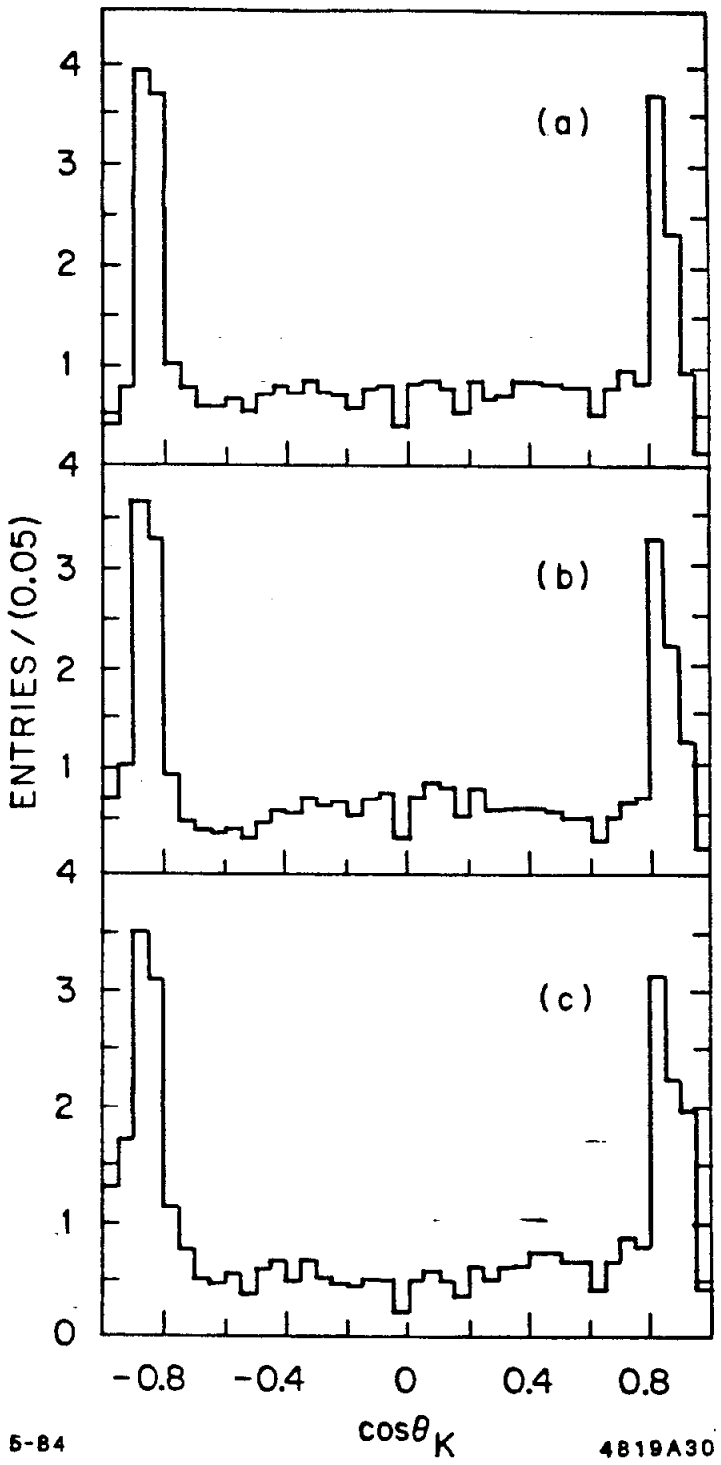

Figure 6.15. The angular distributions for spin fits to the $\xi(2220)$. The expected distribution for $\cos\theta_K$ is displayed for the spin 0, 2 and 4 hypotheses.

hypotheses offered in Table 6.3 at the $1-2\sigma$ level. The data is probably more consistent with $x \sim 1$ and $y \sim 1$, which corresponds to a fairly flat distribution in $\cos\theta_K$, than with $x = 1.0$ and $y = 0.0$, which corresponds to a very peaked distribution. A further practical observation on the determination of x and y should be kept in mind when examining these results. The sign of the ratios is often poorly determined because the diagonal terms in the angular correlation function $(1, x^2, y^2)$ contribute more strongly than the linear terms (x, y, xy) which contain the sign information.

The conclusion of this lengthy discussion is that the most likely hypotheses are $J = 0$ or $J = 2, 4$ with $x \sim 1$ and $y \sim 1$. None of these cases can be reliably distinguished with the current statistics. This section closes with a further discouraging thought. The $J = 2, 4$ case with $x \sim 1$ and $y \sim 1$, which seems to be very weakly suggested here, is the most difficult to distinguish from $J = 0$, as indicated in the $\theta(1700)$ J^P analysis of the preceding chapter. If the $\xi(2220)$ is really $J = 2, 4$ with $x \sim 1$ and $y \sim 1$ it will require a very large increase in statistics over the current sample of events to perform a definitive spin analysis, perhaps more than a factor of 10...

6.5 PROBLEMS

There appears to be one problem with the $\xi(2220)$—the signal observed in 1982 does not agree very well with the signal observed in 1983. A brief historical review will be offered on the problem. This is followed by a discussion of three possible scenarios, none of which are very satisfying. No epiphanies are offered, but an operational conclusion is reached.

In the beginning, there was the 1982 data. In January 1983, the full sample had been analyzed with a consistent and functional reconstruction package. TOF

information existed for runs 500 to 921, or about 0.8×10^6 produced ψ's. The plot shown in Fig. 6.16 provided strong evidence for something new in $\psi \rightarrow \gamma K^+K^-$. This plot was made using the following basic cuts:

$$\text{Kinematic fit } P_{\chi^2} \geq 0.05,$$

$$\text{Kaon weight } \geq 0.05 \quad , \text{ Pion weight } \leq 0.50.$$

The TOF cuts used here have a large momentum bias and were not used in the subsequent analysis, but they did remove some of the high mass background events. The peculiar signal seen here, combined with hints of several other interesting phenomena, encouraged the acquisition of a larger sample of ψ events in the Spring of 1983. The results from the new sample of $\sim 1.8 \times 10^6$ produced ψ's are compared with the 1982 results in Fig. 6.17 and Fig. 6.18. These plots were made using the selection procedure outlined in the *Event Selection* section. The 1983 data were fit with the standard polynomial background plus a Breit-Wigner and a Gaussian resolution function, as described in Appendix A. Two different approaches were taken in fitting the 1982 signal. Figure 6.17 fits the 1982 data with the same procedure used in 1983. The parameters which result from these fits are (the errors correspond to 1σ):

$$m = 2.259^{+0.005}_{-0.008} \text{ GeV} \quad , \quad \Gamma = 0.001^{+0.020} \text{ GeV} \quad (1982),$$

$$m = 2.217^{+0.003}_{-0.004} \text{ GeV} \quad , \quad \Gamma = 0.002^{+0.011} \text{ GeV} \quad (1983).$$

Figure 6.18 has the 1982 mass, width and area of the state fixed at their 1983 values; the fit was allowed to vary the background shape. In this case, the vertical scale was forced to be identical for both data samples, in order to emphasize the limited statistics available in 1982.

Three scenarios can be outlined to discuss the discrepancy shown above. They are listed below in order of plausibility:

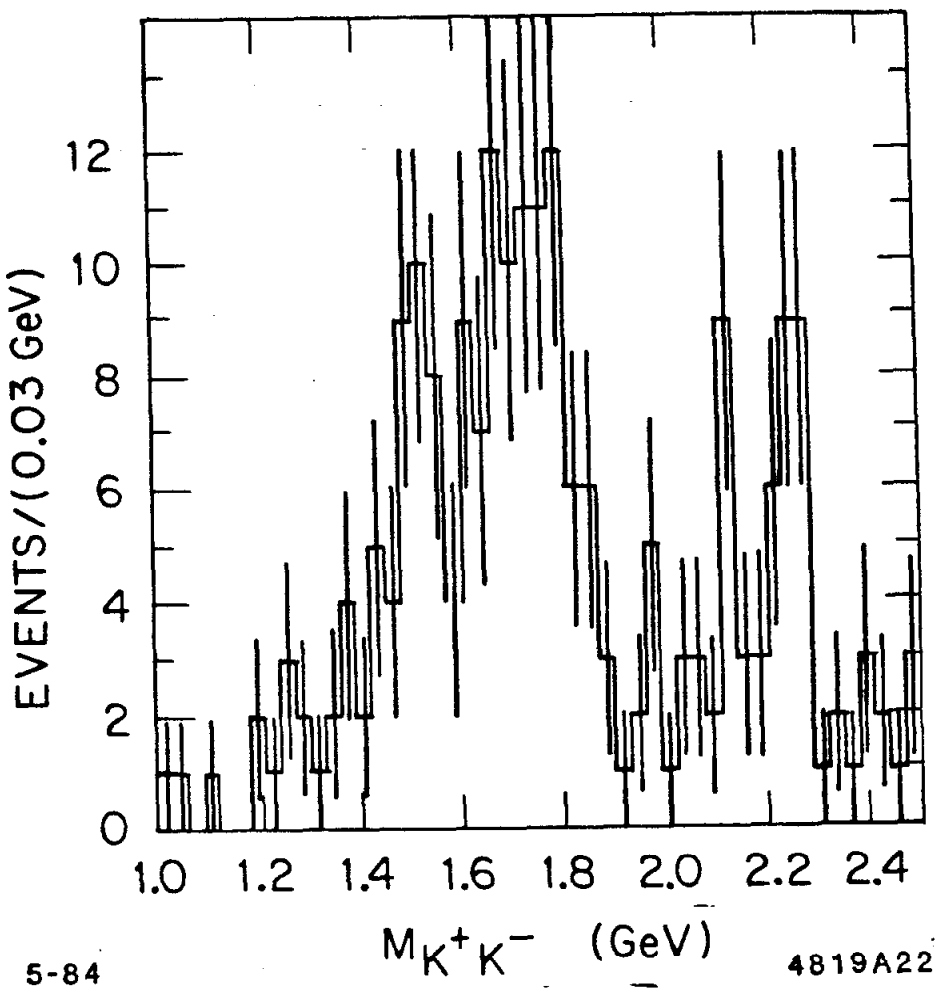

Figure 6.16. The original 1982 mass plot for the $\xi(2220)$. This plot uses a non-standard set of cuts.

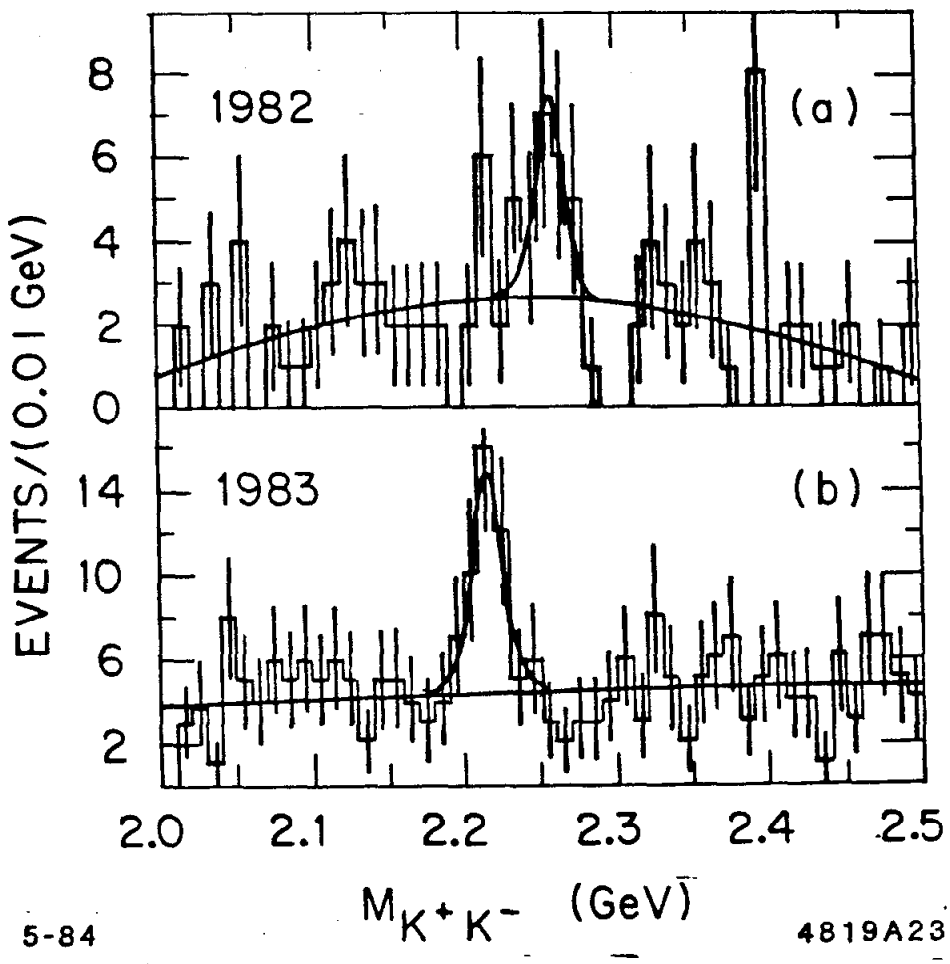

Figure 6.17. A comparison betwen the 1982 data and the 1983 data. These plots contain independent fits to the two data sets.

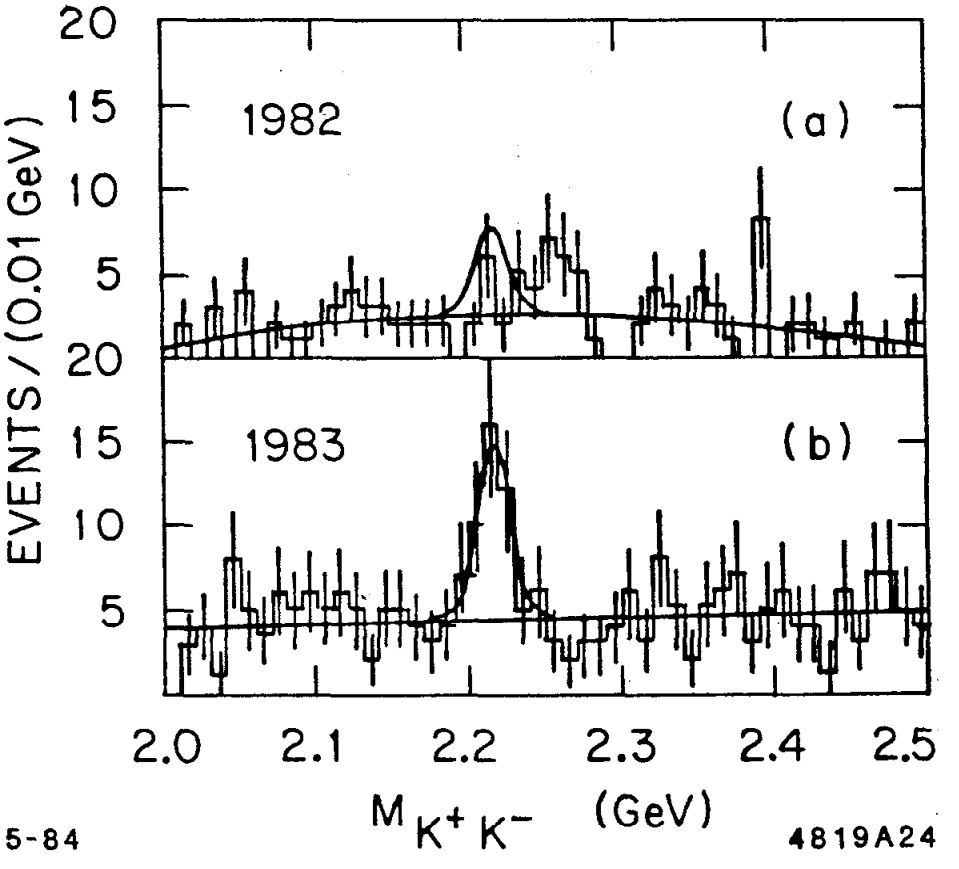

Figure 6.18. A comparison between the 1982 data and the 1983 data. The 1982 data is overplotted with the 1983 predicted results. The vertical scales were forced to be identical.

1. The discrepancy results from largely systematic effects. The $\xi(2220)$ signal is present in both 1982 and 1983, and there is a mass shift between the two data samples which is caused by systematic measurement errors in the 1982 data.

2. The discrepancy results from largely statistical effects.

   (a) The $\xi(2220)$ signal is insignificant in 1982. There is a statistical fluctuation in the background which is mis-interpreted as a signal, and the 1983 results are a good approximation to the 'true' $\xi(2220)$ parameters.

   (b) The $\xi(2220)$ signal is broader than the 1983 sample would indicate. The 'true' $\xi(2220)$ parameters lie somewhere between the 1982 and the 1983 values, and both samples reflect statistical fluctuations.

3. There is no signal in either data sample, just two independent and alarmingly similar statistical fluctuations.

The first two scenarios will be discussed in more detail below; the third is regarded as insufficiently likely to justify further discussion.

Systematic Scenario

The data collected in 1982 was the first physics data sample obtained and there were many potential problems which could contribute to a systematic error in the mass measurement. Numerous attempts were made to find quantities which were correlated in some way with the K^+K^- mass in either 1982 or 1983. The statistics available for conducting such a search is very limited, but no significant correlation was found. In the absence of any obvious problem to fix, an attempt was made to fix potential problems. These problems were, for the most part, associated

with the drift chamber hardware and reconstruction software. The potential sources of drift chamber hardware problems were:

- Layer 1 did not have preamplifiers and was susceptible to time slewing due to relatively high discriminator thresholds.

- Layer 2 did not have preamplifiers or cross-talk compensation resistors. As a result, it was very inefficient and had very large slewing variations.

- The linear region of the time measurement did not cover the entire collection time. This produced somewhat suspicious time measurements at small and large times.

- The charge division system was in very poor condition. There were many dead or erratic channels.

A further list of potential reconstruction problems includes:

- Survey positions and time to distance constants interacted with the hardware problems with uncertain consequences.

- Charge division information was used with no corrections and incorrect measurement errors.

- The resolutions used for fitting the tracks were too small.

In order to try and eliminate these problems, it was decided to re-analyze the γK^+K^- channel in both 1982 and 1983. The goal was to put the two data sets on an equal footing by making the following changes:

- using new drift chamber T_0 constants derived by leading edge fitting to hadronic events

- using new survey constants with a more physically motivated set of wire locations
- using new time-to-distance conversion constants
- using the most recent version of the DCFIND drift chamber reconstruction package
- performing the track fits with Layer 1 and Layer 2 weighted down so that their contribution was very small.

The first four changes represent attempts to make the analysis of the two data samples consistent. The final change eliminates a possible source of systematic error but at significant cost in resolution. The result is that the $\psi \rightarrow \mu^+\mu^-$ momentum resolution changes from $\sigma_p = 45$ MeV to $\sigma_p = 70$ MeV. The Monte Carlo predicts that the raw mass resolution at the $\xi(2220)$ should change from $\sigma_m = 30$ MeV to $\sigma_m = 45$ MeV, but the kinematic fit resolution should only increase from $\sigma_m = 10$ MeV to $\sigma_m = 12$ MeV. In deriving the new drift chamber constants, various checks were performed using dimuon events. The only visible systematic was a small charge asymmetry in the measured momentum: $p_{\mu^+} - p_{\mu^-} \sim 10$ MeV.

The modified reconstruction procedure was applied to the small subset of events which had passed a loose initial event selection. This selection required one track to have a kaon weight > 0.05 and a 4-C kinematic fit to either $\psi \rightarrow \gamma K^+K^-$ or $\psi \rightarrow \gamma\gamma K^+K^-$ with $\chi^2 < 50$. It can be argued that this loose event selection is already biased. This seems unlikely to be a serious problem, and a further consideration is that without this initial selection, the number of events requiring reconstruction is prohibitively large. The two new samples will be labeled 82RF and 83RF (RF for Re-Fit) for future reference. It is worthwhile to try to compare these different samples in an equitable fashion. This is done by making a list of

events in the original samples and histogramming their corresponding masses in the re-fit samples. This is an imperfect method because some of the original events fail to appear in the re-fit sample - they fail the kinematic fit requirement. The results of this method of comparison are shown in Fig. 6.19 and Fig. 6.20. It is apparent that, in the RF sample, the background level is higher and the resolution is somewhat worse than for the standard reconstruction. This is expected, since the drift chamber resolution is substantially poorer when Layer 1 and 2 are ignored. The structure visible in 1982 is broader than before, although this could be caused by the presence of additional background events. These figures give the impression that a mass shift may have occurred. However, if one looks at the event by event mass difference: $m - m_{RF}$ for the events in the signal regions, the result is that the means are shifted from zero by at most 1 MeV. The conclusion which is drawn from this re-fitting procedure is that there is *no* evidence for a systematic error introduced by any obvious problem in the drift chamber.

Even though it has not proved possible to alter the mass by reconstructing the data using a different procedure, one can still ask the hypothetical question: is it possible to have made systematic measurement errors which could shift the mass scale by 30 MeV ?? The answer to this question, discussed in the section on the $\xi(2220)$ mass measurement, appears to be *no*. It is difficult to produce a mass scale error of more than 10 MeV after the kinematic-fitting procedure. This can be checked in a more empirical manner by comparing the measured masses for narrow states observed in the two data samples. In all cases which are not limited by statistics (*e.g.*, $K_s, \eta, \eta', \omega, \phi$), the masses after kinematic fitting are correct within 1 MeV and agree between 1982 and 1983. A further check can be made using the ψ itself. The mode $\psi \rightarrow \mu^+\mu^-$ was used in determining the mass scale and is not an independent check. The mode $\psi \rightarrow p\bar{p}$ has been checked for the two data samples

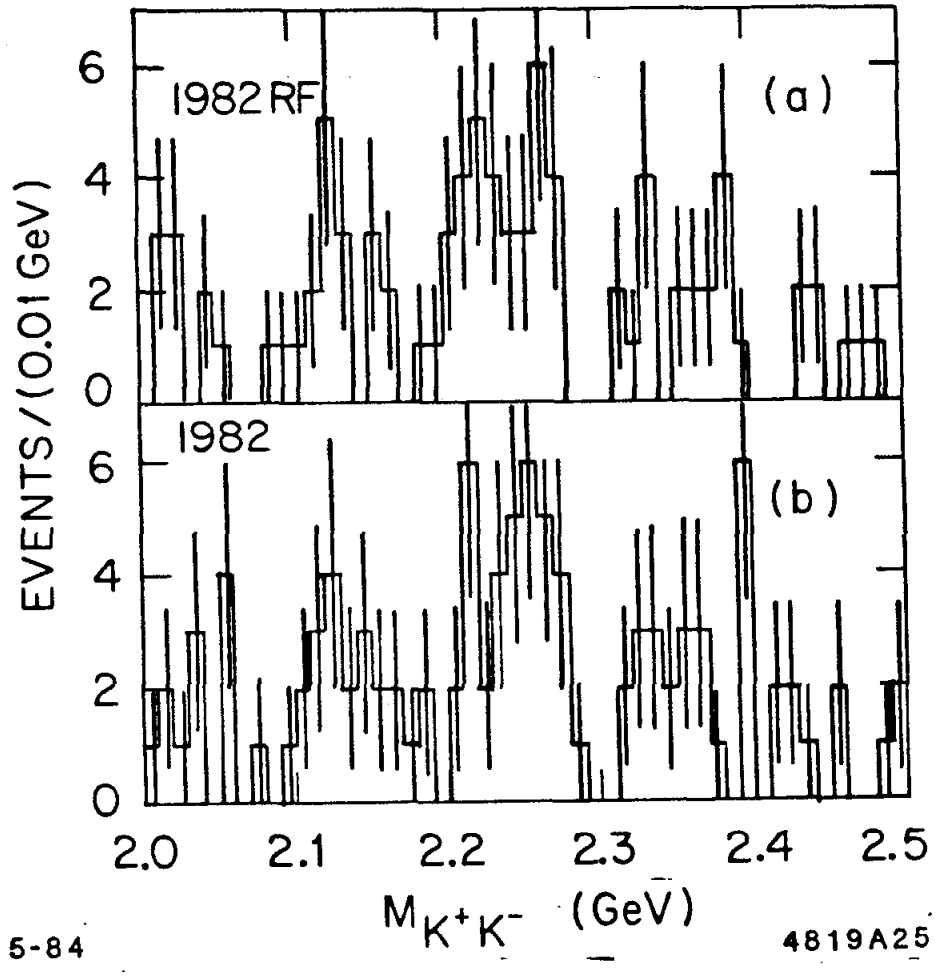

Figure 6.19. A comparison between the 1982 data and the 82RF data. The RF events were required to be a sub-set of those found in the original data sample.

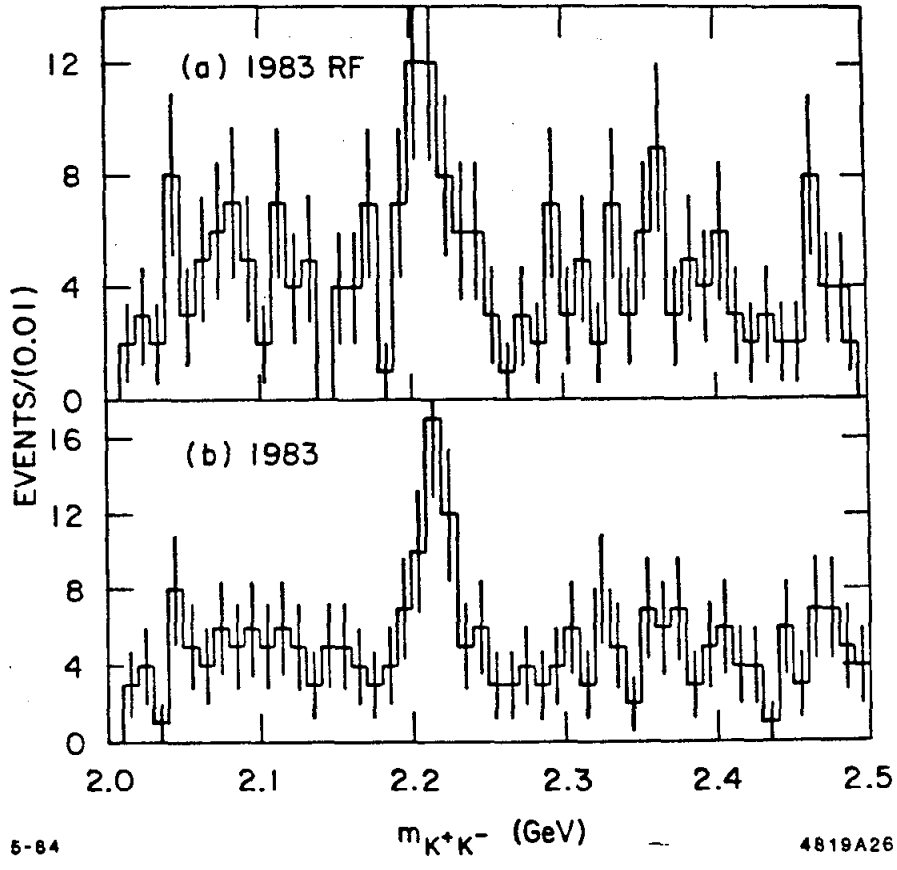

Figure 6.20. A comparison between the 1983 data and the 83RF data. The RF events were required to be a sub-set of those found in the original data sample.

by calculating a mass using the measured momenta. The result is that the mass of the ψ is the same, within statistical errors, for the two samples and it is correct to 5 MeV.

The conclusion which is forced on the innocent observer is that it is very implausible that there could be a mass scale error in 1982 which is sufficient to explain the 1982/1983 difference.

Statistical Scenario

If it is assumed that systematic errors in the measured quantities are not important, the problem becomes purely statistical. There are several different questions which could be asked and answered. One point of view is embodied in the question: how likely is it that the 1982 data should appear as it does ?? This assumes that the 1983 data is essentially correct and may be used as a parent distribution with which to test the 1982 data. A second point of view is embodied in the question: how likely is it that the $\xi(2220)$ is seen in both 1982 and 1983 with an intermediate set of parameters ?? This assumes that neither set of data is totally correct and attempts to assess the probability of this situation.

Statistical View # 1: In examining the first point of view, two approaches will be taken. One uses the traditional maximum likelihood technique to investigate the relative probability of different configurations. The other uses Monte Carlo simulation and sampling to directly model the fluctuations in the problem. Two different hypotheses will be compared for the 1982 data, using the maximum likelihood technique. One hypothesis is that the 1982 data is a large and independent sample, and it should be allowed to determine an independent mass and width for the $\xi(2220)$. This corresponds to the fit shown in Fig. 6.17. A second hypothesis is that the 1982 data is not significant enough to provide an independent

measurement of the mass and width. This corresponds to the fit shown in Fig. 6.18. The relative probability for these two hypotheses is a measure of the agreement of the 1982 and the 1983 data, since the second hypothesis is a prediction for the expected 1982 signal based on the observed 1983 signal. The relative likelihood for these two fits indicates that the second hypothesis has a relative probability of $\sim 1\%$ when compared to the first. This low probability has two sources: there is too little signal in the peak region, and there is too much background outside the peak. One could consider only the first source as being relevant to evaluating the probability. This corresponds to the question: how likely is it that there is no significant signal in the 1982 data ?? The answer is that this should happen $\sim 5\%$ of the time. This is in contrast to the value of $\sim 1\%$ which is obtained by considering both sources. It is not completely obvious which of these relative probabilities is the correct one to use. These considerations lead to the statement that the probability of the observed disagreement between two experiments measuring the same underlying phenomenon is probably $\sim 1 - 5\%$.

A random sampling technique provides a very different approach to the problem. The idea is to use a large representative parent distribution and select sub-samples which are the same size as the 1982 event sample. By studying many such sub-samples, an understanding of the expected fluctuations may be gained. Two different parent distributions are used: the 1983 data, and a Monte Carlo sample which has a mixture of $\xi(2220)$ signal events and $K^{*\pm}K^{\mp}$ background events. Neither one of these parent distributions is ideal. The 1983 sample is not much larger than the 1982 sample, and may itself be a large statistical fluctuation from the 'true' situation. The Monte Carlo data was arranged to look similar to the 1983 data sample, and may embody its own biases.

The results obtained from generating 50 independent random sub-samples

of the 1983 data are shown in Fig. 6.21. These histograms summarize the fit results from the 50 experiments. One concludes that the mass and width are unlikely to fluctuate very much, whereas the area of the signal varies tremendously. Some extreme examples of sub-samples are shown in Fig. 6.22. The implication of this study is that there is a $5-10\%$ chance of the signal fluctuating to an insignificant level in the 1982 data. There are no examples of a background fluctuation taking the place of the signal and thereby shifting the fitted mass.

The results obtained from using a large Monte Carlo parent distribution are similar. Once again, 50 random sub-samples were generated and fit. The one peculiar feature is that the Monte Carlo data has a more diverse spectrum of fluctuations; it is more likely for the sampled signal to bear a poor resemblance to the Monte Carlo parent distribution than was the case for samples drawn from the 1983 parent distribution. It is unclear whether this reflects the smaller size of the 1983 parent, or some subtle essence which is only present in real data. There was a single case in which an apparent mass shift occurred, but it involved a 'signal' which was much smaller than that observed in the 1982 data. The general conclusion from the sampling studies is about the same as for the more analytic statistical approach. It would appear that, assuming the 1983 data is correct, the probability of seeing the combination of signals observed in 1982 and 1983 is $\sim 1\%$, although the probability of seeing an insignificant signal in 1982 is $\sim 5-10\%$.

Statistical View #2: This question is somewhat more difficult to investigate because the 'true' properties of the $\xi(2220)$ are not known. One can postulate a plausible set of 'true' properties by moving the measured parameters within their errors. The 1983 data does not allow the mass to move by more than about $5-10$ MeV, which is too small to reconcile the 1982 and 1983 data. The width has larger errors, and a possible scenario is to move the width up by 2σ to 30 MeV in 1983.

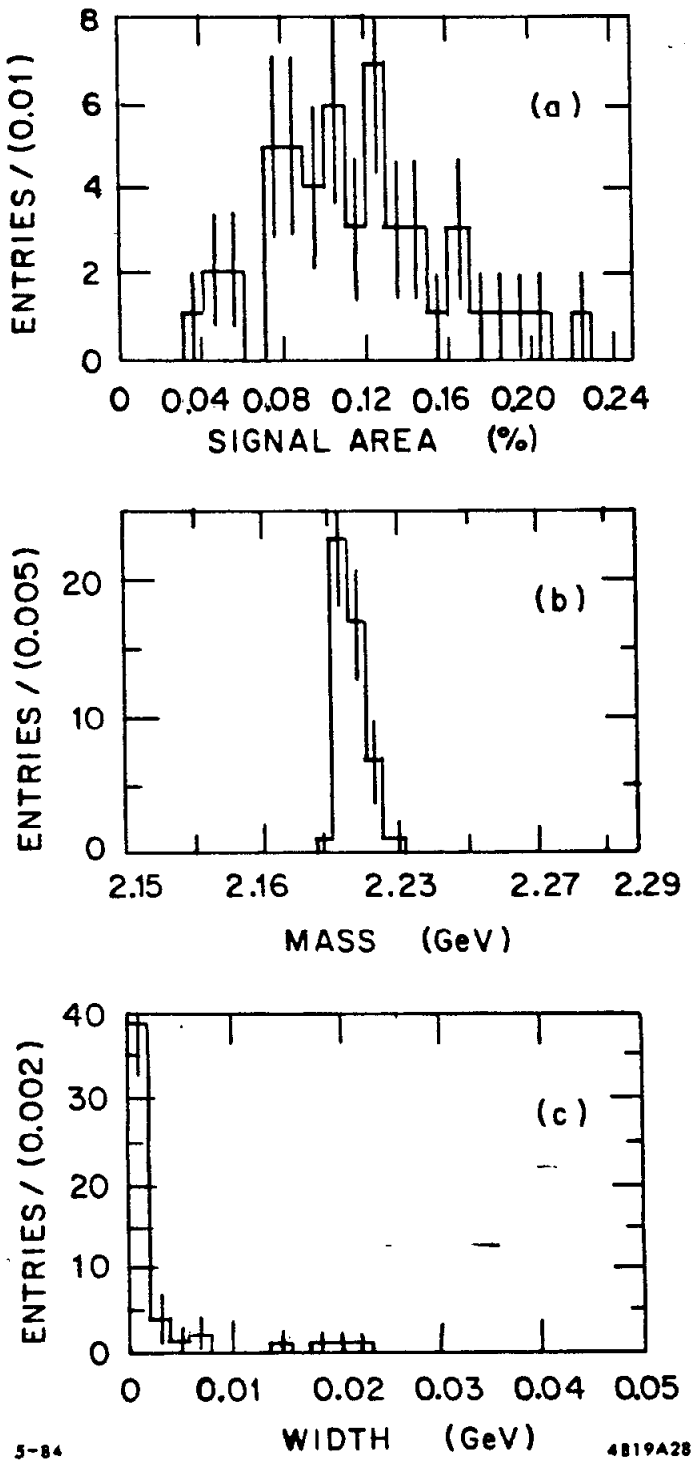

Figure 6.21. Results of sampling experiments using the 1983 data. The experiments contained the same number of events as were observed in the 1982 data.

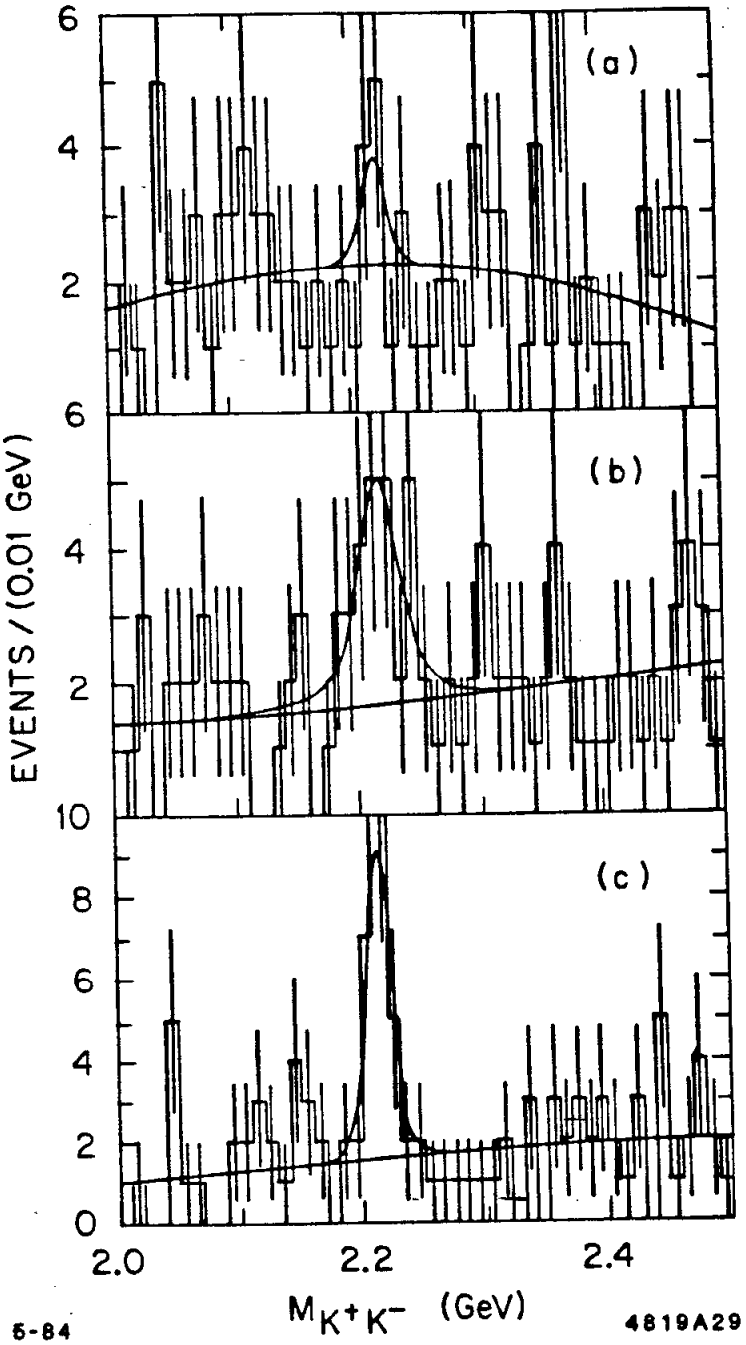

Figure 6.22. Examples of extremes from the sampling experiments. The distributions shown are: (a) the smallest area, (b) the largest width, (c) the 'cleanest'.

Then one can ask how likely it is for the 1982 and 1983 data to agree with this set of parameters. The fits displayed in Fig. 6.23 represent an attempt to devise an intermediate set of parameters for the $\xi(2220)$. The values for the mass and width were fixed to be: $m = 2.230$ GeV and $\Gamma = 0.030$ GeV, and the remaining parameters in the fit were allowed to vary. The probability of the $\xi(2220)$ having these parameters and manifesting itself in the manner observed in 1982 and 1983 is estimated from the relative likelihoods for the different fits. This estimate gives a probability of $\sim 0.5\%$. This small value corresponds to the low probability for the 1983 data to have the mass and width assumed here. Other intermediate sets of parameters may be constructed; none of them have a probability greater than about $\sim 1\%$.

Summary of Problems

There is no appealing solution to the dilemma. For one trained to believe in a rational and orderly universe, the most appealing solution remains the systematic scenario. Nonetheless, in the absence of explicit evidence for systematic problems, a statistical source, however unlikely, must be assumed. This provides the operational conclusion that the two data samples must be combined. The previous sections enclosed the results which are obtained in this manner in boxes. These are to be treated as the correct results for discussion. If a statistical scenario is assumed, then the probability of observing the combination of signals seen in 1982 and 1983 is estimated to be in the range of $\sim 1 - 5\%$, depending on the assumptions made.

6.6 SUMMARY

Evidence for a remarkable high mass object has been observed in the K^+K^- channel. The statistical significance of the signal is $\sim 5\sigma$, but there are unresolved inconsistencies in the appearance of the two available data samples. The properties

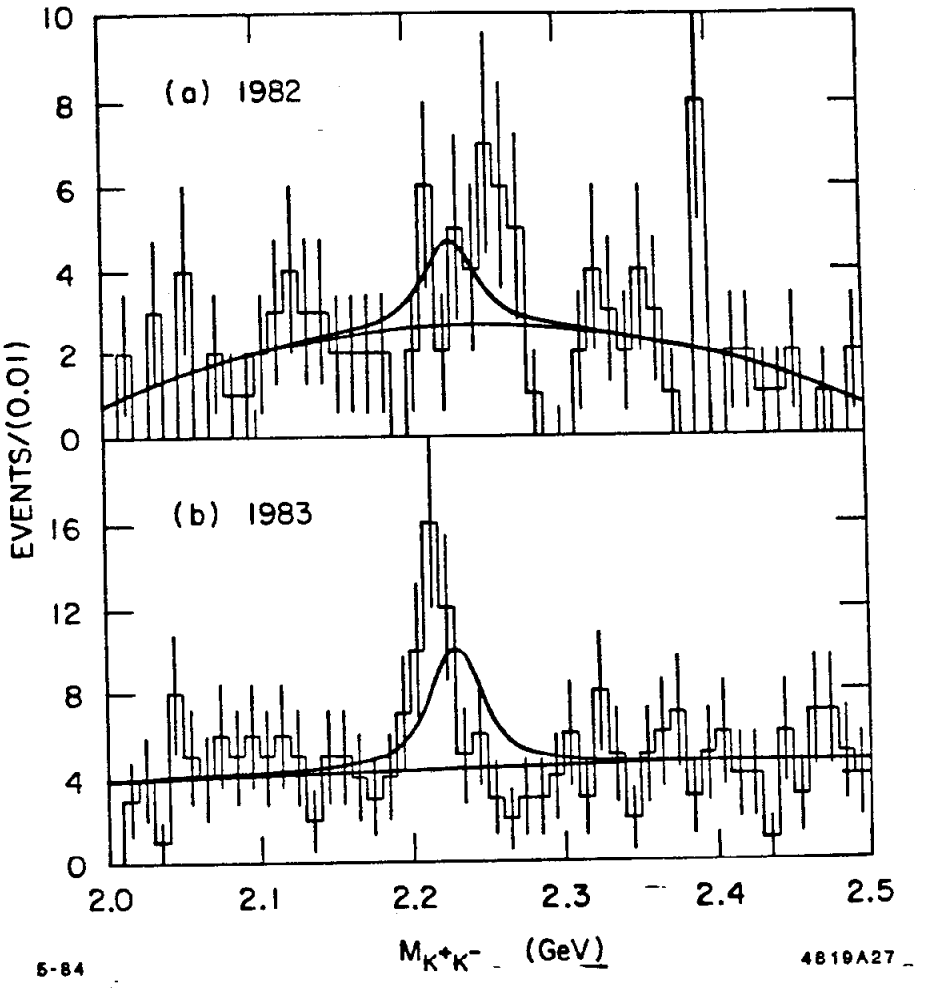

Figure 6.23. An intermediate set of $\xi(2220)$ parameters. They were chosen to interpolate between the 1982 and the 1983 data samples.

of this state, designated the $\xi(2220)$, are measured to be:

$$m = 2.218 \pm 0.003 \pm 0.010 \text{ GeV}$$

$$\Gamma \leq 0.040 \text{ GeV } 95\% \text{ C.L.}$$

$$\text{BR}(\psi \to \gamma\xi(2220))\text{BR}(\xi(2220) \to \text{K}^+\text{K}^-) = (5.7 \pm 1.9 \pm 1.4) \times 10^{-5}$$

Chapter 7. The $\psi \to \gamma K_S K_S$ Final State

7.1 Event Selection

The $K_S K_S$ event selection proceeds from a slightly different perspective than the K^+K^-. One advantage is that there is intrinsically less background because the $K_S K_S$ system can only exist in a $C = +$ eigenstate. Recall that (ignoring CP violation):

$$K^0 = \frac{K_S + K_L}{\sqrt{2}} \quad , \quad \bar{K}^0 = \frac{K_S - K_L}{\sqrt{2}},$$

and the C eigenstates may be written immediately, independent of a choice for the phase convention, as:

$$C = + \; : \quad \frac{K^0\bar{K}^0 + \bar{K}^0 K^0}{\sqrt{2}} = \frac{K_S K_S - K_L K_L}{\sqrt{2}},$$

$$C = - \; : \quad \frac{K^0\bar{K}^0 - \bar{K}^0 K^0}{\sqrt{2}} = \frac{K_L K_S - K_S K_L}{\sqrt{2}}.$$

This means that the processes: $\psi \to K_S K_S$ and $\psi \to K_S K_S \pi^0$ are forbidden by C parity. These backgrounds, which are so important for the K^+K^- analysis, should not trouble the $K_S K_S$ analysis. One can concentrate on getting a clean sample of $K_S K_S$ events without worrying very much about photons and backgrounds. The major background will be $\psi \to \gamma\rho^0\rho^0$, which can be dealt with by making K_S selection cuts. A disadvantage is that the expected signal is much smaller. Assuming that the interesting states are isoscalars, and have the same decay rate to $K^0\bar{K}^0$ and to K^+K^-, one expects the following relative observed rate:

$$\left[\frac{1}{2}\ for\ \frac{K_S K_S}{K^0\bar{K}^0}\right]\left[\frac{2}{3}\ for\ K_S \to \pi^+\pi^-\right]^2\left[\frac{2}{3}\ for\ \frac{\epsilon_{K_S K_S}}{\epsilon_{K^+K^-}}\right] = \frac{4}{27} \sim 0.15.$$

The combined 1982 and 1983 data samples have been used in order to maximize the extremely meager number of candidate events.

The selection process for identifying K_S candidates is partly kinematic and partly geometric, focussing on the two significant properties of the K_S: its mass and its lifetime. Pairs of oppositely charged tracks are selected and their intersection is found in the $(x-y)$ plane. The tracks may cross twice, in which case the intersection closest to the interaction region is used. The tracks may not cross at all, provided that they graze each other. In this case the intersection point is defined to lie along their distance of closest approach. This intersection point is used as a secondary vertex estimate and it must lie in the interval 0.1 cm $\leq r_{xy} \leq$ 20 cm, where r_{xy} is the separation of the secondary vertex from the primary vertex in the $(x-y)$ plane. Once there is an estimate for the secondary vertex, the resolution can be improved slightly by evaluating the pion track parameters at the secondary vertex rather than at the distance of closest approach to the primary vertex.* The angle between the vertex vector and the $\pi^+\pi^-$ momentum vector is calculated. The projection of this angle in the $(x-y)$ plane, called $\cos\theta_V$ for future reference, is a very powerful tool for isolating K_S candidates. It relies on the excellent angular resolution available in the $(x-y)$ plane. For a true secondary vertex, the vertex must lie along the K_S momentum vector. For a random background, there should be no strong correlation between these quantities.

The best two K_S candidates in the event (those closest to the K^0 mass) are chosen for further study. A mass cut on the pion pair mass is made, requiring 0.45 GeV $\leq m_{\pi^+\pi^-} \leq$ 0.55 GeV. In addition, both K_S candidates are required to have $\cos\theta_V \geq 0.98$. These cuts produce the very clean distribution shown in Fig. 7.1(a). The Gaussian fit has:

$$m_{\pi^+\pi^-} = 497.3 \pm 0.4 \text{ MeV} \quad , \quad \sigma = 6.5 \pm 0.4 \text{ MeV}.$$

* This primarily corrects for the curvature of the track in the $(x-y)$ plane due to the magnetic field.

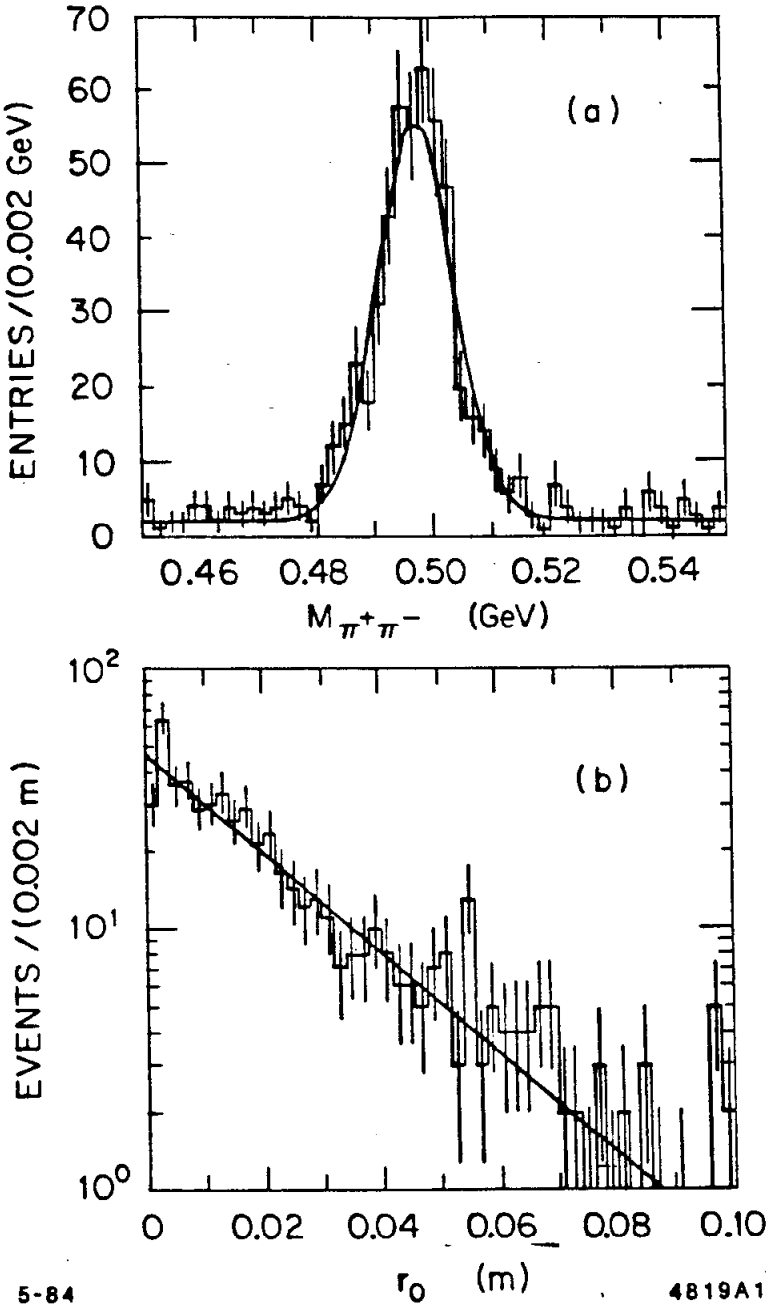

Figure 7.1. Mass and vertex distributions after K_S cuts. (a) is the $\pi^+\pi^-$ mass distribution. (b) is the proper vertex distribution for the K_S candidates. This quantity is measured in the $(x-y)$ projection, and corrected for the momentum and angle of the decaying K_S. The horizontal axis is in units of meters. There are two entries in these histograms per event, both have a vertex angle cut: $\cos\theta_V \geq 0.98$.

The momenta for the pion tracks used in this calculation have been corrected for the dE/dx losses expected when they traverse the detector.

The additional property expected of the K_S is an observable lifetime. Figure 7.1(b) shows the proper decay length for the K_S candidates. This is calculated by using the separation between the secondary vertex and the primary vertex in the $(x-y)$ plane, r_{xy}, as well as the $\pi^+\pi^-$ momentum in the $(x-y)$ plane, P_{xy}. The quantity calculated is:

$$r_0 = \frac{r_{xy}}{(\beta\gamma)_{xy}} = \frac{r_{xy} m_{K^0}}{P_{xy}},$$

which has the advantage of measuring the true three dimensional proper decay length by using only well-measured quantities in the $(x-y)$ plane. It has an additional advantage due to the shape of the interaction region at SPEAR. This region is very small in the $(x-y)$ plane: $\sigma_x \sim 0.5$ mm , $\sigma_y \sim 0.05$ mm, but is quite large in the z direction: $\sigma_z \sim 25$ mm. This means that the variation of the vertex position in the $(x-y)$ plane is negligible, whereas for the z direction it is not. The measured slope of the r_0 distribution is:

$$r_0 = 2.3 \pm 0.2 \text{ cm}.$$

The correct experimental value is 2.675 ± 0.007 cm. The difference is due to acceptance corrections, which are slightly momentum dependent, and agrees well with the Monte Carlo value of $2.2 \pm .1$ cm. The conclusion is that there is unambiguous evidence for the presence of K_S's.

Up to this point, no kinematic fitting has been done, nor have there been any cuts on the radiative photon which is, presumably, in the event. The resolution expected for $\xi(2220) \rightarrow K_S K_S$ is $\sigma \sim 25$ MeV without using a kinematic fit and $\sigma \sim 10$ MeV with a kinematic fit. This improvement in resolution indicates that

kinematic fitting is very desirable. The presence of secondary vertices in the event causes some complications for the kinematic fitting. A large number of choices for action are available, and a simple technique was chosen. The measured drift chamber quantities are transformed to the estimated location of the secondary vertex, as described previously, before use in the kinematic fit. This should be a better approximation than using the values at the distance of closest approach to the interaction region. A 4-C kinematic fit to the hypothesis $\psi \rightarrow \gamma\pi^+\pi^-\pi^+\pi^-$ was performed using the highest energy photon in the event. A cut is made requiring that the confidence level for the kinematic fit, P_{χ^2}, is ≥ 0.02. The $\pi^+\pi^-$ mass distribution after this cut is shown in Fig. 7.2(a) and has been fit to a Gaussian with the parameters:

$$m = 497.1 \pm 0.2 \text{ MeV} \quad , \quad \sigma = 4.5 \pm 0.2 \text{ MeV}.$$

This mass distribution looks narrower than the distribution for the $\pi^+\pi^-$ mass before the kinematic fit and agrees very well with the expected K_S mass. The corresponding scatter plot, containing the evidence for K_SK_S, is shown in Fig. 7.2(b). It would appear that there is a clean K_SK_S signal with virtually no background. Because of the absence of the forbidden transitions: $\psi \rightarrow K_SK_S$ and $\psi \rightarrow \gamma\gamma K_SK_S$, these events should all be due to the radiative transition $\psi \rightarrow \gamma K_SK_S$.

7.2 THE RESULTS FOR $\psi \rightarrow \gamma K_S K_S$

Evidence has just been presented for a clean sample of $\psi \rightarrow \gamma K_SK_S$ events. This analysis has been performed in two ways, one with a kinematic fit and one without. This allows a check on the additional complication of constrained fitting in events with secondary vertices. For the analysis which did not use a kinematic fit, a $p^2_{t_\gamma}$ cut was substituted in its place. If the requirement is made that $p^2_{t_\gamma} \leq 0.002$,

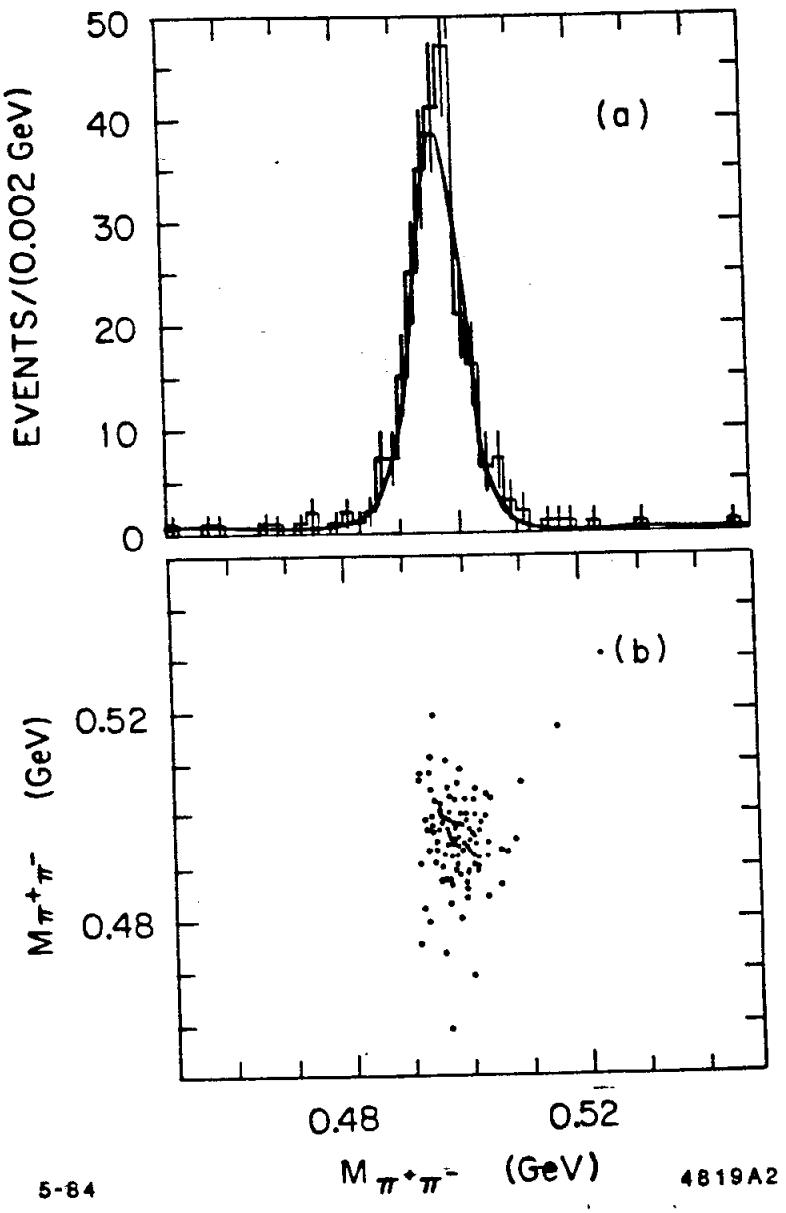

Figure 7.2. The mass distributions after kinematic fitting. (a) shows the $\pi^+\pi^-$ mass distribution. There are two entries per event. (b) shows a scatter plot of one $\pi^+\pi^-$ mass versus the other. A confidence level cut has been made at $P_{\chi^2} \geq 0.02$.

then the resulting mass distribution is shown in Fig. 7.3(a). If the $p^2_{l_\gamma}$ cut is replaced with a cut on the kinematic fit confidence level $P_{\chi^2} \geq 0.02$, then the resulting mass distribution is shown in Fig. 7.3(b). With the small number of events present it is difficult to find any significant differences. There is qualitative agreement between the $\psi \rightarrow \gamma K_S K_S$ final state and the $\psi \rightarrow \gamma K^+ K^-$ final state discussed previously. The important features are: a broad enhancement in the region of the $f'(1515)/\theta(1700)$, and an excess of events in the vicinity of the $\xi(2220)$. Figure 7.4 shows expanded plots of these two interesting regions. These spectra have been fit using the same procedure which was applied to the K^+K^- spectrum. Since the statistics are very meager, the actual fits do not allow all of the parameters to vary.

The fit to the $f'(1515)/\theta(1700)$ region was made with the masses and widths fixed to the values measured in the K^+K^- channel:

$$m_{f'} = 1.525 \quad \text{GeV} \quad , \quad \Gamma_{f'} = 0.085 \quad \text{GeV},$$

$$m_\theta = 1.720 \quad \text{GeV} \quad , \quad \Gamma_\theta = 0.130 \quad \text{GeV}.$$

These values are consistent with the $K_S K_S$ data, as shown by the fit in Fig. 7.4(a). In order to determine the branching ratios for these two states, a Monte Carlo efficiency has been calculated. The efficiency for this region does not suffer from the large acceptance effects observed in the K^+K^- channel. This is because the K_S efficiency does not depend strongly on the momentum of the K_S. This allows a global estimate of the efficiency for the $f'(1515)/\theta(1700)$ mass region. The result is:

$$\epsilon = 0.14 \pm 0.04,$$

where the Monte Carlo events were generated using a phase space decay model. The error on the efficiency includes estimates of the effects of the non-phase space

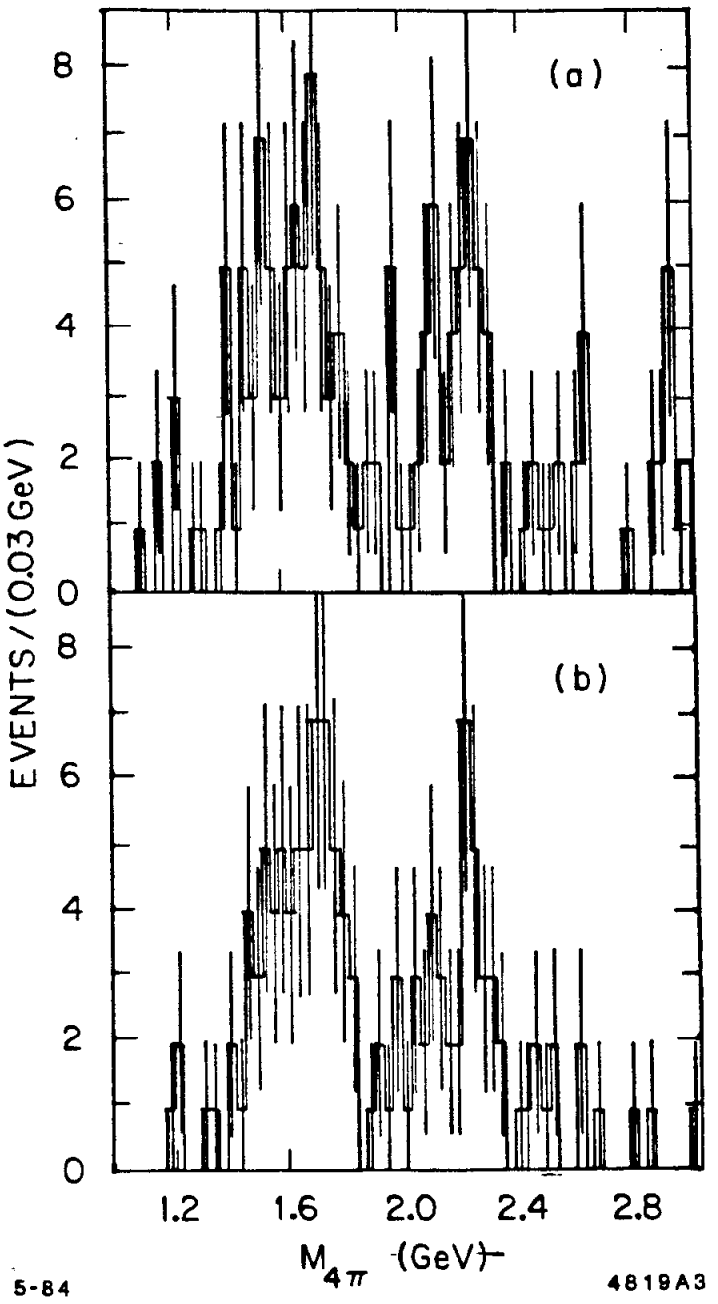

Figure 7.3. The $K_S K_S$ mass distribution. In (a) the events shown have $p^2_{t_\gamma} \leq 0.002$ and the mass is calculated using the measured momenta. In (b) the events shown have the kinematic fit $P_{\chi^2} \geq 0.02$ and the mass is calculated using the kinematically fit momenta.

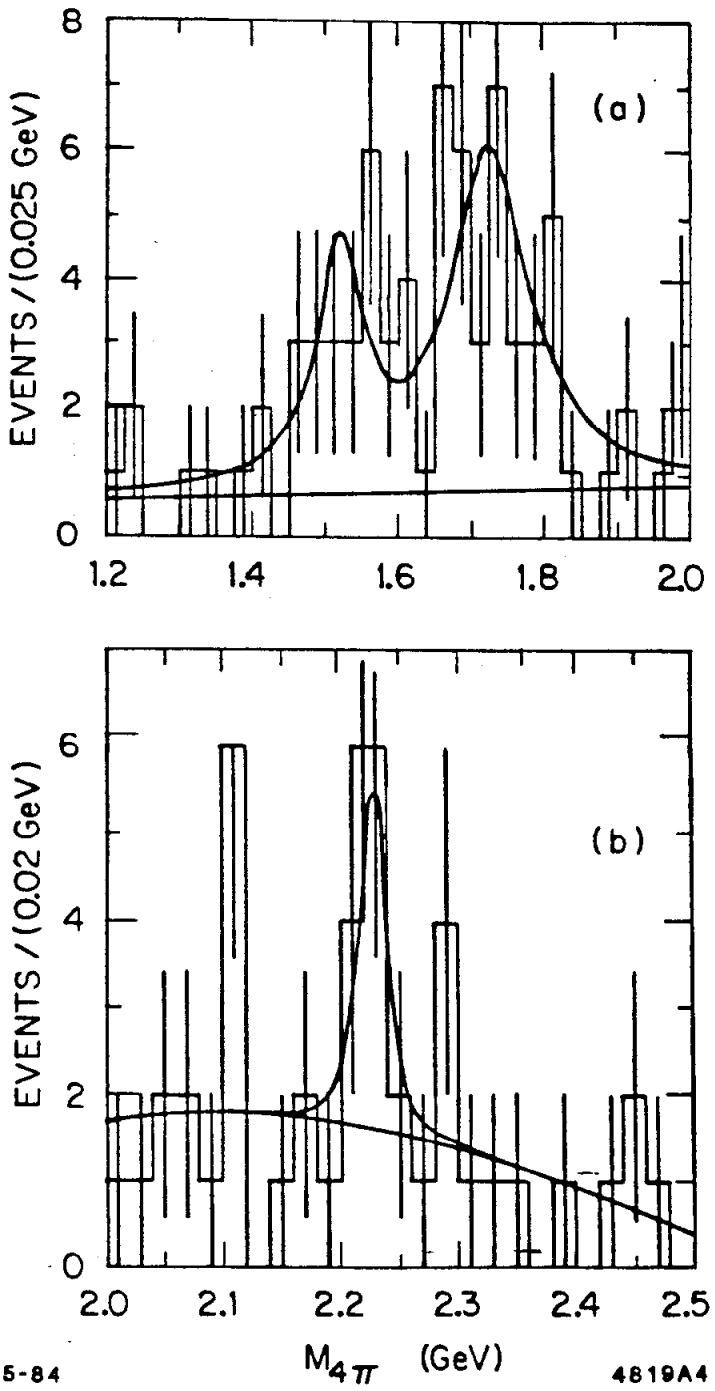

Figure 7.4. Expanded mass distributions for the $\psi \to \gamma K_S K_S$ final state. In (a) the $f'(1515)/\theta(1700)$ region is displayed. In (b) the $\xi(2220)$ region is displayed.

decays of the $f'(1515)/\theta(1700)$. This efficiency leads to the branching ratios:

$$BR(\psi \rightarrow \gamma f'(1515))BR(f'(1515) \rightarrow K^0\bar{K}^0) = (1.9 \pm 0.7 \pm 0.5) \times 10^{-4},$$

$$BR(\psi \rightarrow \gamma\theta(1700))BR(\theta(1700) \rightarrow K^0\bar{K}^0) = (4.5 \pm 1.2 \pm 1.1) \times 10^{-4}.$$

These values are consistent with those observed in the K^+K^- channel.

Although the signals observed here are very feeble, it is still interesting to examine the production and decay angular distributions. The two angles which are most interesting are $\cos\theta_\gamma$ and $\cos\theta_K$. The absolute value of the $\cos\theta_K$ angle is displayed since the two decay particles are indistinguishable. Figure 7.5 shows these distributions for the $f'(1515)$ and the $\theta(1700)$ mass regions used in the K^+K^- spin-parity analysis. The results for $\cos\theta_K$ are consistent with those found in the K^+K^- channel—the $f'(1515)$ is strongly polarized in the center of mass and the $\theta(1700)$ is, perhaps, somewhat less polarized. The $\theta(1700)$ indicates a behavior which is not very consistent with the flat distribution expected for a $J = 0$ object.

The fit to the $\xi(2220)$ region is shown in Fig. 7.4(b). In this case, the fit includes the expected 10 MeV mass resolution in the form of a Gaussian resolution function. The resulting fit parameters are:

$$m = 2.228 \pm 0.008 \pm 0.015 \quad \text{GeV},$$

$$\Gamma = 0.012 \pm 0.040 \quad \text{GeV},$$

where the systematic error in the mass measurement represents possible mass scale errors. This fit is certainly consistent with the K^+K^- result, but the statistical significance is only $\sim 2\sigma$. A typical event contained in the $\xi(2220)$ peak is shown in Fig. 7.6. An expanded view of the inner detector is also shown, and it indicates the presence of secondary vertices.

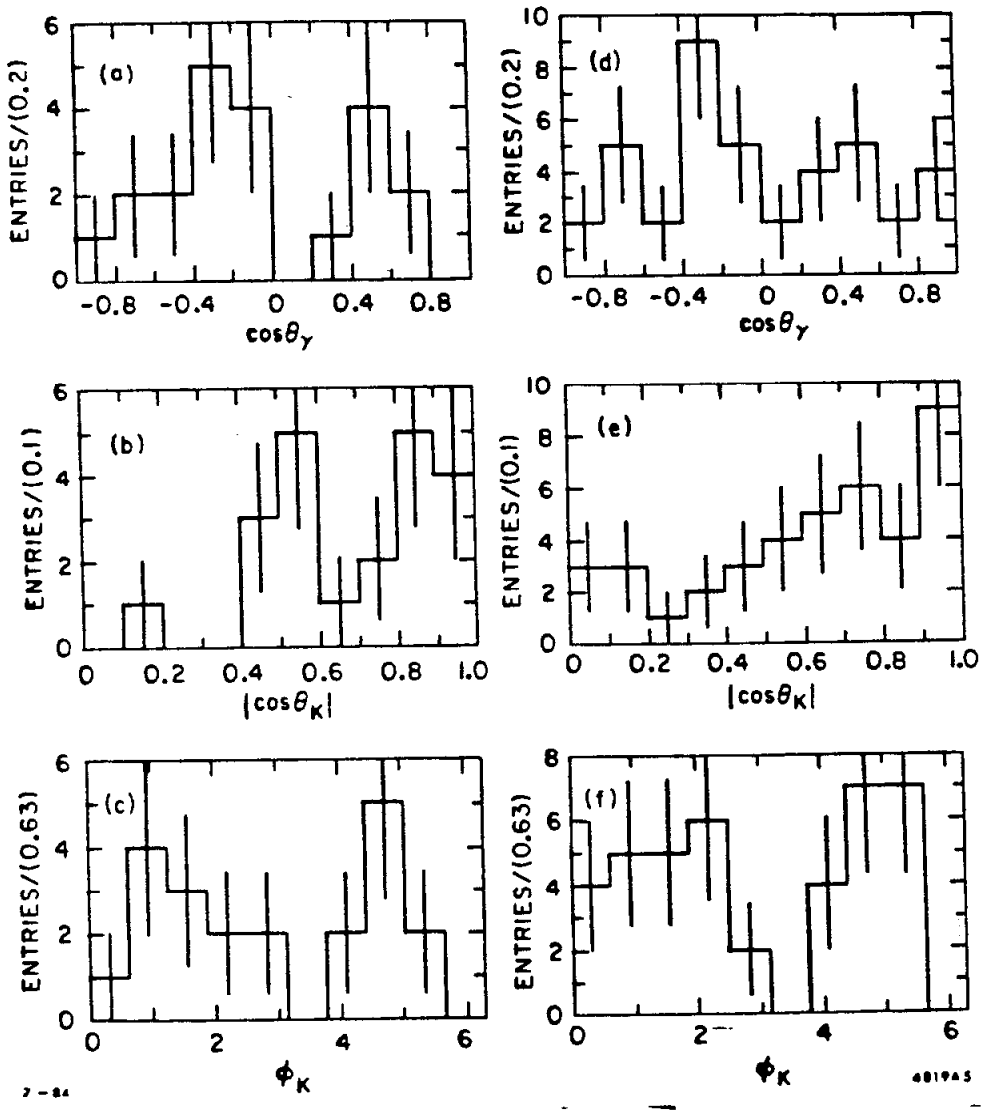

Figure 7.5. The K_SK_S angular distributions for $f'(1515)/\theta(1700)$. Plots (a), (b) and (c) are for the $f'(1515)$, defined to be $1.45 \leq m_{KK} \leq 1.60$ GeV. Plots (d), (e) and (f) are for the $\theta(1700)$, defined to be $1.60 \leq m_{KK} \leq 1.85$ GeV.

TRACK LIST

N	ID	P	E	ID WT
1	0	0.143	0.0	700
2	0	0.753	0.175	300
3	0	0.273	0.114	800
4	0	-1.107	0.233	100
5	1	0.0	0.553	

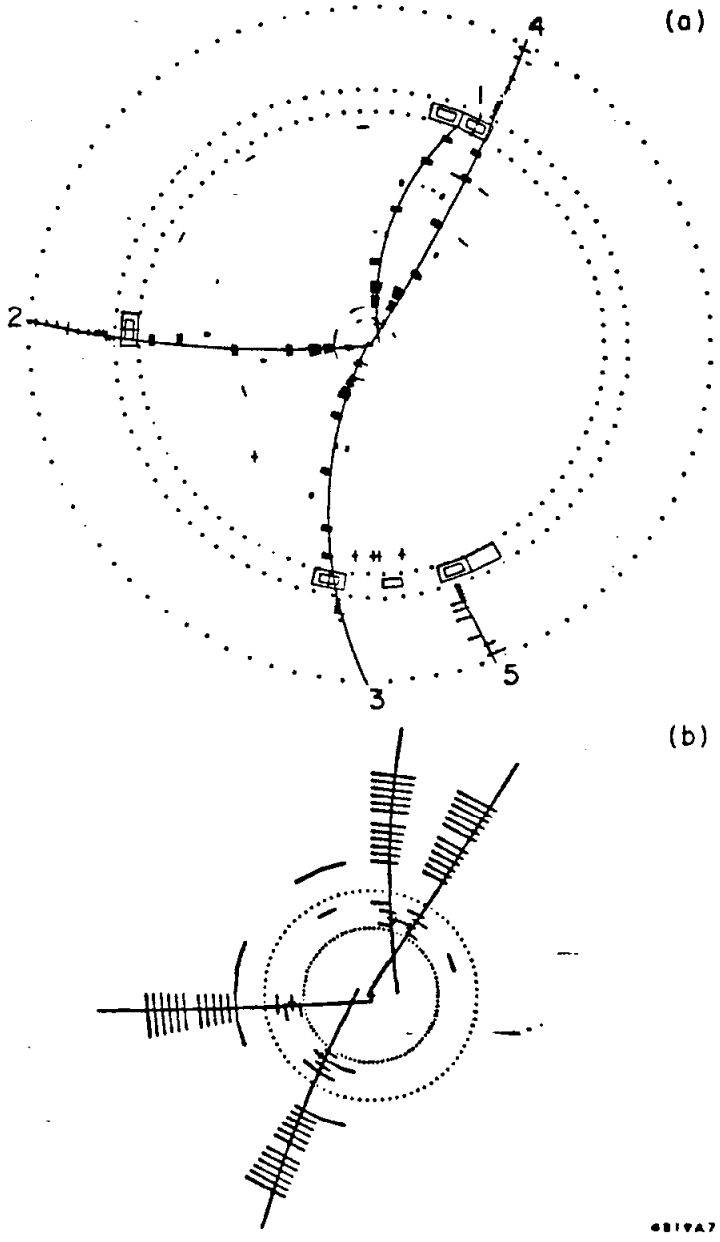

Figure 7.6. A typical $K_S K_S$ one-event display. The event has a mass of 2.266 GeV and has very well isolated secondary vertices for both K_S's.

The estimated efficiency in this mass region is:

$$\epsilon = 0.22 \pm 0.06.$$

Again, a phase space monte Carlo has been used to measure the efficiency. The fit curve in Fig. 7.4 corresponds to 7.3 events and provides the branching ratio:

$$\mathrm{BR}(\psi \to \gamma\xi(2220))\mathrm{BR}(\xi(2220) \to \mathrm{K^0\bar{K}^0}) = (5.6 \pm 2.8 \pm 1.4) \times 10^{-5}.$$

This result is consistent with the signal observed in $\mathrm{K^+K^-}$, although very unconvincing on its own. The angular distributions are plotted for the $\xi(2220)$ region in Fig. 7.7. The results are inconclusive, but consistent with the flat behavior in both $\cos\theta_\gamma$ and $\cos\theta_K$, as observed in the $\mathrm{K^+K^-}$ channel. Individuals possessing great imagination might argue that the distributions are closer to those expected for $J = 2$ than for $J = 0$. Unfortunately, this is not a statistically justifiable conclusion.

7.3 SUMMARY

The mode $\psi \to \gamma \mathrm{K_S K_S}$ has been observed and there is qualitative agreement with the higher statistics analysis of the $\mathrm{K^+K^-}$ channel. There is evidence for the three states which dominate the $\mathrm{K^+K^-}$ mass spectrum, namely, the f', θ and $\xi(2220)$. The observed angular distributions for these states are similar to those found in the $\mathrm{K^+K^-}$ channel. This evidence is consistent with, and hence supports, the $\mathrm{K^+K^-}$ results, although it is rather unconvincing on its own.

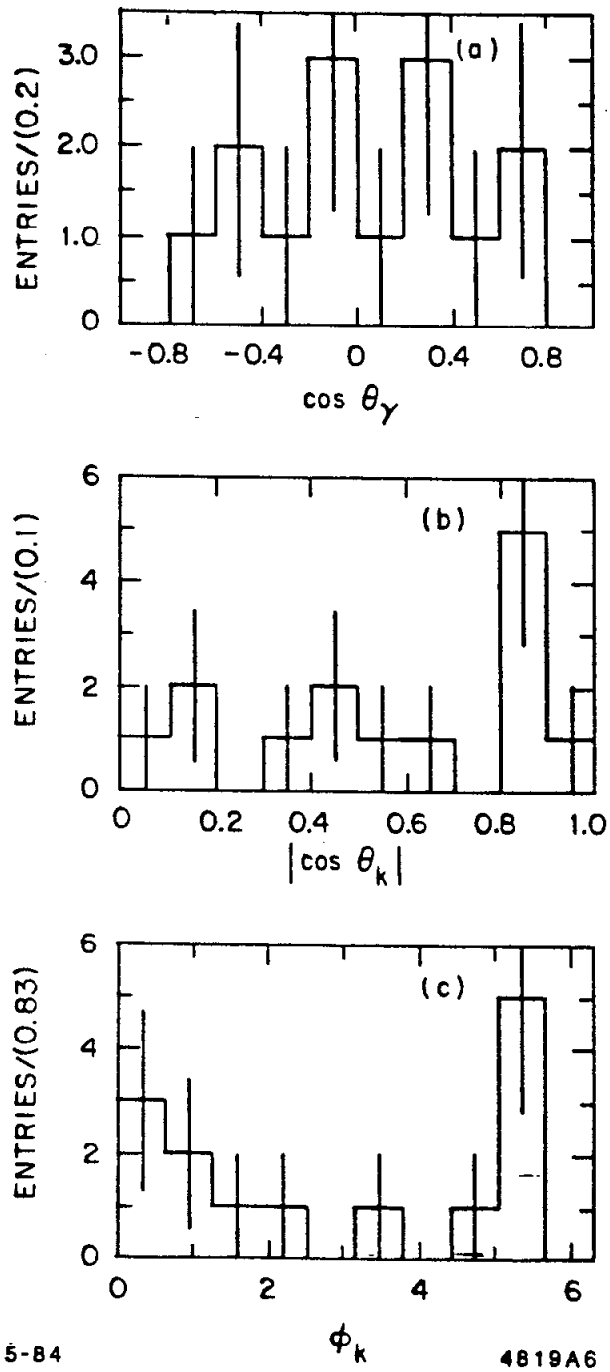

Figure 7.7. The $K_S K_S$ angular distributions for the $\xi(2220)$ region. The $\xi(2220)$ region was defined to be $2.18 \leq m_{KK} \leq 2.28$ GeV.

Chapter 8. Limits on Other Decay Modes

8.1 Limits on Decays of the $\theta(1700)$

In previous experiments, the $\theta(1700)$ has been seen only in the $K\bar{K}$ and $\eta\eta$ decay modes. This is rather surprising for a state of this mass, and so it is interesting to look in other decay channels for evidence of this state. Three modes will be examined: $\rho\rho$, $K\bar{K}\pi$ and $K\bar{K}\pi\pi$. A fourth mode, $\psi \rightarrow \gamma\eta\eta'$, has been checked, but no indication of a signal was observed. Since no $\theta(1700)$ signals are observed, the results are presented as upper limits. The $\theta(1700)$ parameters have been fixed at their values for the K^+K^- system:

$$m = 1.720 \text{ GeV} \quad , \quad \Gamma = 0.130 \text{ GeV}.$$

The $\rho^0\rho^0$ Final State

This final state has been analyzed in great detail. A full spin-parity analysis of $\psi \rightarrow \gamma\pi^+\pi^-\pi^+\pi^-$ has been performed[42] to extract the contributions from different J^P. The analysis includes contributions from the following channels:

$$\rho\rho: \quad 0^+,\ 0^-,\ 1^+,\ 1^-,\ 2^+,\ 2^-, \text{ isotropic}$$

$$\rho\pi\pi,\ \pi A_2,\ 4\pi: \quad \text{isotropic}$$

The fractions for each channel are fitted using a maximum likelihood technique. The low mass enhancement observed by the MARK II experiment is seen to be dominantly $J^P = 0^-$. The contribution from the $J^P = 2^+$ $\rho\rho$ channel was extracted for the $\theta(1700)$ mass region, defined to be:

$$1.60 < m < 1.85 \text{ GeV}.$$

When the errors on the extracted fraction are included, the following limit is obtained:

$$BR(\psi \rightarrow \gamma\theta(1700))BR(\theta(1700) \rightarrow \rho^0\rho^0) < 2.0 \times 10^{-4} \quad 90\% \text{ C.L.}$$

The signal used to set the limit consists of events weighted by the $J^P = 2^+$ $\rho\rho$ fit fraction, and is shown in Fig. 8.1(a).

The $K\bar{K}\pi$ Final State

This final state has been examined in the $K_S K^{\pm}\pi^{\mp}$ channel. The events have been kinematically fit and the K_S was selected by using cuts on the secondary vertex. It is difficult to set a limit for the $\theta(1700)$ in this final state because of the presence of the very large $\iota(1440)$ signal, as shown in Fig. 8.1(b). The procedure which has been used is to fit a polynomial background plus a Breit-Wigner to the region above the $\iota(1440)$. The interval which has been used is: $1.6 - 2.0$ GeV. The resulting limit is:

$$BR(\psi \rightarrow \gamma\theta(1700))BR(\theta(1700) \rightarrow K\bar{K}\pi) < 2.5 \times 10^{-4} \quad 90\% \text{ C.L.}$$

This limit corresponds to a signal of 20 events.

The $K\bar{K}\pi\pi$ Final State

This final state has been examined in the $K^+K^-\pi^+\pi^-$ channel. The observed signal in this final state contains no indication of a $\theta(1700)$ peak, as is shown in Fig. 8.1(c). The K^*K^* threshold is at 1.78 GeV and the decay $\theta \rightarrow K^*K^*$ can proceed in an S wave, so there should be no great difficulty in producing a $\theta \rightarrow K^*K^*$ signal below threshold. Figure 8.1(c) shows no indication of such a threshold enhancement. The limit which is set is:

$$BR(\psi \rightarrow \gamma\theta(1700))BR(\theta(1700) \rightarrow K^+K^-\pi^+\pi^-) < 1.0 \times 10^{-4} \quad 90\% \text{ C.L.}$$

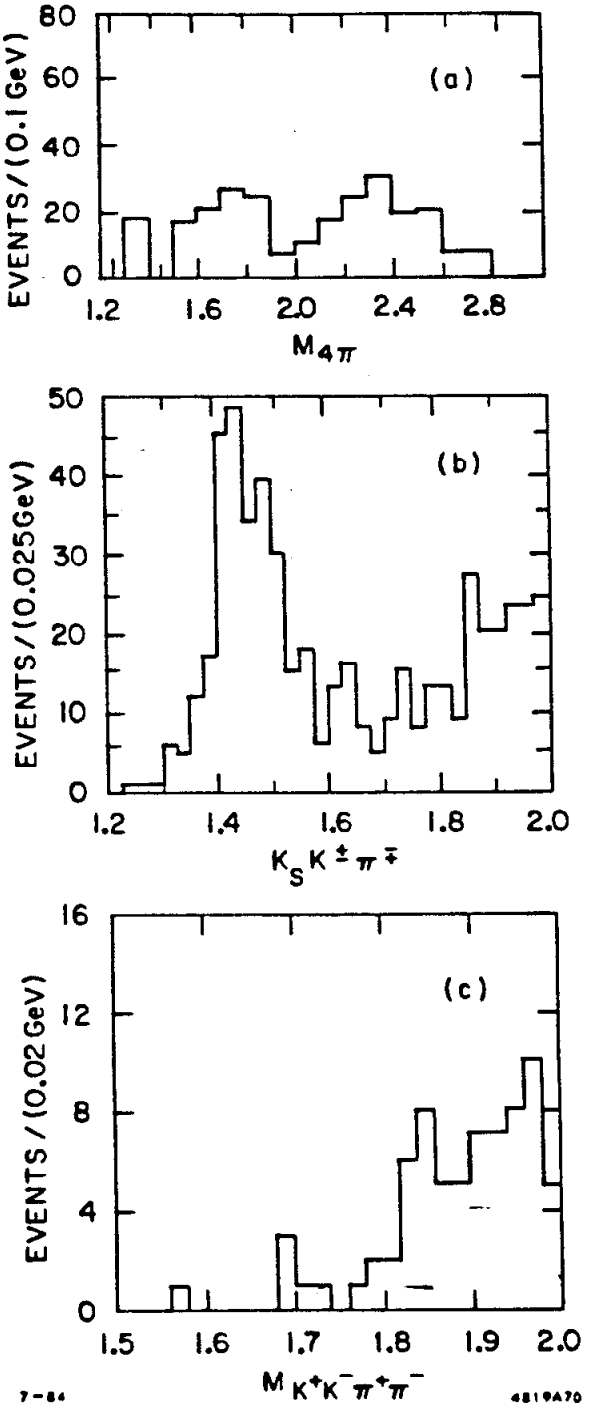

Figure 8.1. Limits on other $\theta(1700)$ decays. (a) shows the $J^P = 2^+$ $\rho^0\rho^0$ signal extracted from the full spin-parity analysis of the $\psi \to \gamma\pi^+\pi^-\pi^+\pi^-$ final state. (b) shows the mass distribution for the $K_S K^{\pm}\pi^{\mp}$ channel. (c) shows the mass distribution for the $K^+K^-\pi^+\pi^-$ channel.

This limit is calculated by taking all of the events in the 1.60 – 1.80 GeV region to be signal events, and then using Poisson statistics to get the 90% C.L. limit. There is no unique coupling of this final state to $I = 0$, so this limit cannot be converted to $K\bar{K}\pi\pi$ without assumptions. If this mode has the same isospin structure as the $K^*\bar{K}^*$ final state, then the Clebsch is 9/2, providing the upper limit:

$$BR(\psi \rightarrow \gamma\theta(1700))BR(\theta(1700) \rightarrow K\bar{K}\pi\pi) < 4.5 \times 10^{-4} \quad 90\% \text{ C.L.}$$

8.2 Limits on Decays of the $\xi(2220)$

The $\xi(2220)$ has been observed in the K^+K^- decay mode, with evidence appearing in the K_SK_S mode as well. It would be strange indeed if the $\xi(2220)$ is this massive and has no other detectable decay modes. In order to investigate this problem more systematically, searches have been made in other plausible final states. No signals have been seen, and the results of the searches are quoted as upper limits. The limits are set using the maximum likelihood technique. A fit was performed to a polynomial background plus a Breit-Wigner convoluted with a Gaussian resolution function. The resolution was fixed at the value determined by Monte Carlo simulation for each individual final state. The mass of the Breit-Wigner was fixed at $m = 2.218$ GeV, which is the value measured in $\psi \rightarrow \gamma K^+K^-$. The question of what value to use for the width is a delicate one. If a large width is used, the limits will be extremely weak. If a width of zero is used, the limits will be much more stringent, but incorrect for a real width greater than zero. For this reason, the width has been fixed at 15 MeV, corresponding to the 1σ upper limit found in the analysis of $\psi \rightarrow \gamma K^+K^-$.

Using these fixed values for the mass and width of the $\xi(2220)$, the 90% C.L. upper limits were set by evaluating the likelihood for different numbers of

observed events. A numerical integration was performed to find the number of events corresponding to the interval which contained 90% of the total probability. The background was allowed to vary during this integration. The assumption that $I = 0$ was used, when necessary, to make corrections for unobserved decay modes.

The $\mu^+\mu^-$ Final State

This measurement is presented in more detail elsewhere.[30] The events have been selected by requiring that the total number of hits in the muon system for the two muon candidates is three out of a possible of four. The number of photons was required to be exactly one and the events were kinematically fit. The expected mass resolution in this analysis is $\sigma_m = 10$ MeV. The expected QED background for the $\psi \rightarrow \gamma\mu^+\mu^-$ has been simulated using a calculation scheme suggested by R. Kleiss.[36] The result of this calculation is an absolute prediction for the rate into $\psi \rightarrow \gamma\mu^+\mu^-$ as a function of $m_{\mu\mu}$. The agreement between the calculation and the data is satisfactory, as shown in Fig. 8.2(a). Figure 8.2(b) shows the upper limit which has been placed on the $\xi(2220)$ in this final state. This limit is directly relevant to the Higgs interpretation, and so the width was fixed at zero, as expected for a Higgs boson. This is different than the procedure used for the other limits, and results in a somewhat more stringent limit than would be obtained using a width of 15 MeV. The limit is:

$$\mathrm{BR}(\psi \rightarrow \gamma\xi(2220))\mathrm{BR}(\xi(2220) \rightarrow \mu^+\mu^-) < 7.3 \times 10^{-6} \quad 90\%\ \mathrm{C.L.}$$

This corresponds to a limit on the ratio:

$$\frac{\mathrm{BR}(\xi \rightarrow \mu^+\mu^-)}{\mathrm{BR}(\xi \rightarrow s\bar{s})} < 6\% \left[\frac{\mathrm{BR}(\xi \rightarrow K\bar{K})}{\mathrm{BR}(\xi \rightarrow s\bar{s})}\right],$$

which should be compared to the naive expectation (which assumes the couplings

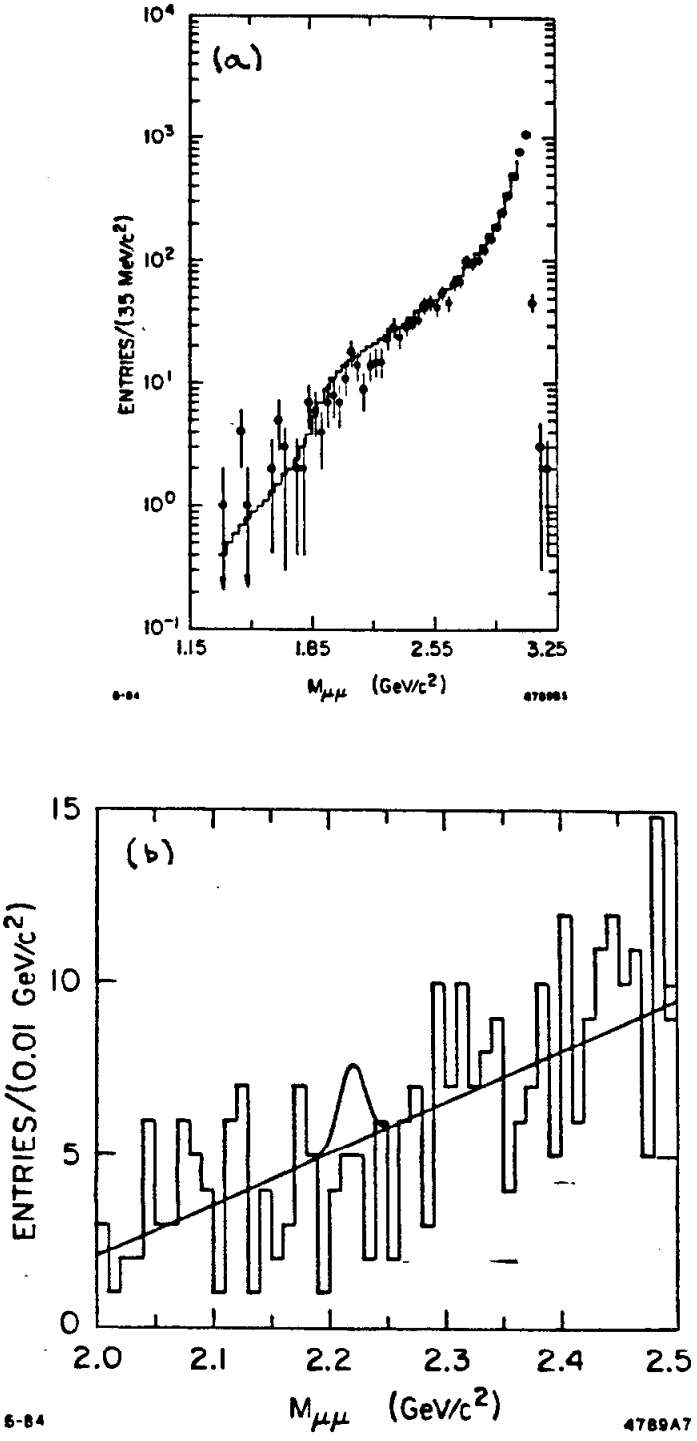

Figure 8.2. The limit on $\xi(2220) \rightarrow \mu^+\mu^-$. (a) shows the $\psi \rightarrow \gamma\mu^+\mu^-$ mass spectrum. The points represent the data and the histogram is the QED Monte Carlo prediction. (b) shows the 90% C.L. for $\xi(2220) \rightarrow \mu^+\mu^-$.

are proportional to the mass):

$$\frac{\mathrm{BR}(\mathrm{H}^0 \to \mu^+\mu^-)}{\mathrm{BR}(\mathrm{H}^0 \to s\bar{s})} \simeq \frac{1}{3}\frac{m_\mu^2}{m_s^2}.$$

This predicts a value of $5 - 15\%$ times the probability for producing the $K\bar{K}$ final state from an $s\bar{s}$ quark pair. This is inconsistent with the measured ratio of partial widths unless one assumes that the $s\bar{s}$ quark pair always decays into a $K\bar{K}$ pair. However, it is not hard to make more complex Higgs models where the couplings are not proportional to the mass, due to the presence of several Higgs multiplets. In this case, there is no prediction for the ratio of the branching ratios.

The $\pi^+\pi^-$ Final State

The analysis of this final state has been described in detail in a preceding chapter. The events are selected by 4-C kinematic fits to the $\psi \to \gamma\pi^+\pi^-$ hypothesis. The number of 'good' gammas is required to be exactly one, and there is no TOF requirement made on the tracks. Background from QED processes has been removed by making the 'pion' cuts described previously. The resulting mass resolution is $\sigma_m = 10$ MeV. The limit is:

$$\mathrm{BR}(\psi \to \gamma\xi(2220))\mathrm{BR}(\xi(2220) \to \pi\pi) < 2 \times 10^{-5} \quad 90\%\ \mathrm{C.L.}$$

This corresponds to a signal of 14 events in the combined 1982 and 1983 data, and a curve corresponding to the limit value is shown in Fig. 8.3(a). The expected relative rates for an $SU(3)$ singlet (ignoring phase space corrections) are:

$$\Gamma(\mathrm{K}^+\mathrm{K}^-) = \Gamma(K^0\bar{K}^0) = \Gamma(\pi^+\pi^-) = 2\Gamma(\pi^0\pi^0).$$

The $\pi\pi$ limit is inconsistent with this simple $SU(3)$ picture, and suggests a suppression of non-strange decays.

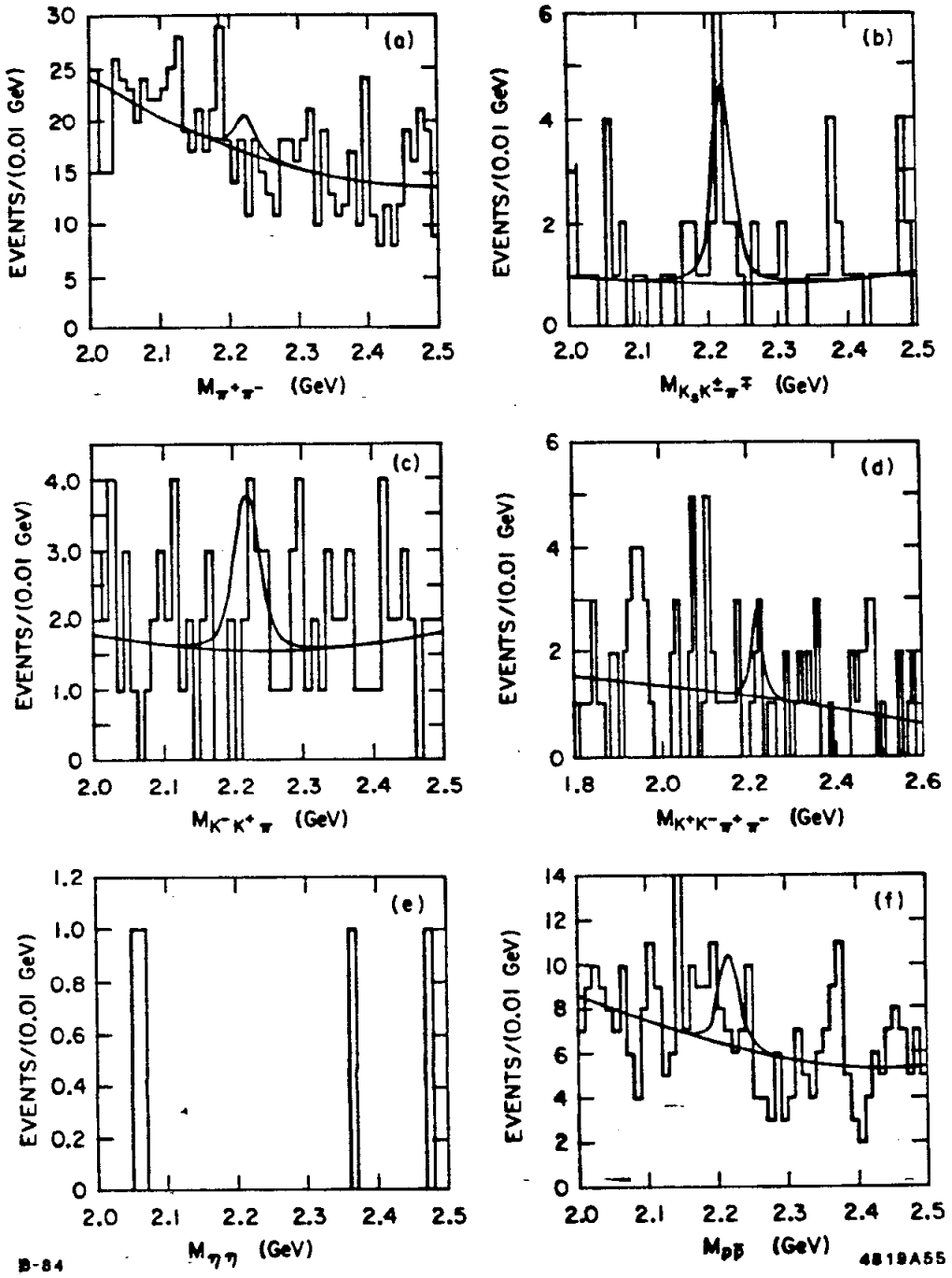

Figure 8.3. Limits on other $\xi(2220)$ decays. The 90% C.L. limits are represented by the fitted curves. (a) the $\pi^+\pi^-$ final state. (b) the $K_S K^\pm \pi^\mp$ final state. (c) the $K^+K^-\pi^0$ final state. (d) the $K^+K^-\pi^+\pi^-$ final state. (e) the $\eta\eta$ final state. (f) the $p\bar{p}$ final state.

*The K*K Final State*

This final state has been examined in two different decay channels: $\psi \rightarrow \gamma K^+K^-\pi^0$ and $\psi \rightarrow \gamma K_S K^{\pm}\pi^{\mp}$. The factor which is required to convert $K^+K^-\pi^0$ to $K\bar{K}\pi$ or K^*K is 6 and the factor required to convert $K_S K^{\pm}\pi^{\mp}$, $K_s \rightarrow \pi^+\pi^-$ to $K\bar{K}\pi$ or K^*K is 9/2. This means that both of these decay channels have about equal sensitivity in the limit analysis.

The $K^+K^-\pi^0$ final state has been 5-C fit and has an estimated mass resolution of $\sigma_m = 15$ MeV. Both charged tracks were required to be consistent with the kaon hypothesis using the TOF information. The combined 1982 and 1983 data sample was used. A limit has been set without making any cuts on the mass of the $K\pi$ system:

$$BR(\psi \rightarrow \gamma\xi(2220))BR(\xi(2220) \rightarrow K\bar{K}\pi) < 4 \times 10^{-4} \quad 90\% \text{ C.L.}$$

This corresponds to a signal of 25 events. A more restrictive limit has been set by requiring that one of the $K\pi$ combinations was within 100 MeV of the K^* mass. This reduces the efficiency slightly, and the limit in this case is:

$$BR(\psi \rightarrow \gamma\xi(2220))BR(\xi(2220) \rightarrow K^*K) < 2 \times 10^{-4} \quad 90\% \text{ C.L.}$$

This corresponds to a signal of 12 events, and the result is shown in Fig. 8.3(c).

The $K_S K^{\pm}\pi^{\mp}$ final state has been 4-C fit and has an estimated mass resolution of $\sigma_m = 10$ MeV. The K_S was selected using cuts on the secondary vertex. The charged kaon was required to be consistent with the kaon hypothesis using the TOF information. The 1983 data sample was used, and the estimated efficiency is $\epsilon \sim 20\%$. A limit has been set without making any cuts on the mass of the $K\pi$ system:

$$BR(\psi \rightarrow \gamma\xi(2220))BR(\xi(2220) \rightarrow K\bar{K}\pi) < 3 \times 10^{-4} \quad 90\% \text{ C.L.}$$

This corresponds to a signal of 24 events. A more restrictive limit has been set by requiring that one of the $K\pi$ combinations was within 100 MeV of the K^* mass. The limit in this case is:

$$BR(\psi \rightarrow \gamma\xi(2220))BR(\xi(2220) \rightarrow K^*K) < 2.5 \times 10^{-4} \quad 90\% \text{ C.L.}$$

This corresponds to a signal of 17 events, and is shown in Fig. 8.3(b). It is possible that the peak observed in Fig. 8.3(b) is actually a signal. If this admittedly farfetched interpretation is made, then the plot should be fit by allowing the mass and width of the Breit-Wigner to vary. The result is displayed in Fig. 8.4 and corresponds to a branching ratio of:

$$BR(\psi \rightarrow \xi(2220))BR(\xi(2220) \rightarrow K\bar{K}\pi) = (1.1 \pm .4 \pm .3) \times 10^{-4}$$

with the Breit-Wigner parameters given by:

$$m = 2.219 \pm .005 \text{ GeV} \quad , \quad \Gamma = 0 \pm .010 \text{ GeV}.$$

This is precisely the right mass and roughly the level one might expect for the branching ratio. If it were real, it would have the very significant implication that the spin of the $\xi(2220)$ could not be zero. However, it is clear that the significance of the signal is inadequate to justify anything beyond idle speculation.

The $K^*\bar{K}^*$ Final State

The decay channel $\psi \rightarrow \gamma K^+K^-\pi^+\pi^-$ has been used to estimate the limit for the $K^*\bar{K}^*$ final state. This particular channel represents 2/9 of the total final state, assuming the $K^*\bar{K}^*$ intermediate state. The data have been 4-C fit and one track was required to be identified as a kaon by the TOF. The other kaon was identified by permuting the kaon hypothesis over the different possibilities in the

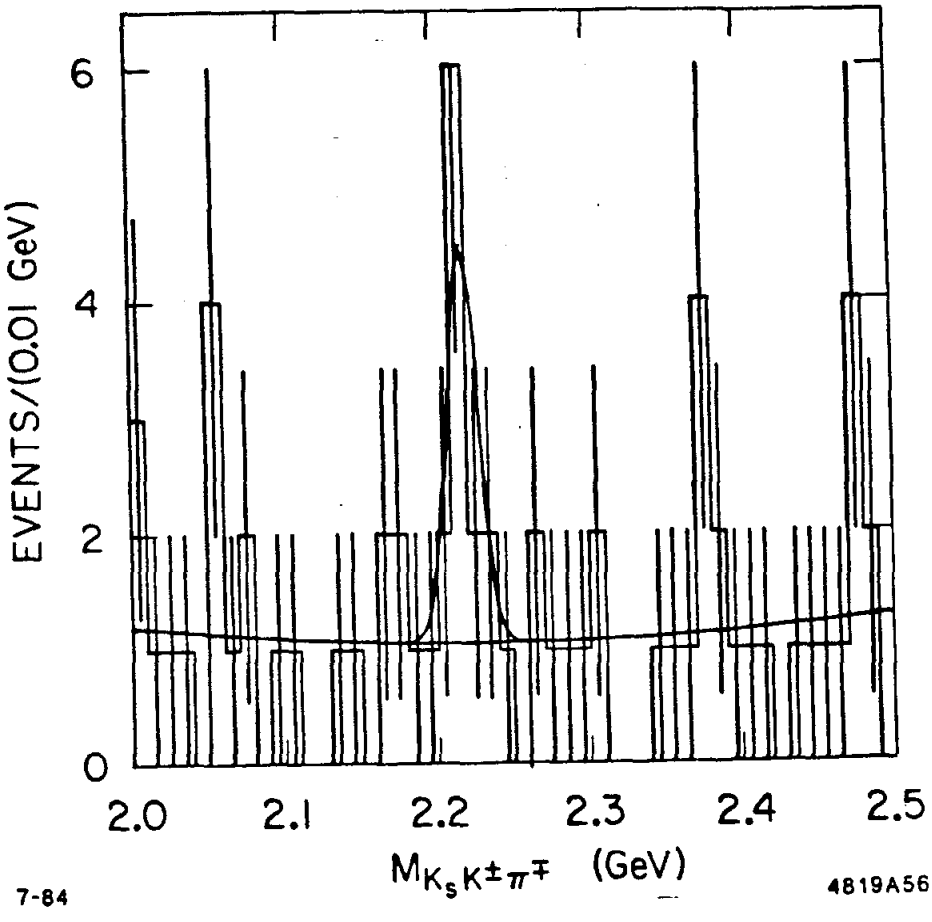

Figure 8.4. A possible signal in $K_S K^\pm \pi^\mp$. The curve represents a fit for a possible narrow peak.

kinematic fit. The mass resolution in this region is $\sigma_m = 15$ MeV. The 1983 data was used to perform the analysis. A limit has been set without making any cuts on the $K\pi$ mass. This is quoted without correcting it to $K\bar{K}\pi\pi$, because the correction factor depends on the isospin of the K^+K^- system. The result is:

$$BR(\psi \to \gamma\xi(2220))BR(\xi(2220) \to K^+K^-\pi^+\pi^-) < 5 \times 10^{-5} \quad 90\% \text{ C.L.}$$

This corresponds to a signal of 9 events. If a cut is made requiring that only one $K\pi$ mass combination is in the K^* region, the result is very similar. Finally, when both $K\pi$ combinations are required to be in the K^* region, the resulting limit is:

$$BR(\psi \to \gamma\xi(2220))BR(\xi(2220) \to K^*\bar{K}^*) < 3 \times 10^{-4} \quad 90\% \text{ C.L.}$$

This corresponds to a signal of 7 events, and is shown in Fig. 8.3(d).

The $\eta\eta$ Final State

This final state has been examined in the channel: $\psi \to \gamma\eta\eta$ where one η decays to $\eta \to \gamma\gamma$ and the other η decays to $\eta \to \pi^+\pi^-\pi^0$. The decays $\eta \to \gamma\gamma$ and $\pi^0 \to \gamma\gamma$ have been used as additional constraints in performing a 6-C kinematic fit. The expected mass resolution is $\sigma_m = 25$ MeV. The combined 1982 and 1983 data sets were used. There are no events found in the 2.2 GeV mass region, and a limit has been set using Poisson statistics. The limit is:

$$BR(\psi \to \gamma\xi(2220))BR(\xi(2220) \to \eta\eta) < 7 \times 10^{-5} \quad 90\% \text{ C.L.}$$

This corresponds to a signal of 3 events, and is shown in Fig. 8.3(e). The expectation for an $SU(3)$ singlet is that :

$$\Gamma(K^+K^-) = \Gamma(K^0\bar{K}^0) = 2\Gamma(\eta\eta)$$

For a normal hadron state, the expected width for $\eta\eta$ is even smaller.

Table 8.1. Various Limits on the $\xi(2220)$ in other modes. A set of six limits on other interesting decay modes is shown

Final State	BR Limit
$\xi(2220) \rightarrow \mu^+\mu^-$	$< 7.3 \times 10^{-6}$ *
$\xi(2220) \rightarrow \pi\pi$	$< 2 \times 10^{-5}$
$\xi(2220) \rightarrow K^*K$	$< 2.5 \times 10^{-4}$
$\xi(2220) \rightarrow K^*\bar{K}^*$	$< 3 \times 10^{-4}$
$\xi(2220) \rightarrow \eta\eta$	$< 7 \times 10^{-5}$
$\xi(2220) \rightarrow p\bar{p}$	$< 2 \times 10^{-5}$

* This limit used a value of 0 for the width

The $p\bar{p}$ *Final State*

This final state has been examined in the 1982 and 1983 data by requiring that both of the charged tracks be identified as a proton by TOF. The radiative photon was required to be well isolated from the charged tracks in the shower counter, especially for the anti-proton. The events were 4-C fit, resulting in a mass resolution of about 10 MeV. The limit which has been set is:

$$\mathrm{BR}(\psi \rightarrow \gamma\xi(2220))\mathrm{BR}(\xi(2220) \rightarrow p\bar{p}) < 2 \times 10^{-5} \quad 90\% \text{ C.L.}$$

This corresponds to a signal of 17.5 events, and is shown in Fig. 8.3(f).

Summary

The results of the investigations above are summarized in Table 8.1. None of these limits is particularly striking. The $\mu^+\mu^-$ limit puts constraints on the Higgs interpretation. The $\pi\pi$ limit is in contradiction with a simple $SU(3)$ singlet decay pattern. The possibility of a K^*K signal is very intriguing, but greater statistics is required.

Chapter 9. Theoretical Interpretations and Conclusions

In this chapter, an attempt is made to summarize the measurements obtained in the preceding chapters, and to place them in a theoretical context. A discussion of the $f(1270)/f'(1515)$ system is conducted to assess the mixing situation. A brief summary of the $\theta(1700)$ experimental situation is provided, followed by a general summary of the possible explanations for the $\theta(1700)$. In addition, a discussion of possible interpretations of the $\xi(2220)$ is offered. Finally, an attempt is made to understand what can be learned from a higher statistics study of these topics.

9.1 The $f(1270)/f'(1515)$ System

These are the two iso-singlet members of the lowest lying $q\bar{q}$ tensor nonet. This nonet is experimentally observed to be almost ideally mixed, and so the $f(1270)$ should be roughly pure $u\bar{u}+d\bar{d}$ and the $f'(1515)$ should be roughly pure $s\bar{s}$. For the standard ψ radiative decay diagram, the photon is radiated from the initial state, and the two gluon system is an $SU(3)$ singlet. This predicts[43] the ratio:

$$R = \frac{\Gamma(\psi \to \gamma f')}{\Gamma(\psi \to \gamma f)} = 0.5,$$

ignoring phase space corrections. There are several previous measurements[44,22, 45] for the $f(1270)$ and the $f'(1515)$. They are summarized in Table 9.1. The value for the ratio was poorly determined. The DASP experiment[46] measured a value of: $< 1/3$, while the PLUTO experiment[47] measured a value of: $< 0.12 \pm 0.05$. The MARK II experiment[24] was the only experiment to actually see a signal, and measured a value of: $\leq 0.16 \pm 0.10$. The indication was that the ratio was smaller than expected.

Table 9.1. Summary of $f(1270)$ and $f'(1515)$ branching ratio measurements. These numbers are from previous experiments as well as the current experiment.

Experiment	BR($\psi \rightarrow \gamma$f)BR(f $\rightarrow \pi\pi$)	$BR(\psi \rightarrow \gamma f')BR(f' \rightarrow K\bar{K})$
MARK II (Ref. 44)	$(1.1 \pm 0.25) \times 10^{-3}$	$(1.8 \pm 0.6 \pm 1.0) \times 10^{-4}$
Crystal Ball (Ref. 22)	$(1.23 \pm 0.21 \pm 0.25) \times 10^{-3}$	
DM-2 (Ref. 45)	$(1.1 \pm 0.35) \times 10^{-3}$	
MARK III	$(1.15 \pm 0.07 \pm 0.19) \times 10^{-3}$	$(6.0 \pm 1.4 \pm 1.2) \times 10^{-4}$

These indications, along with other considerations, motivated suggestions that there was a large gluon admixture in the $f(1270)$. Rosner[48] proposed such a model to resolve differences between the theoretical predictions and the measured values for $\Gamma(f \rightarrow all)$ and $\Gamma(f \rightarrow \gamma\gamma)$. This model postulated the existence of an additional state, the $f^{\perp}$, which mixed with the $f(1270)$. This additional state was required to decouple from the $\pi\pi$ channel, and was predicted to have a mass in the range: $1.45 - 1.85$ GeV. If the $f^{\perp}$ was chosen to be a gg state, then the model provided a natural mechanism to enhance $f(1270)$ production in radiative ψ decays. This model was proposed prior to the observation of the $\theta(1700)$, and was subsequently re-formulated as a three state mixing model for the $f(1270)/f'(1515)/\theta(1700)$ system. It will be discussed in that form in the next section.

A second proposal[49] was motivated by early MIT bag model calculations which placed the lowest lying $J^{PC} = 2^{++}$ glueball at a mass of $\sim$ 1.3 GeV. A fascinating study was performed[50] to understand the phenomenological consequences of the implied $f(1270)$/glueball mixing, using the P matrix formalism. This study indicated the possibility of several strange effects, such as: split mass peaks in some channels, process-dependent widths and branching ratios, and apparent shifts in mass in some channels. Such unusual effects do not appear to be

required by the data, but cannot be ruled out. They serve to remind us that, for overlapping states, simple mixing models which use a linear combination of single particle eigenstates are not the full story.

The value for the ratio:

$$\mathrm{R} = \frac{\Gamma(\psi \rightarrow \gamma \mathrm{f}')}{\Gamma(\psi \rightarrow \gamma \mathrm{f})}$$

cannot be evaluated exactly because $\mathrm{BR}(\mathrm{f}'(1515) \rightarrow \mathrm{K\bar{K}})$ is not known. Using the MARK III values for the radiative rates and the value $\mathrm{BR}(\mathrm{f} \rightarrow \pi\pi) = 0.83 \pm 0.019$ for the $f(1270)$ branching ratio[34] gives:

$$\begin{aligned} R &= \frac{BR(\psi \rightarrow \gamma f')BR(f' \rightarrow \mathrm{K\bar{K}})}{BR(\psi \rightarrow \gamma f)BR(f \rightarrow \pi\pi)} \times \frac{BR(f \rightarrow \pi\pi)}{BR(f' \rightarrow \mathrm{K\bar{K}})} \\ &= \frac{(0.43 \pm 0.15)}{BR(f' \rightarrow \mathrm{K\bar{K}})} \end{aligned}$$

Montanet[40] has quoted a lower bound: $\mathrm{BR}(\mathrm{f} \rightarrow \mathrm{K\bar{K}}) \geq 0.7$. If a value of 0.8 is assumed, then:

$$R = 0.54 \pm 0.19.$$

This is in quite satisfactory agreement with the $SU(3)$ singlet prediction. It disagrees with the previous measurements, but the present measurement has been performed using a large $f'(1515)$ signal and a correct simulation of the full decay angular distributions.

The other measurements which have been made are the helicity ratios for the $\psi \rightarrow \gamma f$ and $\psi \rightarrow \gamma f'$ processes. The $\psi \rightarrow \gamma f$ measurement has been performed previously[47,23,22] and the results are summarized in Table 9.2. The MARK III values are in agreement with the previous measurements, although the MARK III fitting procedure did not make any assumptions about the relative phases of the helicity amplitudes (the previous analyses always assumed that the relative phases

Table 9.2. Summary of polarization measurements. These numbers are from previous experiments as well as the current experiment.

Experiment		Results
$f(1270)$	PLUTO (Ref. 47)	$x = 0.6 \pm 0.3 \quad y = 0.3^{+0.6}_{-1.6}$
	MARK II (Ref. 23)	$x = 0.81 \pm 0.16 \quad y = 0.02 \pm 0.15$
	Crystal Ball (Ref. 22)	$x = 0.88 \pm 0.11 \quad y = 0.04 \pm 0.14$
	MARK III	$x = 0.94 \pm 0.10 \quad y = 0.06 \pm 0.11$
		$\varphi_x = 0.4 \pm 0.7 \quad \varphi_y = -0.1 \pm 2.2$
$f'(1515)$	MARK III	$x = 0.63 \pm 0.10 \quad y = 0.17 \pm 0.20$
		$\varphi_x \sim 0 \quad \varphi_y \sim 0$

were zero). The helicity structure of the $f'(1515)$ has been determined for the first time, and the values are very similar to those found for the $f(1270)$.

The original theoretical calculation was performed for the decay $\psi \rightarrow \gamma f(1270)$ by Krammer.[51] This calculation proceeds by treating the $c\bar{c}$ annihilation into γgg in analogy with the 3γ decay of positronium. The gg system then creates a quark pair in a non-relativistic $^3P_2$ state, corresponding to the tensor meson. The result of this calculation is summarized in Table 9.3. The value for x agrees well with the data, but the value for y is much too large. Several deficiencies in the original calculation have been corrected, and Körner *et al.* have performed a very complete calculation.[52] The authors emphasize that the assumption that the relative phases of the helicity amplitudes are zero may not be valid, and encourage experimentalists to fit with variable phases. This has been done in the current analysis, with the results displayed in Table 9.2. Unfortunately, the results still indicate a large discrepancy with the size of the helicity 2 amplitude.

The theoretical calculations indicate that the helicity amplitude ratios x and y for the process $V \rightarrow \gamma X$ depend only on the ratio M_X/M_V, where V refers to

Table 9.3. The theoretical predictions for the polarization. The values for both the $f(1270)$ and the $f'(1515)$ are displayed when they are available. The pure multipoles are calculated in Appendix B.

Calculation	$f(1270)$ Results	$f'(1515)$ Results
Krammer	$x = 0.76 \quad y = 0.54$	$x = 0.88 \quad y = 0.70$
Körner *et al.*	$x = 0.77 \quad y = 0.55$	$x = 0.90 \quad y = 0.72$
	$\varphi_x = 2.0° \quad \varphi_y = 4.0°$	$\varphi_x = 1.3° \quad \varphi_y = 2.4°$
Li and Shen	$x = 0.66 \quad y = 0.04$	
Close	$x = 0.87 \quad y = 0.0$	
$E1$	$x = \sqrt{3} \quad y = \sqrt{6}$	
$M2$	$x = \sqrt{1/3} \quad y = -\sqrt{2/3}$	
$E3$	$x = -\sqrt{4/3} \quad y = \sqrt{1/6}$	

the initial vector state and X refers to the produced state. These ratios approach pure helicity 0 ($x = y = 0$) when $M_X/M_V \to 0$, and they approach the $E1$ dipole limit ($x = \sqrt{3}$, $y = \sqrt{6}$) when $M_X/M_V \to 1$. However, for all values of M_X/M_V, it appears that $x \sim y$. Thus, in order to explain the data, one needs some mechanism to suppress the helicity 2 amplitude.

There have been two such proposals. Li and Shen,[53] motivated by the possibility of mixing between the $f(1270)$ and a glueball state, have performed a calculation using a $J^{PC} = 2^{++}$ glueball composed of two valence gluons. The results of their calculation are shown in Table 9.3. They agree well with the measured values, but their proposal would require that both the $f(1270)$ and the $f'(1515)$ behave like glueballs composed of two valence gluons. This does not seem tenable.

A second, more heuristic, proposal has been made by Close.[54] He suggests that if the assumption of a quasi-real gg intermediate state is dropped, then in the limit that $M_X/M_V \to 0$, y still vanishes but x is no longer required to vanish. With a little more hand-waving, he suggests the value $x = \sqrt{3}/2$ (note that this corresponds

to a mixture of $E1$ and $M2$ multipoles, as described in Appendix B). This conjecture agrees well with the measured values, but has no particularly strong theoretical justification. It is also necessary that the values of x and y for $M_X/M_V \sim 0$ do not change drastically as $M_X/M_V \rightarrow 0.4-0.5$. This mass-independence is not what the current QCD calculations predict. Experiments involving radiative transitions such as $\Upsilon \rightarrow \gamma f(1270)$ could clarify this situation by probing smaller values of M_X/M_V which are closer to the perturbative QCD regime, but perhaps the real solution is associated with a more relativistic treatment of the produced $q\bar{q}$ meson.

9.2 THE $\theta(1700)$

Several new results on the $\theta(1700)$ have been presented, leading to a fairly complete picture of its properties. The previous measurements,[25,55,24] as well as the new results are summarized in Table 9.4. These numbers lead to the ratios:

$$\frac{BR(\theta \rightarrow \eta\eta)}{BR(\theta \rightarrow K\bar{K})} = 0.40 \pm 0.19$$

and:

$$\frac{BR(\theta \rightarrow \pi\pi)}{BR(\theta \rightarrow K\bar{K})} \leq 0.25 \pm 0.09.$$

The ratio for $\pi\pi$ is quoted as an upper bound because of the possibility that interference effects in this final state can reduce the $\pi\pi$ branching ratio.

The J^P was measured by Crystal Ball, but their measurement did not account for the presence of the $f'(1515)$. They found that $J^P = 2^+$ was preferred at the 95% C.L. The MARK III result is much more reliable since it involves a much larger event sample and the $f'(1515)$ is analyzed separately. The result strongly supports the conclusion that the $\theta(1700)$ is a $J^P = 2^+$ state.

The $\theta(1700)$ remains a very peculiar state, with no clear identity. The possible explanations for this state will be discussed in order of increasing plausibility; none of the explanations are without problems.

Table 9.4. A summary of the $\theta(1700)$ properties. These numbers are from previous experiments as well as the current experiment. The quoted branching ratios are all product branching ratios of the form :$BR(\psi \rightarrow \gamma\theta)BR(\theta \rightarrow \cdots)$, and are in units of 10^{-4}. The assumption that the $\theta(1700)$ has $I = 0$ has been used to correct for unobserved decay modes. The upper limits are 90% C.L. limits.

Measurement	Crystal Ball (Ref. 25 , 55)	MARK II (Ref. 24)	MARK III
m	1.670 ± 0.050	1.700 ± 0.030	1.720 ± 0.010
Γ	0.160 ± 0.080	0.156 ± 0.020	0.130 ± 0.020
$BR(\theta \rightarrow \eta\eta)$	3.8 ± 1.6 *		
$BR(\theta \rightarrow K\bar{K})$		$12.0 \pm 1.8 \pm 5.0$	$9.6 \pm 1.2 \pm 1.8$
$BR(\theta \rightarrow \pi\pi)$	< 6.0	< 3.2	$2.4 \pm 0.5 \pm 0.4$
$BR(\theta \rightarrow \rho\rho)$			< 6.0
$BR(\theta \rightarrow K\bar{K}\pi)$			< 2.8
$BR(\theta \rightarrow K\bar{K}\pi\pi)$			< 4.5

* The original analysis, with no $f'(1515)$, produced the result:
$BR(\theta \rightarrow \eta\eta) = 4.9 \pm 1.4 \pm 1.0$

A $q\bar{q}$ State

Due to the absence/suppression of non-strange decay modes, the $\theta(1700)$ appears somewhat like an ideally mixed $s\bar{s}$ state. Of crucial importance for this statement is the recent MARK III result from the spin-parity analysis of $\psi \rightarrow \gamma\rho\rho$, discussed in a previous chapter, which indicated that there was no strong evidence for a 2^+ state in the $\theta(1700)$ mass region. The MARK II experiment[56] had previously observed an enhancement in this region which was attributed to the $\theta(1700)$ and hence seemed to suggest that there were large non-strange decay modes of the $\theta(1700)$.

If the $\theta(1700)$ were an $s\bar{s}$ state, it would be expected to decay

predominantly to $K\bar{K}$, and at a smaller rate to $\eta\eta$. $SU(3)$ predicts[57] that: $\Gamma(f' \to \eta\eta)/\Gamma(f' \to K\bar{K}) \sim 4/9$. Its decays to $\pi\pi$ or $\rho\rho$ would be strongly suppressed. The problem is that there is no room for such a state in the quark model, nor is there any evidence for it in other production experiments. The members of the lowest lying 2^{++} nonet are all well established. The $\theta(1700)$ could then be either a radially excited, or an orbitally excited, $f'(1515)$. This is implausible because of the very small mass difference. There is some evidence[58] for an $f(1810)$, which could be a radially excited $f(1270)$. A radially excited f' should lie several hundred MeV higher. For the orbital excitations of the 2^{++} nonet, the $L = 3$, 4^{++} nonet has the $h(2040)$ as the orbitally excited partner of the $f(1270)$. Presumably the $L = 3$, 2^{++} nonet would have a similar mass scale. This estimate is in agreement with a QCD potential model[59] which suggests a mass of about 2 GeV for the excited $f(1270)$. One would then expect an excited $f'(1515)$, for which there is no evidence, to appear at $2 - 2.2$ GeV. This makes the $q\bar{q}$ interpretation seem unlikely.[60]

A more radical attempt along these lines is the hypothesis of Cohen, Isgur and Lipkin.[61] They suggest that a combination of the $f(1270)$ and a radially excited $f(1270)$ could mix coherently with the $f'(1515)$ to create an interference peak above the $f'(1515)$. Unfortunately, the shape of the mass spectrum which they predict does not agree with the observed spectrum.

A $q\bar{q}g$ State

The spectrum and properties of such states, known as hermaphrodites, meiktons or hybrids, have been investigated by Chanowitz and Sharpe[62] and by Barnes and Close.[63] They have carried out $O(\alpha_s)$ perturbation calculations in the bag model and find that there are four low lying nonets. These nonets are formed from a $q\bar{q}$ pair in an $L = 0$ state plus a (TE) gluon. The resulting quantum numbers are: $J^{PC} = 1^{--}$, $(0,1,2)^{-+}$. In order to get a 2^{++} state, one needs to consider an

excited state, built with a (TM) gluon. Chanowitz and Sharpe[64] have investigated the properties of such states, and they suggest a $K^*\bar{K}^*$ signature and a mass in the $1.9 - 2.3$ GeV range. Their result is interesting because they find that for a (TM) gluon, decay modes involving strange quarks are greatly enhanced. However, the mass scale is somewhat too high, and it seems unlikely that an excited state should appear at a relatively low mass, before any members of the ground state nonets appear. However, perhaps the $\iota(1440)$ is a ground state $q\bar{q}g$ state, and all is consistent...

A $qq\bar{q}\bar{q}$ State

The existence of such states was investigated extensively in the bag model by Jaffe.[65] Chanowitz[66] has discussed the possibility that the $\theta(1700)$ could be a four quark state. This is intriguing for several reasons. These states are expected to be unobservably broad since they decay by 'falling apart' into two mesons. However, if the state has a mass below the threshold for its 'fall apart' mode, it can be much narrower. Chanowitz suggests that the $\theta(1700)$ could be a $(u\bar{u} + d\bar{d})s\bar{s}$ state which would like to fall apart into $K^*\bar{K}^*$ or $\phi\omega$. In this case, one expects:

$$\Gamma(\theta \to K\bar{K}) = 2\Gamma(\theta \to \eta\eta),$$

with no other significant decay modes. In particular, to lowest order there should be *no* $\pi\pi$ decay mode. However, these predictions were made for a $\theta(1700)$ which was lighter than the current mass value. Thus, one might also expect to see a K^*K^* signal just below threshold. Such a signal seems to be ruled out by the data. The other predictions agree with the data, with the possible exception of the $\pi\pi$ mode (which is at least strongly suppressed). If this hypothesis is correct, then the total branching ratio for the state would be $\Gamma(\psi \to \gamma\theta) \sim 1.5 \times 10^{-3}$. This is a rather large rate for the production of an unusual state, and one might expect to see other

potential four quark states like the $S^*(975)$ at a similar rate. This is not the case. The four quark hypothesis prefers a $J = 0$ state, since it can decay easily into two pseudoscalars. The $J = 2$ state decays to two pseudoscalars via gluon corrections, and Chanowitz has suggested that this could produce three body decay modes like $K\bar{K}\pi$ in addition to the two body modes mentioned previously.

A further flaw in this hypothesis has been discussed by Weinstein and Isgur.[67] They have studied the stability of four quark states using a four body Schrödinger equation. This work indicates that the four quark states are not stable, with the exception of the 0^{++} states. These states can be associated with the $\delta(980)$ and the $S^*(975)$. Thus, although phenomenologically appealing, the four quark scenario may not have any basis in reality.

A Glueball State

In considering this possibility, there are three features of the $\theta(1700)$ which will be discussed: the mass, the width and the decay modes. Although there are fairly rigorous indications that glueballs should exist (*e.g.*, a pure $SU(3)$ gauge theory confines color and has a 'mass gap'), the masses for glueball states cannot be rigorously calculated. Their masses have been estimated in the context of several different models: lattice Monte Carlo models, bag models, QCD sum rules, and potential models. Of these four, the bag model results are perhaps the most believable, and they are discussed in the greatest detail. However, none of the calculations are devoid of problems. These different models are in approximate agreement on the mass spectrum, and will be summarized here.

The lattice Monte Carlo technique is an attempt at performing true QCD calculations in a non-perturbative manner. In order to estimate glueball masses, a pure (no fermions) $SU(3)$ gauge theory is studied on a periodic lattice with $\mathcal{O}(10^4)$ sites. This calculational technique is still quite young, and the ability to perform

the calculations is rapidly evolving. The results of recent calculations have been summarized in a lengthy review by Teper.[68] There appears to be agreement that the 0^{++} state should be at a mass of ~ 750 MeV. The 2^{++} state is more controversial and the calculation by Ishikawa *et al.*[69] gives a mass of:

$$m = 1665^{+110}_{-90} \text{ MeV}.$$

This is in agreement with the $\theta(1700)$ mass, but these calculations are for a theory with no fermions, and are still quite controversial.

A different, somewhat more phenomenological, approach to understanding the glueball spectrum is through the bag model. In this approximation, the effects of confinement are accounted for by placing the quarks and gluons inside a cavity carved out of the QCD vacuum. This cavity is taken to be spherical and static. Inside this cavity, gluons behave like standing electromagnetic waves, and their lowest modes are classified using standard waveguide nomenclature as: $(TE_1), (TE_2), (TM_1)$. This model is relativistic, and contains the proper degrees of freedom for the gluons. It has been successfully applied to the $L = 0$ mesons and baryons[70] and recently, $O(\alpha_s)$ corrections have also been calculated.[62] It has difficulty with the $L = 1$ mesons and baryons[71,72] because of a dynamical uncertainty in the treatment of degrees of freedom associated with the bag itself. This problem arises because the spherical bag is the equilibrium shape only for $L = 0$ states—for higher L states, the bag wants to deform. It would appear that there should be additional states, not present in the naive quark model, which correspond to these excitations of the bag. These states arise because of the non-central forces associated with the bag and are traditionally labeled 'spurious' and discarded.[49] Rebbi[73] has investigated the effect of quantizing the bag excitations. His work indicates that the extra states may be real (an interesting prediction for the mesons, since these states have exotic quantum numbers), and appear at higher

masses, while the non-spurious states are pushed down slightly in mass. It is possible that these extra states should be called '$q\bar{q}g$' states, with the bag excitation playing the role of a valence gluon. These complications tend to raise doubts about the ability of current bag model calculations to describe the spectrum of excited states.

The lowest lying glueball states are formed from two gluons as follows:

$$\begin{aligned}
(TE_1)^2 \quad & J^{PC} = (0,2)^{++} \\
(TE_1)(TE_2) \quad & J^{PC} = [(1,2,3)^{-+}] \\
(TE_1)(TM_1) \quad & J^{PC} = (0,2)^{-+},\ [1^{-+}] \\
(TM_1)^2 \quad & J^{PC} = (0,2)^{++},
\end{aligned}$$

where the $(TE_1)^2$ and $(TM_1)^2$ states with $J^{PC} = 1^{++}$ are forbidden by Bose statistics, and the bracketed states are conventionally labeled as spurious.

If the radiative corrections are ignored, then the masses of these glueball states are determined from fits to the hadron spectrum.[49] The $O(\alpha_s)$ corrections are large, and have been computed by several groups.[62,74] These corrections introduce unknown parameters to the glueball mass spectrum. The gluon self-energy in the bag is not yet calculable, and so there are two constants: c_{TE} and c_{TM}, which must be determined. The necessity of determining these constants makes the bag model glueball spectrum more of a consistency check than a prediction. It is hoped that in the future these constants can be calculated from the loop integrals in cavity perturbation theory, and the ambiguity removed.

The results found by Chanowitz and Sharpe are:

	$c_{TE}/c_{TM} = 1/2$	$c_{TE}/c_{TM} = 1$	$c_{TE}/c_{TM} = 2$
$J^{PC} = 0^{++}$	$m = 0.67$ GeV	$m = 1.14$ GeV	$m = 1.56$ GeV
$J^{PC} = 2^{++}$	$m = 1.75$ GeV	$m = 2.12$ GeV	$m = 2.47$ GeV

The sum $c_{TE} + c_{TM}$ was fixed by forcing the $J^{PC} = 0^{-+}$ $(TE_1)(TM_1)$ mode to

lie at the $\iota(1440)$ mass. In addition, Carlson *et al.*[74] claim that the only reasonable value for C_{TE}/C_{TM} is 1/2, since only in this case is the kinetic energy of the gluon greater than its self-energy.

A very different technique for understanding the QCD mass spectrum is embodied in the QCD sum rules developed by Shifman *et al.*[75] These sum rules are an attempt to calculate resonance parameters by including both perturbative QCD contributions (short distance behavior) and non-perturbative contributions (long distance behavior). The non-perturbative contributions are introduced via vacuum expectation values for higher dimensional operators like:

$$\langle 0|G_{\mu\nu}G_{\mu\nu}|0\rangle \ , \ \langle 0|q\bar{q}|0\rangle$$

where $G_{\mu\nu}$ is the gluon field strength and q is the quark field. The trick is to represent the vacuum polarization in two different ways: one is a 'theoretical' perturbative expression using the operator product expansion for large Q^2, the other is a 'phenomenological' dispersion relation which is approximated by a sum over resonances. The equality of these representations is a refinement of the idea of duality. In this manner, resonance parameters can be related to 'calculable' operator product expansion coefficients, provided that there is an intermediate Q^2 where both representations are valid. With the addition of some numerical trickery (Borel transforms, ...), this scheme seems to yield many correct predictions for the charm sector, as well as for ordinary mesons. It is in disagreement with the bag model on one crucial point. In the bag model, the bag constant is assumed to be relatively independent of the contents of the bag—this is what provides a similar mass scale for both mesons and glueballs. In the sum rule picture, there are additional complications for 0^+ and 0^- states arising from instantons (non-trivial vacuum topologies). These complications alter the mass scales, accounting

for the heavy η' in the usual 0^- $q\bar{q}$ nonet. In effect, these states interact much more strongly with the vacuum, and so the bag constant is very different. For gluonium, the predicted results are:

$$0^+ \quad m \sim 1.4 \text{ GeV},$$

$$0^- \quad m \sim 2.0 - 2.5 \text{ GeV},$$

$$2^+ \quad m \sim 1.6 - 2.0 \text{ GeV}.$$

The 2^+ prediction is similar to that in the bag, while the $J = 0$ masses are much larger. The prediction for the pseudoscalar is particularly interesting because it would rule out any possible association of the $\iota(1440)$ with this state. The crucial question is whether the instanton contributions present in these calculations are correct. If they are ignored, it is likely that the resulting mass spectrum will be very similar to that found in the bag model.

A final type of model, mentioned very briefly, uses massive gluons with a string potential[76] for confinement. This model gives a mass for the 2^{++} state of about 1.6 GeV for a gluon mass of 0.5 GeV. The conclusion of this survey is that a mass of 1.7 GeV for a 2^{++} glueball is roughly what would be expected, although many of these calculations were performed after the $\theta(1700)$ became available as a glueball candidate.

The next measurement to consider is the width of the $\theta(1700)$. Conventional wisdom suggests that glueball states should be narrow, because their decay to $q\bar{q}$ states is OZI suppressed.[77] This rule of thumb goes under the label $\sqrt{OZI}$, since for a glueball decay, the initial $q\bar{q}$ annihilation is absent, and hence the suppression only acts at one vertex. This suppression is also predicted by the $1/N_c$ expansion, where N_c is the number of quark colors, and glueball widths of $10 - 30$ MeV are expected. The naive assumptions underlying this rule have been attacked in recent years. Chanowitz[72] suggests that some OZI suppressed decays

may be small because of cancellations, and OZI suppression itself may not be as large as expected. Soni[78] claims that glueballs should be roughly as wide as hadrons, and the $1/N_c$ expansion does not suppress their decays. In addition, there are further complications if the glueball mixes with nearby $q\bar{q}$ states. The conclusion is that the width of the $\theta(1700)$ is probably not an argument for or against the glueball interpretation.

A further topic is the branching ratios of the $\theta(1700)$. The conventional lore is that a glueball is an $SU(3)$ flavor singlet, and so the decay rates to $\pi\pi$, $K\bar{K}$ and $\eta\eta$ should be related by $SU(3)$:

$$\Gamma(\pi\pi) = \frac{3}{4}\Gamma(K\bar{K}) = 3\Gamma(\eta\eta).$$

The general question of flavor symmetry breaking has been discussed,[79] with the conclusion that forbidden $SU(3)$ singlet decays such as $G \to K^*K$ remain forbidden, but $SU(3)$ allowed decays like $G \to \pi\pi$ or $G \to K\bar{K}$ may be substantially modified due to the large difference between the strange quark mass and the up and down quark masses. The simple $SU(3)$ singlet pattern is clearly violated by the $\theta(1700)$. Several authors have claimed that this is definitive evidence against the glueball interpretation.[80] Others have claimed that an $SU(3)$ symmetry on the quark level may not be manifested on the hadron level.[81] A further interesting discovery was made by Chanowitz and Sharpe.[64] They find that for (TM) gluons in the spherical bag, decay modes to kaons are substantially enhanced. This is intriguing in light of the fact that both the $\iota(1440)$ and the $\theta(1700)$ have a strong preference for decays to strange quarks. This feature appears to be present in the QCD sum rules too.[82] It is due to the appearance of the quark mass in the matrix element for decays of glueballs to quarks. In summary, it appears that no definitive conclusions follow from the observed pattern of decay modes.

Mixing Models

To consider the details of the decays of the $\theta(1700)$, several theorists have studied mixing models for the $f(1270)/f'(1515)/\theta(1700)$ system. None of these models is very successful at accounting for all the measurements. One of the goals is to take an underlying $SU(3)$ singlet, and mix it with the $f(1270)/f'(1515)$ in such a way as to make the physical $\theta(1700)$ state decay as a non-singlet. The model of Rosner[83] uses linear mass formulas and an orthogonal mixing formalism. The result is that it is impossible to suppress both $f' \to \pi\pi$ and $\theta \to \pi\pi$ unless the f' and the θ are very close in mass. This failure rules out this model, but an earlier model[48] which considered only the mixing between the $f(1270)$ and the θ is still viable. In this model, the $f(1270)$ picks up about 10% glue in its wave-function and the $\theta(1700)$ picks up about 10% $(u\bar{u} + d\bar{d})$ in its wave-function. The model of Schnitzer[84] is slightly more general than that proposed by Rosner. The results are that if there is an extra $SU(3)$ singlet state, it is required to mix with the $f'(1515)$. The small rate for $f' \to \pi\pi$ then comes about because of a cancellation between the non-strange quark and the $SU(3)$ singlet contributions to its wave-function. The model predicts a ratio:

$$\frac{\Gamma(\theta \to \eta\eta)}{\Gamma(\theta \to K\bar{K})} \leq 0.18.$$

The exact value for this ratio is very sensitive to the $\eta/\bar{\eta}'$ mixing angle. The small size of this ratio arises from the same mechanism which is suppressing the $\theta \to \pi\pi$ decay mode—a cancellation between the non-strange and $SU(3)$ singlet pieces of the wave-function. This same mechanism also suppresses the total width of the θ and makes it difficult to have a wide state which decays to only $K\bar{K}$ and $\eta\eta$. Both Schnitzer and Rosner have trouble with this pattern of decay modes in the mixing framework. A final model, due to Schechter[85] is very similar to that of Rosner, but includes an additional term arising from an effective Lagrangian model. This

results in the prediction that:

$$\Gamma(\theta \to \eta\eta') \sim 2\Gamma(\theta \to \eta\eta).$$

This model also has difficulty with a wide $\theta(1700)$ which does not have additional decay modes to states like $\rho\rho$.

Helicity Amplitudes

A final topic for discussion is the result of the helicity amplitude analysis for the $\theta(1700)$. The values of x and y for the $\theta(1700)$ are very different from those observed for the $f(1270)$ and the $f'(1515)$. The principle difference is the strong presence of a helicity 2 amplitude. An additional feature is the relative sign of the amplitudes. For the $f(1270)$, x is unambiguously positive. For the $f'(1515)$, the sign of x is ambiguous. For the $\theta(1700)$, both x and y are negative (or equivalently, the helicity 1 and 2 amplitudes have a phase of π relative to the helicity 0 amplitude). Although the physical meaning of these results is unclear, it is an indication of a significant difference between the $\theta(1700)$ and the $f(1270)/f'(1515)$ mesons. This difference is very apparent in the three $x-y$ contour plots presented in the preceding chapters. It is interesting to speculate on the significance of this result in the context of Close's conjecture.[54] He points out that for a non-$q\bar{q}$ state, even in the limit M_X/M_V, there is no need for $y \to 0$, and so a non-$q\bar{q}$ state could well have a large value for y. Perhaps this is the first indication that the $\theta(1700)$ is really different from other $q\bar{q}$ states...

9.3 THE $\xi(2220)$

This new state appears as a very unexpected feature, and there have been many attempts to explain its nature. There are three features requiring explanation: the high mass, the small width and the absence of non-strange decay modes. These

features have been addressed by explanations divided into two broad categories. The first category contains various forms of 'ordinary' hadrons consisting of some number of valence quarks and gluons. These explanations can tolerate widths in the range of 30 – 50 MeV, but are not easily reconciled with widths of less than 15 MeV. This emphasizes the importance of setting a better limit on the width of the $\xi(2220)$. The second category contains various 'extraordinary' states—a Higgs boson being the most mundane of the possibilities. These explanations are highly speculative and are somewhat lacking in predictive power. They generally require that the spin of the $\xi(2220)$ is zero. The possibilities in these two categories are discussed in more detail below, and the implications of the MARK III results are described.

A $q\bar{q}$ State

The presence of a broad enhancement in the $\pi\pi$ final state is an important piece of evidence in favor of this picture. Since the $\pi\pi$ state is very broad ($\Gamma \sim 200$ MeV), it seems likely to be an excited $q\bar{q}$ state, possibly the $h(2040)$ or its $J^P = 2^+$ equivalent. These $L = 3$ nonets are expected to be ideally mixed, as are the $L = 1$ $J^P = 2^+$ and the $L = 2$ $J^P = 3^-$ nonets. This means that the excited $f'(1515)$ (referred to as a ϕ^*) should appear with a rate comparable to that seen for the $\pi\pi$ state (referred to as an ω^*). The ϕ^* state should lie at $\sim$ 2.2 GeV mass, and it is very suggestive that this is where the $\xi(2220)$ is observed. The most problematic feature is the ratio of widths:

$$\frac{\Gamma_{\phi^*}}{\Gamma_{\omega^*}} < 0.2$$

There is a detailed prediction for this case which comes from Godfrey, Kokoski and Isgur.[59] They use a relativistic quark model with QCD corrections to predict the properties of meson states. They hypothesize that the $\xi(2220)$ could be

a $^3F_2$ or a $^3F_4$ $s\bar{s}$ state—this corresponds to an orbital excitation of the $f'(1515)$ with orbital angular momentum $L = 3$. Their model predicts that the $\xi(2220)$ decays predominantly to $K\bar{K}$ and K^*K, at about equal rates, and that the total width of the state is $\sim$ 50 MeV. The $K^*\bar{K}^*$ decay is suppressed by quark model angular momentum factors. The $\pi^+\pi^-$ decay is OZI suppressed and the decay $\Upsilon \rightarrow \gamma\xi$ is suppressed as well. There is also the expectation of a corresponding non-strange isoscalar visible in $\pi\pi$. This picture of the $\xi(2220)$ is very consistent with the measured results, with the exception of the width. If further study confirms the K^*K decay mode, this explanation starts to look more plausible. In particular, as pointed out by Lipkin[79] an $SU(3)$ singlet, *e.g.*, a glueball, would find it very difficult to decay to K^*K.

A Glueball

The traditional predictions for glueball states, discussed in the preceding section, suggest a mass scale of $0.5 - 2$ GeV. These glueballs are associated with the lowest lying cavity modes in the bag model:

$$(TE)^2 \quad J^{PC} = 0^{++}\ ,\ 2^{++}$$

$$(TE)(TM) \quad J^{PC} = 0^{-+}\ ,\ 2^{-+}$$

The decays of such glueballs are expected to be approximately $SU(3)$ symmetric.

This picture does not agree well with the observed $\xi(2220)$ properties—the mass scale is too low and the decay pattern of the $\xi(2220)$ does not seem to be $SU(3)$ symmetric. However, there are several proposals involving excited states in the bag model which correspond to glueballs with higher masses. Chanowitz and Sharpe[64] predict that there is a bag model state with:

$$(TM)^2 \quad J^{PC} = 2^{++}$$

which could have a mass in the 2.2 GeV region. They also make the interesting prediction that, due to the TM nature of this glueball, it should decay predominantly to strange quarks. This effect is due to the strong quark mass dependence of a vertex factor in their spherical cavity approximation. It arises whenever there is a (TM) gluon present. Further study of this hypothesis has been carried out by Ward.[86] There is an additional prediction by Senba and Tanimoto[87] that a three gluon state:

$$(TE)^3 \quad J^{PC} = 0^{++}$$

could be associated with the $\xi(2220)$. This is intriguing because it is a heavy scalar with a purely hadronic character, indicating that a spin measurement of zero may not be a definitive test.

A $q\bar{q}g$ State

Most predictions for $q\bar{q}g$ states place the masses in the $1-2$ GeV region. These states are made in the bag model using a (TE) gluon combined with a $q\bar{q}$ pair in an s=0 or an s=1 state. There are also excited states, made with a (TM) gluon. These have been discussed by Chanowitz[81] and it has been suggested that the $\xi(2220)$ could be an "ω"-like $q\bar{q}g_{TM}$ object. This object is predicted to decay into $K\bar{K}$, $K^*\bar{K}^*$ and the unusual mode $\phi\omega$.

A Higgs Boson

The Higgs is a poorly understood feature of contemporary high energy physics. In simple models, a light Higgs should be narrow, and couple to fermions with a strength proportional to the fermion mass. If such an object had a mass of about 2 GeV, it would couple primarily to $s\bar{s}$ and, at a slightly lower level, to $\mu^+\mu^-$. This makes the $\xi(2220)$ a possible candidate for this state. A fairly complete discussion of this possibility has been given by Haber and Kane[88] and

also by Willey.[89] A slightly different perspective on this question has been taken by Barnett *et al.*[90] In the simplest scheme, there is a single Higgs doublet with a single, neutral Higgs which appears as a physical state. The rate for its production in radiative decays can be computed:[91]

$$\frac{\Gamma(\psi \to \gamma H^0)}{\Gamma(\psi \to \mu^+\mu^-)} = \frac{G_F m_\psi^2}{4\sqrt{2}\pi\alpha}\left(1 - \frac{m_H^2}{m_\psi^2}\right)$$

This predicts a branching ratio:

$$\mathrm{BR}(\psi \to \gamma \mathrm{H}^0) \sim (3.1 \pm 0.5) \times 10^{-5}.$$

This total rate is a factor of about four smaller than the measured rate for $\xi \to K\bar{K}$ alone, and probably rules out such a naive interpretation. A further argument against the single doublet model is that the minimum allowed mass for the neutral Higgs must be greater than the Linde-Weinberg bound[92] of $m_H \sim 7$ GeV in order for the model to be stable against radiative corrections.

It has been pointed out that an anomalously high rate for $\psi \to \gamma H^0$ is a signal for the existence of more than one Higgs doublet. It is also true that the Linde-Weinberg mass bound need not be satisfied if there is more than one Higgs doublet. Clearly, in the case of two or more Higgs doublets, the predictions are less restrictive. It is necessary that all fermions of a given charge couple to a single Higgs doublet, but quarks and leptons may couple to different doublets. For a two doublet model, there are several parameters, one of which is the ratio of vacuum expectation values, denoted by x. In such models, the rate for the radiative decay $\psi \to \gamma H^0$ can be enhanced by a factor of x^2. Such a model, with $x^2 \sim 10$, is quite compatible with the MARK III measurements. However, there are consequences in the Υ region, as pointed out by Willey. The rate for $\Upsilon \to \gamma H^0$ may be either suppressed or enhanced by the factor of x^2. There is an additional prediction that

decays of the form $B \rightarrow H^0 + X$ will be frequent. This is true even for models which have a suppressed $\Upsilon \rightarrow \gamma H^0$ decay. Recent results from CLEO[93] indicate that there is no x^2 enhancement in $\Upsilon \rightarrow \gamma\xi$, and the sequence $B \rightarrow \xi + X$, $\xi \rightarrow K^+K^-$ is not seen at the expected level. These results are inconsistent with the two doublet model.[94] Thus, it appears that the $\xi(2220)$ is not likely to be the neutral Higgs in any plausible model.

Something Truly Strange

There have been several suggestions for strange new physics explanations. The current results have little to say about such speculations, but with larger statistics, these models could be tested. Haber[95] has suggested that the $\xi(2220)$ could be a technicolor object—a pseudo-goldstone boson. He predicts the possibility of very bizarre behavior. There could be two states with similar masses, within the experimental resolution, one of which is a scalar, the other of which is a pseudoscalar. This would appear to the naive experimenter as CP violation. It could be confirmed by seeing a spin zero object which decays to K^*K and K^+K^-.

A different possibility has been raised by Shatz,[96] who offers the speculation that the $\xi(2220)$ is made up of a pair of heavy, neutral, colored scalars. He predicts that one would see a series of new states, some of which could decay to the $\xi(2220)$, and would be seen in $\psi \rightarrow \gamma\pi\pi\xi$. The final state $\psi \rightarrow \gamma KK\pi\pi$ has been examined and there is no sign of the $\xi(2220)$ in the KK mass spectrum.

9.4 Expectations for the Future

In this section, we discuss what one can expect to learn from further study of the analysis topics presented in this thesis. This is particularly germane in light of the possibility that the MARK III experiment could acquire a sample of $\sim 2 \times 10^7$ produced ψ's in the next few years.

The process $\psi \rightarrow \gamma\pi^+\pi^-$ is not primarily limited by statistics, but rather by the very large background from $\psi \rightarrow \rho\pi$. This situation could be improved somewhat with larger statistics, but is not likely to allow significantly better measurements. The best way to study $\psi \rightarrow \gamma\pi\pi$ is by using the $\pi^0\pi^0$ final state. This has very little hadronic background because the processes $\psi \rightarrow \pi^0\pi^0$ and $\psi \rightarrow \pi^0\pi^0\pi^0$ are forbidden by C parity. In the past, the MARK III has been unable to study this final state because of the absence of an all neutral trigger. For the future, there are plans to remedy this situation. Monte Carlo studies indicate that using $6-C$ kinematic fits produces a mass resolution of ~ 20 MeV, which is well suited to studying this region.

A large sample of $\gamma\pi^0\pi^0$ events would allow a significant set of measurements to be made. The previous hints of structure on the high mass side of the $f(1270)$ can be explored. There should be a large enough sample of clean events to decide whether the present structure in the $\theta(1700)$ region has the correct mass, width and J^P to be the $\theta(1700)$. In addition, the signs of structure in the 2 GeV region can be explored. This is relevant to understanding the $\xi(2220)$, since if it is an $s\bar{s}$ state, the corresponding $(u\bar{u}+d\bar{d})$ state should be in this region. Finally, the $\pi^0\pi^0$ final state, which is free of $\rho\pi$ background, is the best place to look for the missing 0^+ glueball, predicted to lie below 1 GeV.

The low mass K^+K^- region has been thoroughly studied with the current data sample, and if there is nothing unusual happening, a larger sample will probably not add significantly to our knowledge of the $\theta(1700)$. However, the possibility has been raised that the $\theta(1700)$ region may contain more than one state. If this is the case, then a very large event sample is required to understand the overlapping resonances. The K_SK_S final state is badly statistics limited in the current data sample, and it is clear that a large increase in statistics would

allow an improved analysis. However, this final state should look like the K^+K^-, with potentially smaller backgrounds, and will probably not add anything to the understanding of the low mass region.

There are several important questions about the $\xi(2220)$ which remain unresolved after the complete analysis of the current data sample. Due to the relatively high interest in this peculiar state, a study has been performed to assess the possibilities for progress. For the purposes of this discussion, a reference sample of 10^7 produced ψ's will be used. This is roughly 5.5 times the size of the 1983 data sample.

There are three general areas of investigation:

- measuring the resonance parameters, especially the width
- measuring the spin
- observation in other decay modes

In order to study the first topic, a large Monte Carlo data set was used. It contained the expected K^+K^- signal plus $K^{*\pm}K^{\mp}$ background. For the reference sample of 10^7 produced ψ's, one would expect $\sim$ 150 signal events in the K^+K^- channel above a background of $\sim$ 100 events. This corresponds to $\sim 10\sigma$ statistical significance in the mass plot. The limit on the width should improve slightly. If the true width is zero, one could expect to set a limit that $\Gamma \leq$ 15 MeV 95% C.L. This estimate was obtained by taking the width analysis which was used on the current data sample and applying it to the Monte Carlo data sample described previously. This limit is significant since it is theoretically quite unlikely to have a hadronic state in this mass region with a width $\ll$ 30 MeV.

The question of the spin analysis is more difficult to evaluate, although it is very important. One way to formulate the question is to ask whether one can expect a safe 3σ determination of the spin. The answer to this is, in general, no. A further

question concerns which channel to use for the analysis. The fundamental problem with the K^+K^- channel is the $K^{*\pm}K^{\mp}$ background. With a larger event sample, it might be possible to remove more of this background with a corresponding loss in efficiency. However, any lingering presence of this background will still impose serious limitations on the ability to resolve different spins. The $K_S K_S$ channel should have ~ 35 events. It is very difficult to extrapolate the signal to background ratio from the current tiny sample. If the background level is favorable, the $K_S K_S$ channel may provide a less ambiguous determination of the spin. It has good acceptance, since the K_s efficiency has very little momentum dependence. The possibility of measuring the spin of the $\xi(2220)$ depends very much on Nature. If the state is really $J = 0$, it will be difficult to prove this, even with 10^7 produced ψ's. If the state is really $J = 2$, it is likely, though not guaranteed, that a spin measurement can be performed, despite the large background.

The final topic involves other decay modes. The most interesting modes are probably:

$$\begin{aligned} \xi(2220) &\to \mu^+\mu^- \\ &\to \pi^+\pi^- \\ &\to K^*\bar{K}^* \\ &\to K^*K \end{aligned}$$

If these modes remain elusive, it will only be possible to improve the upper limits by a factor of 2 to 3. This is not very significant for the non-strange modes, but one of the two K^* modes should start to appear, since it is very hard to imagine an object decaying to $K\bar{K}$ and not to $K\bar{K}+n\pi$. A further significant point is that a state with $J^{PC} = 0^{++}$ cannot decay into a 1^{--} 0^{-+} final state like K^*K. Thus, observation of this decay mode could provide the least ambiguous spin determination. The current limits on $K^*\bar{K}^*$ and K^*K would indicate that possible new limits would be: $K^*\bar{K}^*/K\bar{K} < 0.5 - 1$ and $K^*K/K\bar{K} < 0.3 - 0.5$. If no signal is seen at these

levels, it would be intriguing but not yet astonishing.

It is safe to conclude that a large increase in statistics is vital to an improved understanding of the physics of the radiative ψ decays presented here.

9.5 CONCLUSIONS

The $f(1270)/f'(1515)$ system seems quite consistent with an ideal $q\bar{q}$ nonet. There is no indication of mixing, although it cannot be ruled out.

The $\theta(1700)$ remains a mysterious particle. It appears most likely to be either a four quark state or a glueball. If it is a four quark state, it is unclear why such a state should appear for the first time as a prominent signal in the radiative decays of the ψ. If it is a glueball, then further work is required to understand why it should decay in such a flavor non-symmetric way. The confirmation of a $\theta(1700) \rightarrow \pi\pi$ decay mode at the observed level would be very useful. The presence of this decay at this rate causes difficulties for the four quark hypothesis. On the other hand, it may be quite compatible with an imperfect form of $SU(3)$ flavor symmetry for a glueball. If the $\theta(1700)$ is a single state, there is probably not too much more to be learned about it from radiative ψ decays. If, on the other hand, there is more than one state in this region, a large increase in statistics will be required to understand it.

The $\xi(2220)$ is too poorly measured to be classified. It appears to be inconsistent with even some of the more unorthodox Higgs models. It could well be consistent with an orbitally excited quark state. It could also be consistent with a $q\bar{q}g$ state or a glueball state, especially if the Chanowitz and Sharpe mechanism for enhancing strange decays proves to be correct. The most important measurement, besides the obvious need for confirmation, is a better limit on the total width of the state.

Appendix A. Formalism for Breit-Wigner Fits

In order to extract the parameters for resonances which appear in mass distributions, the maximum likelihood technique has been used. The model which has been chosen consists of a background plus a sum of Breit-Wigners. The likelihood function for this model depends on only one input variable w, which is the invariant mass. The fit will be performed over a finite interval in the invariant mass, denoted by: $[w_{min}, w_{max}]$. The model to be used does not include acceptance corrections, since they are usually described by a slowly varying function over the fit region. It does include the effects of resolution, since they are important for correctly describing narrow resonances.

The background can be represented either as an arbitrary shape by a sum of polynomials, or by a more physically motivated shape such as phase space. For the analyses performed here, only a two-body projection of three-body phase space is required. This can be evaluated analytically[97] for the case where $m \rightarrow m_1+m_2+m_3$ and $w = m_{23}$, in the following form:

$$F_{PS}(m, m_1, m_2, m_3) = \frac{\pi^2}{2m^2 m_{23}} \sqrt{\lambda_1 \lambda_2}$$

$$\lambda_1 = m^4 + m_{23}^4 + m_1^4 - 2\left(m^2 m_{23}^2 + m^2 m_1^2 + m_{23}^2 m_1^2\right)$$

$$\lambda_2 = m_{23}^4 + m_2^4 + m_3^4 - 2\left(m_{23}^2 m_2^2 + m_{23}^2 m_3^2 + m_2^2 m_3^2\right)$$

The only free parameter for this case is the fraction of the total signal which is attributed to background. The normalization of this function over the fit interval is performed numerically:

$$N_{back} = \int_{w_{min}}^{w_{max}} F_{PS}(w) dw$$

and the likelihood function is defined to be:

$$\mathcal{L}_{back} = F_{PS}(w)/N_{back}(w) \qquad (A-1)$$

The polynomial background uses Legendre polynomials with the coefficient for each order being a parameter in the fit. These polynomials are convenient because they are orthogonal over their defined range of $[-1,1]$. This means that the correlations between the coefficients of the different terms in the polynomial sum will be small, and the stability of the fit is enhanced. The background part of the likelihood is written:

$$\mathcal{L}_{back} = \sum_{i=0}^{n_{poly}} a_i P^i(x)$$

where P^i is the i^{th} Legendre polynomial and a scaled variable is defined as the argument of the Legendre polynomials:

$$x = -1 + 2\left[\frac{w - w_{min}}{w_{max} - w_{min}}\right] \quad , \quad x \in [-1,1]$$

In order for this to be a true likelihood, it must be normalized to unity by integrating over the input variable. The normalization is:

$$N_{back} = \int_{w_{min}}^{w_{max}} \mathcal{L}_{back}(w)dw = a_0\,(w_{max} - w_{min})$$

This simple form for the normalization suggests defining new polynomial coefficients:

$$b_i = \frac{a_i}{a_0}$$

and writing a normalized likelihood:

$$\mathcal{L}_{back} = \frac{1}{w_{max} - w_{min}} \sum_{i=0}^{n_{poly}} b_i P^i(x) \qquad (A-2)$$

The resonance part of the likelihood contains two separate models. The first model consists of an incoherent sum of Breit-Wigner probabilities convoluted with a resolution function. This is appropriate for the case where there are resonances with widths which are close to the limits of the detector resolution, or simply for states which do not interfere. The second model consists of a coherent sum of Breit-Wigner amplitudes with relative phases. This model contains no resolution function and is appropriate for the case where there are several overlapping states with large widths.

The resonance model which includes the effects of resolution is constructed in the following manner. The resolution function is assumed to be a Gaussian of the form:

$$R(w,w') = \frac{1}{\sqrt{2\pi}\sigma} e^{-(w-w')^2/2\sigma^2}$$

and the Breit-Wigner is taken to be of the non-relativistic form:

$$f(w) = \frac{1}{\pi} \frac{\Gamma/2}{(w-w_0)^2 + \Gamma^2/4}$$

The non-relativistic form was chosen in part because the convolution can be performed analytically, and in part because the additional complication of a fully relativistic Breit-Wigner with an energy dependent width is only required for very wide resonances near threshold. Using these forms, the likelihood for a single Breit-Wigner can be written:

$$\begin{aligned} \mathcal{L}_{BW} &= \int dw' R(w,w') f(w') \\ &= \frac{1}{\sqrt{2\pi}\sigma} \frac{1}{\pi} \int_{-\infty}^{\infty} dw' \frac{\Gamma/2}{(w-w_0)^2 + \Gamma^2/4} e^{-(w-w')^2/2\sigma^2} \end{aligned}$$

This can be evaluated analytically[98] using the error function of a complex argument:

$$W(x+iy) = e^{-z^2} erfc(-iz) \quad , \quad z = x+iy$$

and the result is:

$$\mathcal{L}_{BW} = \frac{1}{\sqrt{2\pi}\sigma} Re\left[\mathcal{W}\left(\frac{(w-w_0)}{\sqrt{2}\sigma} + i\frac{\Gamma}{2\sqrt{2}\sigma}\right)\right] \qquad (A-3)$$

The $\mathcal{W}$ function can be evaluated numerically, and the normalization over the fit interval:

$$N_{BW} = \int_{w_{min}}^{w_{max}} \mathcal{L}_{BW}(w)dw$$

is evaluated by numeric integration.

The resonance model which includes the effects of interference is constructed in the following manner. The Breit-Wigner is taken to be of the non-relativistic form:

$$f(w) = \frac{\sqrt{\Gamma}}{w - w_0 + i\Gamma/2} \qquad (A-4)$$

or of the relativistic form without an energy-dependent width:

$$f(w) = \frac{\sqrt{w_0\Gamma}}{w^2 - w_0^2 + iw_0\Gamma}$$

(note: the natural normalization for a relativistic Breit-Wigner involves $\int dw^2$ rather than $\int dw$). The non-relativistic form was normally chosen in order to maintain consistency between the coherent and incoherent models. Using these forms, the likelihood for a sum of n_{AMP} Breit-Wigners can be written:

$$\mathcal{L}_{AMP} = \left|\frac{1}{w - w_1 + i\Gamma_1/2} + \sum_{k=2}^{n_{AMP}} \delta_{k-1} e^{-i\varphi_{k-1}} \frac{1}{w - w_k + i\Gamma_k/2}\right|^2 \qquad (A-5)$$

The normalization for the likelihood function can be evaluated numerically over the fit interval:

$$N_{AMP} = \int_{w_{min}}^{w_{max}} \mathcal{L}_{AMP}(w)dw$$

The individual likelihood functions can now be combined to allow fits to any combination of background plus non-interfering Breit-Wigners plus interfering Breit-Wigners. This gives the final form for the likelihood function:

$$\mathcal{L} = \left(1 - \sum_{j=1}^{n_{BW}} \alpha_j - \beta\right) \mathcal{L}_{back} + \sum_{j=1}^{n_{BW}} \alpha_j \frac{\mathcal{L}_{BW}^j}{N_{BW}^j} + \beta \frac{\mathcal{L}_{AMP}}{N_{AMP}} \qquad (A-6)$$

The parameters involved are the $n_{poly} - 1$ background polynomial coefficients b_i, the n_{BW} sets of Breit-Wigner parameters $(\alpha_j, w_{0j}, \Gamma_j, \sigma_j)$, the n_{AMP} sets of Breit-Wigner parameters $(\delta_k, \varphi_k, w_{0k}, \Gamma_k)$ and the fraction β.

In order to evaluate the total likelihood for a set of events, the standard procedure is to form a sum over the $ln\mathcal{L}$ for each event:

$$ln\mathcal{L}_{total} = \sum_{evts} ln\mathcal{L} \qquad (A-7)$$

If there are many events in this sum, it may be very time-consuming to evaluate. A faster technique involves 'classifying' or binning the data, *e.g.*, in a histogram. If the total data sample of n events is divided into N bins, then the total probability is given by the multinomial distribution:

$$\mathcal{L}_{total} = n! \prod_{i=1}^{N} \frac{1}{n_i!} p_i^{n_i}$$

where p_i is the probability to be in the i^{th} bin and n_i is the number of events in the i^{th} bin. The probability is approximated by the likelihood evaluated at the bin center: $p_i = \mathcal{L}(w_i)$. Since the fit parameter dependence is all contained in the p_i, one can ignore the other terms and write:

$$ln\mathcal{L}_{total} = \sum_{bins} n_i ln p_i = \sum_{bins} n_i ln\mathcal{L} \qquad (A-8)$$

It is therefore convenient to perform 'un-binned' fits where the likelihood is summed over individual events, or to perform 'binned' fits where the likelihood is summed over bins weighted by their contents. In either case, the general minimization program MINUIT[99] is used to find the minimum of the function $f = -ln\mathcal{L}_{total}$ and estimate the parameter values and their errors.

A topic requiring further discussion is the estimation of the quality and significance of the fit results. There are two broad areas which are important for the current discussion. The first is interval estimation, or estimating the errors on the fit parameters. The second is hypothesis testing, or deciding which fits best describe the data and quantifying the significance of the conclusions. An excellent discussion of these topics may be found in Ref. 100 , and the present discussion draws heavily from those references.

The question of interval estimation for maximum likelihood fits is a fairly simple one. The standard technique is to associate a change in the likelihood with confidence levels for a normal distribution. This assumes that the likelihood function is approximately parabolic at the maximum, and is a very general technique. The association is:

$$n_\sigma^2 = 2\,[\delta(ln\mathcal{L})]\,,$$

where n_σ is the number of 'standard deviations' calculated using a normal distribution, and $\delta(ln\mathcal{L})$ is the change in the likelihood function. To compute a n_σ confidence interval for a parameter: $\alpha_1 \leq \alpha \leq \alpha_2$, the following procedure is used. The function:

$$f(\alpha) = -ln\mathcal{L}_{max}(\alpha)$$

is evaluated for a series of values for α near the optimal value. Each calculation of f requires a re-maximization of the likelihood. The likelihood change $f(\alpha) - f(\alpha_{fit})$ which corresponds to the correct confidence level determines the desired values of

α_1 and α_2. This procedure correctly accounts for the correlations among differe. fit parameters, and has been used whenever an interval estimate was required. It is implemented in the MINUIT minimization package using the subroutine MINOS.

The question of hypothesis testing is, in general, a difficult problem. The goal is either to compare several hypotheses and choose the best using a relative test, or to make some absolute statement about 'goodness-of-fit' without discussing alternate hypotheses. There are three categories of comparisons which can be made. The first involves a comparison of two simple (*i.e.*, completely determined) hypotheses. This has a simple, rigorous solution and poses no particular challenges. The second category involves comparing composite (*i.e.*, not completely determined) hypotheses from the same common family of functions. In this case, one hypothesis can be transformed into the other by changing the values of the parameters. This case also has a general solution for the large statistics limit. The final category involves comparing unrelated composite hypotheses. This case has no general solution, and the statistical significance of the standard test statistic generally depends on which hypothesis is correct. With this in mind, we proceed to discuss the test statistics which have been used for the Breit-Wigner fits.

Two tests have been used to discuss the fits. The first is a version of the standard Pearson's χ^2 test. This is defined, for a given fit and a given histogram, using the test statistic:

$$\chi^2 = \sum_{i=1}^{n_{bins}} \frac{(n_{fit} - n_i)^2}{n_{fit}} \qquad (A-9)$$

where n_i is the number of events in the i^{th} histogram bin and n_{fit} is the number of events predicted by the fit for that bin. This statistic should be distributed like a χ^2 variable for n_{dof} degrees of freedom. The number of degrees of freedom for this

statistic is not always clear. The additional constraint:

$$\sum_{i=1}^{n_{bins}} n_{fit} = \sum_{i=1}^{n_{bins}} n_i = N$$

has been imposed on the fit. For the case where a 'binned' likelihood fit is performed,

$$n_{dof} = n_{bins} - n_{param} - 1.$$

For the case where an 'un-binned' fit is performed, n_{dof} should be the same, but the result is not as rigorous. This statistic does have the advantage that it describes, in absolute terms, whether the fit is consistent with the data or not. It is a non-parametric statistic, and does not depend on the details of the hypotheses being compared.

The second test is a form of the likelihood ratio test. If the fits contain identical numbers of parameters, then one is comparing two simple hypotheses, and the test statistic is:

$$\lambda = ln\left[\frac{\mathcal{L}_1}{\mathcal{L}_2}\right]. \qquad (A-10)$$

This is the standard Neyman-Pearson test, and the change in likelihood can be interpreted in the manner discussed above for interval estimation. The more general case occurs when one fit is a restricted form of the other. Then the following test statistic is defined:

$$\chi^2 = -2ln\left[\frac{\mathcal{L}(\hat{\Omega})}{\mathcal{L}(\Omega)}\right], \qquad (A-11)$$

where $\hat{\Omega}$ is the subset of the total parameter space over which the first fit is performed, and Ω is the full parameter space over which the second fit is performed. This test statistic should be asymptotically distributed like a χ^2 variable for r degrees of freedom, where $r = dim(\Omega) - dim(\hat{\Omega})$, and $dim()$ is the dimension of the parameter space in question. This statistic is only valid for the case where the

fits are members of the same family of composite hypotheses, as discussed above. In addition, although this technique may work well for small statistics, it has the disadvantage of providing only a relative probability for the specified hypotheses.

Appendix B. Calculation of Angular Distributions for Decays

B.1 The Single Resonance Formulation

A Description in Terms of Helicity Amplitudes

The aim is to calculate the production and decay angular distributions for the decay $\psi \to \gamma X$, $X \to 0^- + 0^-$. The calculation of these angular distributions is carried out using the helicity formalism. The canonical reference on the subject is J. Richman's '*An Experimenter's Guide to the Helicity Formalism*'[101] wherein the great mysteries of Jacob and Wick[102] are discussed with refreshing clarity. The fundamental formula for a two-body decay amplitude $A(X \to a_1 + a_2)$ is:

$$A \sim D^{J}_{M}{}^{*}{}_{\lambda}(\varphi, \vartheta, -\varphi) A_{\lambda_1 \lambda_2} \qquad (B-1)$$

where:

$M =$ the projection of the X spin along the z axis

$\lambda_1, \lambda_2 =$ the helicities of the decay products 1 and 2

$\lambda = \lambda_1 - \lambda_2$

$\vartheta, \varphi =$ the angles of the decay products in the X center of mass

The amplitude for the two sequential two-body decay processes:

$$\psi \to \gamma X$$
$$\qquad\quad \hookrightarrow a + b$$

where a and b are both pseudoscalars involves a sum over the unobservable intermediate helicity. For the case of interest, it can be written in the following form:

$$T_{M\lambda_\gamma}(\Omega) = \sum_{\lambda_X} D^{J}_{\lambda_X}{}^{*}{}_{0}(\Omega_3)\; D^{1}_{M}{}^{*}{}_{\lambda_X - \lambda_\gamma}(\Omega_1)\; A_{\lambda_X \lambda_\gamma} \qquad (B-2)$$

where:

M = the projection of the ψ spin along the z axis

λ_γ = the helicity of the photon along the X direction of motion

λ_X = the helicity of the X along the X direction of motion

$\Omega_1 = (\theta_1, \phi_1)$ for the X in the lab frame (the ψ center of mass)

$\Omega_3 = (\theta_3, \phi_3)$ for the decay meson in the X center of mass

The requirement of parity invariance imposes the constraint that:

$$A_{-\lambda_X-\lambda_\gamma} = \eta_\psi \eta_X \eta_\gamma (-1)^{J_X + J_\gamma - J_\psi} A_{\lambda_X \lambda_\gamma} \qquad (B-3)$$

where η is the intrinsic parity. For the case under consideration here, this means that:

$$A_{-\lambda_X-\lambda_\gamma} = A_{\lambda_X \lambda_\gamma}$$

Thus, the six initial amplitudes:

$$\{A_{21}\ ,\ A_{11}\ ,\ A_{01}\ ,\ A_{0-1}\ ,\ A_{-1-1}\ ,\ A_{-2-1}\}$$

are reduced to the set:

$$\{A_{21}\ ,\ A_{11}\ ,\ A_{01}\}$$

where the second index will be suppressed in subsequent expressions.

The total cross-section is expressed as a sum over the probabilities for the (in principle observable) photon helicity and ψ polarization, weighted by the initial populations of the ψ polarization states. The ψ, being a massive spin one particle, can exist in three possible M states: $M = 0, \pm 1$. However, the e^+e^- production mechanism for the ψ results in a strong suppression of the $M = 0$ component. This is due to the helicity conservation required at the $ee\gamma$ vertex by QED, and results in a suppression of $M = 0$ by $\sim m_e/E_e \sim 10^{-3}$. In addition, at the beam energy

corresponding to the mass of the ψ the polarization of the beams found at SPEAR is not important.[103] This is a delicate point, because synchrotron radiation in a magnetic field is a natural mechanism for producing polarization at SPEAR. The characteristic build-up time for this polarization is:

$$T_{pol} \sim E^{-5}$$

This gives a build-up time for SPEAR at the ψ of about twenty hours, in the absence of depolarization effects due to machine resonances, which introduces a negligible polarization during the normal $1-2$ hour data runs. This means the ψ is prepared for us in a simple initial state, consisting of an incoherent sum of equal parts of $M = \pm 1$. The photon helicity takes on the values $\lambda_\gamma = \pm 1$, as expected for a massless spin one particle. The total cross-section is then expressed as:

$$\frac{d\sigma}{d\Omega} = \sum_{\lambda_\gamma, M} \left| T_{M\lambda_\gamma} \right|^2 \qquad (B-4)$$

The result of completing the summations and substituting for the D functions associated with the production of the X is:

$$\begin{aligned}
\frac{d\sigma}{d\Omega} \sim\ & |A_0|^2 d^J_{00}(\theta_3)^2(1+\cos^2\theta_1) \\
& + 2\,|A_1|^2 d^J_{10}(\theta_3)^2 \sin^2\theta_1 \\
& + |A_2|^2 d^J_{20}(\theta_3)^2(1+\cos^2\theta_1) \\
& + \sqrt{2} Re[A_0 A_1^*] d^J_{10}(\theta_3) d^J_{00}(\theta_3) \sin 2\theta_1 \cos(\phi_3 - \phi_1) \\
& + 2 Re[A_0 A_2^*] d^J_{20}(\theta_3) d^J_{00}(\theta_3) \sin^2\theta_1 \cos 2(\phi_3 - \phi_1) \\
& - \sqrt{2} Re[A_1 A_2^*] d^J_{20}(\theta_3) d^J_{10}(\theta_3) \sin 2\theta_1 \cos(\phi_3 - \phi_1)
\end{aligned}$$

This can be simplified by writing:

$$A_0 = |A_0| e^{i\varphi_0}$$

$$A_1 = |A_1|e^{i\varphi_1}$$

$$A_2 = |A_2|e^{i\varphi_2}$$

and defining:

$$x \equiv \frac{|A_1|}{|A_0|} \quad , \quad \varphi_x \equiv \varphi_1 - \varphi_0$$

$$y \equiv \frac{|A_2|}{|A_0|} \quad , \quad \varphi_y \equiv \varphi_2 - \varphi_0$$

After these substitutions, one gets the following expression:

$$\begin{aligned}\frac{d\sigma}{d\Omega} \sim\ & d^J_{00}(\theta_3)^2(1+\cos^2\theta_1) \\ & + 2x^2 d^J_{10}(\theta_3)^2 \sin^2\theta_1 \\ & + y^2 d^J_{20}(\theta_3)^2(1+\cos^2\theta_1) \\ & + \sqrt{2}x\cos\varphi_x d^J_{10}(\theta_3)d^J_{00}(\theta_3)\sin 2\theta_1\cos(\phi_3-\phi_1) \\ & + 2y\cos\varphi_y d^J_{20}(\theta_3)d^J_{00}(\theta_3)\sin^2\theta_1\cos 2(\phi_3-\phi_1) \\ & - \sqrt{2}xy\cos(\varphi_y-\varphi_x)d^J_{20}(\theta_3)d^J_{10}(\theta_3)\sin 2\theta_1\cos(\phi_3-\phi_1)\end{aligned} \qquad (B-5)$$

The standard coordinate system for evaluating the angles is defined as follows:

lab frame: right handed system (x, y, z)

$\cos\theta_\gamma \equiv \hat{\gamma}\cdot\hat{z}$

$\hat{\gamma}$ is the direction of the photon in the lab

center of mass frame: right handed system (x', y', z')

$\hat{z}' = \hat{\gamma}$

$\hat{y}' \sim \hat{z}\times\hat{z}'$

$\hat{x}' = \hat{y}'\times\hat{z}'$

$\cos\theta_m \equiv \hat{K}^+\cdot\hat{z}'$

$\phi_m \equiv \tan^{-1}\left(\frac{\hat{K}^+\cdot\hat{y}'}{\hat{K}^+\cdot\hat{x}'}\right)$

$\hat{K}^+$ = direction of the K^+ in the X center of mass

The coordinate transformation to the 'standard' coordinate system requires that θ_1 and θ_3 refer to the photon direction rather than the X direction. This corresponds to a rotation about the x axis in the X center of mass frame. This produces the following change:

$$\theta_3 \rightarrow \pi - \theta_3 \quad \phi_3 \rightarrow 2\pi - \phi_3$$

Examination of the expression for the cross-section shows that this coordinate transformation is equivalent to a change in the sign of x in the cross-section expression.

The association with the angles in the standard coordinate system can then be made in the following manner:

$$\theta_\gamma \leftrightarrow \theta_1$$

$$\theta_m \leftrightarrow \theta_3$$

$$\phi_m \leftrightarrow \phi_3 - \phi_1$$

The definition of ϕ_m as the difference between the production angle ϕ_1 and the decay angle ϕ_3 is consistent because ϕ_3 is the same in the X center of mass frame and the lab frame. It is also necessary that the cross-section depend on the difference of these angles, since there is no natural origin for either ϕ_1 or ϕ_3. This finally leads us to the general form for the angular distribution:

$$\begin{aligned} W_J(\Omega) \sim\ & d^J_{00}(\theta_m)^2(1+\cos^2\theta_\gamma) \\ & + 2x^2 d^J_{10}(\theta_m)^2 \sin^2\theta_\gamma \\ & + y^2 d^J_{20}(\theta_m)^2(1+\cos^2\theta_\gamma) \\ & - \sqrt{2}x\cos\varphi_x d^J_{10}(\theta_m) d^J_{00}(\theta_m) \sin 2\theta_\gamma \cos\phi_m \\ & + 2y\cos\varphi_y d^J_{20}(\theta_m) d^J_{00}(\theta_m) \sin^2\theta_\gamma \cos 2\phi_m \\ & + \sqrt{2}xy\cos(\varphi_y - \varphi_x) d^J_{20}(\theta_m) d^J_{10}(\theta_m) \sin 2\theta_\gamma \cos\phi_m \end{aligned} \qquad (B-6)$$

Note that a change of convention from $\hat{z}$ in the positron direction (the convention used here) to $\hat{z}$ in the electron direction leaves the angular correlation function invariant, as expected. This can be seen by performing a rotation about the x axis by π. The corresponding angular transformation is:

$$\theta_\gamma \rightarrow \pi - \theta_\gamma$$

$$\theta_m \rightarrow \theta_m$$

$$\phi_m \rightarrow \phi_m + \pi$$

Upon substituting into Eqn. (B-6), one finds that the sign change in $\sin 2\theta_\gamma$ is compensated by the sign change in $\cos \phi_m$.

No restrictions have been made on the relative phases of the helicity amplitudes. The standard approximation is that the amplitudes are relatively real, which corresponds to $\varphi_x = \varphi_y = 0$. The introduction of the phases corresponds to the following substitutions in the various terms in the angular correlation function:

$$1 \leftrightarrow 1$$

$$x^2 \leftrightarrow x^2$$

$$y^2 \leftrightarrow y^2$$

$$x \leftrightarrow x \cos \varphi_x$$

$$y \leftrightarrow y \cos \varphi_y$$

$$xy \leftrightarrow xy \cos(\varphi_y - \varphi_x)$$

The effect of varying the phases is felt only in the off-diagonal terms and has a weak influence on the results since these terms integrate to zero when averaged over ϕ_m. It is also useful to calculate the normalization, defined by:

$$N_J \equiv \int_{-1}^{1} d\cos\theta_\gamma \int_{-1}^{1} d\cos\theta_m \int_0^{2\pi} d\phi_m \, W_J(\Omega)$$

and the one dimensional projections, defined by:

$$P_J^1(\cos\theta_\gamma) \equiv \int_{-1}^{1} d\cos\theta_m \int_0^{2\pi} d\phi_m \, W_J(\Omega)$$

$$P_J^2(\cos\theta_m) \equiv \int_{-1}^{1} d\cos\theta_\gamma \int_0^{2\pi} d\phi_m \, W_J(\Omega)$$

$$P_J^3(\phi_m) \equiv \int_{-1}^{1} d\cos\theta_\gamma \int_{-1}^{1} d\cos\theta_m$$

These equations may be explicitly evaluated for the cases of interest. This produces the formulae displayed on the following pages.

$\boxed{J = 0:}$

$$W_0(\Omega) = 1 + \cos^2\theta_\gamma$$

$$N_0 = \frac{32\pi}{3}$$

$\boxed{J = 2:}$

$$
\begin{aligned}
W_2(\Omega) = {} & \frac{1}{4}(3\cos^2\theta_m - 1)^2(1 + \cos^2\theta_\gamma) \\
& + \frac{\sqrt{3}}{4}x\cos\varphi_x(3\cos^2\theta_m - 1)\sin 2\theta_m \sin 2\theta_\gamma \cos\phi_m \\
& + \frac{\sqrt{6}}{4}y\cos\varphi_y(3\cos^2\theta_m - 1)\sin^2\theta_m \sin^2\theta_\gamma \cos 2\phi_m \\
& + 3x^2\sin^2\theta_m\cos^2\theta_m\sin^2\theta_\gamma \\
& - \frac{3\sqrt{2}}{8}xy\cos(\varphi_y - \varphi_x)\sin^2\theta_m \sin 2\theta_m \sin 2\theta_\gamma \cos\phi_m \\
& + \frac{3}{8}y^2\sin^4\theta_m(1 + \cos^2\theta_\gamma)
\end{aligned}
$$

$$
\begin{aligned}
P_2^1(\cos\theta_\gamma) &= \frac{8\pi}{5}x^2\sin^2\theta_\gamma + \frac{4\pi}{5}(1 + y^2)(1 + \cos^2\theta_\gamma) \\
P_2^2(\cos\theta_m) &= \frac{4\pi}{3}(3\cos^2\theta_m - 1)^2 + 8\pi x^2\cos^2\theta_m\sin^2\theta_m + 2\pi y^2\sin^4\theta_m \\
P_2^3(\phi_m) &= \frac{16}{15}(1 + x^2 + y^2) - \frac{8\sqrt{6}}{45}y\cos\varphi_y\cos 2\phi_m
\end{aligned}
$$

$$
N_2 = \frac{32\pi(1 + x^2 + y^2)}{15}
$$

$\boxed{J = 4:}$

$$
\begin{aligned}
W_4(\Omega) = {} & \frac{1}{64}(35\cos^4\theta_m - 30\cos^2\theta_m + 3)^2(1+\cos^2\theta_\gamma) \\
& + \frac{\sqrt{10}}{64}x\cos\varphi_x(7\cos^2\theta_m - 3)(35\cos^4\theta_m - 30\cos^2\theta_m + 3)\sin 2\theta_m \sin 2\theta_\gamma \cos\phi_m \\
& + \frac{\sqrt{10}}{32}y\cos\varphi_y(7\cos^2\theta_m - 1)(35\cos^4\theta_m - 30\cos^2\theta_m + 3)\sin^2\theta_m \sin^2\theta_\gamma \cos 2\phi_m \\
& + \frac{5}{8}x^2(7\cos^2\theta_m - 3)^2\cos^2\theta_m \sin^2\theta_m \sin^2\theta_\gamma \\
& - \frac{5}{16}xy\cos(\varphi_y - \varphi_x)(7\cos^2\theta_m - 1)(7\cos^2\theta_m - 3)\sin^3\theta_m \cos\theta_m \sin 2\theta_\gamma \cos\phi_m \\
& + \frac{5}{32}y^2(7\cos^2\theta_m - 1)^2\sin^4\theta_m(1+\cos^2\theta_\gamma)
\end{aligned}
$$

$$
\begin{aligned}
P_4^1(\cos\theta_\gamma) &= \frac{8\pi}{9}x^2\sin^2\theta_\gamma + \frac{4\pi}{9}(1+y^2)(1+\cos^2\theta_\gamma) \\
P_4^2(\cos\theta_m) &= \frac{\pi}{12}(35\cos^4\theta_m - 30\cos^2\theta_m + 3)^2 \\
&\quad + \frac{5\pi}{3}x^2(7\cos^2\theta_m - 3)^2\cos^2\theta_m \sin^2\theta_m \\
&\quad + \frac{5\pi}{6}y^2(7\cos^2\theta_m - 1)^2\sin^4\theta_m \\
P_4^3(\phi_m) &= \frac{16}{27}(1+x^2+y^2) - \frac{16\sqrt{10}}{135}y\cos\varphi_y\cos 2\phi_m
\end{aligned}
$$

$$
N_4 = \frac{32\pi(1+x^2+y^2)}{27}
$$

A Description in Terms of Multipole Amplitudes

An alternate description of the radiative decay $\psi \rightarrow \gamma X$ can be defined using a multipole expansion for the radiative photon.[104] In this case, one has an initial state with spin J and parity P_ψ. There are two final state particles with spins and parities labeled s_1, P_1 (the X) and s_2, P_2 (the γ) which combine with an orbital angular momentum l to give the total $J = l + s_1 + s_2$. The amplitudes for this case are classified by the angular momentum: $j_2 = l + s_2$ and the parity: $P = (-1)^{j_2}\omega$, $\omega = P_1 P_\psi (-1)^{j_2}$ of the radiated photon.

j_2	ω	Multipole
1	+1	$E1$
1	−1	$M1$
2	+1	$E2$
2	−1	$M2$
	Etc.	

The helicity amplitudes defined previously can be re-expressed in terms of multipole amplitudes. The result of performing the calculations is:

$$A_{\lambda_1\lambda_2} = \sum_{j_2} B^{j_2}_{\lambda_1\lambda_2} M^{\omega}_{j_2}$$

where

$A_{\lambda_1\lambda_2}$ are the helicity amplitudes,

$B^{j_2}_{\lambda_1\lambda_2}$ are calculated coefficients,

$M^{\omega}_{j_2}$ are the multipole amplitudes.

For the special case of $\psi \rightarrow \gamma X$, the $B^{j_2}_{\lambda_1\lambda_2}$ are given by:

λ_1	λ_2	$j_2 = s_1 - 1$	$j_2 = s_1$	$j_2 = s_1 + 1$
0	1	$(-1)^{s_1}\sqrt{\frac{s_1-1}{2(2s_1+1)}}$	$\frac{-1}{\sqrt{2}}(-1)^{s_1}$	$(-1)^{s_1}\sqrt{\frac{s_1+2}{2(2s_1+1)}}$
1	1	$(-1)^{s_1}\sqrt{\frac{s_1^2-1}{s_1(2s_1+1)}}$	$-\sqrt{\frac{1}{s_1(s_1+1)}}$	$-(-1)^{s_1}\sqrt{\frac{s_1(s_1+2)}{(s_1+1)(2s_1+1)}}$
2	1	$(-1)^{s_1}\sqrt{\frac{(s_1+1)(s_1+2)}{2s_1(2s_1+1)}}$	$(-1)^{s_1}\sqrt{\frac{(s_1-1)(s_1+2)}{2s_1(s_1+1)}}$	$(-1)^{s_1}\sqrt{\frac{s_1(s_1-1)}{(2s_1+1)(2s_1+2)}}$

The cases of interest here are:

$\underline{J^P(x) = 2^+}$ $\Rightarrow$ the allowed amplitudes are: $E1$, $M2$, $E3$.

$$\begin{aligned} A_{01} &= \sqrt{\tfrac{1}{10}}M_1^+ - \sqrt{\tfrac{1}{2}}M_2^- + \sqrt{\tfrac{2}{5}}M_3^+ \\ A_{11} &= \sqrt{\tfrac{3}{10}}M_1^+ - \sqrt{\tfrac{1}{6}}M_2^- - \sqrt{\tfrac{8}{15}}M_3^+ \\ A_{21} &= \sqrt{\tfrac{3}{5}}M_1^+ + \sqrt{\tfrac{1}{3}}M_2^- + \sqrt{\tfrac{1}{15}}M_3^+ \end{aligned}$$

The pure multipoles produce the following helicity amplitude ratios:

$$\begin{aligned} E1: &\quad x = \sqrt{3} \quad y = \sqrt{6} \\ M2: &\quad x = \sqrt{\tfrac{1}{3}} \quad y = -\sqrt{\tfrac{2}{3}} \\ E3: &\quad x = -\sqrt{\tfrac{4}{3}} \quad y = \sqrt{\tfrac{1}{6}} \end{aligned}$$

If one assumes that the $E3$ multipole is negligible, then the following relation exists:

$$y = 2\sqrt{2}\left[x - \sqrt{3}/2\right]$$

and one solution is: $x = \sqrt{3}/2, \quad y = 0.$

$\underline{J^P(x) = 4^+}$ $\Rightarrow$ the allowed amplitudes are: $E3$, $M4$, $E5$.

$$\begin{aligned} A_{01} &= \sqrt{\tfrac{1}{6}}M_3^+ - \sqrt{\tfrac{1}{2}}M_4^- + \sqrt{\tfrac{1}{3}}M_5^+ \\ A_{11} &= \sqrt{\tfrac{5}{12}}M_3^+ - \sqrt{\tfrac{1}{20}}M_4^- - \sqrt{\tfrac{8}{15}}M_5^+ \\ A_{21} &= \sqrt{\tfrac{5}{12}}M_3^+ + \sqrt{\tfrac{9}{20}}M_4^- + \sqrt{\tfrac{2}{15}}M_5^+ \end{aligned}$$

Direct Decays of the ψ

The sequential two body decay helicity formulation can also be used to calculate the angular distributions for the direct decays of the $\psi \rightarrow 1^- + 0^-$, with $1^- \rightarrow 0^- + 0^-$. These decays appear as backgrounds for the radiative decays, in the form of $\psi \rightarrow \rho\pi$ and $\psi \rightarrow K^{*\pm}K^{\mp}$. The equivalent of Eqn. (B-2) is written as:

$$T_M(\Omega) = \sum_{\lambda_V} D^{1}_{\lambda_V}{}^{*}{}_{0}(\Omega_3)\; D^{1}_{M}{}^{*}{}_{\lambda_V}(\Omega_1)\; A_{\lambda_V} \qquad (B-7)$$

where:

M = the projection of the psi spin along the z axis

λ_V = the helicity of the vector along the its direction of motion

$\Omega_1 = (\theta_1, \phi_1)$ for the vector in the lab frame

$\Omega_3 = (\theta_3, \phi_3)$ for the decay meson in the vector center of mass

The requirement of parity invariance is imposed through Eqn. (B-3) resulting in the following relationship:

$$A_{-\lambda_V} = -A_{\lambda_V}$$

This means that the amplitude for $\lambda_V = 0$ must vanish, and the amplitudes for $\lambda_V = \pm 1$ are equal and opposite in sign. It now follows that the angular distributions are uniquely specified, since there is only an overall scale left. The remainder of the calculation is straight-forward, and the result is:

$$W_{PV}(\Omega) = \sin^2\theta_3 \left[1 + \cos^2\theta_1 + \sin^2\theta_1 \cos 2(\phi_3 - \phi_1)\right] \qquad (B-8)$$

There are several interesting properties of this result. One is that the vector is completely polarized (it has a helicity of ± 1 only). This gives rise to the $\sin^2\theta$ distribution for the decay products in the vector center of mass. Another feature is

that when the cross-section is integrated over ϕ, the remaining dependence for θ_1 is $1 + \cos^2\theta$. A final feature is that the cross-section vanishes when $\theta_1 = \pi/2$ and $\phi_3 - \phi_1 = \pi/2$. This corresponds to the case where the decay plane for the three pseudo-scalars is normal to the beam axis.

B.2 THE MULTIPLE RESONANCE FORMULATION

The previous discussion evaluated the formulas for the production and decay angular distributions of a single resonance. In that case, there is no need to consider the mass dependence of the amplitudes. A more complex situation arises if there are two overlapping resonances. This situation will be discussed in a qualitative manner in order to shed some light on the additional complications which arise when the full mass and angle dependent amplitudes are allowed to interfere.

For the case of two resonances, the total cross-section will be of the form:

$$\frac{d\sigma}{dm d\Omega} = |A_1(m,\Omega) + A_2(m,\Omega)|^2 \qquad (B-9)$$

These amplitudes can be written as a product of a Breit-Wigner amplitude, such as that in Eqn. (A-4), for the mass dependence, and a helicity amplitude sum, such as that in Eqn. (B-2), for the angular dependence. In Appendix A the procedure for extracting Breit-Wigner parameters from the mass distribution was discussed. For the purpose of comparison with those results, it is interesting to study the mass projection of the cross-section in Eqn. (B-9). The projection of the cross-section is of the form:

$$\frac{d\sigma}{dm} = \frac{d\sigma_1}{dm} + \frac{d\sigma_2}{dm} + 2\int Re\,[A_1(m,\Omega)^* A_2(m,\Omega)]\, d\Omega$$

Substituting from Eqn. (B-2) gives the result for the cross-term:

$$\sim Re\left[(A_1(m)^* A_2(m))\sum_{\lambda_X}\sum_{\lambda_{X'}}\int D^{J_1\,*}(\Omega_3)D^{J_2}(\Omega_3)D^{1\,*}(\Omega_1)D^{1}(\Omega_1)d\Omega\right]$$

Here we can use the orthogonality of the D^J functions:

$$\int D^J_{mn}(\Omega)D^{J'}_{m'n'}(\Omega)d\Omega = \delta_{JJ'}\delta_{mm'}\delta_{nn'},$$

to derive the result that the interference term vanishes unless $J_1 = J_2$. This result depends on our being able to perform the integrations over $d\Omega$ correctly. This may not be strictly true if the detector which is measuring this cross-section does not have complete acceptance, but it should still be a good approximation.

Appendix C. The Full Spin Analysis Formalism

C.1 The Fit Formalism

The fitting technique to be used for the spin analysis is the well known maximum likelihood method. This has a number of advantages which will become more apparent as the formalism is described.

For a perfect detector, the definition of the likelihood function for the spin analysis is:

$$ln\mathcal{L} = \sum_{evts} ln\left[\frac{W_J(\Omega_i;x)}{N_J(x)}\right]$$

where W_J and N_J are the angular correlation function and the normalization described in Appendix B. The Ω_i are the set of measured angles for an event i. The x are the set of parameters for the given hypothesis. This likelihood represents the "probability" that the given set of events are distributed as expected for a state with the given J and x. The $ln\mathcal{L}$ function is normally used for calculation since it requires a sum over event probabilities rather than the numerically imprecise product of event probabilities.

An imperfect detector has two features which require modification of the likelihood function: acceptance and resolution. They can be taken into account by defining two functions. The first function is the acceptance function $\epsilon(\Omega)$, which represents the probability that an event with angles Ω will be detected. The second function is a resolution function $R(\Omega',\Omega)$, which represents the probability that an event with angles Ω' would be measured to have angles Ω. The full likelihood function then becomes:

$$ln\mathcal{L} = \sum_{evts} ln\left[\frac{\int d\Omega' R(\Omega',\Omega)\epsilon(\Omega')W_J(\Omega';x)}{\int d\Omega \int d\Omega' R(\Omega',\Omega)\epsilon(\Omega')W_J(\Omega';x)}\right]$$

For this analysis, the resolution in angles is very good and so the resolution function can be approximated by a δ function: $R(\Omega', \Omega) = \delta(\Omega' - \Omega)$. In this approximation, the likelihood function can be written:

$$\begin{aligned} ln\mathcal{L} &= \sum_{evts} ln\left[\frac{\epsilon(\Omega)W_J(\Omega;x)}{\int d\Omega\epsilon(\Omega)W_J(\Omega;x)}\right] \\ &= \sum_{evts} ln\left[\frac{W_J(\Omega;x)}{\int d\Omega\epsilon(\Omega)W_J(\Omega;x)}\right] + ln\left[\epsilon(\Omega)\right] \end{aligned}$$

Since $\epsilon(\Omega)$ does not depend on the parameters in the problem, the $ln\epsilon$ term gives a constant contribution to the likelihood and can be ignored. This produces the very elegant result that the $ln\mathcal{L}$ function depends on the acceptance only through the normalization integral. As a practical matter, this means that the acceptance function is never explicitly evaluated. This is one of the advantages of using the likelihood technique; a χ^2 fit would require evaluating the acceptance for each event.

In order to evaluate the normalization integral, a Monte Carlo technique[105] is used. We want to calculate the integral of a function $f(x)$:

$$N = \int_a^b f(x)dx$$

To approximate this integral, let X be a random variable, uniformly distributed over the integration interval $[a, b]$. Then:

$$N \sim \frac{1}{n}\sum_{i=1}^{n} f(x_i)$$

where the sum is over n values for the random variable X. For the integral required here:

$$N \sim \frac{1}{n}\sum_{i=1}^{n} W_J(\Omega_i; x)\epsilon(\Omega_i)$$

where the Ω_i are uniformly distributed over the integration region. The measure used for this problem has the following variables uniformly distributed:

$$\cos\theta_\gamma, \cos\theta_m \in [-1, 1]$$

$$\phi_m \in [0, 2\pi]$$

The definition of the acceptance function means that the sum:

$$\sum_i W_J(\Omega_i; x)\epsilon(\Omega_i)$$

is the same as the sum:

$$\sum_{accepted} W_J(\Omega_i; x)$$

where the *accepted* sum means that only events passing the analysis cuts are used. This gives the approximate value for the normalization integral:

$$N \sim \frac{1}{n} \sum_{accepted} W_J(\Omega_i; x)$$

This is not yet in optimal form since N depends on x. In evaluating the $ln\mathcal{L}$ function, if the x change, then the Monte Carlo integration must be performed again. This is very inefficient. Fortunately, the dependence on x is simple and can be factorized. The approximation $\varphi_x = \varphi_y = 0$ is assumed to simplify the discussion. In order to include the phases, one just uses the substitutions defined in Appendix B. The factored form can be written:

$$W_J(\Omega; x) = \sum_{i,j=0}^{2} W_J^{ij}(\Omega) x^i y^j$$

The normalization factorizes in the same manner:

$$N_J(x) = \sum_{i,j=0}^{2} N_J^{ij} x^i y^j$$

and the coefficients N_J^{ij} need only be evaluated once.

We now have a tractable expression for the $ln\mathcal{L}$ function:

$$ln\mathcal{L} = \sum_{evts} lnW_J(\Omega;x) - N_{evts} ln \sum_{i,j} N_J^{ij} x^i y^j$$

The standard minimization program MINUIT is then used to minimize the function $f = -ln\mathcal{L}$ and determine the values and errors for the parameters.

C.2 Evaluating the Fit Results

Once the parameters are determined for the spin fits, the very important task of evaluating the significance of the results remains. The estimation of errors on the fit parameters has been discussed in detail in Appendix A, and will not be repeated here. The most important question is: which J^P hypothesis is most probable, and how unlikely are the other hypotheses. For a maximum likelihood fit, this question has no general answer. At best, for hypotheses which are members of the same family of functions, one can find a test statistic for comparing two hypotheses which has a known (χ^2) distribution in the limit of large event samples. For the present case, even this asymptotic property is not available.

The χ^2 technique discussed in Appendix A is not very well suited to the fits performed here. There are two reasons for this. One is that the fit is three dimensional, and the one dimensional projections do not contain all the information. The more serious problem is that the acceptance function was never explicitly evaluated. This means that there is no explicit form for the function which has been fit to the data, and using Eqn. (A-9) becomes impossible. However, one would like to know the shapes of the angular distributions that correspond to the fit values of the parameters. If the acceptance function were known, then the projection for

one of the variables could be evaluated:

$$P(\cos\theta_\gamma) = \int d\cos\theta_m \int d\phi_m \epsilon(\theta_\gamma, \theta_m, \phi_m) W_J(\theta_\gamma, \theta_m, \phi_m; x)$$

and plotted. The technique which is used instead is to generate Monte Carlo distributions with shapes that correspond to those expected for the fit results. This can be done by taking the uniformly distributed Monte Carlo events in the normalization sample and weighting them with the angular correlation function $W_J(\theta_\gamma, \theta_m, \phi_m; x)$. The resulting weighted histograms indicate the expected distribution for each of the variables and can be compared directly with the observed distributions. The acceptance corrections are implicitly present in the normalization sample. This comparison gives an indication of how well the fit results match the real distributions. The Monte Carlo expected results can be used to define a χ^2 for the one dimensional angular distributions. Such a test statistic has been defined and used for the $\cos\theta_m$ angular distribution, since it contains the most information. The correct normalization for this statistic is somewhat difficult, since it contains errors due to limited Monte Carlo statistics as well as potential systematic differences between the Monte Carlo and the real data. The conclusion is that this fitting procedure has no simple, conventional indicator of 'goodness-of-fit'.

An alternate approach to evaluating the fit results relies more heavily on the Monte Carlo simulation, but it has the advantage of taking the true statistics and systematics of the problem into account. The technique is to generate a large representative sample of Monte Carlo events and then select many independent sub-samples (experiments), each one the same size as the real data sample. The full spin analysis is applied to each Monte Carlo experiment (sub-sample) in this ensemble, and the values of the $ln\mathcal{L}$ and the fit parameters are tabulated. This gives a distribution of expected likelihoods which can be compared to the results from

the real data. It also gives a distribution of the measured parameters for known input values.

There are many benefits which arise from this technique.

1. It contains no explicit parameterization of the statistical fluctuations, but instead generates them using the known underlying statistics of the measurement process which are contained in the MARK III Monte Carlo. Therefore, it should have no problems with small statistics experiments.

2. The results of the ensemble of experiments serve to normalize the mean and variance for the likelihood. This can be done both for the correct hypothesis and for the incorrect hypothesis. It provides a measure of 'goodness-of-fit' for the correct hypothesis (this is the 'significance' of the test, in statistical language) as well as providing a measure of the discrimination against the incorrect hypothesis (this is the 'power' of the test, in statistical language).

3. The results of the Monte Carlo experiments check that the errors on the fit parameters are in agreement with the distribution of measured parameters. In addition, if there are any systematic biases in the fitting procedure, they will be easily observable. Such systematic biases are difficult to avoid in the presence of acceptance corrections which distort the observed event spectrum, since these distortions may be similar in shape to the theoretical fit function.

For these reasons, this Monte Carlo technique is very powerful and will be used to understand the significance of the results of the spin analysis.

References

1. B. J. Bjorken and S. L. Glashow, Phys. Lett. **11**, 255 (1964).

2. S. L. Glashow, J. Iliopoulos and L. Maiani, Phys. Rev. **D2**, 1285 (1970).

3. M. K. Gaillard and B. W. Lee, Phys. Rev. **D10**, 897 (1974).

4. J. J. Aubert *et al.*, Phys. Rev. Lett. **33**, 1404 (1974);
   J. E. Augustin *et al.*, Phys. Rev. Lett. **33**, 1406 (1974).

5. S. Okubo, Phys. Lett. **5**, 165 (1963);
   G. Zweig, CERN Preprints CERN-TH-401,402,412 (1964);
   J. Iizuka, Prog. Theor. Phys. Suppl. **37-38**, 21 (1966).

6. T. Appelquist and H. D. Politzer, Phys. Rev. Lett. **34**, 43 (1975);
   Phys. Rev. Lett. **34**, 365 (1975).

7. M. Chanowitz, Phys. Rev. **D12**, 918 (1975).

8. T. Appelquist, R. M. Barnett, and K. Lane, Ann. Rev. Nucl. Sci. **28**, 387 (1978).

9. P. B. Mackenzie and G. P. Lepage, Phys. Rev. Lett. **47**, 1244 (1981);
   P. B. Mackenzie and G. P. Lepage, in *Proceedings of Conference on Perturbative QCD*, Tallahassee (1981).

10. S. J. Brodsky, G. P. Lepage and P. B. Mackenzie, Phys. Rev. **D28**, 228 (1983).

11. A. Ore and J. L. Powell, Phys. Rev. **75**, 1696 (1949).

12. S. J. Brodsky, T. A. DeGrand, R. R. Horgan and D. G. Coyne, Phys. Lett. **73B**, 203 (1978);
K. Koller and T. Walsh, Nucl. Phys. **B140**, 449 (1978).

13. M. T. Ronan *et al.*, Phys. Rev. Lett. **44**, 367 (1980);
D. L. Scharre *et al.*, Phys. Rev. **D23**, 43 (1981).

14. A. Billoire *et al.*, Phys. Lett. **80B**, 381 (1979);
R. Lacaze and H. Navelet, Nucl. Phys. **B186**, 247 (1981).

15. M. Creutz, L. Jacobs and C. Rebbi, Phys. Rep. **95**, 201 (1983).

16. H. Fritzsch and M. Gell-Mann, in *Proceedings of the XVI International Conference on High Energy Physics*, Batavia, Illinois (1972);
H. Fritzsch and P. Minkowski, Nuovo Cim. **30A**, 393 (1975).

17. F. E. Close, in *Conference on Unified Theories and their Experimental Tests*, Venice, Italy, (1982).

18. K. Gottfried, in *Proceedings of the International Europhysics Conference on High Energy Physics*, Brighton (1983).

19. D. Hitlin (private communication).

20. D. L. Scharre *et al.*, Phys. Lett. **B97**, 329 (1980).

21. C. Edwards *et al.*, Phys. Rev. Lett. **49**, 259 (1982).

22. C. Edwards *et al.*, Phys. Rev. **D25**, 3065 (1982).

23. D. L. Scharre, in 10^{th} *International Symposium on Lepton and Photon Interactions at High Energy*, Bonn (1981).

24. M. E. B. Franklin, Thesis, SLAC Report No. 254, (1982).

25. C. Edwards *et al.*, Phys. Rev. Lett. **48**, 458 (1982).

26. A preliminary form of the MARK II analysis can be found in:
E. D. Bloom, in *Proceedings of 21st International Conference on High Energy Physics*, Paris (1982).
The figure shown is from the preliminary analysis, and used slightly different cuts than those used for the final analysis.

27. D. Bernstein *et al.*, SLAC Preprint SLAC-PUB-3222 (1983), Submitted to Nucl. Instrum. and Methods.

28. J. Roehrig *et al.*, SLAC Preprint SLAC-PUB-3199 (1983), Submitted to Nucl. Instrum. and Methods.

29. J. S. Brown *et al.*, SLAC Preprint SLAC-PUB-3180 (1983), Submitted to Nucl. Instrum. and Methods.

30. J. S. Brown, Ph. D. Thesis, University of Washington (1984).

31. The barrel shower counter is described in :
K. Bunnell *et al.*, Nucl. Instrum. and Methods **219**, 479 (1984);
The endcap shower counters are described in :
R. Fabrizio *et al.*, UC Santa Cruz Preprint SCIPP 83/23 (1984), Submitted to Nucl. Instrum. and Methods.

32. J. Thaler *et al.*, IEEE Trans. Nucl. Sci. NS-30, 236 (1982).

33. A. L. Spadafora, Ph. D. Thesis, University of Illinois (1984).

34. Particle Data Group, Review of Particle Properties, LBL-100 Revised (1982).

35. This association is slightly post-hoc, but was pointed out by H. J. Willutzki, (Private communication).

36. Thanks to A. L. Spadafora, who implemented an algorithm of Kleiss: R. H. P. Kleiss, PhD. thesis, Leiden University (1982).

37. Ch. Berger in Proceedings of the 1983 International Symposium on Lepton and Photon Interactions, Cornell, 1983 and references contained therein.

38. M. E. B. Franklin (Private communication); J. L. Rosner and S. F. Tuan Phys. Rev. **D27**, 1544 (1983).

39. W. T. Eadie *et al.*,"Statistical Methods in Experimental Physics" (North Holland, Amsterdam 1971).

40. L. Montanet, Rep. Prog. Phys. **46**, 337 (1983).

41. A. G. Frodesen *et al.*, *Probability and Statistics in Particle Physics* (Universitatsforlaget, Bergen, 1979).

42. N. Wermes, XIX Rencontre de Moriond, La Plagne, France (1984), and SLAC-PUB-3312 (1984).

43. H. J. Lipkin and H. R. Rubenstein, Phys. Lett. **76B**, 324 (1978).

44. D. L. Scharre, VI International Conference on Experimental Meson Spectroscopy (1980).

45. B. Louis, Ph. D. Thesis, Universite de Paris-Sud (1984).

46. R. Brandelik *et al.*, Phys. Lett. **74B**, 292 (1978).

47. G. Alexander *et al.*, Phys. Lett. **76B**, 652 (1978).

48. J. L. Rosner, Phys. Rev. **D24**, 1347 (1981).

49. J. F. Donoghue, K. Johnson, and B. A. Li, Phys. Lett. **99B**, 416 (1981).

50. J. F. Donoghue, Phys. Rev. **D25**, 1875 (1982).

51. M. Krammer, Phys. Lett. **74B**, 361 (1978).

52. J. G. Körner, J. H. Kühn and H. Schneider, Phys. Lett. **120B**, 444 (1983); J. G. Körner, M. Krammer, J. H. Kühn and H. Schneider, Nucl. Phys. **B229**, 115 (1983).

53. B. A. Li and Q. X. Shen, Phys. Lett. **126B**, 125 (1983).

54. F. E. Close, Phys. Rev. **D27**, 311 (1983).

55. K. Wacker, XVIII Rencontre de Moriond, La Plagne, France (1983).

56. D. L. Burke *et al.*, Phys. Rev. Lett. **49**, 632 (1982).

57. This result is based on a calculation performed with the guidance of M. Peskin. The calculation starts with the phenomenological Lagrangian:

$$\mathcal{L} = Tr\left[\tilde{f}_{\mu\nu}\{\partial^\mu\tilde{\pi}, \partial^\nu\tilde{\pi}\}\right]$$

where $\tilde{f}$ is the $J^P = 2^+$ octet and $\tilde{\pi}$ is the $J^P = 0^-$ octet. The normalization for the $SU(3)$ matrices is:

$$Tr[\lambda^a, \lambda^{b\dagger}] = \frac{1}{2}\delta^{ab}$$

$$\eta_0 = \frac{1}{\sqrt{6}}\begin{pmatrix} 1 & & \\ & 1 & \\ & & 1 \end{pmatrix} \qquad \eta_8 = \frac{1}{\sqrt{12}}\begin{pmatrix} 1 & & \\ & 1 & \\ & & -2 \end{pmatrix}$$

$$f' = \frac{1}{\sqrt{2}} \begin{pmatrix} 0 & & \\ & 0 & \\ & & 1 \end{pmatrix} \qquad K^+ = \frac{1}{\sqrt{2}} \begin{pmatrix} 0 & 1 & \\ & 0 & 0 \\ & & 0 \end{pmatrix}$$

In calculating the rate for identical particles, there are two factors to be included: a factor of 2 in the amplitude for counting and a factor of 1/2 in the rate for phase space. The results are then:

$$\Gamma(f' \to \eta_8\eta_8) = 2\left(\frac{\sqrt{2}}{3}\right)^2 = \frac{4}{9}$$

$$\Gamma(f' \to \eta_0\eta_0) = 2\left(\frac{\sqrt{2}}{6}\right)^2 = \frac{1}{9}$$

$$\Gamma(f' \to K^+K^-) = \left(\frac{\sqrt{2}}{2}\right)^2 = \frac{1}{2}$$

This leads to the result that the ratio of $f' \to \eta\eta$ to $f' \to K\bar{K}$ is 4/9.

58. N. M. Cason *et al.*, Phys. Rev. Lett. **48**, 1316 (1982).

59. S. Godfrey, R. Kokoski and N. Isgur, University of Toronto Preprint 84-0293.

60. An alternate point of view has been suggested by W. Dunwoodie (private communication). He proposes the following mass estimates for excited states:

$$\text{for radial excitations } (\Delta n = 1): \quad \overline{\Delta m^2} = 1.20$$

$$\text{for orbital excitations } (\Delta l = 1): \quad \overline{\Delta m^2} = 1.20$$

This leads to the result:

$g(1690)$	$[l = 2\ f(1270)]$	$m = 1.68$
$h(2040)$	$[l = 3\ f(1270)]$	$m = 2.00$
h'	$[l = 3\ f'(1515)]$	$m = 2.17$
	$[n = 1\ f(1270)]$	$m = 1.68$
	$[n = 1\ f'(1515)]$	$m = 1.87$

If this pattern is further modified by a possible mixing scheme in which the orbital excitations are ideally mixed and the radial excitations are not, then one concludes that the $\theta(1700)$ could be a superposition of two states: the radially excited $f(1270)$ and the radially excited $f'(1515)$. In this scheme, the structure seen in $\gamma\pi\pi$ is the $h(2040)$ and the $\xi(2220)$ is the h'.

61. I. Cohen, N. Isgur, and H. J. Lipkin, Phys. Rev. Lett. **48**, 1074 (1982).

62. M. Chanowitz and S. Sharpe, Nucl. Phys. **B222**, 211 (1983).

63. T. Barnes and F. E. Close, Nucl. Phys. **B224**, 241 (1983).

64. M. Chanowitz and S. Sharpe, LBL Preprint LBL-16489 (1983).

65. R. Jaffe, Phys. Rev. **D15**, 267 (1977).

66. M. Chanowitz, 1981 Division of Particles and Fields of American Physical Society, Santa Cruz, 1981.

67. J. Weinstein and N. Isgur, Phys. Rev. Lett. **48**, 659 (1982);
J. Weinstein and N. Isgur, Phys. Rev. **D27**, 588 (1983).

68. M. Teper, Preprint LAPP-TH-91, Invited talk at 1983 Int. Europhysics Conference on High Energy Physics, Brighton, 1983.

69. K. Ishikawa, A. Sato, G. Schierholz, M. Teper, DESY Preprint DESY 83-061 (1983).

70. T. DeGrand *et al.*, Phys. Rev. **D12**, 2060 (1975).

71. T. DeGrand and R. Jaffe, Ann. Phys. **100**, 425 (1976).

72. M. Chanowitz, Proc SLAC Summer Institute, Ed. A. Mosher (1981).

73. C.Rebbi, Phys. Rev. **D12**, 2407 (1975); Phys. Rev. **D14**, 2362 (1976).

74. C. E. Carlson, T. H. Hansson and C. Peterson, Phys. Rev. **D27**, 1556 (1983); Preprint Print-84-0078 (1984);
T. Barnes, F. E. Close and S. Monaghan, Phys. Lett. **110B**, 159 (1982).

75. M. A. Shifman, A. I. Vainshtein, V. I. Zakharov, Nucl. Phys. **B147**, 385 (1979); Nucl. Phys. **B147**, 448 (1979).
V. A. Novikov, M. A. Shifman, A. I. Vainshtein, V. I. Zakharov, Nucl. Phys. **B165**, 67 (1980);
V. A. Novikov, M. A. Shifman, A. I. Vainshtein, V. I. Zakharov, Nucl. Phys. **B191**, 301 (1981).

76. J. M. Cornwall and A. Soni, Phys. Lett. **120B**, 431 (1983).

77. D. Robson, Nucl. Phys. **B130**, 328 (1977).

78. A. Soni, UCLA Preprint UCLA-83-TEP-6, Non-Perturbative QCD Workshop, Stillwater, Oklahoma (1983).

79. H. J. Lipkin Phys. Lett. **109B**, 326 (1982);
P. M. Fishbane *et al.*, NBS Preprint Print-81-0896 (1981).

80. S. Meshkov, Int. Conf. on Experimental meson Spectroscopy, Upton, N.Y. (1983);
P. M. Fishbane UCLA Preprint UCLA-82-TEP-18 (1982).

81. M. Chanowitz, Proc. XIV International Conference on Multi-Particle Dynamics at High Energy (1983).

82. P. Pascual and R. Tarrach, Phys. Lett. **113B**, 495 (1982).

83. J. L. Rosner, Phys. Rev. **D27**, 1101 (1983);
J. L. Rosner and S. F. Tuan, Phys. Rev. **D27**, 1544 (1983).

84. H. J. Schnitzer, Nucl. Phys. **B207**, 131 (1982).

85. J. Schechter, Phys. Rev. **D27**, 1109 (1983).

86. B. F. L. Ward, Print-84-0520 (1984).

87. K. Senba and M. Tanimoto, Ehime University Preprint EHU-84-01.

88. H. E. Haber and G. L. Kane, SLAC-PUB-3209 (1983).

89. R. S. Willey, University of Pittsburgh Preprint PITT-17-83.

90. R. M. Barnett, G. Senjanovic, L. Wolfenstein and D. Wyler, Phys. Lett. **136B**, 191 (1984);
R. M. Barnett, G. Senjanovic and D. Wyler, Santa Barbara Preprint NSF-ITP-84-45.

91. F. Wilczek, Phys. Rev. Lett. **39**, 1304 (1977).

92. A. D. Linde, Phys. Lett. **70B**, 306 (1977);
S. Weinberg, Phys. Rev. Lett. **36**, 294 (1976).

93. S. Behrends *et al.*, Phys. Lett. **137B**, 277 (1984).

94. M. Ogg, Cornell preprint CLNS-84/604(1984).

95. H. E. Haber, SLAC-PUB-3193 (1983).

96. M. Shatz, Caltech Preprint CALT-68-1089 (1983).

97. E. Byckling and K. Kajantie, *Particle Kinematics* (John Wiley and Sons, New York, 1973).

98. M. Abramowitz and I. A. Stegun *Handbook of Mathematical Functions* (Dover, New York, 1970).

99. F. James and M. Roos, CERN Internal Report D506 (1977); F. James and M. Roos, Computer Phys. Comm. **10**, 343 (1975).

100. W. T. Eadie *et al.*, *Statistical Methods in Experimental Physics* (North Holland, Amsterdam, 1971); A. G. Frodesen *et al.*, *Probability and Statistics in Particle Physics* (Universitatsforlaget, Bergen, 1979).

101. J. D. Richman, Caltech Report CALT-68-1148 (1984).

102. M. Jacob and G. C. Wick, Ann. Phys. **7**, 404 (1959).

103. J. R. Johnson *et al.*, Nucl. Instrum. and Meth. **204**, 261 (1983).

104. G. Ascoli and B. Eisenstein, Internal MARK III Note (1983).

105. T. Lund, CERN Preprint CERN-HS-RP/067, (1981).